Department of Physics

Master thesis

Supercell-based characterization of hyperbolic tight-binding models

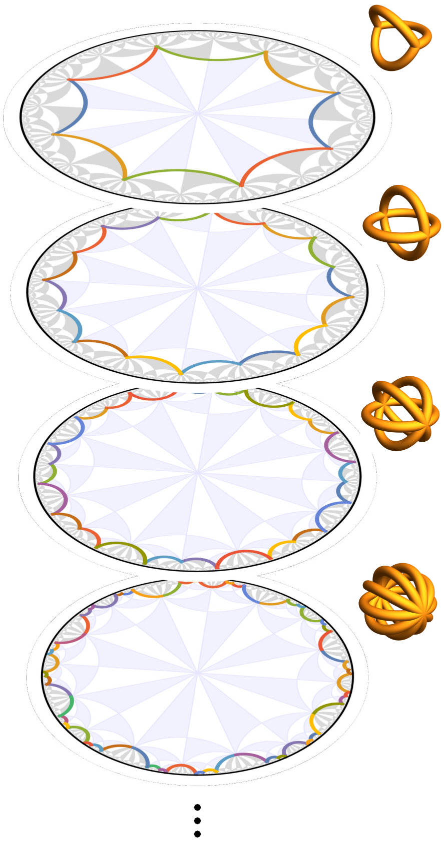

Author: Marcelo Looser
BSc UZH Physics, University of Zürich, CH

Thesis advisor: Prof. Dr. Tomáš Bzdušek
Co-advisor: Dr. Patrick M. Lenggenhager

May 27, 2024

Contents

Remarks:

- The Einstein summation convention over repeated indices is implied unless specified.
- We will use natural units, unless indicated otherwise, such that $\hbar = e = c = 1$ where $\hbar$ is the reduced planck constant, $-e$ is the electron charge and c is the speed of light.
- All figures depicting the Poincaré disk and hyperbolic lattices were produced with the **HyperBloch** [1] package in Mathematica in tandem with the **HyperCells** [2] package in GAP, developed by P. M. Lenggenhager et al. [3].

1 Introduction

Hyperbolic lattices constitute a novel experimental platform with an emergent negative curvature. These lattices are regularly tiled by p-sided polygons that meet with q identical copies at each corner, denoted by $\{p,q\}$ in the **Schläfli notation**, with $(p-2)(q-2) > 4$, [3]. Recent experimental realizations triggered a staidly growing interest for experimental and theoretical studies, which aim to investigate emergent physical properties. These physical phenomena range from elasticity considerations to quantum gravity. The intrinsic negative curvature of these systems may facilitate quantum error correction codes [4], shed light on the holographic principle [5, 6], enable the engineering of new meta-materials and provides an intriguing new playground for the study of topological phases in condensed matter physics [7–13].

This field of research has been fueled by experimental works of two principal set-ups. A. J. Kollár et al. [14] have constructed the first experimental realization of a two-dimensional quantum hyperbolic lattice. They have built a hyperbolic circuit quantum electrodynamical network through the use of interconnected superconducting resonators, which exhibit flat bands in the density of states. This set-up enables the study of quantum mechanical properties in curved spaces through photonics. Further, an electric circuit network emulating classical hyperbolic lattices was built by P. M. Lenggenhager et al. [15]. They have demonstrated that signals propagating in the electric circuit travel on the geodesics of hyperbolic space. These experimental realizations have elevated two-dimensional hyperbolic lattices from purely theoretical academic concepts to physically realizable systems for the study of emergent physical phenomena on curved spaces.

The intrinsic negative curvature of hyperbolic lattices gives rise to remarkable features that are in a sharp distinction with Euclidean lattices. Recall that the Bloch theorem is induced when endowing a crystal lattice on regular tessellated 2D Euclidean space with periodic boundary conditions. As such, the unit cell is compactified on a closed Riemann surface of genus-one and the Brillouin zone (BZ) can be understood as a 2D torus. As a result, the Euclidean lattice and its associated BZ torus have the same physical dimension. The corresponding Hilbert space is separable and is decomposed into blocks corresponding to various momenta in the BZ torus, which drastically improves the computational difficulty.

In contrast, periodic boundary conditions and the corresponding notion of the Bloch theorem become more subtle and involved in the hyperbolic lattice. The unit cells of a hyperbolic lattice cannot be compactified on a closed Riemann surface of genus-one, but on higher genus surfaces. Additionally, translations in hyperbolic spaces do in general not commute, thus the Bloch theorem has to be generalize in order to properly incorporate the non-Abelian translation groups [16–19].

1.1 State of the art

A generalization of the Bloch theorem is of fundamental importance for any fruitful attempt at a theoretical or computational characterization of models on lattices in the hyperbolic plane. J. Maciejko et al. [19] have developed such a theory, denoted as hyperbolic band theory (HBT), for the $\{8,8\}$-lattice. It generalizes the Abelian Bloch theorem by means of algebraic geometry. They have considered a large class of Hamiltonians obeying the symmetry of the underlying hyperbolic lattice. The construction of collections of Bloch eigenstates was shown to be feasible. Further, I. Boettcher et al. [16] have generalized the notions of Euclidean crystallography to hyperbolic lattices. The study of hyperbolic geometry on higher genus Riemann surfaces reveals that $\{p,q\}$-hyperbolic lattices of regular Bravais lattices can be classified into sets of common properties. They have derived a list of example hyperbolic lattices by using this classification methodology, which lays the foundation for the application of concepts in condensed matter studies on hyperbolic lattices.

In a subsequent work conducted by D. M. Urwyler et al. [13], exact digitalization (ED) and HBT was used in order to study the Haldane model [20] and a simplified Kane-Mele model on the $\{8,3\}$-lattice. By applying the classification of the hyperbolic lattices of Ref. [16] they were able to implement the models on hyperbolic lattices and have revealed topological phases by means of non-vanishing first Chern numbers. Additionally, the bulk-boundary correspondence was demonstrated by comparing the bulk and boundary density of states. Further, higher dimensional topological invariants, like the second Chern numbers, were calculated but turned out to be trivial in the models considered.

Independently of one another Z.-R. Liu et al. [8] and Y.-L. Tao et al. [10] were able to show manifestations of a higher-order topological phases in a selection of hyperbolic $\{p,q\}$-lattices. To this end, they used almost identical models, both related to the Kane-Mele model in [13]. They explicitly break time reversal symmetry T through a nearest neighbor hopping term, which renders the edge modes massive. Although the required rotational symmetry C_p is broken too, the Hamiltonian remains invariant under the combined $\mathrm{T}C_p$ symmetry and in combination with the remaining symmetries of the system, corner modes can be verified in finite flakes.

Localized states can be revealed in non-Hermitian models too as demonstrated by J. Sun et al. [9]. The inclusion of an additional complex staggered on-site potential in the Haldane model, together with the irregular boundary of hyperbolic lattice flakes, gives rise to corner modes. By modeling the boundary as 1D Zigzag chain enmeshed with the appropriate on-site and hopping terms, they were able to show that the complex on-site terms, acting as gains and losses, drive the localization of the boundary states due to their irregular distribution on the edge.

Real-space topology can also be considered in order to study the extreme localization of states in flat bands. Hyperbolic kagome- and Lieb-lattices were used by T. Bzdušek et al. [12] for a limited set of hyperbolic lattices. In analogy to the Euclidean case, they constructed compact localized states in real-space and extended noncontractible-loop states in order to show the characteristics of **flat-band degeneracy**. The analysis of Abelian as well as the first non-Abelian Bloch state characterization was shown to be in agreement with their proposed properties of flat bands in hyperbolic lattices.

Strong correlations in hyperbolic lattices, besides from flat bands, may also be used to study the interplay of general relativity (GR) and quantum field theory (QFT) in Minkowski space. The 2D hyperbolic spaces can be thought of as stereographical projections of hyperboloids embedded in 2+1 dimensional Minkowski space projected onto the 2D unit disk [15]. The holographic principle proposes that D+1 dimensional gravitational systems are equivalent to D dimensional QFT without gravity [6]. P. Basteiro et al. [5] have made a step towards a discrete holographic principle. They have applied an XXZ spin chain model to the boundaries of 2D hyperbolic lattices and studied the considered parameters of the model using renormalization group (RG) techniques. The holographic principle proposes that the translation symmetries of the bulk extend to the boundary. Although some aspects of the bulk-boundary correspondence were subject of their study, they propose that further studies will be needed.

Furthermore, the tools of QFT can also provide insights into challenges posed by the non-Abelian Bloch theorem. The non-Abelian gauge theories, known as Yang-Mills theories, in the minimal Standard model couple gauge bosons, like gluons in QCD, to quarks and leptons. QCD is enforced by a local SU(3) invariance of its Lagrangian, which enforces the aforementioned coupling by promoting the derivative to a covariant derivative. The gauge field coupling in hyperbolic lattices can be seen in the hyperbolic band theory, which reveals Bloch factors valued in $\mathrm{U}(N)$ [19]. G. Shankar et al. [21] have established a connection between HBT and Yang-Mills theories. They showed that the volume of the non-Abelian BZ is equal to the discretized path integral of the $\mathrm{U}(N)$ gauge field kinetic term. Further, they showed that the moments of the density of states of hyperbolic tight-binding models correspond to expectation values of Wilson loops in the BZ torus. In combination, these relations reveal the exact spectrum in the large-N limit. Effectively, this proves that the density of states computed by an appropriate random sampling method captures the thermodynamic limit exactly. However, they did not offer a method for implementing such a random sampling procedure.

Recently, P. M. Lenggenhager et al. [3] have developed a supercell-based Abelian hyperbolic band theory (AHBT) which provides a sampling strategy. Their approximative method enables the systematic access of non-Abelian Bloch states by utilizing group theory. They were able to demonstrate the convergence of their method to the thermodynamic limit, and by extension the work of Ref. [21] may yield the necessary tools providing deeper explanations.

1.2 Motivation and goals

Deriving Abelian as well as non-Abelian Bloch theorems requires the construction of finite clusters of lattice sites and the imposition of periodic boundary conditions (PBC), called PBC clusters [18]. However, for hyperbolic lattices the construction of PBC clusters is highly non-trivial and requires advanced notions from group theory. Besides one-dimensional irreducible representations the elements in the hyperbolic translation groups admit higher-dimensional irreducible representations, for which there is no explicit parameterization, making analytical descriptions challenging [3]. Previous studies have used AHBT on the primitive cell which do in general not capture the thermodynamic limit. Alternatively, they have used brute force exact digitalization, which is computationally costly. Therefore, these circumstances motivate the application of approximative methods.

As aforementioned, P. M. Lenggenhager et al. [3] have very recently developed a method that computationally outperforms the previous approaches. Through the application of the supercell method they were able to access non-Abelian Bloch states by considering one-dimensional irreducible representations of reduced translation groups. Specifically, they suggested to apply AHBT to a appropriately constructed sequence of supercells, assembled as increasingly large aggregates of the primitive cells to supercells, and showcased the convergence of this method by selected hyperbolic tight-binding models. In conjunction, P. M. Lenggenhager has implemented the supercell method within a Mathematica and GAP package [1, 2].

As such, the main objective of this thesis is the study of diverse aspects of topology and band theory in hyperbolic lattices accessed through the use of the supercell method. We aim to explore and broaden some of the recent studies in these systems such as higher-order topological phases [3, 8, 10], anomalous quantum Hall effects [7, 13], flat bands in realizations of Lieb lattices [12, 22, 23] and **non-Hermiticity driven** topological phenomena [9].

2 Symmetries of regular Euclidean lattices

Lattices in the Euclidean plane present vast and diverse platforms for the study of condensed matter physics. A substantial amount of progress in understanding emergent physical properties and their topological characterization [24–26] has been conducted. In this chapter we will review the fundamental notions for the description of lattices in the Euclidean plane, followed by a review of the Bloch theorem in order to study bulk properties in these systems. We will do this through the application of group theory in preparation for the description of lattices in the hyperbolic plane.

2.1 Euclidean spaces

The Euclidean plane is a two-dimensional metric space $\mathbb{R}^2$ with metric $\eta_E^{ij} = \delta_{ij}$, where $i, j \in \{1, 2\}$. Spatial symmetry operations such as rotations and translations in the Euclidean plane are intuitive, as these operations commute, rendering their symmetry groups Abelian. We can use this fact to establish a first comprehensive basis for our future studies in the hyperbolic plane.

2.2 Euclidean lattices

In this section, we will review some of the basic group theoretical notions for the study of regular lattices in two spatial dimensions, based largely on [27] and [16, 28, 29]. These tools will play an essential role in our pursuit of understanding and modeling regular lattices in hyperbolic spaces.

The symmetry operations that leave a regular lattice invariant form an infinite group called **space group** $\mathcal{S}$. In two dimensions they take the form:

$$\mathcal{S} = \bigcup_i \{R_i|\mathbf{v}_i\}\mathcal{T}, \tag{2.1}$$

where $R_i \in \mathrm{O}(2)$, $\mathbf{v}_i \in \mathbb{R}^2$ and $\mathcal{T}$ is the group of translations. As such, the **translation group** $\mathcal{T}$ constitutes translation vectors $\mathbf{t}$ that leave the regular lattice invariant. These vectors can be decomposed into a set of linearly independent vectors $\mathbf{a}_i$, the **Bravais vectors**, with $i = 1, 2$ which generate the translation group $\mathcal{T}$:

$$\mathcal{T} = \left\{\{\mathbb{1}|\mathbf{t}\} \mid \mathbf{t} = \sum_{i=1}^{2} n_i\mathbf{a}_i\,,\, n_i \in \mathbb{Z}\right\} \cong \mathbb{Z}^2. \tag{2.2}$$

The multiplication of two elements in $\mathcal{S}$, and as a special case of elements in $\mathcal{T}$, is defined as:

$$\{R_2|\mathbf{v}_2\}\{R_1|\mathbf{v}_1\} = \{R_2R_1|R_2\mathbf{v}_1 + \mathbf{v}_2\}. \tag{2.3}$$

A general vector $\mathbf{x} \in \mathbb{R}^2$ and some function $f(\mathbf{x})$ are defined to transform under a general symmetry $\{R|\mathbf{v}\}$ as:

$$\begin{aligned} \{R|\mathbf{v}\}\,\mathbf{x} &= R\mathbf{x} + \mathbf{v}, \\ \{R|\mathbf{v}\}\,f(\mathbf{x}) &= f(\{R|\mathbf{v}\}^{-1}\mathbf{x}) = f(R^{-1}(\mathbf{x} - \mathbf{v})). \end{aligned} \tag{2.4}$$

The inverse of an element $\{R|\mathbf{v}\} \in \mathcal{S}$ is:

$$\begin{aligned} &\{R|\mathbf{v}\}^{-1} = \{R^{-1}| - R^{-1}\mathbf{v}\}, \\ \text{then} \quad &\{R|\mathbf{v}\}\{R|\mathbf{v}\}^{-1} = \{RR^{-1}|R(-R^{-1}\mathbf{v}) + \mathbf{v}\} = \{\mathbb{1}|\mathbf{0}\}. \end{aligned} \tag{2.5}$$

where $\mathbb{1} \in \mathrm{O}(2)$ and $\mathbf{0} \in \mathbb{Z}^2$ are the corresponding identity elements. Given the definition of the space group $\mathcal{S}$, it is apparent that the translation group $\mathcal{T}$ is a subgroup of $\mathcal{S}$, denoted as $\mathcal{T} < \mathcal{S}$. Furthermore, $\mathcal{T}$ exhibits another property constraining the subgroup relation. Given an element $\{R|\mathbf{v}\} \in \mathcal{S}$ and an element $\{\mathbb{1}|\mathbf{t}\} \in \mathcal{T}$ we see:

$$\begin{aligned} \{R|\mathbf{v}\}\{\mathbb{1}|\mathbf{t}\}\{R|\mathbf{v}\}^{-1} &= \{R|\mathbf{v}\}\{\mathbb{1}|\mathbf{t}\}\{R^{-1}| - R^{-1}\mathbf{v}\} \\ &= \{\mathbb{1}| - RR^{-1}\mathbf{v} + R\mathbf{t} + \mathbf{v}\} \\ &= \{\mathbb{1}|R\mathbf{t}\}, \end{aligned} \tag{2.6}$$

therefore, $\{R|\mathbf{v}\}\{\mathbb{1}|\mathbf{t}\}\{R|\mathbf{v}\}^{-1} \in \mathcal{T}$. This implies that the translation group $\mathcal{T}$ is a **normal subgroup** of $\mathcal{S}$, denoted as $\mathcal{T} \lhd \mathcal{S}$. Consequently, the quotient $\mathcal{S}/\mathcal{T}$ forms a group:

$$\tilde{\mathcal{S}} \equiv \mathcal{S}/\mathcal{T} = \{\{R_i|\mathbf{v_i}\}\mathcal{T} \mid \{R_i|\mathbf{v_i}\} \in \mathcal{S}\}. \tag{2.7}$$

The elements in the quotient group $\tilde{\mathcal{S}}$ consists of the set of **cosets** $\{R_i|\mathbf{v_i}\}\mathcal{T}$. We are free to choose an element $\{R_i|\mathbf{w}_i\}$ of each coset as a representative of that coset. A **coset** with a representative $\{R_i|\mathbf{w}_i\}$ is then denoted as:

$$[\{R_i|\mathbf{w}_i\}] \equiv \{R_i|\mathbf{v_i}\}\mathcal{T} \in \mathcal{S}/\mathcal{T}. \tag{2.8}$$

The set of **coset representatives** $\{R_i|\mathbf{w}_i\}$ is called a **transversal** $\mathrm{T}_{\mathcal{S}}(\mathcal{T})$. It is defined as a subset of the space group $\mathrm{T}_{\mathcal{S}}(\mathcal{T}) \subset \mathcal{S}$ such that for any coset $\{R_i|\mathbf{v_i}\}\mathcal{T}$ the intersection $\mathrm{T}_{\mathcal{S}}(\mathcal{T}) \cap \{R_i|\mathbf{v_i}\}\mathcal{T}$ contains only one element, the chosen $\{R_i|\mathbf{w}_i\}$.

If the space group is symmorphic, it is possible to choose the transversal to be a group. Further, we can define a reference unit cell by choosing the representatives in the transversal $\mathrm{T}_{\mathcal{S}}(\mathcal{T})$ appropriately, such that $C = \cup_{\{R|\mathbf{w}\} \in \mathrm{T}_{\mathcal{S}}(\mathcal{T})}\mathbf{w}$. Furthermore, subgroups of the space group can be identified whose elements leave a point $\mathbf{x}$ invariant called the **stabilizer subgroup**:

$$\mathcal{S}_{\mathbf{x}} = \{\{R_i|\mathbf{v_i}\} \in \mathcal{S} \mid \{R_i|\mathbf{v_i}\}\mathbf{x} = \mathbf{x}\,, \mathbf{x} \in \mathbb{R}^2\}. \tag{2.9}$$

The stabilizer subgroups, also referred to as **little groups**, are in general not normal subgroups of the space group. We may interpret space groups as defining infinite lattice with translated copies of the reference unit cell C by the **coset decomposition**:

$$\mathcal{S} = \bigcup_{\{R|\mathbf{w}\}\in \mathrm{T}_{\mathcal{S}}(\mathcal{T})} \{R|\mathbf{w}\}\mathcal{T}. \tag{2.10}$$

Further, we can define a group that is isomorphic to the quotient group $\tilde{\mathcal{S}}$, called the **point group** $\mathcal{P}$:

$$\mathcal{P} = \bigcup_{\{R|\mathbf{v}\}\in \mathcal{S}} R \cong \tilde{\mathcal{S}}. \tag{2.11}$$

Hence, the point group consists of all rotations and reflections devoid of their translation component. If the space group $\mathcal{S}$ is symmorphic, the point group is a subgroup of the space group $\mathcal{P} < \mathcal{S}$ and $\mathcal{S}$ is the **semi direct product** of $\mathcal{P}$ and $\mathcal{T}$, i.e. $\mathcal{S} = \mathcal{P} \ltimes \mathcal{T}$.

Further, let ϕ be a group homomorphism $\phi : \mathcal{S} \to \mathcal{P}$. The kernel of ϕ is given by $\ker(\phi) = \{\{\mathbb{1}|\mathbf{t}\} \in \mathcal{T} \mid \phi(\{\mathbb{1}|\mathbf{t}\}) = \mathbb{1}\}$, and thus it only consists of elements in the translation group. This, once again, implies that $\mathcal{T} \triangleleft \mathcal{S}$ since for any element $x \in \ker(\phi)$ and $s \in \mathcal{S}$:

$$\phi(s\,x\,s^{-1}) = \phi(s)\phi(x)\phi(s^{-1}) = \phi(s)\phi(s)^{-1} = \mathbb{1}. \tag{2.12}$$

The kernels of a group homomorphisms are always normal subgroups, which we will use extensively in order to construct hyperbolic lattices. However, before we discuss their construction, let us dwell in the Euclidean space to review the Bloch theorem and its manifestation in a selection of Euclidean models.

2.3 Bloch theorem

The usual derivation of Bloch theorem relies on the realization that the set of translation operators in $\mathcal{T}$ mutually commute, implying that they can be diagonalized simultaneously. The corresponding Hilbert space is rendered separable such that the individual blocks are labeled by irreducible representations of the translation group. The periodicity of the lattice then suggests to impose **periodic boundary conditions** on the reference unit cell boundaries. We then call the set of sites within the reference unit cell a periodic-boundary-condition cluster, or **PBC cluster** for short, [18]. The corresponding eigenstates, the Bloch eigenstates, span the Hilbert space.

However, we may as well use group theory in order to perform these classifications of eigenstates and eigenvalues in periodic systems. Therefore, let us review the Bloch theorem with the notions reviewed in Section 2.2.

To this end, let us impose periodic boundary conditions in two dimensions. This amounts to requiring the eigenstates $\psi(\mathbf{x})$ of the Hamiltonian to be constrained as:

$$\begin{aligned}\{\mathbb{1}|N_1\mathbf{a}_1 + N_2\mathbf{a}_2\}\psi(\mathbf{x}) &= \psi(\{\mathbb{1}|N_1\mathbf{a}_1 + N_2\mathbf{a}_2\}^{-1}\mathbf{x}) \\ &= \psi(\mathbf{x} - (N_1\mathbf{a}_1 + N_2\mathbf{a}_2)) = \psi(\mathbf{x})\end{aligned} \tag{2.13}$$

where $N_1, N_2 \in \mathbb{Z}$. The translation operators $\{\mathbb{1}|N_1\mathbf{a}_1\}$, $\{\mathbb{1}|N_2\mathbf{a}_2\}$ generate a group:

$$\mathcal{T}_{\mathrm{PBC}} = \Big\{\{\mathbb{1}|n_{i_1}N_1\mathbf{a}_1 + n_{i_2}N_2\mathbf{a}_2\} \mid n_{i_1}, n_{i_2} \in \mathbb{Z}\Big\} \cong N_1\mathbb{Z} \times N_2\mathbb{Z}. \tag{2.14}$$

We see by Eq. (2.6) that $\mathcal{T}_{\mathrm{PBC}}$ is a normal subgroup of $\mathcal{T}$, i.e. $\mathcal{T}_{\mathrm{PBC}} \lhd \mathcal{T}$, and thus the quotient of $\mathcal{T}/\mathcal{T}_{\mathrm{PBC}}$ forms a group. Recall that $\mathcal{T} \cong \mathbb{Z}^2$, then:

$$\mathcal{T}/\mathcal{T}_{\mathrm{PBC}} \cong \mathbb{Z}_{N_1} \times \mathbb{Z}_{N_2} \tag{2.15}$$

where $\mathbb{Z}_{N_j} = \mathbb{Z}/N_j\mathbb{Z} = \{0, 1, .., N_j - 1\}$. Analogous to the coset decomposition of the space group $\mathcal{S}$ in Eq. (2.10), the translation group $\mathcal{T}$ is given by:

$$\mathcal{T} = \bigcup_{\{\mathbb{1}|\mathbf{t}\}\in \mathrm{T}_{\mathcal{T}}(\mathcal{T}_{\mathrm{PBC}})} \{\mathbb{1}|\mathbf{t}\}\mathcal{T}_{\mathrm{PBC}} \tag{2.16}$$

where the transversal $\mathrm{T}_{\mathcal{T}}(\mathcal{T}_{\mathrm{PBC}})$ is the set of chosen representatives of each coset in $\mathcal{T}/\mathcal{T}_{\mathrm{PBC}}$. The number of elements in the quotient is called the **index** $|\mathcal{T} : \mathcal{T}_{\mathrm{PBC}}|$ and in this case it is $|\mathcal{T} : \mathcal{T}_{\mathrm{PBC}}| = N_1N_2$, also note that it is equal to the **order** of the quotient group denoted $|\mathcal{T}/\mathcal{T}_{\mathrm{PBC}}|$. The imposition of PBCs thus amounts to the determination of normal subgroups $\mathcal{T}_{\mathrm{PBC}}$ of the translation group $\mathcal{T}$ [18].

The cosets of $\mathcal{T}/\mathcal{T}_{\mathrm{PBC}}$ are sets of translations that act non-trivially on the PBC cluster. Each representative of a coset in the transversal $\mathrm{T}_{\mathcal{T}}(\mathcal{T}_{\mathrm{PBC}})$ may be chosen such that it is associated with a translation within the cluster. The number of sites within the PBC cluster corresponds to the index $N = |\mathcal{T} : \mathcal{T}_{\mathrm{PBC}}|$, for this reason we may at times also refer to PBC clusters as **size-N clusters**. The translation vectors in PBC clusters are thus:

$$\mathbf{t} = \sum_{i=1}^{2} n_i\mathbf{a}_i, \quad n_i \in \{0, 1, ..N_i - 1\}. \tag{2.17}$$

Since $\mathcal{T}/\mathcal{T}_{\mathrm{PBC}}$ is isomorphic to direct product of cyclic groups $\mathbb{Z}_{N_i}$, the **irreducible representations** of the elements in the cosets are one-dimensional [28]. Using the notation in [28] we find that the irreducible representations are given by:

$$D_{\mathbf{k}}(\{\mathbb{1}|\mathbf{t}\}) = e^{-i\mathbf{k}\cdot\mathbf{t}} \tag{2.18}$$

with

$$\mathbf{k} = \sum_{i=1}^{2} k_i \mathbf{b_i}, \quad k_i = \frac{m_i}{N_i}, \quad m_i \in \{0, 1, .., N_i - 1\} \tag{2.19}$$

and

$$\mathbf{b}_i \cdot \mathbf{a_j} = 2\pi\delta_{ij} \quad i, j = 1, 2 \tag{2.20}$$

where $\mathbf{b}_i$ are **reciprocal vectors** and $\mathbf{k}$ is the crystal momentum. Note, since the **character** of the irreducible representation of elements in the group $\mathbb{Z}_{N_1} \times \mathbb{Z}_{N_2}$ coincides with the irreducible representation, we will denote it as:

$$\chi_{\mathbf{k}}(\{\mathbb{1}|\mathbf{t}\}) \equiv D_{\mathbf{k}}(\{\mathbb{1}|\mathbf{t}\}). \tag{2.21}$$

In the thermodynamic limit $N_1, N_2 \to \infty$, $\mathbf{k}$ becomes dense such that the **Brillouin zone** (BZ) becomes continuous:

$$\mathrm{BZ} = \Big\{\mathbf{k} \in \mathbb{R}^2 \mid \mathbf{k} = \sum_{i=1}^{2} k_i \mathbf{b}_i, \quad k_i \in [0, 1)\Big\}. \tag{2.22}$$

The thermodynamic limit is thus the culmination of constructing an infinite sequence of suitable normal subgroups $\mathcal{T}_{\mathrm{PBC}} \triangleleft \mathcal{T}$ with increasing size-N clusters. Further, note that $\mathbf{k} \in (\mathbb{R}/2\pi\mathbb{Z})^2$ therefore the BZ can be associated with two-dimensional torus since $(\mathbb{R}/2\pi\mathbb{Z})^2 \cong \mathbb{T}^2$, which we denote as the **Brillouin zone torus**, or BZ torus. On the other hand, the imposed periodic boundary conditions on the refernce unit cell can be seen as a **compactification** on a closed **two-dimensional** Riemann-surface Σ with one hole isomorphic to a torus $\mathbb{T}^2$, where closed means Σ has no boundary. As such, the dimension of the BZ tours coincides with the dimension of the compactified unit cell [18].

Let us explicitly label the eigenstate $\psi(\mathbf{x})$ transforming in the representation (2.18) as $\psi_{\mathbf{k}}(\mathbf{x})$. Under a general translation $\{\mathbb{1}|\mathbf{t}\} \in \mathcal{T}$ the state $\psi_{\mathbf{k}}(\mathbf{x})$ transforms as:

$$\begin{aligned}\{\mathbb{1}|\mathbf{t}\}\psi_{\mathbf{k}}(\mathbf{x}) &= \psi_{\mathbf{k}}(\mathbf{x} - \mathbf{t}) \\ &= \chi_{\mathbf{k}}(\{\mathbb{1}|\mathbf{t}\})\psi_{\mathbf{k}}(\mathbf{x}) = e^{-i\mathbf{k}\cdot\mathbf{t}}\psi_{\mathbf{k}}(\mathbf{x}).\end{aligned} \tag{2.23}$$

Let $u_{\mathbf{k}}(\mathbf{x}) = e^{-i\mathbf{k}\cdot\mathbf{x}}\psi_{\mathbf{k}}(\mathbf{x})$ then:

$$\begin{aligned}u_{\mathbf{k}}(\mathbf{x} - \mathbf{t}) &= e^{-i\mathbf{k}\cdot\mathbf{x}}e^{i\mathbf{k}\cdot\mathbf{t}}\psi_{\mathbf{k}}(\mathbf{x} - \mathbf{t}) \\ &= e^{-i\mathbf{k}\cdot\mathbf{x}}\psi_{\mathbf{k}}(\mathbf{x}) = u_{\mathbf{k}}(\mathbf{x}).\end{aligned} \tag{2.24}$$

thus:

$$\psi_{\mathbf{k}}(\mathbf{x}) = e^{i\mathbf{k}\cdot\mathbf{x}} u_{\mathbf{k}}(\mathbf{x}), \qquad u_{\mathbf{k}}(\mathbf{x}+\mathbf{t}) = u_{\mathbf{k}}(\mathbf{x}) \tag{2.25}$$

which is the statement of Bloch's theorem. The function $u_{\mathbf{k}}(\mathbf{x})$ is known as the **cell-periodic Bloch state**.

2.4 Symmetries of Euclidean lattices

In the last section we have seen that the imposition of periodic boundary conditions reveals the transformation behavior of Bloch states $\psi_{\mathbf{k}}(\mathbf{x}) = e^{i\mathbf{k}\cdot\mathbf{x}} u_{\mathbf{k}}(\mathbf{x})$ and the periodicity of $u_{\mathbf{k}}(\mathbf{x})$ under a general translation $\{\mathbb{1}|\mathbf{t}\} \in \mathcal{T}$. We are now interested in the remaining symmetry operations of the space group $\mathcal{S}$, which will be useful in our pursuit of understanding topological phenomena in the Euclidean and hyperbolic space. Thus, let us briefly review how Bloch states transform under symmetry transformations of the space group $\mathcal{S}$ following Ref. [3].

A general symmetry transformation $\{R|\mathbf{v}\} \in \mathcal{S}$ transforms a Bloch state as:

$$\begin{aligned} \{R|\mathbf{v}\}\psi_{\mathbf{k}}(\mathbf{x}) &= \psi_{\mathbf{k}}(R^{-1}(\mathbf{x}-\mathbf{v})) \\ &= e^{i\mathbf{k}\cdot R^{-1}(\mathbf{x}-\mathbf{v})} u_{\mathbf{k}}(R^{-1}(\mathbf{x}-\mathbf{v})). \end{aligned} \tag{2.26}$$

The transformed state then transforms under a general translation $\{\mathbb{1}|\mathbf{t}\} \in \mathcal{T}$ as:

$$\begin{aligned} \{\mathbb{1}|\mathbf{t}\}\{R|\mathbf{v}\}\psi_{\mathbf{k}}(\mathbf{x}) &= \{R|\mathbf{v}+\mathbf{t}\}\psi_{\mathbf{k}}(\mathbf{x}) \\ &= e^{i\mathbf{k}\cdot R^{-1}(\mathbf{x}-\mathbf{v}-\mathbf{t})} u_{\mathbf{k}}(R^{-1}(\mathbf{x}-\mathbf{v}-\mathbf{t})) \\ &= e^{-i\mathbf{k}\cdot R^{-1}\mathbf{t}} e^{i\mathbf{k}\cdot R^{-1}(\mathbf{x}-\mathbf{v})} u_{\mathbf{k}}(R^{-1}(\mathbf{x}-\mathbf{v}) - R^{-1}\mathbf{t}) \\ &= e^{-i\mathbf{k}R^{-1}\cdot\mathbf{t}} \{R|\mathbf{v}\}\psi_{\mathbf{k}}(\mathbf{x}). \end{aligned} \tag{2.27}$$

We know that $R \in \mathrm{O}(2)$ and thus $R^{-1} = R^{\mathrm{T}}$. Using index notation, we see that:

$$\mathbf{k} \cdot R^{\mathrm{T}}\mathbf{y} = k_i R_j{}^i y^j = R_j{}^i k_i y^j = (R\mathbf{k}) \cdot \mathbf{y} \tag{2.28}$$

thus:

$$\{\mathbb{1}|\mathbf{t}\}\{R|\mathbf{v}\}\psi_{\mathbf{k}}(\mathbf{x}) = e^{-iR\mathbf{k}\cdot\mathbf{t}}\{R|\mathbf{v}\}\psi_{\mathbf{k}}(\mathbf{x}) = \chi_{R\mathbf{k}}(\{\mathbb{1}|\mathbf{t}\})\{R|\mathbf{v}\}\psi_{\mathbf{k}}(\mathbf{x}). \tag{2.29}$$

The momenta $\mathbf{k}$ of a transformed state $\{\mathbb{1}|\mathbf{t}\}\{R|\mathbf{v}\}\psi_{\mathbf{k}}(\mathbf{x})$ are therefore rigidly rotated by R and the transformed state thus transforms as a Bloch state. In conclusion, the symmetries of the lattice constrain the Hilbert space spanned by the Bloch states, which enables us to study how lattice symmetries are manifested.

2.5 Bloch Hamiltonian

The Bloch theorem implies that the Hamiltonian is block-diagonal in the quasiparticle basis $\{|\mathbf{k},\alpha\rangle\}_{\mathbf{k},\alpha}$ with each block spanning the Bloch states $\langle \mathbf{x} \,|\, \mathbf{k},\alpha\rangle = \psi_{\mathbf{k},\alpha}(\mathbf{x})$, where α captures additional degrees of freedom within the unit cell and $\mathbf{k} \in \mathbb{T}^2$, [27, 30]. As such, the Hamiltonian can be written as:

$$\mathcal{H} = \sum_{\mathbf{k},\mathbf{k}',\alpha,\beta} \langle \mathbf{k},\alpha|\mathcal{H}|\mathbf{k}',\beta\rangle |\mathbf{k},\alpha\rangle\langle \mathbf{k}',\beta| = \sum_{\mathbf{k},\mathbf{k}',\alpha,\beta} H^{\alpha\beta}(\mathbf{k})\delta_{\mathbf{k},\mathbf{k}'}|\mathbf{k},\alpha\rangle\langle \mathbf{k}',\beta|, \tag{2.30}$$

where $H(\mathbf{k})$ is known as the **Bloch Hamiltonian**. There are two most natural choices for the quasiparticle basis, which we will use in this thesis. Let us motivate why we will use both of them, by following the description in Ref. [27]. Consider a general tight-binding model on a lattice with N sites, written in second quantization:

$$\mathcal{H} = \sum_{i,j,\alpha,\beta} h_{ij}^{\alpha,\beta} c_i^{\alpha\dagger} c_j^{\beta}, \tag{2.31}$$

where α, β captures additional degrees of freedom within the unit cell and i, j are site indices. Further, consider an orbital $|j,\alpha\rangle = c_j^{\alpha\dagger}|0\rangle$ in the lattice localized at $\mathbf{r}_j^\alpha = \mathbf{R}_j + \boldsymbol{\delta}^\alpha$, where $\mathbf{R}_j$ denotes the unit cell position at the site j in the lattice and $\boldsymbol{\delta}^\alpha$ the position of the orbital relative to the site j in the unit cell. The elements of the quasiparticle basis can be written as the Fourier transform of orbitals [31]:

$$|\mathbf{k},\alpha\rangle_B = \frac{1}{\sqrt{N}}\sum_{j=1}^{N} e^{i\mathbf{k}\cdot\mathbf{R}_j}|j,\alpha\rangle\,, \quad |\mathbf{k},\alpha\rangle_P = \frac{1}{\sqrt{N}}\sum_{j=1}^{N} e^{i\mathbf{k}\cdot\mathbf{r}_j^\alpha}|j,\alpha\rangle, \tag{2.32}$$

where B stands for Bloch convention and P for periodic convention. They can be written in terms of the creation operators:

$$c_{B,\mathbf{k}}^{\alpha\dagger} = \frac{1}{\sqrt{N}}\sum_{j=1}^{N} c_j^{\alpha\dagger} e^{i\mathbf{k}\cdot\mathbf{R}_j}\,, \qquad c_{P,\mathbf{k}}^{\alpha\dagger} = \frac{1}{\sqrt{N}}\sum_{j=1}^{N} c_j^{\alpha\dagger} e^{i\mathbf{k}\cdot\mathbf{r}_j^\alpha}\,. \tag{2.33}$$

where $|\mathbf{k},\alpha\rangle = c_{\mathbf{k}}^{\alpha\dagger}|0\rangle$. The rewritten tight-binding Hamiltonian is:

$$\mathcal{H} = \sum_{\mathbf{k}\in\mathbb{T}^2}\sum_{\alpha,\beta} c_{\mathbf{k}}^{\alpha\dagger} H^{\alpha\beta}(\mathbf{k}) c_{\mathbf{k}}^{\beta}, \tag{2.34}$$

with Bloch Hamiltonians given by:

$$H_B^{\alpha\beta}(\mathbf{k}) = \sum_{l} h_l^{\alpha\beta} e^{-i\mathbf{k}\cdot(l+\boldsymbol{\delta}^\alpha-\boldsymbol{\delta}^\beta)}\,, \quad H_P^{\alpha\beta}(\mathbf{k}) = \sum_{l} h_l^{\alpha\beta} e^{-i\mathbf{k}\cdot l}. \tag{2.35}$$

The Bloch convention depends on the choice of unit cell, while the periodic convention does not. We will exclusively use the convention P for Euclidean lattices and convention B for hyperbolic lattices. The **unit-cell independent** convention P is more appropriate for the description of topological aspects [31]. On the other, convention B is a convenient choice for hyperbolic lattices as it is easier to construct corresponding Bloch Hamiltonians as we will see in the subsequent chapter.

3 Symmetries of regular hyperbolic lattices

The extension to lattices in the hyperbolic plane reveals subtle and unprecedented features, that are in a sharp distinction with lattices in the Euclidean plane. In recent years the interest to study these lattices has been growing, [3, 5, 7–12, 16–18, 21, 27, 32–34], fueled by the experimental realizations of hyperbolic lattices in Ref. [14, 15]. In this chapter, we will review the methodology to construct hyperbolic lattices through group theory. This enables us to comprehend and apply **Abelian hyperbolic band theory** on symmetrical aggregates of primitive cells to **supercells**. This method, called **supercell method**, developed in Ref. [3], will be the central tool to study hyperbolic lattices in this thesis. As such, our review will be largely based on Ref. [27] and [3].

3.1 Hyperbolic spaces

Before we describe the construction of hyperbolic lattices, let us illustrate the emergent negative curvature of the hyperbolic plane by reviewing selected aspects in Ref. [27, 35, 36]. Consider a metric space in $\mathbb{R}^{2+1}$. The metric in a 3 dimensional Euclidean space is given by the identity matrix $\eta_E^{\mu\nu} = \delta^{\mu\nu}$, where $\mu, \nu \in \{0, 1, 2\}$ with squared distance from the origin $\mathbf{x}^2 = \eta_E^{\mu\nu} x_\mu x_\nu = x_0^2 + x_1^2 + x_2^2$. In order to identify the hyperbolic plane we modify the Euclidean metric and abandon the Euclidean space. A modification by $\eta_M^{\mu\nu} = \mathrm{diag}(-1, 1, 1)$, with $\mathbf{x}^2 = -x_0^2 + x_1^2 + x_2^2$, leads us to the metric in a 3 dimensional **Minkowski space**, the **Minkowski metric**.

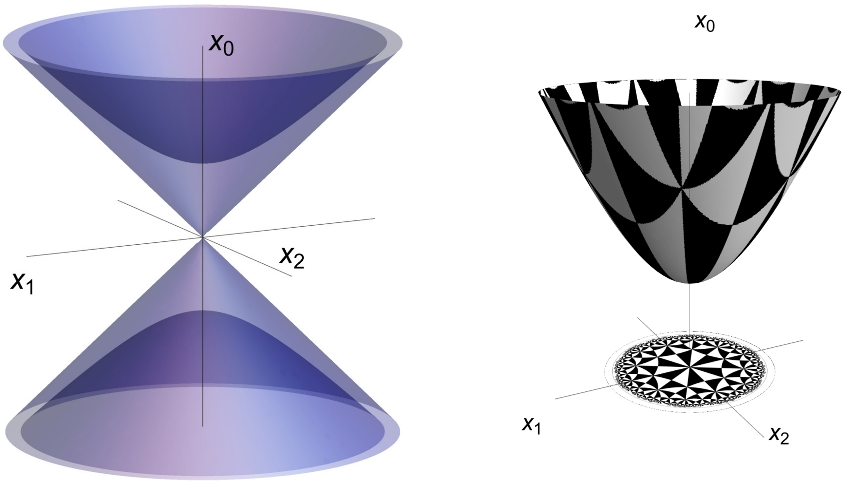

Figure 1: **Minkowski space in $2+1$ dimensions**. Left: Illustration of hyperboloids, dark violet, spanned by a set of points in $\mathbb{R}^{2+1}$ with constant squared distance from the origin. The set of null vectors $\eta_M^{\mu\nu} x_\mu x_\nu = 0$ are depicted as cones enveloping the hyperboloids. Figure reproduced from Ref. [36]. Right: Schematics of Poincaré disk model via stereographic projection.

We identify the hyperbolic plane with the upper violet hyperboloid depicted on the left of Fig. 1, which is the set of points with constant squared distance from the origin

$\{\mathbf{x} \in \mathbb{R}^{2+1} \mid \eta_M^{\mu\nu} x_\mu x_\nu = -\kappa^2\}$, where $0 < \kappa^2 \in \mathbb{R}$. We can define the so-called **hyperboloid model** H^2:

$$H^2 = \{\mathbf{x} \in \mathbb{R}^{2+1} \mid \eta_M^{\mu\nu} x_\mu x_\nu = -\kappa^2 \text{ with } x_0 > 0\}. \tag{3.1}$$

In analogy to the unit sphere $\{\mathbf{x} \in \mathbb{R}^{2+1} \mid \eta_E^{\mu\nu} x_\mu x_\nu = 1\}$ one can think of a hyperboloid $\{\mathbf{x} \in \mathbb{R}^{2+1} \mid \eta_M^{\mu\nu} x_\mu x_\nu = -1\}$ as a "sphere" with imaginary radius. However, unlike the sphere which is an embedding in $\mathbb{R}^3$ with constant positive curvature, a hyperboloid with constant negative curvature can not be embedded in $\mathbb{R}^3$ by Hilbert's theorem [37]. As such, we choose to work in the **Poincaré disk model**. This is the stereographic projection of the hyperboloid model (3.1) onto the unit disk parameterized by points in the complex plane [35], schematically depicted on the right of Fig. 1. The Poincaré disk $\mathbb{D}$ is defined as the set of points $z = x_1 + ix_2$:

$$\mathbb{D} = \{z \in \mathbb{C} : |z| < 1\}. \tag{3.2}$$

In order to obtain the corresponding metric, we need to construct the coordinate maps from the hyperboloid model H^2 to the Poincaré disk model $\mathbb{D}$. This is given by the aforementioned stereographic projection which preserves the angles at which curves in the hyperboloid meet. It is defined as the mapping of a point in H^2 to a point in $\mathbb{D}$ as, [35]:

$$z = \frac{\kappa}{\kappa + x_0}(x_1 + ix_2). \tag{3.3}$$

Following [27] we perform a hyperbolic parameterization of the coordinates x_0, x_1, x_2, such that:

$$\begin{aligned} x_0 &= \kappa \cosh(\varphi), \\ x_1 &= \kappa \sinh(\varphi)\cos(\theta), \\ x_2 &= \kappa \sinh(\varphi)\sin(\theta). \end{aligned} \tag{3.4}$$

Let $\alpha_i \in \{\varphi, \theta\}$, such that the reparameterized squared line element is given by:

$$ds^2 = \eta_M^{\mu\nu} dx_\mu dx_\nu = \eta_M^{\mu\nu} \frac{\partial x_\mu}{\partial \alpha_i} \frac{\partial x_\nu}{\partial \alpha_j} d\alpha_i d\alpha_j \equiv g_M^{ij} d\alpha_i d\alpha_j, \tag{3.5}$$

therefore:

$$g_M^{ij} = \eta_M^{\mu\nu} \frac{\partial x_\mu}{\partial \alpha_i} \frac{\partial x_\nu}{\partial \alpha_j} = \kappa^2 \begin{bmatrix} 1 & 0 \\ 0 & \sinh^2(\varphi) \end{bmatrix}. \tag{3.6}$$

Let $z_k \in \{z, z^*\}$ where z^* is the complex conjugate coordinate. Rescaling the hyperbolic parametrization by κ^{-1} and substituting the coordinates in Eq. (3.3):

$$z = \frac{\sinh(\varphi)}{1 + \cosh(\varphi)} e^{i\theta} \tag{3.7}$$

and:

$$ds^2 = g_M^{ij} d\alpha_i d\alpha_j = g_M^{ij} \frac{\partial \alpha_i}{\partial z_k} \frac{\partial \alpha_j}{\partial z_l} dz_k dz_l \equiv g_{\mathbb{D}}^{kl} dz_k dz_l. \tag{3.8}$$

The metric in the Poincaré disk model is thus given by:

$$g_{\mathbb{D}}^{kl} = g_M^{ij} \frac{\partial \alpha_i}{\partial z_k} \frac{\partial \alpha_j}{\partial z_l} = \frac{2\kappa^2}{(1 - |z|^2)^2} \begin{bmatrix} 0 & 1 \\ 1 & 0 \end{bmatrix}. \tag{3.9}$$

It can be shown that the distance between two points z, z' in the Poincaré disk is [16, 35]:

$$d(z, z') = \kappa \operatorname{arcosh}\Big(1 + \frac{2|z - z'|^2}{(1 - |z|^2)^2(1 - |z'|^2)^2}\Big). \tag{3.10}$$

The curvature, explicitly twice the Gaussian curvature, of the hyperbolic plane can be computed via the Ricci scalar R. To this end, we will compute the Christoffel symbols Γ^i_{jk} as well as the Riemann tensor R^i_{jkl} and the Ricci tensor $R_{jl} = R^i_{jil}$, a detailed discussion on these objects can be found in [38] for example. The parameterization of the metric in terms of x_1 and x_2 coordinates gives:

$$g_{\mathbb{D}}^{kl} = \frac{(2\kappa)^2}{(1 - x_1^2 - x_2^2)^2} \begin{bmatrix} 1 & 0 \\ 0 & 1 \end{bmatrix}. \tag{3.11}$$

The entries in the Christoffel Symbols are:

$$\begin{aligned} \Gamma^{x_1}{}_{x_1 x_1} &= -\Gamma^{x_1}{}_{x_2 x_2} = \Gamma^{x_2}{}_{x_1 x_2} = \Gamma^{x_2}{}_{x_2 x_1} = \frac{2x_1}{1 - x_1^2 - x_2^2} \\ \Gamma^{x_1}{}_{x_1 x_2} &= \Gamma^{x_1}{}_{x_2 x_1} = -\Gamma^{x_2}{}_{x_1 x_1} = \Gamma^{x_2}{}_{x_2 x_2} = \frac{2x_2}{1 - x_1^2 - x_2^2} \end{aligned} \tag{3.12}$$

and thus the non zero entries in the Riemann tensor and Ricci tensor are:

$$\begin{aligned} R^{x_1}{}_{x_2 x_1 x_2} &= -R^{x_1}{}_{x_2 x_2 x_1} = -R^{x_2}{}_{x_1 x_1 x_2} = R^{x_2}{}_{x_1 x_2 x_1} = -\frac{4}{(1 - x_1^2 - x_2^2)^2} \\ R_{x_1 x_1} &= R_{x_2 x_2} = -\frac{4}{(1 - x_1^2 - x_2^2)^2} \end{aligned}, \tag{3.13}$$

Finally, the Ricci scalar is:

$$R = R^l{}_l = g_{\mathbb{D}}^{lk} R_{kl} = -\frac{2}{\kappa^2} < 0\,. \tag{3.14}$$

We see that the curvature in the Poincaré disk model is negative, which leads to remarkable features that we will explore in the subsequent sections. From now on, let $\kappa = 1/2$ such that the Gaussian curvature K is given by $K \equiv R/2 = -\kappa^{-2} = -4$.

3.2 Hyperbolic lattices

In this section, we will build the necessary framework for the construction of hyperbolic lattices by following the treatment of P. M. Lenggenhager et al. in Ref. [3]. This will allow us to build models in hyperbolic lattices and enable us to set up the proper descriptions for the **HyperCells** and **HyperBloch** package tutorials. Our considerations in the Euclidean lattice will play a crucial role to facilitate the understanding of the **group theoretical** aspects in these lattices.

Hyperbolic lattices are regularly tiled by p-sided polygons meeting with q identical copies of themselves at each corner, denoted by $\{p, q\}$ in the Schläfli notation, with $(p-2)(q-2) > 4$ [3]. These lattices are most naturally described using the notion of **triangle groups**. As such, a triangle group constitutes a set of operations such that a triangle, called **fundamental Schwarz triangle** s_f, after repeated actions of the elements in the triangle group tessellates the (Euclidean or hyperbolic) plane. The internal angles of s_f are thus $\frac{\pi}{2}$, $\frac{\pi}{q}$ and $\frac{\pi}{p}$. The **space group** for hyperbolic $\{p, q\}$-lattices is given by the presentation:

$$\Delta(2, q, p) = \left\langle \mathrm{a}, \mathrm{b}, \mathrm{c} \mid \mathrm{a}^2, \mathrm{b}^2, \mathrm{c}^2, (\mathrm{ab})^2, (\mathrm{bc})^q, (\mathrm{ca})^p \right\rangle . \tag{3.15}$$

The generators a, b, c are reflections of the fundamental Schwarz triangle s_f across its sides, depicted in Fig. 2. Rotations can be constructed by applying the reflections in succession, such that $\mathrm{x} = \mathrm{ab}$, $\mathrm{y} = \mathrm{bc}$ and $\mathrm{z} = \mathrm{ca}$ as illustrated in Fig. 2. The **relators**, appearing on the right of the generators in Eq. (3.15), form the set of constraints for the generators. Each relator is equal to the identity.

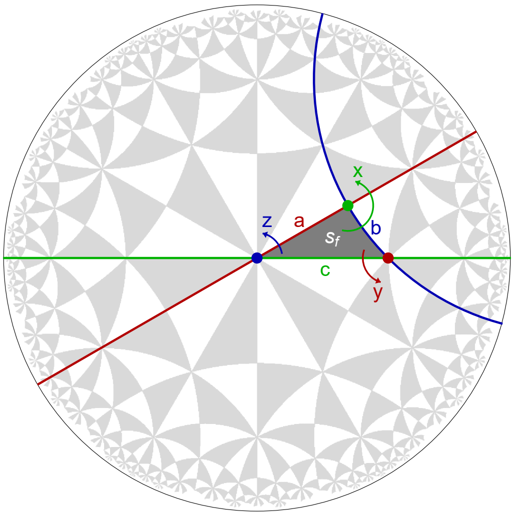

Figure 2: **Symmetries in the $\{6, 4\}$-lattice**. Symmetries of the tessellated hyperbolic plane with 6-sided polygons meeting with 4 identical copies at each corner. The polygons are subdivided into a set of copies of the fundamental Schwarz triangle s_f. The symmetry operations are indicated and constitute reflections a, b, c across a corresponding axes and rotations x, y, z around corresponding points indicated by matching colors, cf. [3, 7].

As aforementioned, we can tessellate the hyperbolic plane, which can be achieved by constructing the **orbit** of the fundamental Schwarz triangle under a group action, we here make the canonical choice of taking **right actions**:

$$S = s_f \cdot \Delta\,. \tag{3.16}$$

Instead of using reflections as generators we may as well choose to work with **orientation-preserving** elements, such as the rotations x, y and z. The group that contains these orientation-preserving elements is a normal subgroup of the triangle group Δ, called the **proper triangle group** $\Delta^+(2,\, q,\, p)$ and is given by:

$$\Delta^+(2,\, q,\, p) = \left\langle \mathrm{x},\, \mathrm{y},\, \mathrm{z} \mid \mathrm{xyz},\, \mathrm{x}^2,\, \mathrm{y}^q,\, \mathrm{z}^p \right\rangle, \tag{3.17}$$

where $\mathrm{x} = \mathrm{ab}$, $\mathrm{y} = \mathrm{bc}$ and $\mathrm{z} = \mathrm{ca}$. Since the proper triangle group Δ^+ is a normal subgroup Δ, the quotient of them is a group as well isomorphic to a reflection group $\mathbb{Z}_2$. We see that $\mathbb{Z}_2 \cap \Delta^+ = \mathbb{1}$ with $\mathbb{1} \in \Delta$ and thus the triangle group Δ is the semidirect product of the reflection group and the proper triangle group $\Delta = \Delta^+ \rtimes \mathbb{Z}_2$.

Analogous to our discussion in the Euclidean plane, the space group $\Delta(2,\, p,\, q)$ of hyperbolic $\{p,\, q\}$-lattices can be decomposed into translated copies of a unit cell via the **coset decomposition**. Let $\Gamma(2,\, q,\, p)$ be the **translation group** consisting of translations γ as orientation preserving elements without a fixed-point. The translation group Γ must be a normal subgroup of Δ, analogous to our discussion in the Euclidean case of Section 2.2. Further, let $\mathrm{T}_\Delta(\Gamma)$ be a **right transversal**, containing the set of coset representatives $g_j \in \mathrm{T}_\Delta(\Gamma)$, then:

$$\Delta = \bigcup_{g_j \in \mathrm{T}_\Delta(\Gamma)} g_j \Gamma. \tag{3.18}$$

The proper triangle group Δ^+ can be decomposed analogously:

$$\Delta^+ = \bigcup_{g_j \in \mathrm{T}_{\Delta^+}(\Gamma)} g_j \Gamma. \tag{3.19}$$

The number of elements in the right transversal $\mathrm{T}_\Delta(\Gamma)$ is equal to the number of cosets in the quotient group Δ/Γ, which is called the **index** $|\Delta : \Gamma|$ of Γ in Δ and is equal to the **order** of the quotient group denoted $|\Delta/\Gamma|$.

The unit cell is then defined as the image of of the fundamental Schwarz triangle s_f under the right action of the transversal:

$$C = s_f \cdot \mathrm{T}_\Delta(\Gamma). \tag{3.20}$$

The choice of representatives in the right transversal thus defines the unit cell. The orbit S may also be written in terms of the unit cell explicitly:

$$S = s_f \cdot \Delta = \bigcup_{g_j \in \mathrm{T}_\Delta(\Gamma)} s_f \cdot g_j \Gamma = \bigcup_{\gamma \in \Gamma} s_f \cdot \mathrm{T}_\Delta(\Gamma)\gamma = \bigcup_{\gamma \in \Gamma} C \cdot \gamma. \tag{3.21}$$

In order to construct the orbit S we have to identify the translation group Γ. The construction of the translation group requires us to search for normal subgroups of the proper triangle group Δ^+. This can be achieved by so-called low-index-normal-subgroup algorithms that identify normal subgroups with lowest index $|\Delta : \Gamma|$. We circumvent the calculation by using tabulated quotient groups Δ^+/Γ as we may as well use the property of kernels of a group homomorphisms to construct them, recall Eq. (2.12). Thus, the group homomorphism Φ from the proper triangle group to the quotient group $\Phi : \Delta^+ \to \Delta^+/\Gamma$ has a kernel $\ker(\Phi)$ that is a normal subgroup of Δ^+ and is isomorphic to the translation group Γ.

The **point group** G is isomorphic to the quotient Δ/Γ:

$$G \cong \Delta/\Gamma. \tag{3.22}$$

We may as well choose to work with the orientation preserving proper triangle group Δ^+ again, such that the **proper point group** G^+ is given by:

$$G = G^+ \ltimes \mathbb{Z}_2, \quad G^+ \cong \Delta^+/\Gamma. \tag{3.23}$$

Let us now make an example reviewing some of the key concepts for the {6, 4}-lattice, using the HyperCells package. The presentations of the triangle group and the proper triangle group have the following form:

$$\begin{aligned} \Delta(2,4,6) &= \left\langle \mathrm{a},\, \mathrm{b},\, \mathrm{c} \mid \mathrm{a}^2,\, \mathrm{b}^2,\, \mathrm{c}^2,\, (\mathrm{ab})^2,\, (\mathrm{bc})^4,\, (\mathrm{ca})^6 \right\rangle, \\ \Delta^+(2,4,6) &= \left\langle \mathrm{x},\, \mathrm{y},\, \mathrm{z} \mid \mathrm{xyz},\, \mathrm{x}^2,\, \mathrm{y}^4,\, \mathrm{z}^6 \right\rangle. \end{aligned} \tag{3.24}$$

The quotient group of the proper triangle group and the **lowest index** subgroup is retrieved from Ref. [39]. Its presentation is isomorphic to the proper point group:

$$G^+_{\{6,4\}} \cong \Delta^+(2,4,6)/\Gamma_{\{6,4\}} = \left\langle \mathrm{x},\, \mathrm{y},\, \mathrm{z} \mid \mathrm{xyz},\, \mathrm{x}^2,\, \mathrm{y}^4,\, \mathrm{z}^6,\, (\mathrm{yz}^{-1})^2 \right\rangle, \tag{3.25}$$

by using the kernel of the group homomorphism $\Phi : \Delta^+(2,4,6) \to G^+_{\{4,6\}}$ we find the corresponding translation group $\Gamma_{\{6,4\}}$:

$$\begin{aligned} &\Gamma_{\{6,4\}} = \left\langle \gamma_1,\, \gamma_2,\, \gamma_3,\, \gamma_4 \mid \gamma_4\gamma_1\gamma_3\gamma_4^{-1}\gamma_3^{-1}\gamma_2^{-1}\gamma_1^{-1}\gamma_2 \right\rangle, \\ &\text{where} \quad \gamma_1 = (\mathrm{zy}^3)^2,\, \gamma_2 = (\mathrm{y}^3\mathrm{z})^2,\, \gamma_3 = \mathrm{yz}^2\mathrm{y}^3\mathrm{z}^2,\, \gamma_4 = \mathrm{z}^5\mathrm{yz}^3\mathrm{yz}^4 \end{aligned} \tag{3.26}$$

and the representatives within the right transversal of the proper triangle group can be chosen as:

$$\mathrm{T}_{\Delta^+}(\Gamma_{\{6,4\}}) = \left\{ \mathrm{y}^i\mathrm{z}^j \mid \mathrm{y},\, \mathrm{z} \in \Delta^+(2,4,6),\, i \in \{0,1,2,3\},\, j \in \{0,1,2,3,4,5\} \right\}. \tag{3.27}$$

The corresponding hyperbolic $\{6, 4\}$-lattice is depicted in Fig.3. The Schwarz triangles within the unit cell, shaded dark gray, correspond to copies of the fundamental Schwarz triangle upon the action of elements in the right transversal $\mathrm{T}_{\Delta^+}(\Gamma_{\{6,4\}})$ in Eq. (3.27). The actions of generators of the translation group $\Gamma_{\{6,4\}}$ in Eq. (3.26) are indicated with colored arrows that follow the hyperbolic geodesics.

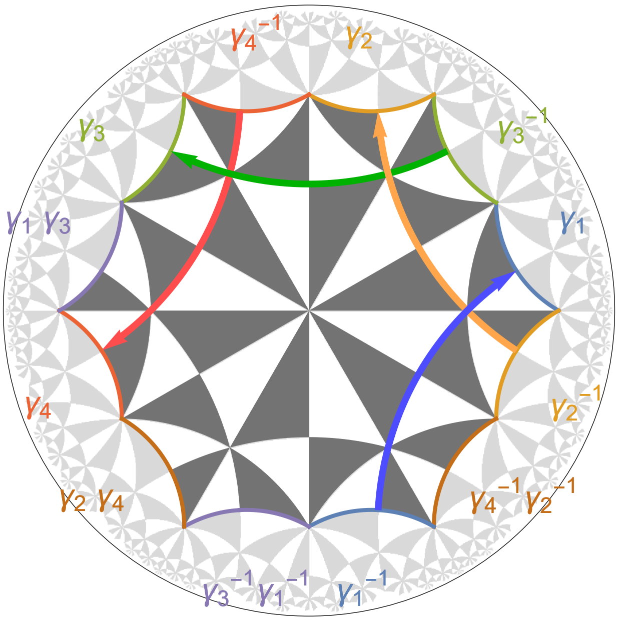

Figure 3: **A unit cell of the $\{6, 4\}$-lattice together with associated translations**. The hyperbolic $\{6, 4\}$-lattice together with a choice of a unit cell. The Schwarz triangles within the unit cell, shaded dark gray, correspond to copies of the fundamental Schwarz triangle upon the action of elements in the right transversal $\mathrm{T}_{\Delta^+}(\Gamma_{\{6,4\}})$. The action of generators of the translation group $\Gamma_{\{6,4\}}$ is indicated with colored arrows that follow the hyperbolic geodesics.

Modeling lattices in the hyperbolic plane requires the identification and labeling of **Wyckoff positions**. We thus proceed by reviewing the labeling procedure developed in [3] in detail, since this will be of fundamental importance for understanding the labeling and construction of Hamiltonians for models on hyperbolic $\{p, q\}$-lattices.

The three rotation generators x, y, z are symmetry operations associated with three corresponding vertices in the fundamental Schwarz triangle s_f. Each copy of these vertices, within the tessellated hyperbolic plane, is left invariant under a corresponding **stabilizer subgroup** of the proper triangle group Δ^+ called the **on-site symmetry group**. As such, the set of Wyckoff-positions of the hyperbolic lattice V^{lat} decays into a union of three sets of distinct vertices $V^{\mathrm{lat}} = V_{\mathrm{x}}^{\mathrm{lat}} \cup V_{\mathrm{y}}^{\mathrm{lat}} \cup V_{\mathrm{z}}^{\mathrm{lat}}$, labeled according to the rotation generators that leave these points invariant.

Therefore, the on-site symmetry groups are:

$$\begin{aligned}
\Delta^+_{\mathrm{x}} &= \{g \in \Delta^+ \mid w_{\mathrm{x}} \cdot g = w_{\mathrm{x}},\, w_{\mathrm{x}} \in V^{\mathrm{lat}}_{\mathrm{x}}\} = \left\langle \mathrm{x} \mid \mathrm{x}^2 \right\rangle, \\
\Delta^+_{\mathrm{y}} &= \{g \in \Delta^+ \mid w_{\mathrm{y}} \cdot g = w_{\mathrm{y}},\, w_{\mathrm{y}} \in V^{\mathrm{lat}}_{\mathrm{y}}\} = \left\langle \mathrm{y} \mid \mathrm{y}^q \right\rangle, \\
\Delta^+_{\mathrm{z}} &= \{g \in \Delta^+ \mid w_{\mathrm{z}} \cdot g = w_{\mathrm{z}},\, w_{\mathrm{z}} \in V^{\mathrm{lat}}_{\mathrm{z}}\} = \left\langle \mathrm{z} \mid \mathrm{z}^p \right\rangle.
\end{aligned} \tag{3.28}$$

The orbit $v_{\mathrm{w}} \cdot \Delta^+ = V^{\mathrm{lat}}$ is again the set of all Wyckoff positions in the lattice, with $v_{\mathrm{w}} \in V^{\mathrm{lat}}_{\mathrm{w}}$ and $\mathrm{w} = \mathrm{x, y, z}$. The **orbit stabilizer** theorem then states that for all on-site symmetry groups there exists bijective maps $\Delta^+/\Delta^+_{\mathrm{w}} \to v_{\mathrm{w}} \cdot \Delta^+$. This implies that each vertex v_{w} is associated with a coset in $\Delta^+/\Delta^+_{\mathrm{w}}$ and thus with a coset representative in the right transversal $\mathrm{T}_{\Delta^+}(\Delta^+_{\mathrm{w}})$. Therefore:

$$V^{\mathrm{lat}}_{\mathrm{w}} \cong \mathrm{T}_{\Delta^+}(\Delta^+_{\mathrm{w}}), \quad \mathrm{w} = \mathrm{x, y, z}. \tag{3.29}$$

Now let h be a representative in the transversal $h \in \mathrm{T}_{\Delta^+}(\Delta^+_{\mathrm{w}})$, such that the right coset decomposition for any $\mathrm{w} = \mathrm{x, y, z}$ is given by:

$$\Delta^+ = \bigcup_{h \in \mathrm{T}_{\Delta^+}(\Delta^+_{\mathrm{w}})} \Delta^+_{\mathrm{w}} h\,. \tag{3.30}$$

Further, let $[h]_{\mathrm{w}}$ denote a coset such that $[h]_{\mathrm{w}} \in \Delta^+/\Delta^+_{\mathrm{w}}$ associated with the corresponding Wyckoff position, then:

$$V^{\mathrm{lat}} \cong \Big\{(\mathrm{w}, [h]_{\mathrm{w}}) \mid \mathrm{w} \in \{\mathrm{x, y, z}\},\, h \in \mathrm{T}_{\Delta^+}(\Delta^+_{\mathrm{w}})\Big\}. \tag{3.31}$$

Let us restrict the set of vertices to the unit cell C. The set of these vertices V^{cell} is invariant under the action of the proper point group G^+ in Eq. (3.23). This implies that the proper point group is the stabilizer subgroup of vertices V^{cell}. Analogously, V^{cell} decays into the union of three sets of distinct vertices $V^{\mathrm{cell}} = V^{\mathrm{cell}}_{\mathrm{x}} \cup V^{\mathrm{cell}}_{\mathrm{y}} \cup V^{\mathrm{cell}}_{\mathrm{z}}$ with corresponding stabilizers G^+_{w}.

As such, let δ be a representative in the transversal $\delta \in \mathrm{T}_{G^+}(G^+_{\mathrm{w}})$, such that the right coset decomposition for any $\mathrm{w} = \mathrm{x, y, z}$ is given by:

$$G^+ = \bigcup_{\delta \in \mathrm{T}_{G^+}(G^+_{\mathrm{w}})} G^+_{\mathrm{w}} \delta\,. \tag{3.32}$$

Further, let $[\delta]_{\mathrm{w}}$ be a particular coset such that $[\delta]_{\mathrm{w}} \in G^+/G^+_{\mathrm{w}}$ associated with the corresponding Wyckoff position, then:

$$V^{\mathrm{cell}} \cong \Big\{(\mathrm{w}, [\delta]_{\mathrm{w}}) \mid \mathrm{w} \in \{\mathrm{x, y, z}\},\, \delta \in \mathrm{T}_{G^+}(G^+_{\mathrm{w}})\Big\}. \tag{3.33}$$

Recall, that by definition an on-site symmetry group Δ^+_w contains elements in terms of a single rotation generator, and thus it can only contain the trivial translation. This implies that the subgroup of the proper point group G^+_w is isomorphic to the on-site symmetry group $G^+_\mathrm{w} \cong \Delta^+_\mathrm{w}$.

The decomposition of the proper point group G^+ (3.32) implies that the elements of the proper triangle group Δ^+ can be written in terms of the established constituents. It follows from Eq. (3.19) that an arbitrary element $t \in \Delta^+$ can be written as:

$$t = g_j \gamma' , \tag{3.34}$$

where $g_j \in \mathrm{T}_{\Delta^+}(\Gamma)$ and $\gamma' \in \Gamma$. The proper point group G^+ is isomorphic to the quotient group Δ^+/Γ, Eq. (3.23), thus there exists an isomorphism $i : \Delta^+/\Gamma \to G^+$ which maps elements in the cosets Δ^+/Γ to the elements in G^+. As such, the image of the coset $[g_j] \in \Delta^+/\Gamma$ can be written as:

$$i([g_j]) = i([\mathrm{w}^n])\delta_k, \tag{3.35}$$

with $\mathrm{w}^n \in \mathrm{T}_{G^+}(G^+_\mathrm{w})$ and $\delta_k \in \mathrm{T}_{G^+}(G^+_\mathrm{w})$ which follow from Eq. (3.32). We see that elements in the coset $[g_j]$ are identifiable with specific Wyckoff positions in the unit cell associated with a particular $\mathrm{w} \in \{\mathrm{x}, \mathrm{y}, \mathrm{z}\}$. Let $i^{-1}(\delta_k) = [g_{u_\mathrm{w}}]$ with $[g_{u_\mathrm{w}}] \in \Delta^+/\Gamma$ such that the inverse isomorphism of Eq. (3.35) is:

$$[g_j] = [\mathrm{w}^n] i^{-1}(\delta) = [\mathrm{w}^n][g_{u_\mathrm{w}}]. \tag{3.36}$$

Then, by Eq. (3.19) we find:

$$g_j = \mathrm{w}^n g_{u_\mathrm{w}} \gamma'' , \tag{3.37}$$

where $\gamma'' \in \Gamma$, $n \in \{0, 1, ..., |G^+_\mathrm{w}| - 1\}$ and n depends on the choice of representative g_j, therefore:

$$t = \mathrm{w}^n g_{u_\mathrm{w}} \gamma, \tag{3.38}$$

where $\gamma = \gamma'' \gamma' \in \Gamma$, this implies that an arbitrary element t has a representative $\mathrm{w}^n \in \mathrm{T}_{G^+}(G^+_\mathrm{w})$. Note that the representative w^n appears to the very left by the orbit stabilizer theorem.

Therefore, for the isomorphism $i : \Delta^+/\Gamma \to G^+$, the Wyckoff positions in the unit cell C are labeled by:

$$\mathcal{C} = \Big\{ u = (\mathrm{w}, [g_{u_\mathrm{w}}]_\mathrm{w}) \mid g_{u_\mathrm{w}} \in \mathrm{T}_{\Delta^+}(\Gamma),\ i([g_{u_\mathrm{w}}]) \in \mathrm{T}_{G^+}(G^+_\mathrm{w}) \Big\}. \tag{3.39}$$

Further, let us relabel the Wyckoff positions in V^lat, Eq. (3.31), such that it is apparent that V^lat consists of translated copies of the Wyckoff positions in the unit cell C:

$$V^{\mathrm{lat}} \cong \bigcup_{\gamma\in\Gamma} \Big\{(u,\gamma) \mid u \in \mathcal{C}\Big\}. \tag{3.40}$$

Once again, let us make an example reviewing some of the newly acquired key concepts for the $\{6, 4\}$-lattice with the HyperCells package. Recall, that the on-site symmetry groups Δ^{+}_{w}, given in Eq. (3.28), are isomorphic to the subgroups G^{+}_{w}, and that we have chosen the representatives in the right transversal $\mathrm{T}_{\Delta^{+}}(\Gamma_{\{6,4\}})$ in Eq. (3.27). The right transversals $\mathrm{T}_{G^{+}}(G^{+}_{\mathrm{w}})$ are given by:

$$\begin{aligned}
\mathrm{T}_{G^{+}}(G^{+}_{\mathrm{x}}) &= \Big\{\mathrm{z}^{i},\, \mathrm{y}^{3}\mathrm{z}^{i} \mid i \in \{0,1,2,3,4,5\}\Big\},\\
\mathrm{T}_{G^{+}}(G^{+}_{\mathrm{y}}) &= \Big\{\mathrm{z}^{i} \mid i \in \{0,1,2,3,4,5\}\Big\},\\
\mathrm{T}_{G^{+}}(G^{+}_{\mathrm{z}}) &= \{\mathbb{1},\, \mathrm{yz},\, \mathrm{y}^{2}\mathrm{z},\, \mathrm{yz}^{2}\}.
\end{aligned} \tag{3.41}$$

The representatives in the right transversals $\mathrm{T}_{G^{+}}(G^{+}_{\mathrm{w}})$ coincide with the number and kind of representatives in the vertices such that $(\mathrm{w},\, [g_{u_{\mathrm{w}}}]_{\mathrm{w}}) = (\mathrm{w},\, g_{u_{\mathrm{w}}})$ and thus:

$$\begin{aligned}
V^{\mathrm{cell}}_{\mathrm{x}} &\cong \Big\{(\mathrm{x},\, g_{u_{\mathrm{x}}}) \mid g_{u_{\mathrm{x}}} \in \mathrm{T}_{G^{+}}(G^{+}_{\mathrm{x}})\Big\},\\
V^{\mathrm{cell}}_{\mathrm{y}} &\cong \Big\{(\mathrm{y},\, g_{u_{\mathrm{y}}}) \mid g_{u_{\mathrm{y}}} \in \mathrm{T}_{G^{+}}(G^{+}_{\mathrm{y}})\Big\},\\
V^{\mathrm{cell}}_{\mathrm{z}} &\cong \Big\{(\mathrm{z},\, g_{u_{\mathrm{z}}}) \mid g_{u_{\mathrm{z}}} \in \mathrm{T}_{G^{+}}(G^{+}_{\mathrm{z}})\Big\}.
\end{aligned} \tag{3.42}$$

3.3 Graph theory and compactification

Analogous to the Euclidean case, we now want to impose periodic boundary conditions in order to describe the bulk properties of hyperbolic lattices. Recall that in the thermodynamic limit of infinite lattices in the Euclidean plane, the imposed PBCs on the boundary of the unit cell, lead to a compactification on the surface of a **two-dimensional** torus $\mathbb{T}^2$, cf. section 2.3.

Dissimilar to the compactification of lattices in the Euclidean plane, taking the thermodynamic limit after imposing PBCs in hyperbolic lattices is highly non-trivial. The non-Abelian translation groups imply the existence of higher dimensional irreducible representations of elements in the translation groups such that in general $D_{\mathbf{k}}(\gamma) \neq \chi_{\mathbf{k}}(\gamma)$, where $\gamma \in \Gamma$. This implies that general hyperbolic Bloch states are non-Abelian [18]. Amidst these complications, the normal subgroups $\Gamma_{\mathrm{PBC}} \triangleleft \Gamma$ that identify the PBC clusters, recall section 2.3, are generated by a growing number of translation operators. Thus, imposing PBCs on the boundaries of PBC clusters requires a growing number of identifications of translations associated with the corresponding boundaries.

For now, let us postpone the discussion of how we work around these features of hyperbolic lattices. Instead, let us review aspects of graph theory in order to understand what a compactification of a lattice in the hyperbolic plane amounts to, following [16, 27, 35]

Consider for example the primitive cells as shown in Fig. 4, the cell boundaries are colored according to specific translation operations that indicate the transition to a copy of the primitive cell. Each pair of identically colored boundary segments can be identified with each other such that crossing these boundaries, indicated with red lines, amounts to returning to the same primitive cell on a related side, resulting in periodic boundary conditions.

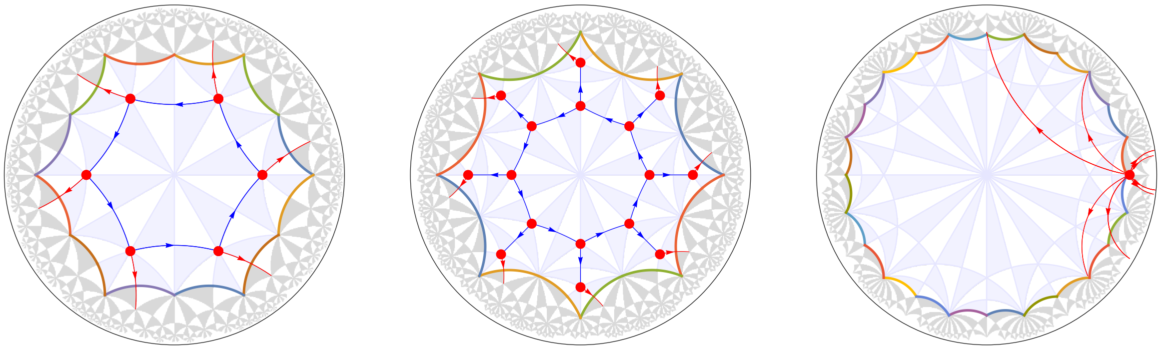

Figure 4: **Graph representations of hyperbolic lattices with primitive cells endowed with PBCs**. Left: $\{6, 4\}$-lattice. Center: $\{8, 3\}$-lattice. Right: $\{12, 3\}$-lattice.

The imposed periodic boundary condition can be seen as a tessellation of a closed Riemann surface $\Sigma_{\mathfrak{g}}$, where closed means $\Sigma_{\mathfrak{g}}$ has no boundary [27]. The number of holes in that surface, called the **genus**, is denoted as $\mathfrak{g}$. For each $\{p,\, q\}$-lattice, the unit cell, primitive or not, consist of **vertices** corresponding to sites within the unit cell, **edges** corresponding to the connection between a pair of adjacent vertices, and **faces** corresponding to p-gons that tile the hyperbolic plane. The number of vertices, edges and faces, denoted as $\mathcal{V}$, $\mathcal{E}$, $\mathcal{F}$ respectively, satisfy the identity:

$$p\mathcal{F} = 2\,\mathcal{E} = q\,\mathcal{V}\,. \tag{3.43}$$

For example, in the primitive cell on the $\{6,\, 4\}$-lattice to the very left in Fig. 4 we see that $\mathcal{V} = 6$ and $\mathcal{E} = 12$. The number of faces can be obtained by counting the triangles shaded in light blue and dividing it by the number of light blue triangles that make up the central hyperbolic hexagon, $\mathcal{F} = \frac{4 \cdot 6}{6} = 4$.

Another relation between $\mathcal{V}$, $\mathcal{E}$, $\mathcal{F}$ is given by the **Euler characteristic** χ, [40]:

$$\chi = \mathcal{V} - \mathcal{E} + \mathcal{F}\,. \tag{3.44}$$

The Euler characteristics for orientable surfaces $\Sigma_{\mathfrak{g}}$ is proportional to the genus $\mathfrak{g}$ of $\Sigma_{\mathfrak{g}}$, and according to Ref. [41] given by:

$$\chi = 2\,(1 - \mathfrak{g}). \tag{3.45}$$

Thus, imposing PBCs amounts to a compactification on a closed Riemann surface $\Sigma_{\mathfrak{g}}$ with genus given by:

$$\mathfrak{g} = \frac{(p - 2)(q - 2) - 4}{4p} \mathcal{V} + 1 . \tag{3.46}$$

Recall, that the tilling of the hyperbolic plane by p-sided polygons meeting with q identical copies at a corner, are restricted by $(p - 2)(q - 2) > 4$, which implies that $\mathfrak{g} \geq 2$. In the subsequent section we will see what this implies for the Brillouin zone.

3.4 Hyperbolic Bloch Hamiltonian

The graph theoretical considerations in the previous section have shown that hyperbolic PBC clusters are compactified on closed Riemann surfaces of genus $\mathfrak{g} > 1$. As in the Euclidean case discussed in Section 2.3, we now want to construct the normal subgroup $\Gamma_{\text{PBC}} \triangleleft \Gamma$ that identifies the PBC cluster. This is achieved by the coset decomposition of Γ. Recall, we canonically chose right actions, thus the right coset decomposition of Γ is given by:

$$\Gamma = \bigcup_{\eta_i \in \mathrm{T}_\Gamma(\Gamma_{\text{PBC}})} \eta_i \Gamma_{\text{PBC}} \tag{3.47}$$

and let $N = |\Gamma : \Gamma_{\text{PBC}}|$. The groups Γ_{PBC} are in general not normal subgroups of Δ. As a consequence, the quotient $\Delta/\Gamma_{\text{PBC}}$ is in general not a group, recall (2.7). This implies that the PBC cluster $C^{\text{PBC}} = s_f \cdot \Gamma_{\text{PBC}}$ is not left invariant under the repeated action of the set isomorphic to the quotient $\Delta/\Gamma_{\text{PBC}}$. As such, we restrict the groups Γ_{PBC} to be normal subgroups of the form $\Gamma_{\text{PBC}} \triangleleft \Delta$ and $\Gamma_{\text{PBC}} \triangleleft \Gamma \triangleleft \Delta$. These normal subgroups can be used to form a non-primitive unit cell C^{PBC}, which are called **supercell**, [3].

Further, F. R. Lux et al. [42] have shown the convergence to the thermodynamic limit by restricting the sequences of normal subgroups that identify PBC clusters to so-called **coherent sequences** of normal subgroups [43]:

$$\Delta^+ \triangleright \Gamma^{(1)} \triangleright \Gamma^{(2)} \triangleright \cdots, , \tag{3.48}$$

$$\bigcap_{n \geq 0} \Gamma^{(n)} = \{1\} , \tag{3.49}$$

where $\Gamma^{(0)} \equiv \Delta^+$. The imposed condition for selecting sequences of normal subgroups has been demonstrated to result in a converging approximation of the bulk properties in the thermodynamic limit [42] and shown convergence of moments of the density of states of hyperbolic tight-binding models in the thermodynamic limit [21].

Let us construct the hyperbolic tight-binding Hamiltonian on the infinite lattice following Ref. [3] and [18]. The decomposition in Eq. (3.40) gives:

$$\mathcal{H} = \sum_{\tilde{\gamma},\gamma'\in\Gamma}\sum_{u,v} h^{uv}(\tilde{\gamma},\gamma')c^{u\dagger}_{\tilde{\gamma}}c^{v}_{\gamma'}, \tag{3.50}$$

where u, v label the orbitals within the unit cell C, Eq. (3.20) such that $u, v \in \mathcal{C}$ Eq. (3.39) and c^u_γ is an annihilation operator for the orbital u in the unit cell C translated by $\gamma \in \Gamma$. The hopping amplitude $h^{uv}(\tilde{\gamma},\gamma')$ couples orbitals u in the unit cell translated by $\tilde{\gamma}$ with orbitals v in the unit cell translated by γ'. We can simplify $h^{uv}(\tilde{\gamma},\gamma')$ since $h^{uv}(\tilde{\gamma},\gamma') = h^{uv}(\tilde{\gamma}\gamma'^{-1},\mathbb{1})$ for any $\gamma',\tilde{\gamma} \in \Gamma$. Thus, let $\gamma = \tilde{\gamma}\gamma'^{-1}$ and $h^{uv}(\gamma) \equiv h^{uv}(\gamma,\mathbb{1})$ then it follows:

$$\mathcal{H} = \sum_{\gamma,\gamma'\in\Gamma}\sum_{u,v} h^{uv}(\gamma)c^{u\dagger}_{\gamma\gamma'}c^{v}_{\gamma'}. \tag{3.51}$$

Next, imposing periodic boundary conditions requires the construction of the Hamiltonian on the PBC cluster with the corresponding normal subgroup Γ_{PBC}. Thus, we restrict translations to the PBC cluster by Eq. (3.47), while retaining the labels u, v of the orbitals in the unit cell C:

$$\mathcal{H}_{\mathrm{PBC}} = \sum_{i=1}^{N}\sum_{\gamma\in\Gamma}\sum_{u,v} h^{uv}(\gamma)c^{u\dagger}_{[\gamma\eta_i]_{\mathrm{PBC}}}c^{v}_{[\eta_i]_{\mathrm{PBC}}}, \tag{3.52}$$

where $[\gamma\eta_i]_{\mathrm{PBC}} \in \Gamma/\Gamma_{\mathrm{PBC}}$. From now on let $\Gamma_{\mathrm{PBC}} = \Gamma^{(n)}$ and likewise $C^{\mathrm{PBC}} = C^{(n)}$, which denotes the n'th PBC cluster. The action of a general translation $\gamma \in \Gamma$ on the n'th PBC cluster amounts to some permutation of the N primitive cells C within the supercell $C^{(n)}$. Then, by Cayley's theorem there exists a homomorphism from the quotient group $\Gamma/\Gamma^{(n)}$ to the permutation group S_N with $N \times N$ matrix representations $\mathcal{U} : \Gamma/\Gamma^{(n)} \to S_N$, [18], namely:

$$\mathcal{U}_{ij}([\gamma]) = \delta_{[\eta_i],[\gamma\eta_j]}, \tag{3.53}$$

such that:

$$c^{u\dagger}_{[\gamma\eta_j]} = \sum_i c^{u\dagger}_{[\eta_i]}\mathcal{U}_{ij}([\gamma]), \tag{3.54}$$

where $[\gamma] \in \Gamma/\Gamma^{(n)}$. These so-called **regular representations** are in general further reducible into their irreducible components $D^{(\lambda)}$ of dimension $d_\lambda \geq 1$ with $D^{(\lambda)} : \Gamma/\Gamma^{(n)} \mapsto \mathrm{U}(d^{(\lambda)})$ by an appropriate unitary transformation $P \in \mathrm{U}(N)$:

$$P\mathcal{U}([\gamma])P^\dagger = \bigoplus_{\lambda=1}^{\mathcal{N}} d_\lambda D^{(\lambda)}([\gamma]), \tag{3.55}$$

where λ labels the equivalence classes of $\Gamma/\Gamma^{(n)}$, $\mathcal{N}$ is the number of equivalence classes and the dimension of the irreducible representation $d^{(\lambda)}$ is equal to the multiplicity of $D^{(\lambda)}$ in Eq. (3.55), [18]. In the special case where the translation group is Abelian, the irreducible representations are one dimensional and thus equal to their character. Then:

$$D^{(\lambda)}(\gamma) = \chi^{(\lambda)}(\gamma), \tag{3.56}$$

where $\chi^{(\lambda)} : \Gamma/\Gamma^{(n)} \to \mathrm{U}(1)$, such that:

$$P\mathcal{U}([\gamma])P^{-1} = \begin{bmatrix} \chi^{(1)}([\gamma]) & & \\ & \ddots & \\ & & \chi^{(N)}([\gamma]) \end{bmatrix}. \tag{3.57}$$

Using Eq. (3.54) with subsequent unitary transformation of the representation $\mathcal{U}$ with Eq. (3.57), we find that the n'th PBC cluster Hamiltonian for general irreducible representations becomes:

$$\begin{aligned} \mathcal{H}_{n\text{-PBC}} \equiv \mathcal{H}_{\text{PBC}} &= \sum_{i,j=1}^{N} \sum_{\gamma\in\Gamma} \sum_{u,v} h^{uv}(\gamma) c^{u\dagger}_{[\eta_i]} \mathcal{U}_{ij}([\gamma]) c^{v}_{[\eta_j]} \\ &= \sum_{k,l} \sum_{u,v} \Big(\sum_{i} P_{ki} c^{u}_{[\eta_i]} \Big)^{\dagger} \Big[\sum_{\gamma\in\Gamma} h^{uv}(\gamma) \Big(\bigoplus_{\lambda=1}^{\mathcal{N}} d_\lambda D^{(\lambda)}([\gamma]) \Big)_{kl} \Big] \Big(\sum_{j} P_{lj} c^{v}_{[\eta_j]} \Big) \end{aligned} \tag{3.58}$$

and we see:

$$\sum_{\gamma\in\Gamma} h^{uv}(\gamma) \Big(\bigoplus_{\lambda=1}^{\mathcal{N}} d_\lambda D^{(\lambda)}([\gamma]) \Big)_{kl} = \Big(\bigoplus_{\lambda=1}^{\mathcal{N}} d_\lambda \sum_{\gamma\in\Gamma} h(\gamma) \otimes D^{(\lambda)}([\gamma]) \Big)^{uv}_{kl}. \tag{3.59}$$

Let:

$$H(D) = \sum_{\gamma\in\Gamma} h(\gamma) \otimes D([\gamma]) \quad \text{and} \quad \hat{c}^{u}_{k} = \sum_{i} P_{ki} c^{u}_{[\eta_i]}, \tag{3.60}$$

then, the n'th PBC cluster Hamiltonian is:

$$\mathcal{H}_{n\text{-PBC}} = \sum_{k,l} \sum_{u,v} \hat{c}^{u\dagger}_{k} \Big(\bigoplus_{\lambda=1}^{\mathcal{N}} d_\lambda H(D^{(\lambda)}) \Big)^{uv}_{kl} \hat{c}^{v}_{l}. \tag{3.61}$$

In the limit $n \to \infty$ the supercell $C^{(n)}$ covers the infinite lattice and $\Gamma/\Gamma^{(n)}$ is replaced by Γ such that the cosets $[\gamma]$ are replaced by γ, recall Eq. (3.48). Therefore, the hyperbolic tight-binding Hamiltonian is block-diagonalized as:

$$\mathcal{H} = \sum_{k,l} \sum_{u,v} \hat{c}^{u\dagger}_{k} \Big(\bigoplus_{\lambda} d_\lambda H(D^{(\lambda)}) \Big)^{uv}_{kl} \hat{c}^{v}_{l}, \tag{3.62}$$

where lambda now labels representations of the original translation group of the infinite lattice. We can identify the Bloch Hamiltonian as:

$$H(D) = \sum_{\gamma\in\Gamma} h(\gamma) \otimes D(\gamma) \tag{3.63}$$

and annihilation operators are:

$$\hat{c}_k^u = \sum_i P_{ki} c_{\eta_i}^u \,, \tag{3.64}$$

where η_i now labels a translated primitive cell $C^{(1)}$ on the infinite lattice, and we abuse the notation by keeping the symbol $\bigoplus$ which now runs over a continuous space over infinitely many irreducible representations. In the special case where the translation group is Abelian, the irreducible representations are one-dimensional, and therefore the Bloch Hamiltonian in Eq. (3.63) reduces to:

$$H(\chi) = \sum_{\gamma \in \Gamma} h(\gamma) \chi(\gamma). \tag{3.65}$$

The space of one-dimensional irreducible representations forms a $2\mathfrak{g}$ Recall from Section 3.3 that the primitive cell is compactified on a closed Riemann surface $\Sigma_\mathfrak{g}$. For one-dimensional irreducible representations, we can think of threading the $2\mathfrak{g}$ non-contractible cycles of $\Sigma_\mathfrak{g}$ by magnetic fluxes associated with the mapping $\chi : \Gamma \to \mathrm{U}(1)$, such that the $2\mathfrak{g}$ components form the Abelian hyperbolic Brillouin zone torus $\mathbb{T}^{2\mathfrak{g}}$, [3, 18]. The Brillouin zone is then defined as:

$$\mathrm{BZ}^{(1,1)} = \Big\{ \gamma_i \mapsto \chi_\mathbf{k}(\gamma_i) = e^{ik_i} \mid \mathbf{k} \in [0, 2\pi)^{2\mathfrak{g}} \cong \mathbb{T}^{2\mathfrak{g}} \Big\}, \tag{3.66}$$

where the superscript $(1,1)$ indicates the primitive cell and the dimension of the irreducible representations, respectively. Thus, the **Abelian Bloch Hamiltonian** is given by:

$$H(\mathbf{k}) = \sum_{\gamma \in \Gamma} h(\gamma) e^{i \sum_{i=1}^{2\mathfrak{g}} K_i(\gamma) k_i}, \tag{3.67}$$

where $K_i(\gamma)$ corresponds to the number of times the generator γ_i of Γ appears in γ, where the inverse generator γ_i^{-1} is counted negatively.

3.5 Supercells on hyperbolic lattices

The compactification via PBC clusters is more subtle in the hyperbolic plane. Recall the case of the Euclidean plane in section 2.3, we have seen that in order that the compactification correctly reproduces the thermodynamic limit, we need to make sure to find an appropriate sequence of normal subgroups. The translation group of the Euclidean plane is Abelian. Consequently its normal subgroups are Abelian as well and thus the irreducible representations are one-dimensional. The translation group Γ of the hyperbolic plane, however, is non-Abelian. This implies that the normal subgroups $\Gamma^{(m)}$ are in general non-Abelian, such that in order to correctly describe finite systems and the thermodynamic limit, one needs to consider higher-dimensional irreducible representations. To circumvent this predicament, P. M. Lenggenhager et al. [3] have developed the **supercell method** which enables the systematic access to non-Abelian Bloch states through the use of the **Abelian hyperbolic band theory** (AHBT) applied to particular sequences of normal subgroups.

The supercell method requires the construction of normal subgroups $\Gamma^{(m)} \triangleleft \Delta^+$ such that supercells can be assembled via symmetric aggregation of primitive unit cells, followed by a labeling procedure for the Wyckoff positions within the supercells. Figure 5 depicts the first supercell constructed via the aforementioned method. The supercell boundaries are colored such that each color indicates a pair of edges that are related to each other by elements of the supercell translation group.

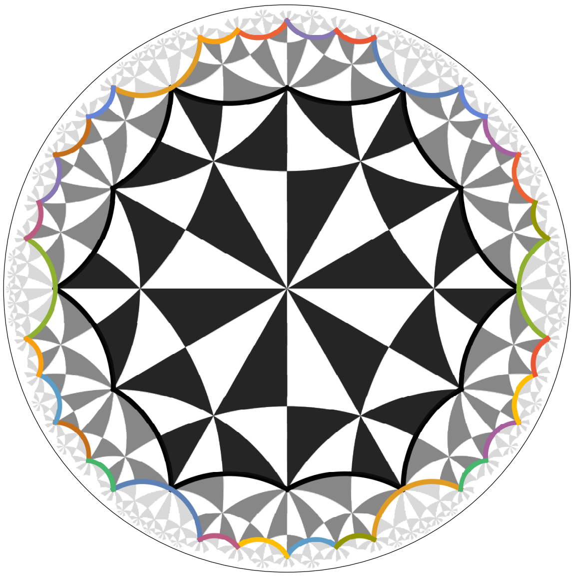

Figure 5: **1st supercell corresponding to** $\Delta^+(2,\,4,\,6)/\Gamma^{(2)}_{\{6,\,4\}}$. The primitive cell of the $\{6,\,4\}$-lattice is indicated with black Schwarz triangles, the corresponding cell boundary is shown with black lines that surround this cluster of triangles. The symmetric aggregation of 4 additional primitive cells makes up the 1st supercell, which is indicated with dark gray Schwarz triangles surrounded by colored lines that indicate the 1st supercell boundary. The differently colored lines indicate a pair of edges that are related to each other by elements of the supercell translation group. The compactification of the lattice via periodic boundary condition and subsequent considerations of solely one dimensional irreducible representations on the primitive cell and indicated supercell amounts to a Brillouin zone isomorphic to $\mathbb{T}^4$ and $\mathbb{T}^{10}$ torus respectively.

A sequence of normal subgroups required for the supercell method is:

$$\Delta^+ = \Gamma^{(0)} \triangleright \Gamma^{(1)} \triangleright \Gamma^{(2)} \cdots \triangleright \Gamma^{(m)} \triangleright \cdots, \tag{3.68}$$

where $\Gamma^{(0)} \equiv \Delta^+$ and $\Gamma^{(m)} \triangleleft \Delta^+$. As pointed out in section 3.2 instead of constructing normal subgroups $\Gamma^{(m)}$ by a low-index normal subgroup algorithms, we rely on tabulated quotient groups $\Delta^+/\Gamma^{(m)}$ such that we can use the kernels of the group homomorphisms to retrieve the normal subgroups $\Gamma^{(m)}$.

An example of the normal subgroup relations for the tabulated quotient groups up to genus 50 is shown in Figure 6 for the {6, 4}-lattice. Every vertex corresponds to a normal subgroup $\Delta^+/\Gamma^{(m)}$. They are labeled by a corresponding quotient group $\Delta^+/\Gamma^{(m)}$ in [39], denoted as T$\mathfrak{g}.n$, where $\mathfrak{g}$ is the genus of the corresponding Riemann surface $\Sigma_{\mathfrak{g}}$ and n is the n'th quotient group with that genus. Vertices highlighted in red indicate that Schwarz triangles can be assembled mirror symmetrically, given an appropriate choice of representatives in the right transversal. Blue vertices do not admit a mirror-symmetric unit cell, and they cannot be analyzed with the present version of the HyperCells package. Pairwise distinct vertices $\Gamma^{(m)}$,$\Gamma^{(m+1)}$ connected by a directed edge obey the normal subgroup relation $\Gamma^{(m)} \triangleright \Gamma^{(m+1)}$. It is apparent that some of the sequences of normal subgroups in the Figure are disconnected from others, however, this may change as one constructs larger-index quotient groups.

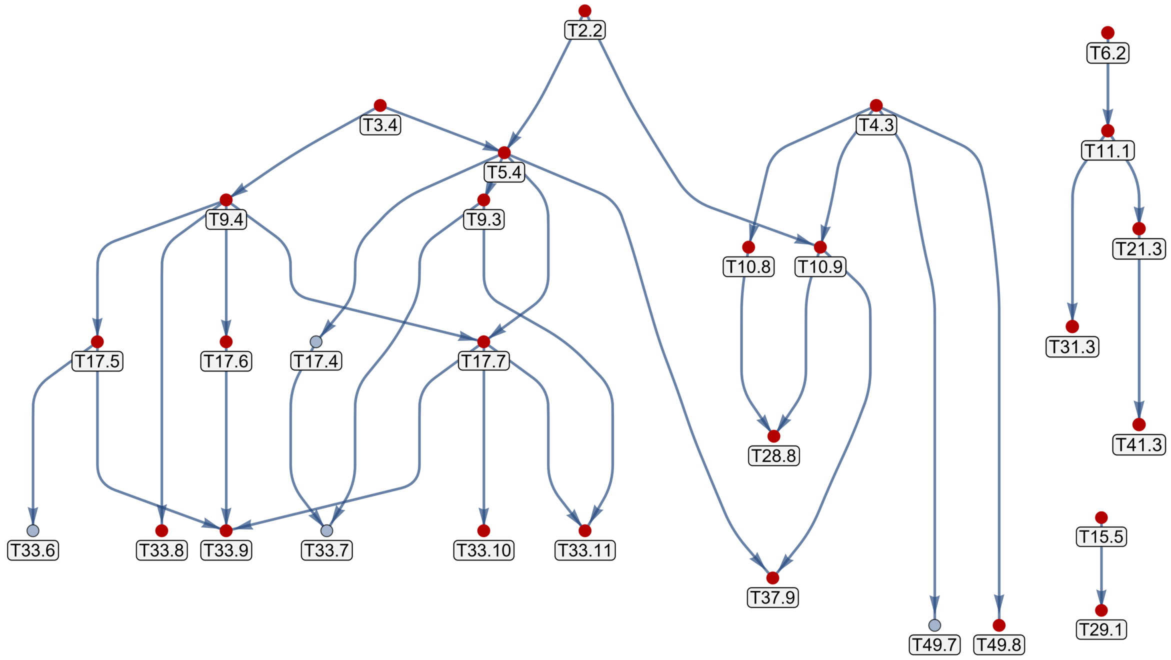

Figure 6: **Tree graph of normal subgroups relations between pairwise distinct $\Gamma^{(m)}$.** Each vertex in the graph, corresponds to a normal subgroup $\Gamma^{(m)} \triangleleft \Delta^+(2,4,6)$ labeled by the quotient group corresponding quotient groups $\Delta^+/\Gamma^{(m)}$ in the list [39], denoted as T$\mathfrak{g}.n$. Vertices $\Gamma^{(m)}$,$\Gamma^{(m+1)}$ connected by a directed edge obey the normal subgroup relation $\Gamma^{(m)} \triangleright \Gamma^{(m+1)}$. The tree graph depicts such relations up to genus $\mathfrak{g} < 50$. GAP code provided by Tomáš Bzdušek.

Labeling the Wyckoff positions in supercells amounts to performing right coset decompositions of the translations group $\Gamma^{(1)}$, analogous to the Euclidean case in Eq. (2.16). Thus:

$$\Gamma^{(1)} = \bigcup_{\eta_i^{(1)} \in \mathrm{T}_{\Gamma^{(1)}}(\Gamma^{(m)})} \eta_i^{(1)} \Gamma^{(m)}, \tag{3.69}$$

thus for an arbitrary $\gamma^{(1)} \in \Gamma^{(1)}$:

$$\gamma^{(1)} = \eta_i^{(1)} \gamma^{(m)}, \tag{3.70}$$

where $\gamma^{(m)} \in \Gamma^{(m)}$. The cosets of $\Gamma^{(1)}/\Gamma^{(m)}$ are sets of translations that act non-trivially on the supercell $C^{(m)}$, with index $N^{(1,m)} = |\Gamma^{(1)} : \Gamma^{(m)}|$. Each representative of a coset in the transversal $\mathrm{T}_{\Gamma^{(1)}}(\Gamma^{(m)})$ is associated with a particular primitive cell $C^{(1)}$ within the supercell $C^{(m)}$. Therefore, we extend the labeling of Wyckoff positions in the primitive cell, Eq. (3.39), by adding another label $\eta_i^{(1)}$ indicating which primitive cell in the supercell the Wyckoff position is located in.

3.6 The supercell method

The supercell method consists of a sampling procedure to systematically access the higher-dimensional irreducible representations of the translation group $\Gamma^{(1)}$ without explicitly constructing them, [3]. This procedure consists of compactifying the m'th supercell $C^{(m)}$, identifying with normal subgroups $\Gamma^{(m)} \triangleleft \Gamma^{(1)} \triangleleft \Delta$, on a closed Riemann surface $\Sigma_{\mathfrak{g}}$.

Let us construct the corresponding Hamiltonian from supercells by following Ref. [3]. The extension of the labeling procedure modifies the tight-binding Hamiltonian (3.50) as:

$$\begin{aligned}\mathcal{H} &= \sum_{\tilde{\gamma}^{(1)},\gamma'^{(1)}\in\Gamma^{(1)}} \sum_{u,v} h^{uv}(\tilde{\gamma}^{(1)},\gamma'^{(1)}) c^{u\dagger}_{\tilde{\gamma}^{(1)}} c^{v}_{\gamma'^{(1)}} \\ &= \sum_{\tilde{\gamma}^{(m)},\gamma'^{(m)}\in\Gamma^{(m)}} \sum_{i,j=1}^{N^{(1,m)}} \sum_{u,v} h^{uv}(\eta_i^{(1)}\tilde{\gamma}^{(m)},\eta_j^{(1)}\gamma'^{(m)}) c^{u\dagger}_{\eta^{(1)}\tilde{\gamma}^{(m)}} c^{v}_{\eta_j^{(1)}\gamma'^{(m)}} ,\end{aligned} \tag{3.71}$$

where $u, v \in \mathcal{C}$. Let the labels for orbitals within the m'th supercell be equipped with $\eta_i^{(1)}$ such that $\mu = (u, \eta_i^{(1)})$. Thus, the orbital μ is located in a primitive cell that has been translated by $\eta_i^{(1)}$ within the supercell and the location within that primitive cell is given by u. The hopping matrix h^{uv}, which couples orbital u in the primitive cell translated by $\eta_i^{(1)}\tilde{\gamma}^{(m)}$ with orbital v in the primitive cell translated by $\eta_j^{(1)}\gamma'^{(m)}$, can be explicitly rewritten in terms of the labels in the supercells:

$$h^{uv}(\eta_i^{(1)}\tilde{\gamma}^{(m)},\eta_j^{(1)}\gamma'^{(m)}) = \mathrm{h}^{\mu\nu}(\tilde{\gamma}^{(m)},\gamma'^{(m)}), \tag{3.72}$$

which can be simplified further $\mathrm{h}^{\mu\nu}(\tilde{\gamma}^{(m)},\gamma'^{(m)}) = \mathrm{h}^{\mu\nu}(\tilde{\gamma}^{(m)}\gamma'^{(m)-1},\mathbb{1})$. Finally, let $\gamma^{(m)} = \tilde{\gamma}^{(m)}\gamma'^{(m)-1}$ and $\mathrm{h}^{\mu\nu}(\gamma^{(m)},\mathbb{1}) \equiv \mathrm{h}^{\mu\nu}(\gamma^{(m)},\mathbb{1})$ then it follows:
such that:

$$\mathcal{H} = \sum_{\gamma^{(m)},\gamma'^{(m)}\in\Gamma^{(m)}} \sum_{\mu,\nu} \mathrm{h}^{\mu\nu}(\gamma^{(m)}) c^{\mu\dagger}_{\gamma^{(m)}\gamma'^{(m)}} c^{\nu}_{\gamma'^{(m)}} . \tag{3.73}$$

This is structurally equivalent to the Hamiltonian (3.51). Thus, we can proceed as we did in section 3.4 and block-diagonalize the Hamiltonian. Then the Bloch Hamiltonian is given by:

$$H(D) = \sum_{\gamma^{(m)}\in\Gamma^{(m)}} \mathrm{h}(\gamma^{(m)}) \otimes D(\gamma^{(m)}) , \tag{3.74}$$

where $D : \Gamma^{(m)} \mapsto \mathrm{U}(d)$ with $d \in \mathbb{N}_{\geq 1}$. The special case for one-dimensional irreducible representations with $\chi : \Gamma^{(m)} \mapsto \mathrm{U}(1)$, is therefore given by:

$$H(\chi) = \sum_{\gamma^{(m)} \in \Gamma^{(m)}} \mathrm{h}(\gamma^{(m)}) \chi(\gamma^{(m)}). \tag{3.75}$$

P. M. Lenggenhager et al. [3] then argue that higher dimensional irreducible representations of $\Gamma^{(1)}$ are accessed via one dimensional irreducible representations of normal subgroups $\Gamma^{(m)}$, and thus this provides an effective sampling procedure for accessing non-Abelian Bloch states. They further conjecture that the sequence of m'th supercells in the $m \to \infty$ limit, converges to the thermodynamic limit. Additionally, they provide a rationalization of this conjecture through the introduction of PBC clusters constructed by symmetrically aggregating supercells into larger supercells, called **super-supercells**. This, requires an additional label by another right coset decomposition of $\Gamma^{(m)}$ such that the super-supercell is identified by a normal subgroup $\Gamma^{(n)} \triangleleft \Gamma^{(m)} \triangleleft \Delta$. The construction of the Hamiltonian and the block-diagonalization into blocks of Bloch Hamiltonians then follows by the same arguments as we have seen above and in section 3.4, see [3] for a detailed derivation and discussion.

Thus, finally, the **Abelian Bloch Hamiltonian** on supercells identified with normal subgroup $\Gamma^{(m)}$ is given by:

$$H(\mathbf{k}) = \sum_{\gamma^{(m)} \in \Gamma^{(m)}} h(\gamma^{(m)}) e^{i \sum_{i=1}^{2\mathfrak{g}} K_i(\gamma^{(m)}) k_i}, \tag{3.76}$$

where $K_i(\gamma^{(m)})$ corresponds to the number of times the generator $\gamma_i^{(m)}$ of $\Gamma^{(m)}$ appears in $\gamma^{(m)}$, where the inverse generator $\gamma_i^{(m)-1}$ is counted negatively. The lattice with periodic boundary conditions endowed on the supercell is compactified on the closed Riemann surface $\Sigma_{\mathfrak{g}}$, 3.3. Once again, we can think of threading the $2\mathfrak{g}$ non-contractible cycles of $\Sigma_{\mathfrak{g}}$ by magnetic fluxes associated with the mapping $\chi : \Gamma^{(m)} \to \mathrm{U}(1)$, such that the $2\mathfrak{g}$ components form the Abelian hyperbolic Brillouin zone torus $\mathbb{T}^{2\mathfrak{g}}$, [3, 18]. The corresponding Brillouin zone is then defined as:

$$\mathrm{BZ}^{(m,1)} = \left\{ \gamma_i^{(m)} \mapsto \chi_{\mathbf{k}}(\gamma_i^{(m)}) = e^{ik_i} \mid \mathbf{k} \in [0, 2\pi)^{2\mathfrak{g}} \cong \mathbb{T}^{2\mathfrak{g}} \right\}, \tag{3.77}$$

where the superscript $(m, 1)$ indicates the m'th normal subgroup $\Gamma^{(m)}$ and the dimension of the one-dimensional irreducible representations, respectively.

4 Modeling of bulk properties

In this chapter we will study the bulk properties of regular lattices in two dimensional Euclidean and hyperbolic spaces, with an emphasize on hyperbolic lattices. As such, we start with an interlude in the Euclidean plane by reviewing the nearest-neighbor tight-binding model on the honeycomb lattice. This enables us to put our considerations of chapter 2 into practice. Subsequently, we will contrast the study of the honeycomb lattice with the hyperbolic $\{6,4\}$ and $\{8,3\}$-lattices. In particular, the application of the group theoretical aspects are highlighted and the bulk properties of the tight-binding models are studied through the use of the supercell method, following the methodology reviewed in chapter 3.

4.1 Honeycomb lattice

The honeycomb lattice forms an ideal platform to establish some key concepts concerning band theory and topology. The corresponding lattice is formed by a regular tessellation of the Euclidean plane by hexagons that meet with 3 identical copies at each corner, which constitutes a $\{6,3\}$-lattice. Figure 7 depicts the honeycomb lattice together with the nearest-neighbor vectors $\mathbf{a}_i$ and Bravais lattice vectors $\mathbf{b}_i$ where $i = 1,2,3$. We set the lattice constant to 1 for convenience.

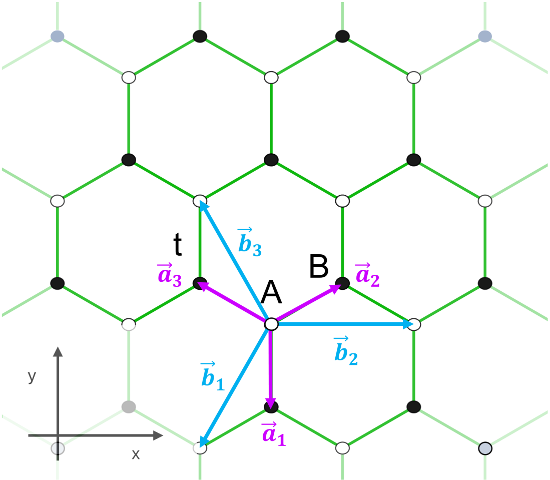

Figure 7: **The Honeycomb lattice**, formed by regularly tessellating the Euclidean plane with hexagons. The sublattices A and B are indicated with white and black colored sites, respectively. A nearest-neighbor tight-binding model endows the lattice with hopping amplitude t which couples sites on sublattices A and B. The nearest-neighbor vectors $\mathbf{a}_i$ and lattice vectors $\mathbf{b}_i$ are indicated in blue and pink, respectively.

The nearest-neighbor vectors $\mathbf{a}_i$ and lattice vectors $\mathbf{b}_i$ are given by:

$$\begin{aligned} \mathbf{a}_1 &= (0,\,-1) \qquad & \mathbf{b}_1 &= \mathbf{a}_1 - \mathbf{a}_2, \\ \mathbf{a}_2 &= (\sqrt{3}/2, 1/2) \qquad & \mathbf{b}_2 &= \mathbf{a}_2 - \mathbf{a}_3, \\ \mathbf{a}_3 &= (-\sqrt{3}/2, 1/2) \qquad & \mathbf{b}_3 &= \mathbf{a}_3 - \mathbf{a}_1, \end{aligned} \tag{4.1}$$

The tight-binding Hamiltonian for spin-less electrons can be constructed by considering the lattice as bipartite with sublattices A and B, as indicated in Fig. 7. As such, we denote the annihilation operators accordingly as a_i, b_i, such that:

$$\mathcal{H} = t \sum_{<i,j>} a_i^\dagger b_j + \text{h.c.} \, . \tag{4.2}$$

where $< i, j >$ indicates a sum over nearest neighbor sites. Let us block-diagonalize the Hamiltonian $\mathcal{H}$ by following the methodology established in section 2.3. The primitive cell of the honeycomb lattice can be compactified on a two-dimensional torus by imposing periodic boundary conditions. This induces the Bloch theorem, which leads to the block-diagonalization of the tight-binding Hamiltonian with an emergent BZ torus $\mathbb{T}^2$ such that the Bloch Hamiltonian is given by:

$$\begin{aligned} H(\mathbf{k}) &= t \sum_{i=1}^{3} \begin{bmatrix} 0 & e^{-i\mathbf{k}\cdot\mathbf{a}_i} \\ e^{i\mathbf{k}\cdot\mathbf{a}_i} & 0 \end{bmatrix} = \mathbf{h}(\mathbf{k}) \cdot \boldsymbol{\sigma}, \\ \text{with } \; \mathbf{h}(\mathbf{k}) &= t \sum_{i=1}^{3} (\cos(\mathbf{k}\cdot\mathbf{a}_i), \sin(\mathbf{k}\cdot\mathbf{a}_i), 0), \end{aligned} \tag{4.3}$$

where $\boldsymbol{\sigma} = (\sigma_1, \sigma_2, \sigma_3)$ are the Pauli matrices in the fundamental representation of SU(2). The eigenvalue problem can be solved analytically, resulting in eigenvalues:

$$\epsilon^{\pm}(\mathbf{k}) = \pm \left\| \mathbf{h}(\mathbf{k}) \right\| . \tag{4.4}$$

The band structure together with the density of states, as shown in Fig. 8, reveal a van-Hove singularity at the high-symmetry point M and a Dirac point at K where linearly-dispersing Dirac cones meet, forming a semimetal.

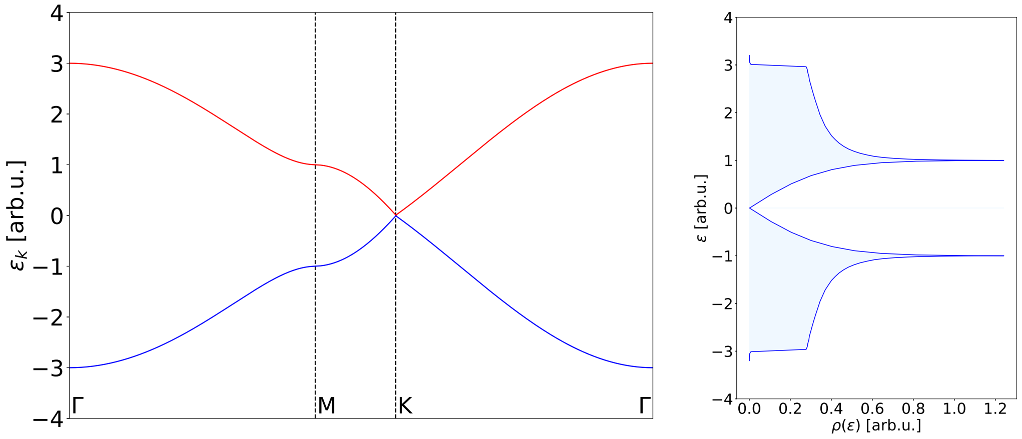

Figure 8: **Band structure and density of states for the nearest-neighbor tight-binding model on honeycomb lattice**. The band structure is particle-hole symmetric. The high symmetry points M and K exhibit a van Hove singularity and a Dirac point, respectively.

The corresponding Brillouin zone forms a hexagon, which is reflected in the density plot of the energy eigenvalues $\epsilon^+(\mathbf{k})$ as well, depicted in Fig. 9.

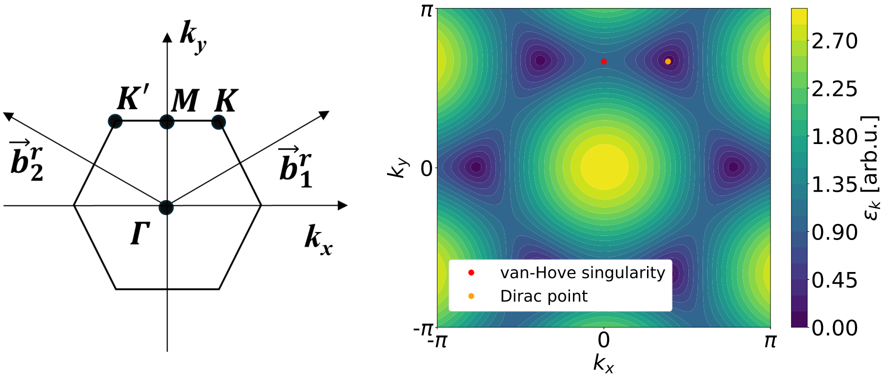

Figure 9: **Brillouin zone**. Left: Brillouin zone of the honeycomb lattice together with its high symmetry points and reciprocal lattice vectors $\mathbf{b}_i^r$. Right: Density plot of the energy eigenvalues $\epsilon^+(k_x, k_y)$, with a van Hove singularity and Dirac point indicated as a red and orange dot respectively.

The corresponding reciprocal lattice vectors are given by:

$$\mathbf{b}_1^r = \frac{2\pi}{3}(\sqrt{3}, 1), \quad \mathbf{b}_2^r = \frac{2\pi}{3}(-\sqrt{3}, 1)\,. \tag{4.5}$$

In subsequent chapters we may change to the non-orthogonal basis of reciprocal lattice vectors $\mathbf{b}_i^r$ in order to conveniently compute topological invariants over the BZ, such that:

$$\begin{bmatrix} k_x \\ k_y \end{bmatrix} = \frac{1}{2\pi} \begin{bmatrix} \mathbf{b}_1^r & \mathbf{b}_2^r \end{bmatrix} \begin{bmatrix} k_1 \\ k_2 \end{bmatrix} \,. \tag{4.6}$$

The change of basis leads to a **band folding**, as indicated in the Fig. 10.

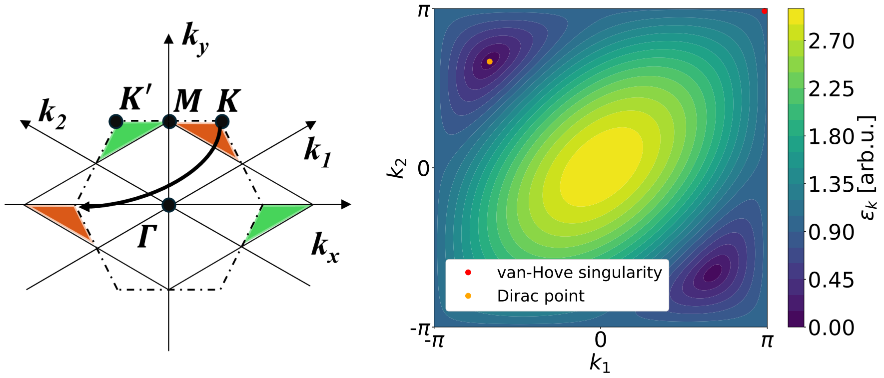

Figure 10: **Brillouin zone**. Left: Band folding schematics in Brillouin zone for a change of basis to k_1, k_2 coordinates. Right: Density plot of the energy eigenvalues $\epsilon^+(k_1, k_2)$, with a van Hove singularity and Dirac point indicated as a red and orange dot respectively.

Further, the termination of the infinite honeycomb lattice to semi-finite ribbons treated with **open boundary conditions** reveals that certain geometries can host localized edge states, a review is included in Appendix 10.1.

4.2 Hyperbolic lattices

The group theoretical considerations for the construction of hyperbolic lattices of section 3.2 can now be put into practice. To do so, we construct the $\{6,4\}$ and $\{8,3\}$-lattices on primitive cells as well as on supercells to study the their bulk properties. We will generally focus on these two hyperbolic lattices, and occasionally consider other $\{p,q\}$-lattices in subsequent chapters. The framework to construct the hyperbolic lattices is implemented in the GAP package **HyperCells** [2], which can be used in tandem with the Mathematica package **HyperBloch** [1] to construct Abelian Bloch Hamiltonians, both of which were developed in Ref. [3]. These packages will be the central tools for the study of hyperbolic lattices in this thesis.

4.2.1 Hyperbolic $\{6,4\}$ and $\{8,3\}$-lattices

In this subsection we will study the bulk properties of the $\{6,4\}$ and $\{8,3\}$-lattices through the density of states, by applying the supercell method, described in section 3.6. This enables us to access non-Abelian Bloch states without an explicit construction of higher-dimensional irreducible representations by applying Abelian hyperbolic band theory on supercells.

We identify the primitive cells and supercells by constructing an appropriate sequence of normal subgroups under the constraint in Eq. (3.68). The sequences of normal subgroups $\Gamma^{(m)}_{\{6,4\}} \triangleleft \Delta^+(2,4,6)$ and $\Gamma^{(m)}_{\{8,3\}} \triangleleft \Delta^+(2,3,8)$ are constructed via the quotient groups tabulated in Ref. [39]:

$$\begin{aligned} &\{6,4\}\text{-lattice}: \quad && \text{T2.2, T5.4, T9.3, T33.11, T65.9} \\ &\{8,3\}\text{-lattice}: \quad && \text{T2.1, T5.1, T17.2, T33.1} \end{aligned} \tag{4.7}$$

This is followed by a labeling procedure of Wyckoff positions $V_{\mathrm{y}}^{\mathrm{cell}}$ within the chosen unit cell per Eq. (3.39), which we equip with labels according to the right coset decomposition in Eq. (3.69). The graph representation of the nearest-neighbor tight-binding Hamiltonian on the primitive cell for the $\{6,4\}$ and $\{8,3\}$-lattices are depicted in Fig. 11. We equip the lattice with coupling constants set to t for inter and intra-cell **nearest neighbor** interactions, indicated in blue and red respectively.

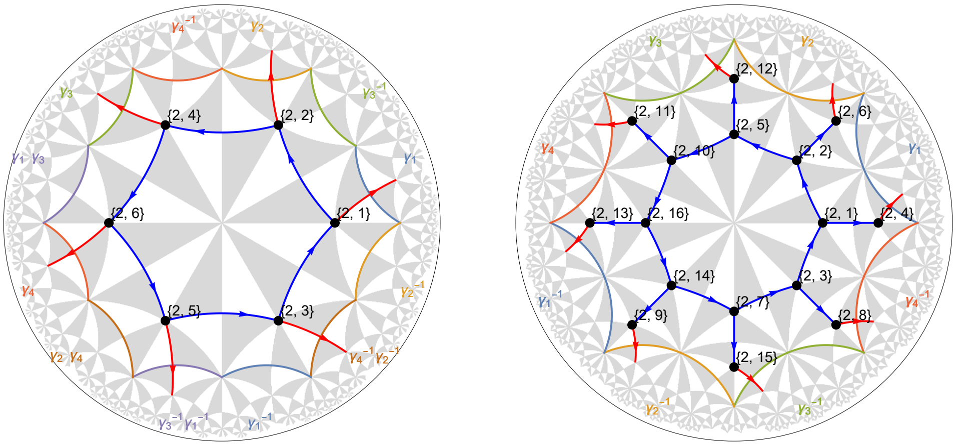

Figure 11: **Graph representation of nearest-neighbor tight-binding Hamiltonian on primitive cells of $\{6, 4\}$ and $\{8, 3\}$-lattice**. The inter and intra-cell hopping amplitudes t are indicated in blue and red, respectively. Left: The primitive cell of the $\{6, 4\}$-lattice together with 6 sites located at Wyckoff positions in $V_{\mathrm{y}}^{\mathrm{cell}}(2, 4, 6)$, as given in Eq. (3.42). Right: The primitive cell of the $\{8, 3\}$-lattice together with 16 sites located at Wyckoff positions in $V_{\mathrm{y}}^{\mathrm{cell}}(2, 3, 8)$. The primitive cell endowed with PBCs is compactified on a four dimensional surface called the **Bolza surface** [18].

The corresponding nearest-neighbor tight-binding Hamiltonian is:

$$\mathcal{H} = t \sum_{<i,j>} c_i^\dagger c_j \tag{4.8}$$

The construction of the Abelian Bloch Hamiltonians in Eq. (3.76) follows by AHBT. Consider for example the $\{6, 4\}$-lattice on the primitive cell. The translation group $\Gamma^{(1)}_{\{6,4\}}$ is generated by four operators γ_i as given in Eq. (3.26), where $i = 1, 2, 3, 4$. Thus, four linearly independent momenta appear in the one dimensional irreducible representations $\gamma_i \mapsto e^{ik_i}$ when applying AHBT, which amounts to a **four-dimensional** BZ torus $\mathbb{T}^4$. The corresponding Abelian Bloch Hamiltonian is given by:

$$H(\mathbf{k}) = t \begin{bmatrix} 0 & 1+e^{ik_2} & 1+e^{-ik_1} & 0 & 0 & 0 \\ 1+e^{-ik_2} & 0 & 0 & 1+e^{ik_3} & 0 & 0 \\ 1+e^{ik_1} & 0 & 0 & 0 & 1+e^{i(k_2+k_4)} & 0 \\ 0 & 1+e^{-ik_3} & 0 & 0 & 0 & 1+e^{ik_4} \\ 0 & 0 & 1+e^{-i(k_2+k_4)} & 0 & 0 & 1+e^{i(k_1+k_3)} \\ 0 & 0 & 0 & 1+e^{-ik_4} & 1+e^{-i(k_1+k_3)} & 0 \end{bmatrix}. \tag{4.9}$$

We proceed by calculating the density of states by exact diagonalization via random sampling in the Brillouin zones $\mathrm{BZ}^{(m,1)}$, Eq. (3.77). Figure 12 shows the corresponding DOS, each produced by $5 \cdot 10^4$ randomly sampled points with subsequent application of a kernel density estimation with a Gaussian kernel using a energy bandwidth of 0.01. The DOS of the $\{8, 3\}$-lattice, shown on the right, is in agreement with the computation via the real space **continued fraction method** in [33], as has been demonstrated in [3].

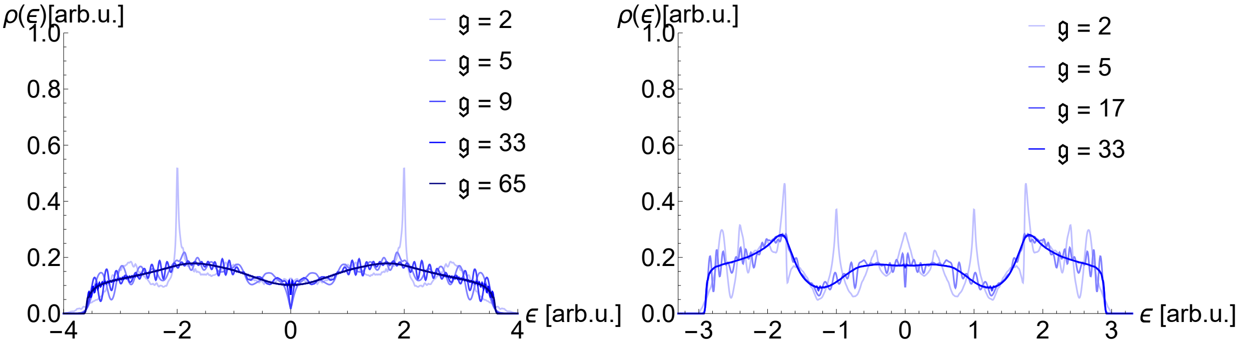

Figure 12: **Density of states for nearest-neighbor tight-binding model on $\{6,4\}$ and $\{8,3\}$-lattice**, left and right respectively. The sequence of supercells listed in Eq. (4.7) are indicated with the corresponding genuses $\mathfrak{g}$ in the legends.

4.2.2 Hyperbolic $\{6,4\}$ and $\{8,3\}$ Lieb lattices

Lieb lattice originate from square lattices in the Euclidean plane. Each square unit cell is endowed with three sites placed at Wyckoff positions $V_{\mathrm{x}}^{\mathrm{cell}}$,$V_{\mathrm{y}}^{\mathrm{cell}}$. These lattices exhibit energy bands of constant energy over an extended region in the Brillouin zone, which leads to pronounced flat-bands in density of states. This makes Lieb lattices ideal platforms to study strongly correlated systems [44], due to the diverging ratio between the interaction potential and the kinetic energy [22].

In the non-interacting nearest-neighbor tight-binding models, the relation between real-space and momentum-space properties can be used to understand key aspects of flat-bands. T. Bzdušek et al. [12] have studied the manifestation of flat-bands in hyperbolic Kagome and dice lattices by real-space and momentum-space considerations. They show that the properties of flat-bands such as band degeneracy and band touchings with other dispersive bands are quantifiable by applying non-Abelian and Abelian hyperbolic band theory. In particular, they conjecture that for all flat-band hyperbolic lattices the fraction of states that lie within the flat-bands, the **flat-band fraction**, remains unchanged when restricting to Abelian states. P. M. Lenggenhagger [27] has verified their prediction through the application of the supercell method in the $\{8,3\}$ Kagome lattice for the supercell sequence in Eq. (4.7).

We extend the HyperCells package through the addition of Lieb lattices in the hyperbolic plane. Thus, we incorporate additional sites within the $\{p,q\}$-lattices by including sites on both Wyckoff positions in $V_{\mathrm{x}}^{\mathrm{cell}}$ and $V_{\mathrm{y}}^{\mathrm{cell}}$. The graph representations of the tigh-binding Hamiltonian of the $\{6,4\}$ and $\{8,3\}$ Lieb lattices are depicted in Fig. 13.

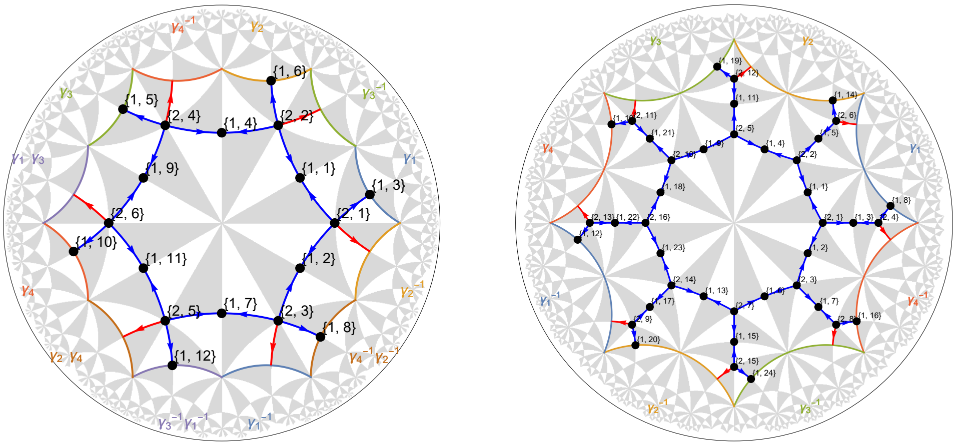

Figure 13: **Graph representation of nearest-neighbor tight-binding Hamiltonian on primitive cells of $\{6,4\}$ and $\{8,3\}$ Lieb lattices**, left and right, respectively. The inter- and intra-cell hopping amplitudes t are indicated in blue and red respectively. The primitive cell together with sites located at Wyckoff positions in $V_{\mathrm{x}}^{\mathrm{cell}}$ and $V_{\mathrm{y}}^{\mathrm{cell}}$, as given in Eq. (3.42).

The corresponding density of states are shown in Fig. 14, each produced by $5 \cdot 10^4$ randomly sampled points. The DOS is smoothed by a kernel density estimation with a Gaussian kernel of energy bandwidth 0.009 for the main plot and energy bandwidth 0.003 for the insets. The pronounced flat bands are centered around zero energy.

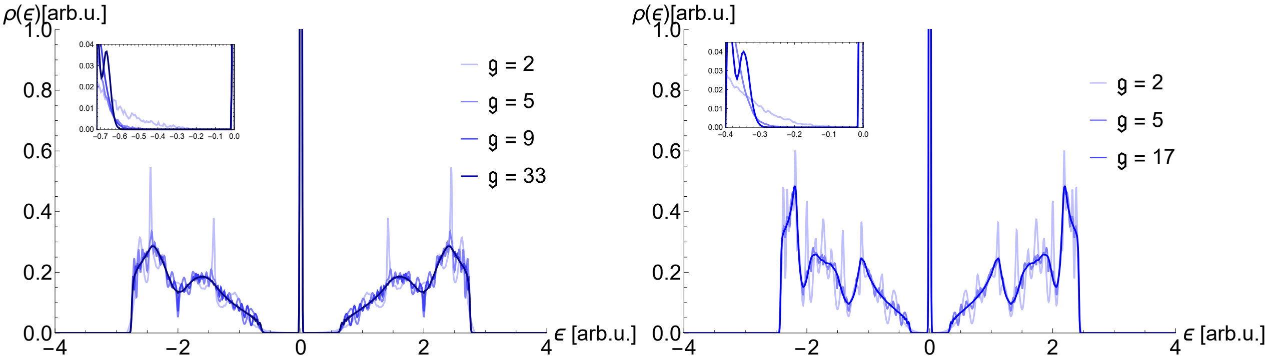

Figure 14: **Density of states in the tight-binding model for the $\{6,4\}$ and $\{8,3\}$ Lieb lattice**, left and right, respectively. Each figure depicts density of states with a pronounced flat band at zero energy. The insets, show the behavior of the DOS in the vicinity of the flat band. The small sample size might obscure a band touching.

We calculate the fraction of states within an energy region $\pm 10^{-12}$ in the vicinity of the flat bands without smoothed data. The flat-band fraction for all unit cells in the $\{6,4\}$ and $\{8,3\}$ Lieb lattices are $1/3$ and $1/5$, respectively. No band-touching was observed, however, this might be obscured by the small sample size.

5 Topological insulators

Topological insulators are characterized by emergent bulk band gaps and protected metallic boundary states. They can be classified by **topological invariants**, which differentiate ordinary insulators from topological insulators, [45–47]. In this chapter, we will review and study topological insulators in Euclidean and hyperbolic lattices.

5.1 Haldane model

The Haldane model on the honeycomb lattice describes a **topological insulator** manifested by the **anomalous quantum Hall effect** (AQHE),[48]. Recall, that the **quantum Hall effect** arises if time reversal is explicitly broken globally by an externally applied magnetic field, leading to gapped bulk states and conducting boundary states in the topological phase. However, time reversal symmetry can also be broken by local magnetic fluxes as well, giving rise to the anomalous quantum Hall effect in the Haldane model. In the pursuit of studying variants of the Haldane model on hyperbolic lattices in the subsequent section, let us review the basic spectral and topological properties of the Haldane model [20].

The Haldane model endows the honeycomb lattice with a staggered on-site potential $\pm M$ at the sublattices A and B, respectively. Besides nearest-neighbor interactions (NN-interactions) t_1, a coupling of sites through next-nearest-neighbor interaction (NNN-interactions) t_2 is considered. Additionally, local magnetic fluxes are threaded through the entire lattice such that the net flux in each hexagon is rendered zero. These fluxes are imposed such that the hopping amplitude t_2 acquires a phase through **Peierls substitution** [45], namely $t_2 \to e^{i\phi} t_2$, see Fig. 15.

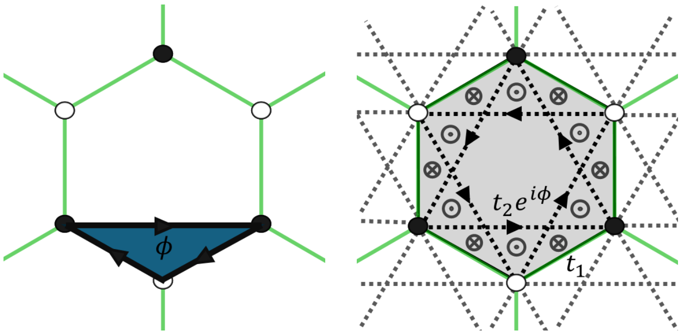

Figure 15: **NNN-hopping terms and magnetic fluxes in hexagon plaquette**. Left: The honeycomb lattice is endowed with one local flux ϕ indicated with blue triangular plaquette, its boundaries form a **Wilson loop**,[49]. Right: The Haldane model endows the entire honeycomb lattice by local fluxes of the form indicated on the left. The NNN-hopping terms are chosen to develop an additional phase factor by parallel transport, such that the NN-hopping terms are left unchanged. The phases ϕ correspond to perpendicular magnetic fluxes with alternating signs, indicated with symbols $\otimes$ and $\odot$, across parts of the hexagon. The sum of fluxes within a hexagon is zero.

The corresponding tight-binding Hamiltonian is given by:

$$\mathcal{H} = \frac{M}{2}\sum_i (a_i^\dagger a_i - b_i^\dagger b_i) + t_1 \sum_{<i,j>} a_i^\dagger b_j + t_2\, e^{i\phi} \sum_{\overleftarrow{ij}} (a_i^\dagger a_j + b_i^\dagger b_j) + \text{h.c.}\,, \tag{5.1}$$

where $\overleftarrow{ij}$ denotes the sum over next-nearest-neighbor contributions in clockwise directions. The block-diagonalization through the imposition of Bloch theorem yields:

$$H(\mathbf{k}) = \sum_{i=1}^{3} \begin{bmatrix} 2\,t_2 \cos(\mathbf{k}\cdot\mathbf{b}_i + \phi) + M & t_1\, e^{-i\mathbf{k}\cdot\mathbf{a}_i} \\ t_1\, e^{i\mathbf{k}\cdot\mathbf{a}_i} & 2\,t_2 \cos(\mathbf{k}\cdot\mathbf{b}_i - \phi) - M \end{bmatrix}. \tag{5.2}$$

We can rewrite this compactly:

$$H(\mathbf{k}) = \hat{h}(\mathbf{k})\sigma_0 + \mathbf{h}(\mathbf{k})\cdot\boldsymbol{\sigma}, \tag{5.3}$$

where σ_0 is the 2×2 identity matrix and:

$$\begin{aligned} \hat{h}(\mathbf{k}) &= 2\,t_2 \sum_{i=1}^{3} \cos(\mathbf{k}\cdot\mathbf{b}_i)\cos(\phi), \\ \mathbf{h}(\mathbf{k}) &= (t_1 \sum_{i=1}^{3} \cos(\mathbf{k}\cdot\mathbf{a}_i),\, t_1 \sum_{i=1}^{3} \sin(\mathbf{k}\cdot\mathbf{a}_i),\, M - 2\,t_2 \sum_{i=1}^{3} \cos(\mathbf{k}\cdot\mathbf{b}_i)\sin(\phi)). \end{aligned} \tag{5.4}$$

The energy eigenvalues are given by:

$$\epsilon^{\pm}(\mathbf{k}) = \hat{h}(\mathbf{k}) \pm \|\mathbf{h}(\mathbf{k})\|\;. \tag{5.5}$$

The spectrum of the Haldane model exhibits gaps at specific values of coupling constants. An example of three distinct configurations is depicted in Fig. 16. The first figure on the left depicts a gapped band structure at $t_1 = 1$, $\phi = \pi/2$ and $\eta = M/t_2 = 2.5\sqrt{3}$. In the central figure we increase η to $\eta = 3\sqrt{3}$, the gap closes at the K-points and pairs of Dirac cones emerge and touch at the Dirac point. Increasing η further reopens the gap, depicted in the right for $\eta = 3.5\sqrt{3}$.

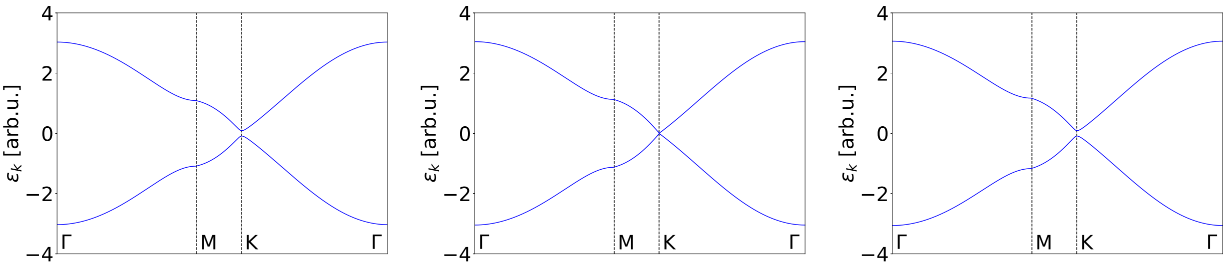

Figure 16: **Band structure of the Haldane model**. Left: The band structure is gapped at $t_1 = 1$, $\phi = \pi/2$ and $\eta = M/t_2 = 2.5\sqrt{3}$. Center: As we increase η to $\eta = 3\sqrt{3}$, the gap closes at the K-points and pairs of Dirac cones emerge and touch at the Dirac point. Right: Increasing η further reopens the gap, for example at $\eta = 3.5\sqrt{3}$.

The corresponding phases can be identified by a **topological invariant**, the **first Chern number** $C_{(1)}$. Thus, let us review the geometrical interpretation of the first Chern number following Refs. [7, 47, 50, 51] a more formal description can be found in Ref. [40].

The introduction of local fluxes within the honeycomb lattice raises the question how the Hilbert space spanned by the Bloch states is modified. Bloch states can no longer be compared without considering how phases accumulate as we sweep across the Brillouin zone torus $\mathbb{T}^2$. Consider a non-degenerate system with a general Bloch Hamiltonian $H(\mathbf{k})$ and the corresponding BZ torus $\mathbb{T}^2$ such that $\mathbf{k} \in (\mathbb{R}/2\pi\mathbb{Z})^2$. We are interested in how the Bloch states transform as they are transported on a closed loop in the BZ torus. For a cell-periodic Bloch eigenstates in the b'th band $|b(\mathbf{k})\rangle$ we find:

$$H(\mathbf{k})|b(\mathbf{k})\rangle = \epsilon_b(\mathbf{k})|b(\mathbf{k})\rangle\,, \tag{5.6}$$

where $\epsilon_b(\mathbf{k})$ is the energy eigenvalue of the state $|b(\mathbf{k})\rangle$. Crucially, the states are ambiguously defined since the multiplication with a phase factor $e^{i\theta}$ is a valid eigenstate as well and fulfills $\langle e^{i\theta}b(\mathbf{k})\,|\,e^{i\theta}b(\mathbf{k})\rangle = \langle b(\mathbf{k})\,|\,b(\mathbf{k})\rangle = 1$. We may not be able to define a global phase factor for the state $|b(\mathbf{k})\rangle$ for every value of $\mathbf{k}$, thus in general the states may acquire locally varying phase factors as we sweep across the BZ tours. We think of tracing out a path in the BZ torus as a time evolution of the state which is governed by the Schrödinger equation:

$$i\partial_t|\Psi_b(t)\rangle = H(\mathbf{k}(t))|\Psi_b(t)\rangle, \tag{5.7}$$

where we have chosen a specific parameterization by t. Thus, let us perform an **adiabatic time evolution** such that the parameterization of $\mathbf{k}(t)$ from $t = 0$ to $t = T$ forms a closed loop $\partial\Gamma$ in the BZ torus and thus the time evolution of the state $|b(\mathbf{k}(0))\rangle$ is given by:

$$|\Psi_b(t)\rangle = \exp\Big(-i\int_0^t dt'\epsilon_b(\mathbf{k}(t'))\Big)e^{i\theta_b(t)}|b(\mathbf{k}(t))\rangle \tag{5.8}$$

The first exponential is the usual dynamical phase factor. We are interested in the second phase factor. It cannot be rewritten as a function of $\mathbf{k}$ and it is in general not equal to the phase factor at the start of the closed loop such that $\theta(T) \neq \theta(0)$. We can insert this state into the Schrödinger equation and multiply by $\langle b(\mathbf{k}(t))|$ and find after some straightforward manipulations that:

$$\theta_b(\partial\Gamma) = i\oint_{\partial\Gamma}\langle b(\mathbf{k})\,|\,\partial_i b(\mathbf{k})\rangle dk^i\,, \tag{5.9}$$

where $\partial_i \equiv \frac{\partial}{\partial k^i}$. The necessary object to compare states is thus given by the so-called **Berry connection** $A_i^b(\mathbf{k})$ defined as:

$$A_i^b(\mathbf{k}) \equiv \langle b(\mathbf{k})|\partial_i|b(\mathbf{k})\rangle \tag{5.10}$$

and we call θ_b the **Berry phase**, such that:

$$\theta_b(\partial\Gamma) = i \oint_{\partial\Gamma} A_b^i(\mathbf{k}) dk_i. \tag{5.11}$$

Thus, the geometry of the parameter space in which $\mathbf{k}$ resides necessitates the introduction of a connection which relates neighboring points by accounting for phases accumulated during transport, known as **parallel transport**. Analogous notions can be found for example in QFT and General relativity. For example, in quantum electrodynamics (QED), enforcing the invariance under a local U(1) symmetry necessitates the introduction of a connection, the photon field A^μ. Fermionic fields couple to the photon filed such that A^μ connects phase transformations at neighboring points in space-time [52]. The analog of the **field strength tensor** $F^{\mu\nu}$ of QED, is the **Berry curvature** $F_{ij}^b(\mathbf{k})$ defined as:

$$F_{ij}^b(\mathbf{k}) = \partial_i A_j^b(\mathbf{k}) - \partial_j A_i^b(\mathbf{k}), \tag{5.12}$$

Let us look at how the Berry connection transforms under a local U(1) transformation. We know that states $|b(\mathbf{k})\rangle$ transform as:

$$|b(\mathbf{k})\rangle \to e^{i\alpha(\mathbf{k})}|b(\mathbf{k})\rangle \tag{5.13}$$

therefore:

$$A_j^b(\mathbf{k}) \to A_j^b + i\partial_j\alpha(\mathbf{k}) \tag{5.14}$$

The Berry connection is not invariant under a gauge tranformation. We can further conclude that the Berry curvature is invariant under a general gauge transformation, apparent by its definition. The Berry phase is also invariant under a gauge transformation. Consider for example a Hamiltonian parameterized by three dimensional parameter space $H(\mathbf{R}(\mathbf{k}))$ with $\mathbf{R}(\mathbf{k}) \in \{R_1(\mathbf{k}), R_2(\mathbf{k}), R_3(\mathbf{k})\}$, then we may explicitly write the Berry phase in terms of the Berry curvature by using Stokes theorem:

$$\theta_b(\Gamma) = \frac{i}{2} \oint_{\Gamma} ds_i \epsilon^{ijk} F_{jk}^b(\mathbf{R}(\mathbf{k})), \tag{5.15}$$

where ϵ^{ijk} is the Levi-Civita-Symbol, $i, j, k = 1, 2, 3$ with derivatives in the Berry connection given by $\partial_i \equiv \frac{\partial}{\partial R^i}$. We proceed by constructing a topological invariant that characterizes the phases of the Haldane model. Consider the vector $\mathbf{h}(\mathbf{k})$ given in Eq. (5.4), the simple structure of the Hamiltonian $H(\mathbf{k})$ in Eq. (5.3) suggests a parameterization in terms of $\mathbf{h}(\mathbf{k})$ such that $H(\mathbf{h})$. Further, $\hat{h}(\mathbf{k})$ in Eq. (5.4) leads to an energy shift of the spectrum and has no effect on topological properties, provided the system remains in an insulating phase. The eigenstates are given by [45]:

$$u_\pm(\mathbf{h}) = \frac{1}{N(\mathbf{h})^{1/2}} \begin{bmatrix} \frac{\epsilon^\pm(\mathbf{h})}{h_1+ih_2} \\ 1 \end{bmatrix}, \quad N(\mathbf{h}) = \Big(1 + \frac{h_3 + (\epsilon^\pm(\mathbf{h}))^2}{h_1^2 + h_2^2}\Big). \tag{5.16}$$

Thus the Berry phase takes the form:

$$\theta_{-}(\Gamma) = \frac{i}{2}\int_{\Gamma} dk^2\, \frac{\mathbf{h}(\mathbf{k})}{\|h\|^3} \cdot \Big(\frac{\partial \mathbf{h}(\mathbf{k})}{\partial k_x} \times \frac{\partial \mathbf{h}(\mathbf{k})}{\partial k_y}\Big). \tag{5.17}$$

We recognize that the integrand is the signed parallelogram spanned by $\frac{\partial \mathbf{h}(\mathbf{k})}{\partial k_x}$ and $\frac{\partial \mathbf{h}(\mathbf{k})}{\partial k_y}$. As such, as $\mathbf{k}$ spreads over the BZ torus, $\mathbf{h}$ describes a closed surface Σ [20], and the total Berry phase over the entire BZ torus is proportional to the number of times the BZ wraps around the surface Σ. It can be shown [40], that this number is an integer times 2π. Therefore, we can characterize the topology of the system by the first **Chern number** of the b'th band, defined as:

$$C^b_{(1)} = \frac{1}{2\pi i}\int_{\mathbb{T}^2} d^2k\, F^b_{xy}(\mathbf{k}). \tag{5.18}$$

For our purpose, we need to compute total first Chern number up to n filled bands:

$$C_{(1)} = \frac{1}{2\pi i}\sum_{b=1}^{n}\int_{\mathbb{T}^2} d^2k\, F^b_{xy}(\mathbf{k}). \tag{5.19}$$

Figure 17 shows the corresponding phase diagram of the Haldane model. The topological phase is characterized by a non-zero first Chern number $C_{(1)} = \pm 1$ at half filling, indicated in shades of blue and red. The black curves indicates the semi-metallic phase, which separates the topological phase from the trivial phase in white.

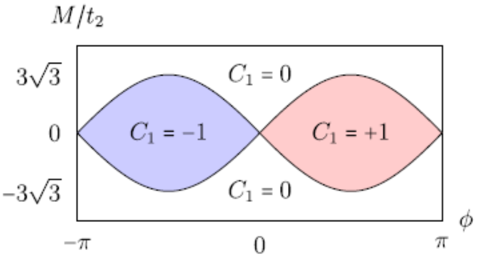

Figure 17: **Phase diagram of the Haldane model**. The topological phases in the Haldane model are characterized by a non-vanishing first Chern number indicated in shades of blue and red. The semi-metallic phase is characterized by black curves separating the topological phase from the trivial phase in white. Figure reproduced from Ref. [20].

We proceed by computing the first Chern number numerically following [53, 54]. Consider the corresponding BZ torus $\mathbb{T}^2$, we construct a grid of equidistantly spaced k_x, k_y values on $\mathbb{T}^2$ with distance l. The analog of the Berry connection is given by the U(1) link variable on the discretized surface:

$$U^b_i(\mathbf{k}) \equiv \langle b(\mathbf{k})\,|\,b(\mathbf{k}+l\hat{\imath})\rangle, \tag{5.20}$$

where $\hat{\imath}$ is a unit vector $\hat{k}_x$ or $\hat{k}_y$. Analogous to the Berry connection, the link variable $U^b_i(\mathbf{k})$ describes the phase acquired during parallel transport. The total flux of Berry curvature $F^b_{xy}(\mathbf{k})$

through a square in the k_x, k_y grid can be accounted for by constructing **Wilson loops** [49] which describes the Berry phase accumulated during parallel transport in counterclockwise direction around that square:

$$W^b_{xy,\mathbf{k}} = U^b_x(\mathbf{k})U^b_y(\mathbf{k}+l\hat{k}_x)U^b_x(\mathbf{k}+l\hat{k}_y)^{-1}U^b_y(\mathbf{k})^{-1}, \tag{5.21}$$

such that $F^b_{xy}(\mathbf{k})$ is given by:

$$l^2 F^b_{xy}(\mathbf{k}) = \ln(W^b_{xy,\mathbf{k}}). \tag{5.22}$$

Thus, the first Chern number $C^b_{(1)}$ of the b'th band is given by:

$$C^b_{(1)} = \frac{1}{2\pi i}\lim_{l\to 0}\sum_{\mathbf{k}} l^2 F^b_{xy}(\mathbf{k}), \tag{5.23}$$

Figure 18 shows the flux of Berry curvature in the discretized k_x, k_y grid with positive and negative local fluxes of Berry curvature generated in the vicinity of the K points. In the topological phase, the negative and positive fluxes of Berry curvature are generated in different bands such that the Chern number at half filling is ±1, which can be computed conveniently by performing a change of basis as given in Eq. (4.6).

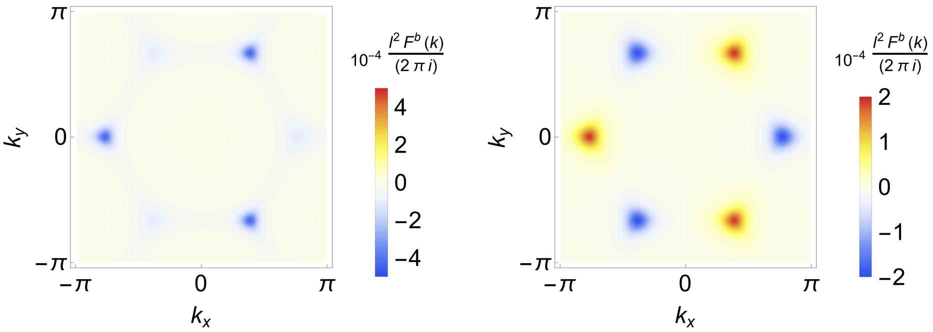

Figure 18: **Sinks and sources of Berry curvature in the Haldane model**. Berry curvature at half filling $F^-_{xy}(\mathbf{k})$. Left: In the topological phase at half filling for $\phi = \frac{\pi}{2}$ and $\eta = \sqrt{3}$ the local fluxes of non-vanishing Berry curvature $F^b(\mathbf{k}) \equiv F^-_{xy}(\mathbf{k})$ are negative, and located in the vicinity of the high symmetry points K. Right: The trivial phase at $\phi = 0$ and $\eta = \sqrt{3}$ exhibits alternating positive and negative local fluxes of Berry curvature.

A characteristic feature of two-dimensional topological insulators is the ability to host gapless one dimensional edge state according to the **bulk boundary correspondence** [46]. The appearance of these states can be demonstrated by terminating the infinite lattice to semi-finite **ribbons**, which reveals that the Haldane model can host edge states in the Chern insulating phase. We have included a discussion of the development of localized states in the Haldane model on semi-finite ribbons, treated with open boundary conditions, in Appendix 10.2.

5.2 Haldane model on the hyperbolic $\{6,4\}$ and $\{8,3\}$-lattice

In the last section we were able to characterize the topological phase of the Haldane model on the Euclidean honeycomb lattice via one momentum-space first Chern number calculated by performing an integration over the two-dimensional BZ torus $\mathbb{T}^2$. The analogous topological characterization via momentum-space first Chern numbers in Haldane models on hyperbolic lattices must consider the higher dimensionality of BZ tori $\mathbb{T}^{2\mathfrak{g}}$ involved when applying the supercell method. Defining a momentum-space first Chern number for each two dimensional subtorus of $\mathbb{T}^{2\mathfrak{g}}$ leads to $\binom{2\mathfrak{g}}{2} = \mathfrak{g}(2\mathfrak{g}-1)$ first Chern numbers. However, some of these Chern numbers may be constrained by hyperbolic lattice symmetries. In preparation for our symmetry considerations, we will review the construction of the $\{6,4\}$ and $\{8,3\}$ Haldane models by A. Chen et al. [7] and compute the DOS for a particular configuration of parameters. In section 7.3 we will elaborate the formulation of the 1st and 2nd Chern numbers and their derived symmetry imposed constraint equations. Finally, in section 8.2 we will explicitly extend their hyperbolic lattice symmetry considerations to supercells.

The $\{6,4\}$ and $\{8,3\}$ Haldane models are constructed by considering the lattices as bipartite with sublattices A and B endowed with a staggered on-site potential $\pm m$, indicated in Fig. 19 as white and black circles, respectively. The spin-less electrons are coupled to their nearest-neighbors and next-nearest-neighbors through hopping amplitudes t_1, t_2, shown in Fig. 19 as blue and dashed red lines, respectively. Each lattice is threaded by local magnetic fluxes ϕ such that the net flux in each p-gon, $p = 6, 8$, is rendered zero. As such, the next-nearest-neighbor hopping amplitudes t_2 acquires a phase $e^{i\phi}$ when hopping in clockwise direction, indicated with orange arrows.

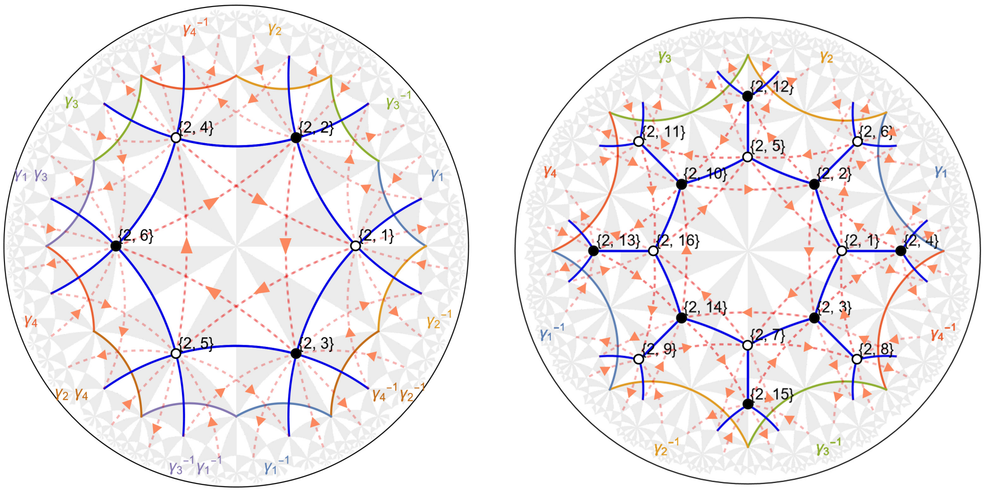

Figure 19: $\{6,4\}$ **and** $\{8,3\}$ **Haldane models on the primitive cell**, left and right respectively. The sublattices A and B are indicated as white and black circles, and nearest and next-nearest-neighbor couplings are indicated as blue and dashed red lines. Next-nearest-neighbor acquires a phase $e^{i\phi}$ when hopping in clockwise direction, indicated with orange arrows.

The corresponding Hamiltonians are given by:

$$\mathcal{H} = \frac{m}{2}\Big(\sum_{i\in A} c_i^\dagger c_i - \sum_{i\in B} c_i^\dagger c_i\Big) + t_1 \sum_{<i,j>} c_i^\dagger c_j + t_2 e^{i\phi} \sum_{\vec{ij}} c_j^\dagger c_i + \text{h.c.}\,, \tag{5.24}$$

where $\vec{ij}$ denotes the sum over next-nearest-neighbor contributions in clockwise directions. In the limit where $t_2 = m = 0$ the model reduces to the nearest-neighbor tight-binding model considered in section 4.2.1. The corresponding density of states are gapless as shown in Fig. 12. Further, an example of the DOS in the topological phase at $t_2 = 0.5$, $m = 0$ and $\phi = \pi/2$ is shown in Fig. 20. Each DOS is computed by exact diagonalization of the corresponding Abelian Bloch Hamiltonian by 10^4 randomly sample momentum points. The DOS is smoothed by a kernel density estimation with a Gaussian kernel of energy bandwidth 0.01.

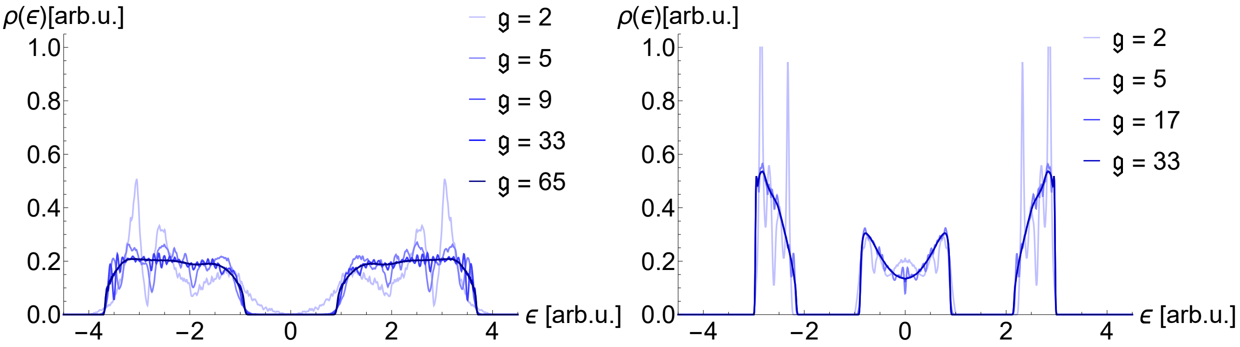

Figure 20: **Density of states for $\{6,4\}$ and $\{8,3\}$ Haldane models**, left and right respectively. The sequence of supercells of Eq. (4.7) are indicated with the corresponding genuses $\mathfrak{g}$ in the legends.

The DOS of the $\{6,4\}$ Haldane model shows that the states in the vicinity of zero energy are strongly suppressed with increasing supercell size. Although our sampling size is small, this suggests that the band-touching observed on the primitive cell in [7] is indeed a finite sized effect as the authors hypothesized.

5.3 Higher order topological insulators

The Chern insulating phase of the Haldane model emerges due to explicit breaking of internal symmetries, as we have seen in the previous sections 5.1 and 5.2. In this section we will look at higher-order topological insulators (HOTI), which emerge due to protected spatial symmetries. According to the bulk-boundary correspondence [46, 47], conventional topological insulators, in d dimensions can host $(d-1)$-dimensional boundary states. Higher-order topological insulators in d dimensions, on the other hand, can host $(d-n)$-dimensional boundary states [55, 56]. W. A. Benalcazar et al. have generalized the notions of multipole moments to the context of crystalline solids [57]. They have constructed a model protected by mirror symmetry which develops a quantized multipole moment and corner modes, known as the Benalcazar-Bernevig-Hughes (BBH) model [57, 58]. In this section, we will study two variants of the BBH model. Once again, we start with a Euclidean lattice, in order to establish an intuitive grasp for HOTIs. We will then proceed with a HOTI on a hyperbolic lattice.

5.3.1 BBH model on the ruby lattice

We consider a variant of the **BBH model** [57] in the **ruby lattice** [59] in order to study a manifestation of a higher-order topological insulator. The ruby lattice is the honeycomb lattice endowed with three orbitals per site. In order to ascribe a variant of the BBH on the ruby lattice, we endow the lattice with inter-site hopping amplitudes t_1 that couple orbitals on the same site, as indicated by the red lines in Fig. 21. Orbitals on adjacent sites are coupled by intra-site hopping amplitude $(-)t_2$, indicated in Fig. 21 by (dashed) green lines. Each hexagon, as well as each rectangle between two hexagons, is threaded by a magnetic π-flux.

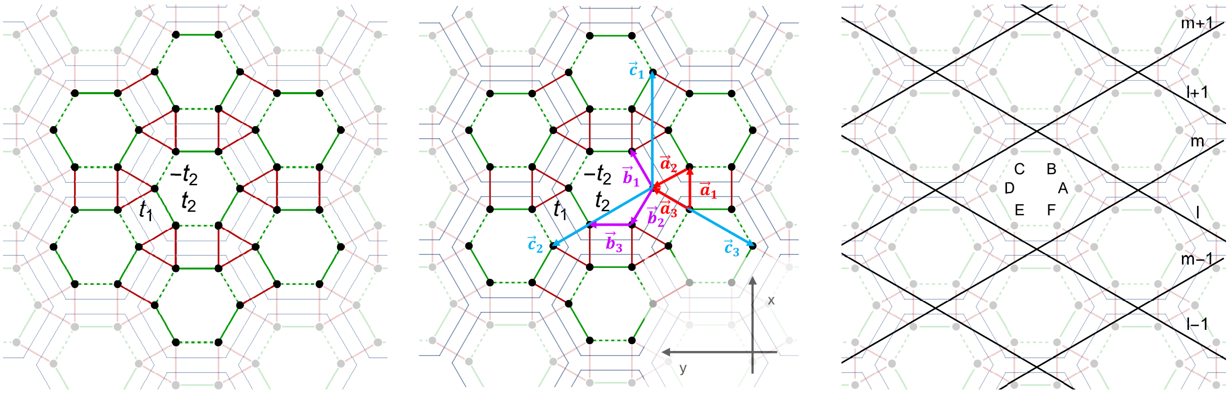

Figure 21: **Ruby lattice**. Left: The ruby lattice with hexagonal primitive cells, indicated in an transparent blue, slightly shrunken down. The inter-site hopping amplitudes t_1 and the intra-site hopping amplitudes $(-)t_2$ are indicated with red lines and green (dashed) lines, respectively. Middle: The nearest-neighbor vector $\mathbf{a}_i, \mathbf{b}_i$ and Bravais lattice vectors $\mathbf{c}_i$. Right: A grid of black lines indicates how the orbitals are labeled for the construction of the tight-binding Hamiltonian. The sublattices labels A, B, C, D, E, F are indicated in the center.

We consider the ruby lattice as a hexpartite lattice with sublattices labeled as A, B, C, D, E, F and lattice constant set to 1. The vectors that connect nearest-neighbor orbitals are given by :

$$\begin{aligned} \mathbf{a}_1 &= s(1,\, 0) & \mathbf{b}_1 &= (1-2s)(\sqrt{3}/2,\, 1/2), \\ \mathbf{a}_2 &= s(1/2,\, \sqrt{3}/2) & \mathbf{b}_2 &= (1-2s)(-\sqrt{3}/2,\, \sqrt{3}/2), \\ \mathbf{a}_3 &= s(1/2,\, \sqrt{3}/2) & \mathbf{b}_3 &= (1-2s)(0,\, 1), \end{aligned} \tag{5.25}$$

where $s \in [0, \frac{1}{2}]$. The parameter s deforms the lattice into its limiting cases, where $s = 0$ corresponds to the honeycomb lattice and $s = \frac{1}{2}$ to a triangular lattice. Unless specified otherwise, we will set s to $s = \frac{1}{3}$ which corresponds to equidistantly spaced orbitals, its use will become clear later. Further, the lattice vectors are given by:

$$\begin{aligned} \mathbf{c}_1 &= \mathbf{a}_1 + \mathbf{b}_1 - \mathbf{b}_2 \\ \mathbf{c}_2 &= \mathbf{a}_2 + \mathbf{b}_2 + \mathbf{b}_3 \\ \mathbf{c}_3 &= -\mathbf{a}_3 - \mathbf{b}_1 - \mathbf{b}_3. \end{aligned} \tag{5.26}$$

the position vectors of the orbitals, labeled by the corresponding sublattices, are:

$$\begin{aligned} &\mathbf{r}^a_{l,m} = -(l\mathbf{c}_2 + m\mathbf{c}_3), \quad \mathbf{r}^b_{l,m} = \mathbf{r}^a_{l,m} - (\mathbf{a}_3 + \mathbf{b}_3), \quad \mathbf{r}^c_{l,m} = \mathbf{r}^a_{l,m} - \mathbf{a}_3, \\ &\mathbf{r}^d_{l,m} = \mathbf{r}^a_{l,m} - (\mathbf{a}_2 + \mathbf{a}_2 + \mathbf{b}_3), \quad \mathbf{r}^e_{l,m} = \mathbf{r}^a_{l,m} - \mathbf{a}_2, \quad \mathbf{r}^f_{l,m} = \mathbf{r}^a_{l,m} - (\mathbf{a}_2 + \mathbf{b}_3). \end{aligned} \tag{5.27}$$

The corresponding Hamiltonian written in this hexpartite configuration, with corresponding annihilation operators $a_{l,m}$, $b_{l,m}$, $c_{l,m}$, $d_{l,m}$, $e_{l,m}$, $f_{l,m}$, is given by:

$$\begin{aligned} \mathcal{H} = \sum_{l,m} \big[& t_1 (a^\dagger_{l,m} e_{l,m} + a^\dagger_{l,m} c_{l,m} + b^\dagger_{l,m} d_{l,m} + b^\dagger_{l,m} f_{l,m} + c^\dagger_{l,m} e_{l,m} + d^\dagger_{l,m} f_{l,m}) \\ & + t_2 (-a^\dagger_{l,m} b_{l,m+1} + a^\dagger_{l+1,m} f_{l,m} + b^\dagger_{l,m} c_{l,m} - d^\dagger_{l,m} c_{l+1,m} - e^\dagger_{l,m} f_{l,m} + e^\dagger_{l,m} d_{l,m+1}) + \text{h.c.} \big], \end{aligned} \tag{5.28}$$

after imposing the Bloch theorem, the Hamiltonian can be written in terms of the Bloch Hamiltonian $H(\mathbf{k})$ such that $\mathcal{H} = \sum_{\mathbf{k}} \mathbf{C}^\dagger_{\mathbf{k}} H(\mathbf{k}) \mathbf{C}_{\mathbf{k}}$ with $\mathbf{C}_{\mathbf{k}} = (a_{\mathbf{k}}, b_{\mathbf{k}}, c_{\mathbf{k}}, d_{\mathbf{k}}, e_{\mathbf{k}}, f_{\mathbf{k}})$, and:

$$H(\mathbf{k}) = \begin{bmatrix} 0 & -t_2 e^{i\mathbf{k}\mathbf{b}_1} & t_1 e^{-i\mathbf{k}\mathbf{a}_3} & 0 & t_1 e^{-i\mathbf{k}\mathbf{a}_2} & t_2 e^{i\mathbf{k}\mathbf{b}_2} \\ -t_2 e^{-i\mathbf{k}\mathbf{b}_1} & 0 & t_2 e^{i\mathbf{k}\mathbf{b}_3} & t_1 e^{-i\mathbf{k}\mathbf{a}_2} & 0 & t_1 e^{i\mathbf{k}\mathbf{a}_1} \\ t_1 e^{i\mathbf{k}\mathbf{a}_3} & t_2 e^{-i\mathbf{k}\mathbf{b}_3} & 0 & -t_2 e^{i\mathbf{k}\mathbf{b}_2} & t_1 e^{i\mathbf{k}\mathbf{a}_1} & 0 \\ 0 & t_1 e^{i\mathbf{k}\mathbf{a}_2} & -t_2 e^{-i\mathbf{k}\mathbf{b}_2} & 0 & t_2 e^{-i\mathbf{k}\mathbf{b}_1} & t_1 e^{i\mathbf{k}\mathbf{a}_3} \\ t_1 e^{i\mathbf{k}\mathbf{a}_2} & 0 & t_1 e^{-i\mathbf{k}\mathbf{a}_1} & t_2 e^{i\mathbf{k}\mathbf{b}_1} & 0 & -t_2 e^{-i\mathbf{k}\mathbf{b}_3} \\ t_2 e^{-i\mathbf{k}\mathbf{b}_2} & t_1 e^{-i\mathbf{k}\mathbf{a}_1} & 0 & t_1 e^{-i\mathbf{k}\mathbf{a}_3} & -t_2 e^{i\mathbf{k}\mathbf{b}_3} & 0 \end{bmatrix}. \tag{5.29}$$

The corresponding band structure is shown in Fig. 22, where three distinct phases can be identified, each with doubly degenerate energy bands. In the topological phase for $t_2/t_1 = 1.5$ the spectrum is gapped,as shown in the left. A gap closing occurs between the middle pair and the upper pair of bands at the Γ-point for $t_2/t_1 = \sqrt{3}$, revealing a semi-metallic phase, depicted in the center. As t_2 is increased beyond $\sqrt{3}t_1$ a trivial phase is reached and the gap reopens, indicated in the right figure for $t_2/t_1 = 2$.

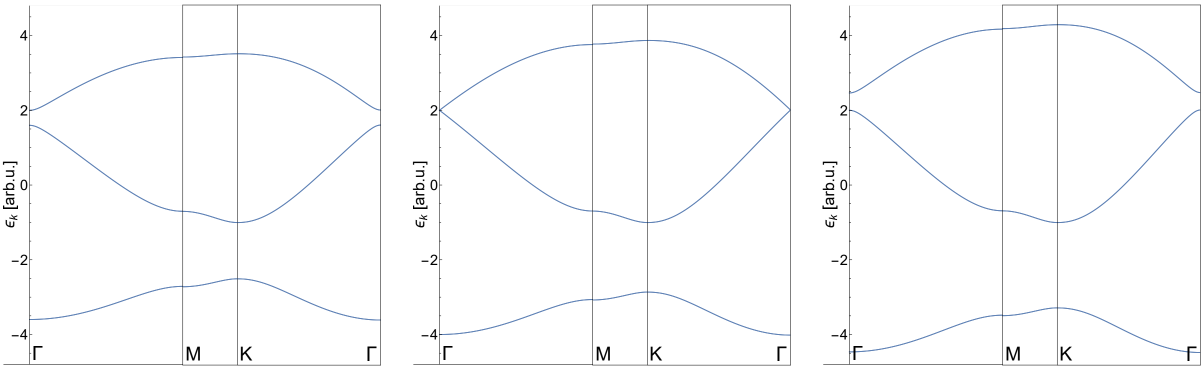

Figure 22: **Bulk band structures of BBH model on the Ruby lattice**. Left: The spectrum of the bulk develops a gap between the degenerate upper pair of bands for $t_2 = 1.5t_1$. This is a topological phase exhibiting corner modes. Center: As we sweep across increasing t_2 the upper pair of bands approach each other and the gap eventually closes at $t_2 = \sqrt{3}t_1$. Right: A gap reappears as we further increase t_2 such as for $t_2 = 2t_1$. The length of the x-axes corresponds to the Euclidean norm between high symmetry points.

A characteristic feature of higher-order topological phases is the quantization of the bulk polarization, which can be used as a **topological index**, [58]. In the modern theory of polarization, the accumulation of phases during the parallel transport of states is the defining feature for description of the polarization in crystalline materials, [50]. As such, let us return to the first Chern number in preparation for the description of the polarization in the topological phase.

The system is invariant under time reversal, which renders the first Chern number zero. The degenerate energy bands require us to adapt the description of the first Chern number in Eq. (5.18) from an isolated band scenario to the general case of degenerate energy bands. In order to verify the vanishing of the first Chern number. As such, let us review aspects in Refs. [50, 53, 54].

The Berry connection needs to incorporate the band degeneracy. For cell periodic Bloch eigenstates $|a(\mathbf{k})\rangle$, $|b(\mathbf{k})\rangle$ in a multiplet of n filled bands:

$$\Psi(\mathbf{k}) = \big(|1(\mathbf{k})\rangle, |2(\mathbf{k})\rangle, ..., |n(\mathbf{k})\rangle\big), \tag{5.30}$$

the generalized Berry connection, called the **Berry-Wilczek-Zee** (BWZ) connection is defined as [7, 60]:

$$(A_i^\Psi(\mathbf{k}))^{ab} = \langle a(\mathbf{k})|\partial_i|b(\mathbf{k})\rangle, \tag{5.31}$$

where A_i^Ψ forms a $n \times n$ matrix. The correspondingly adjusted non-Abelian Berry curvature, known as the **BWZ curvature** is given by:

$$F_{ij}^\Psi(\mathbf{k}) = \partial_i A_j^\Psi(\mathbf{k}) - \partial_j A_i^\Psi(\mathbf{k}) + i[A_i^\Psi(\mathbf{k}), A_j^\Psi(\mathbf{k})] \tag{5.32}$$

where $[\cdot,\cdot]$ is the **Lie bracket**. The BWZ curvature connects $\mathrm{U}(N)$ transformations at neighboring points in the parameter space. This is analogous to notions found in QFTs, where Yang-Mills theories enforce a local $\mathrm{SU}(N)$ symmetry invariance giving rise gauge fields that connect $\mathrm{SU}(N)$ transformations at neighboring points in space-time [52]. Further, the total first Chern number up to n filled bands is thus:

$$C^{\Psi}_{(1)} = \frac{1}{2\pi i}\int_{\mathbb{T}^2} d^2k\, \mathrm{Tr}[F^{\Psi}_{xy}(\mathbf{k})], \tag{5.33}$$

which reduces to Eq. (5.19) for non-degenerate bands. We obtain the first Chern number by numerical calculations following Refs. [53, 54]. Analogous to the discretization for the Abelian case in section 5.1, we construct a grid of equidistantly spaced k_x, k_y values on $\mathbb{T}^2$ with distance l, such that discretized integral is approximated by:

$$C^{\Psi}_{(1)} = \frac{1}{2\pi i}\lim_{l\to 0}\sum_{\mathbf{k}} l^2\mathrm{Tr}[F^{\Psi}_{xy}(\mathbf{k})]. \tag{5.34}$$

The total flux of BWZ-curvature $F^{\Psi}_{xy}(\mathbf{k})$ through a square in the k_x, k_y grid can be accounted for by constructing Wilson loops:

$$W^{\Psi}_{xy,\mathbf{k}} = U^{\Psi}_{x}(\mathbf{k})U^{\Psi}_{y}(\mathbf{k}+l\hat{k}_x)U^{\Psi}_{x}(\mathbf{k}+l\hat{k}_y)^{-1}U^{\Psi}_{y}(\mathbf{k})^{-1} \tag{5.35}$$

such that $F^{\Psi}_{xy}(\mathbf{k})$ is given by:

$$l^2F^{\Psi}_{xy}(\mathbf{k}) = \ln(W^{\Psi}_{xy,\mathbf{k}}). \tag{5.36}$$

with $\mathrm{U}(N)$ link tensor $U^{\Psi}_{i}(\mathbf{k})$ given by:

$$U^{\Psi}_{i}(\mathbf{k}) = \Psi^{\dagger}(\mathbf{k})\Psi(\mathbf{k}+l\hat{\imath}). \tag{5.37}$$

The tensor $U^{\Psi}_{i}(\mathbf{k})$ describes the phase acquired during parallel transport. We can rewrite $U^{\Psi}_{i}(\mathbf{k})$ with the well known identity $\mathrm{Tr}[\ln(M)] = \ln(\det(M))$, where M is an non-singular matrix, such that:

$$U_i(\mathbf{k}) \equiv \det\big(\Psi^{\dagger}(\mathbf{k})\Psi(\mathbf{k}+l\hat{\imath})\big). \tag{5.38}$$

It is convenient to perform a change of basis as defined in Eq. (4.6), in order to compute the first Chern number in the topological phase at 2/3 filling. As expected for a time-reversal invariant system, we find that the first Chern number vanishes.

The Wilson loop formulation for the calculation of the first Chern number can also be used to formulate a description of the bulk polarization. Consider a discretized Wilson loop that goes across the entire Brillouin zone in increments $\delta_{\mathbf{k}_x} = (2\pi/N_x, 0)$:

$$W^{\Psi}_{x,\mathbf{k}} = U^{\Psi^\dagger}_x(\mathbf{k} + (N_x - 1)\delta_{\mathbf{k}_x}) \cdots U^{\Psi^\dagger}_x(\mathbf{k} + \delta_{\mathbf{k}_x}) U^{\Psi^\dagger}_x(\mathbf{k}) \,, \tag{5.39}$$

where $U^{\Psi^\dagger}_x(\mathbf{k}) = \Psi^\dagger(\mathbf{k} + \delta_{\mathbf{k}_x})\Psi(\mathbf{k})$. It can be shown [57], that the relative positions of electrons in the unit cells are given by the phases of the Wilson loop eigenvalues $\nu^j_x(k_y)$, called **Wannier centers** [50]. As such, the electronic contribution to the polarization is the sum over the Wannier centers for the multiplet of n filled bands $\Psi(\mathbf{k})$ [57]:

$$p^{\Psi}_x(k_y) = \sum_{j=1}^{n} \nu^j_x(k_y) = -\frac{i}{2\pi}\ln(\det(W^{\Psi}_{x,\mathbf{k}})). \tag{5.40}$$

In the thermodynamic limit $N_x \to \infty$, the polarization as a function of k_y becomes:

$$p^{\Psi}_x(k_y) = \frac{i}{2\pi}\int_0^{2\pi} dk_x \, \mathrm{Tr}[A^{\Psi}_x(\mathbf{k})], \tag{5.41}$$

which is proportional to the Berry phase along a non-contractible path $0 \to 2\pi$ in the k_x direction. The total polarization along x direction is the sum of $p^{\Psi}_x(k_y)$ over discretized k_y values. In the thermodynamic limit where $\frac{1}{N_y}\sum_{k_y} \to \frac{1}{2\pi}\int dk_y$, it is given by:

$$p^{\Psi}_x = \frac{i}{(2\pi)^2}\int_{\mathbb{T}^2} d^2k \, \mathrm{Tr}[A^{\Psi}_x(\mathbf{k})], \tag{5.42}$$

We numerically calculate the polarization in the non-orthogonal basis given in Eq. (4.6) in a equidistantly spaced k_1, k_2 grid at 2/3 filling. The calculated polarization vanishes $\mathbf{P} = (0, 0)$. Intriguingly, in higher-order topological phases a **filling anomaly** can arise when corners are introduced through **finite flakes** in C_n symmetric lattices with vanishing bulk polarization, [58]. Consequently, the finite system may host fractional corner charges, [56].

The ruby lattice is invariant under C_6 rotation symmetry. However, the Bloch Hamiltonian in Eq. (5.29) is not invariant C_6 symmetry, due to threaded π-fluxes, also referred to as **gauge fluxes**, [61]. As such, consider the $\hat{r}_6$ rotation operator which transforms the Bloch Hamiltonian at momentum $\mathbf{k}$ to those at $R_6\mathbf{k}$, where R_6 is the 6-fold rotation matrix. The counter clockwise rotation operator $\hat{r}_6$ is given by:

$$\hat{r}_6 = \begin{bmatrix} 0 & 0 & 0 & 0 & 0 & 1 \\ 1 & 0 & 0 & 0 & 0 & 0 \\ 0 & 1 & 0 & 0 & 0 & 0 \\ 0 & 0 & 1 & 0 & 0 & 0 \\ 0 & 0 & 0 & 1 & 0 & 0 \\ 0 & 0 & 0 & 0 & 1 & 0 \end{bmatrix} . \tag{5.43}$$

We see that $\hat{r}_6 H(\mathbf{k}) \hat{r}_6^\dagger \neq H(R_6\mathbf{k})$. The rotation operation has changed the gauge flux configuration such that the intra-site hopping amplitudes flip signs $\pm t_2 \to \mp t_2$. We can restore the configuration by an appropriate gauge transformation. As such, the symmetry operation which leaves the lattice and the gauge configuration of the system invariant is a combination of a gauge transformation and a 6-fold rotation, given by:

$$\tilde{r}_6 = \begin{bmatrix} 0 & 0 & 0 & 0 & 0 & 1 \\ -1 & 0 & 0 & 0 & 0 & 0 \\ 0 & 1 & 0 & 0 & 0 & 0 \\ 0 & 0 & -1 & 0 & 0 & 0 \\ 0 & 0 & 0 & 1 & 0 & 0 \\ 0 & 0 & 0 & 0 & -1 & 0 \end{bmatrix}, \tag{5.44}$$

where $\tilde{r}_6 H(\mathbf{k}) \tilde{r}_6^\dagger = H(R_6\mathbf{k})$. The rotation operator $\tilde{r}_6$ describes a **projective representation** of the rotation symmetry [61]. In order to see the interplay between C_6 symmetry and charge neutrality we terminate the system to finitely sized flakes, such as the hexagonal finite flakes shown in Fig. 23.

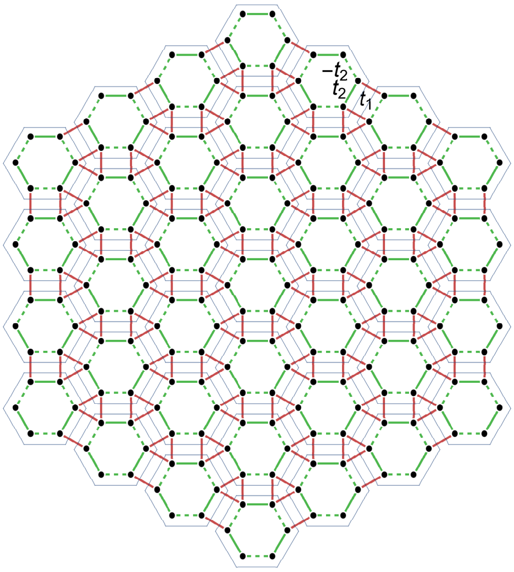

Figure 23: **Hexagonal ruby lattice flake**. A finite sized hexagonal ruby lattice flake consisting of 37 hexagonal primitive cells.

Each flake consists of $N = 1 + 3n(n+1)$ primitive cells, where $n \in \mathbb{N}_{\geq 0}$. The corresponding Hamiltonian for $n \in \mathbb{N}_{\geq 2}$ is given by:

$$\begin{aligned} H = {} & t_1 \sum_{i=2-n}^{n-1} \sum_{j=2-n}^{i} \left(a_{i,j}^\dagger c_{i,j} + a_{i,j}^\dagger e_{i,j} + b_{j,i}^\dagger f_{j,i} + c_{i,j}^\dagger e_{i,j} + d_{j,i}^\dagger b_{j,i} + d_{j,i}^\dagger f_{j,i}\right) \\ & + t_2 \sum_{i=2-n}^{n} \sum_{j=1-n}^{n-1} \left(-a_{i,j}^\dagger b_{i,j+1} + a_{i,j}^\dagger f_{i-1,j} - d_{j,i}^\dagger c_{j+1,i} + d_{j,i}^\dagger e_{j,i+1} + b_{i,j+1}^\dagger c_{i,j+1} - e_{i-1,j}^\dagger f_{i-1,j}\right) \\ & + t_1 \sum_{j=2-n}^{n-2} \left(a_{n,j+1}^\dagger c_{n,j+1} + a_{j,1-n}^\dagger e_{j,1-n} + b_{j+1,n}^\dagger d_{j+1,n} + b_{j-1+n,j-1}^\dagger f_{j-1+n,j-1} \right. \\ & \left. + c_{j,j-1+n}^\dagger e_{j,j-1+n} + d_{1-n,j}^\dagger e_{1-n,j}\right) + \text{h.c.}\,. \end{aligned} \tag{5.45}$$

We compute the spectrum of a flake with $N = 721$ hexagonal unit cells by exact diagonalization. Its spectra in the topological phase are shown in Fig. 24. For $t_2 = 0.1t_1$, shown in the left figure, the system exhibits in-gap states at energies ± 0.1 that are localized at the six corners of the flake. In-gap states in the interval $(-0.1, 0.1)$ and $(0.9, 1.1)$ are localized at the edges of the flake. As t_2 is increased to $t_2 = 0.3t_1$, the in-gap state start to approach the bulk spectrum, as depicted in the center. As t_2 is increased further, localized states start to hybridize with the bulk states as shown in the spectrum on the right at $t_2 = 0.7t_1$.

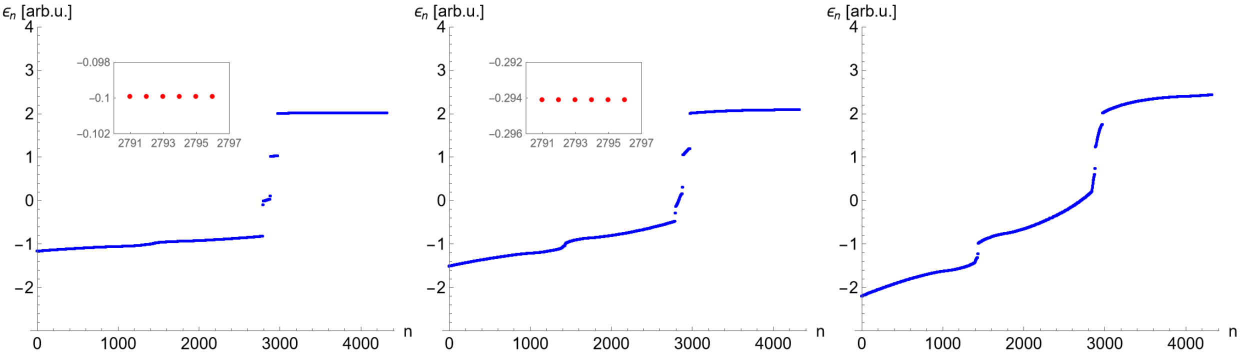

Figure 24: **Spectra of hexagonal ruby lattice flake in the topological phase**, for a flake consisting of 721 hexagonal primitive cells and inter-cell hopping amplitude $t_1 = 1$. Left: For $t_2 = 0.1t_1$ the system exhibits in-gap states. In-gap states at energy ± 0.1 are localized at the corners of the hexagonal flake. The inset shows the energy eigenvalues of a selection of these states at energies -0.1. Center: As t_2 is increased to $t_2 = 0.3t_1$, the in-gap states start to approach the bulk spectrum, with in-gap states at energies ~ -0.294 shown in the inset. Right: At $t_2 = 0.7t_1$ some in-gap states start to hybridize with the bulk.

The C_6 projective symmetry of the ruby lattice enforces the existence of two sets of 6-fold degenerate states that are localized at the corners of the flake. The sets of lower energy for $t_2/t_1 = 0.1, 0.3$ are shown insets of Fig. 24, left and center, respectively. The degenerate set of states lead to an inability to place the Fermi energy at a filling factor of exactly $2/3$, since the spectrum in the topological phase exhibits gaps at filling $4N - 4$ or $4N + 2$. As such, the system is in a predicament when accounting for the ionic contribution to the total charge density, either obey charge neutrality and break C_6 symmetry or preserve C_6 symmetry and lose charge neutrality. Since the former is not possible without introducing a C_6 symmetry breaking term, a **charge imbalance** is invoked, [58]. It can be shown [58] that the Wannier centers at the unit cell boundaries are cut in the topological phase at $4N - 4$ or $4N + 2$ filling. The invariance under C_6 symmetry then requires an equal distribution of the total charge in each sector subtended by an angle $\pi/3$, which explains the appearance of **fractional corner charges**.

We can show this charge fractionalization in the ruby lattice by explicitly computing the total charge density. Thus, in order to compute the total charge density, we place the Fermi energy at 0.9 at a filling $4N+2$. Further, we place ions in Wyckoff positions located in the centers of hexagonal primitive cells. Each ion contributes 4 electronic charges. The electronic charge density is computed afterwards and redistributed to the Wyckoff positions of the ions by adjusting the parameter s, introduced in Eq. (5.25). As such, s is tuned to $s = 1/2$ such that the six orbital positions within each hexagonal primitive cell coincide with the Wyckoff position in the center. The ionic contribution to the charge density is subtracted from the redistributed electronic charge density. The resulting total charge density at $4N+2$ filling in the topological phase are depicted in Fig. 25.

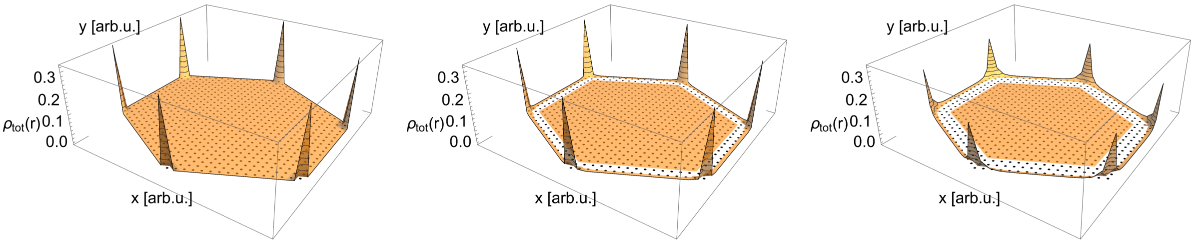

Figure 25: **Total charge density at $4N+2$ filling in the topological phase**, for ruby lattice flake consisting of $N = 721$ hexagonal primitive cells with inter-cell hopping amplitude set to $t_1 = 1$. The Wyckoff position in the centers of the primitive cells are depicted as black dots. Left: The total charge density reveals fractional corner charges $1/3$ for $t_2 = 0.1t_1$. Center: Corner modes start to hybridize with the bulk such that the corner charges are redistributed. In the vicinity of the edges the charge density is negative with a minimal value around ~ -0.0002. This is indicated as a white hexagonal section within the orange surface. Right: At $t_2 = 0.7t_1$, the hybridization of corner modes depletes the corner charges and the negative sections indicated in white are further extended, with a minimal value around ~ -0.0033.

In the left figure, the total charge density reveals fractional corner charges $1/3$ for $t_2 = 0.1t_1$. As t_2 is increased, the corner modes start to hybridize with the bulk such that the corner charges are depleted, shown in the center. In particular, in vicinity of the edges the charge density becomes slightly negative, indicated as a white hexagonal section within the orange surface. The right figure shows the total charge density at $t_2 = 0.7t_1$. We see that the hybridization of corner modes depletes the corner charges with a redistribution in the vicinity of the corners. Notably, in vicinity of the edges the negative charge density region, indicated as a white hexagonal section within the orange surface, extend further into the bulk. In all three cases the integrated total charge density over a sector subtended by an angle $\pi/3$, that includes one corner, is $\sim 1/3$ rounded to the 12 decimal place.

Further, the total charge density in the topologically trivial phase at $t_1 = 1$ and $t_2 = 2t_1$ exhibits no corner charges and the integrated total charge density over a sector subtended by an angle $\pi/3$ is vanishing.

5.3.2 BBH model on $\{6,4\}$-lattice

In this section we study the BBH model on the $\{6,4\}$-lattice introduced in [3]. In order to probe the bulk boundary correspondence we introduce finite flakes with **disclination defects**, which enables us to demonstrate the existence of fractional charges at the disclination core.

Analogous to the original BBH model [57] we endow the hyperbolic $\{6,4\}$-lattice with four orbitals per site, such that each orbital couples to four nearest neighbor orbitals as shown in Fig. 26. The inter-site hopping amplitudes $(-)h_0$ couples a cycle of four orbitals, labeled by 1 to 4, indicated with (dashed) red lines. Each plaquette formed by such a cycle, is threaded by a magnetic π-flux. The intra-site hopping amplitudes $(-)h_1$ are indicated with (dashed) green lines. Plaquettes with alternating red and green lines, located between hyperbolic hexagons, are threaded by a magnetic π-fluxes as well.

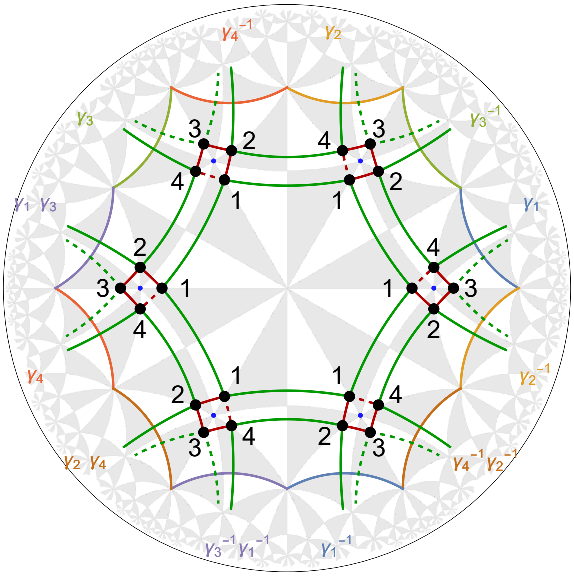

Figure 26: **BBH model on $\{6,4\}$-lattice**, shown in the primitive cell. Each site at Wyckoff position in $V_{\mathrm{y}}^{\mathrm{cell}}$, as given in Eq. (3.42), is endowed with a cycle of four orbitals, indicated as black dots. The inter-site hopping amplitudes $(-)h_0$ couple a cycle of four orbitals, labeled by 1 to 4, indicated with (dashed) red lines. The intra-site hopping amplitudes $(-)h_1$ are indicated with (dashed) green lines. The primitive cell boundary together with the corresponding translation operators are indicated with a colored line segments. The corresponding generators are given in Eq. (3.26).

The corresponding tight-binding Hamiltonian is:

$$\mathcal{H} = \frac{h_0}{2}\sum_i \vec{c}_i^{\dagger}\begin{bmatrix} 0 & 1 & 0 & -1 \\ 1 & 0 & 1 & 0 \\ 0 & 1 & 0 & 1 \\ -1 & 0 & 1 & 0 \end{bmatrix}\vec{c}_i + h_1 \sum_{<i,j>_c} \vec{c}_i^{\dagger}\begin{bmatrix} 1 & 0 & 0 & 0 \\ 0 & 0 & 0 & 1 \\ 0 & 0 & 0 & 0 \\ 0 & 0 & 0 & 0 \end{bmatrix}\vec{c}_j^{\dagger} + h_1 \sum_{<i,j>_b} \vec{c}_i^{\dagger}\begin{bmatrix} 0 & 0 & 0 & 0 \\ 0 & 0 & 0 & 1 \\ 0 & 0 & -1 & 0 \\ 0 & 0 & 0 & 0 \end{bmatrix}\vec{c}_j^{\dagger} + \text{h.c.}. \tag{5.46}$$

where $< i,j >_b$ indicates the NN-interactions that cross the boundary of the primitive cell, and $< i,j >_c$ denotes the NN-interactions within the primitive cell. Analogous to the ruby lattice in the Euclidean plane discussed in Section 5.3.1, the system is in the topological trivial phase for $|h_0| \gg |h_1|$, and in the topological nontrivial phase for $|h_0| \ll |h_1|$.

The corresponding density of states for a sequence of supercells identified with the corresponding quotient groups in Eq. (4.7), is shown in Fig. 27. Each DOS is computed by exact diagonalization with $5 \cdot 10^3$ randomly sampled points in the BZ tori $\mathbb{T}^{2\mathfrak{g}}$. In addition, the data is smoothened by the application of a kernel density estimation with a Gaussian kernel of energy bandwidth 0.015. A computation with significantly more data points can be found in Ref. [3].

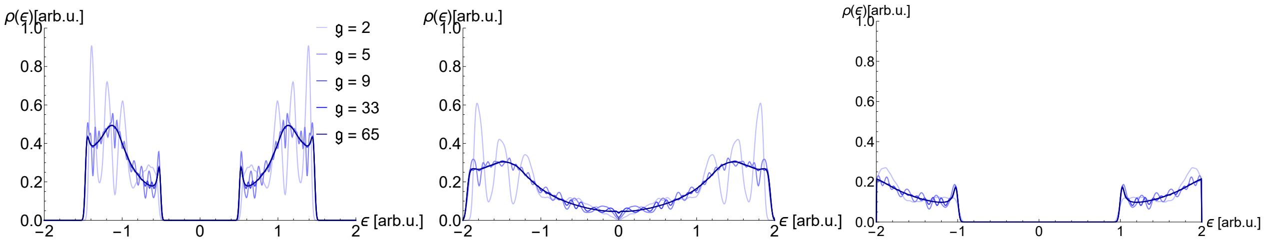

Figure 27: **Density of states of BBH model on the $\{6,4\}$ lattice**, with intra-site hopping amplitude set to $|h_1| = 1$. Left: For $|h_0| = 0.38$ the DOS is gapped and the system is in a topologically insulator phase. Center: At $|h_0| = 0.77$ the gap closes at $\epsilon = 0$. Right: For $h_0 = 1.5$ the system is in a trivial phase. Figure reproduced from Ref. [3].

For $|h_0/h_1| = 0.38$, shown in the left Figure 27, the system is in a topological insulator phase and the density of states exhibits a gap. The gap starts to close as we approach the critical value for increasing $|h_0|$. Notably, the density of states for small supercells appears to be semi-metallic, with a vanishing density of states at $\epsilon = 0$, for $|h_0/h_1| \approx 0.77$, depicted in the center. However, this appears to be a finite-size effect that disappears for larger supercells with an appearance of a metallic phase [3]. The gap reopens as $|h_0|$ is increased further, such that the system is in a trivial phase, shown on the right for $|h_0/h_1| = 1.5$.

Similarly to the BBH model on the ruby lattice of section 5.3.1, we consider the construction of finite flakes in order to probe the bulk-boundary correspondence for the $\{6,4\}$ BBH model. To this end, we introduce a disclination defect in finite flakes, which has been shown to give rise to fractional charges at the disclination core, [58, 62]. We can motivate this idea by reconsidering the BBH model on the ruby lattice of Section 5.3.1. In the topological phase of the BBH model on the ruby lattice, the fractional corner charges in the hexagonal flake add up to an integer. A disclination can be introduced by cutting away a sector subtended by an angle $\pi/3$ that includes a corner, the remaining flake is then glued together at the cut edges. This configuration contains five corners and thus, the sum of charges over the remaining corners is fractional. This results in a fractional charge appearing at the disclination core such that the total charge is again an integer, [62].

We proceed by constructing finite flakes of the $\{6,4\}$-lattice. Our construction of flakes, with and without disclinations, consists of determining a sequence of supercells with the methodology in chapter 3. The cluster of sites at Wyckoff positions $V_{\mathrm{y}}^{\mathrm{cell}}$ within the supercells make up the flakes without disclinations. These flakes are shown in Fig. 28:

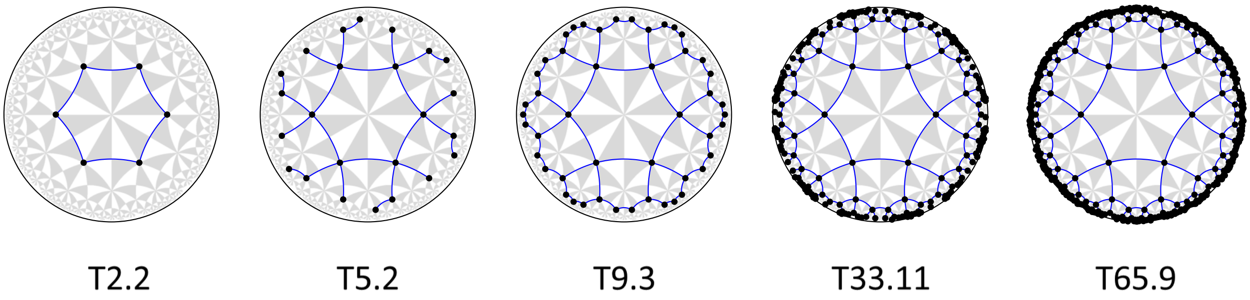

Figure 28: **Finite flakes of the $\{6,4\}$-lattice**. The finite flakes are constructed from sites within single supercells identified by corresponding quotient groups T2.2, T5.4, T9.3, T33.11, T65.9.

The hyperbolic variant of the BBH model is then imposed onto each flake. The corresponding spectra for $|h_0/h_1| = 0.38$ are shown in Fig. 29. Notably, the gaplessness implies the existence of boundary modes.

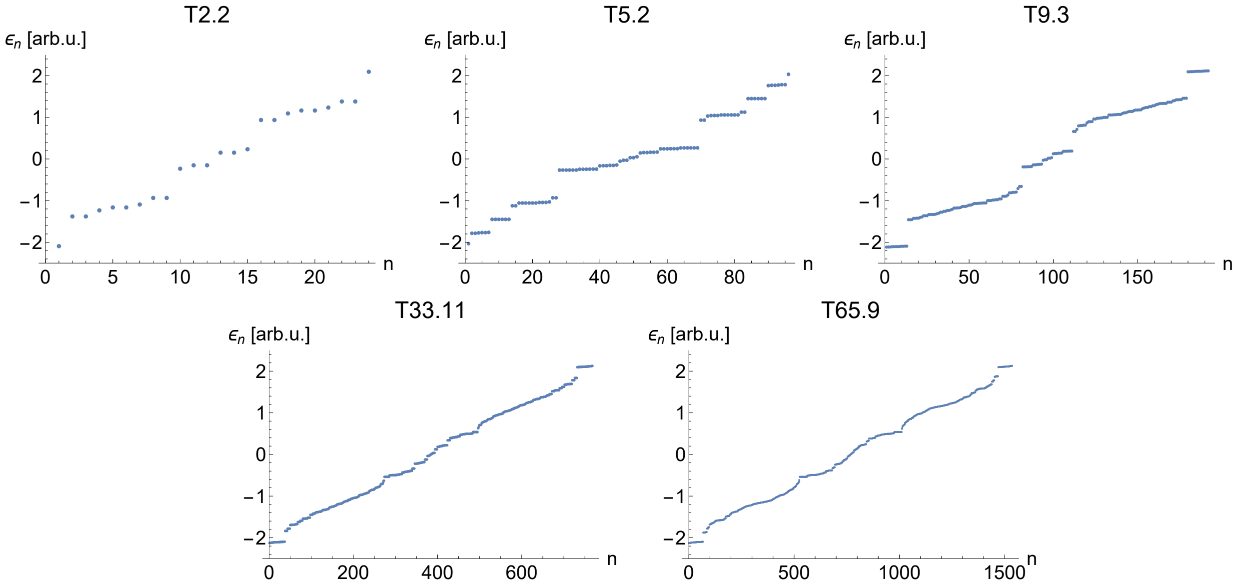

Figure 29: **Energy spectra of finite flakes of the $\{6,4\}$-lattice in the BBH model**. Each spectrum corresponds to a finite flake constructed from sites within a single supercell, labeled according to the corresponding quotient group they have been constructed with.

The introduction of disclinations consists of identifying a subset of vertices in flakes that lie within a wedge of Frank angle $\theta = -\pi/3$. The corresponding vertices are cut out of the flakes and dangling bonds of vertices located at the same radial distance away from the center are glued together by new edges. A set of flakes with introduced disclinations is shown in Fig. 30.

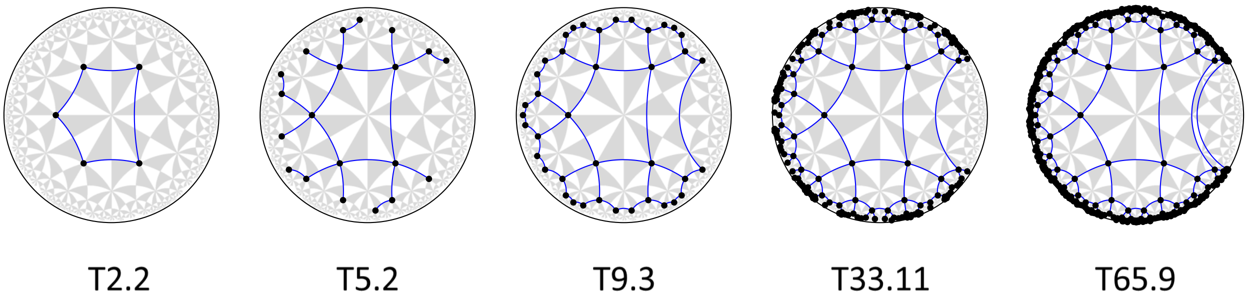

Figure 30: **Disclination on $\{6,4\}$-lattice flakes with Frank angle $-\pi/3$.** The finite flakes are constructed from sites within single supercells identified by corresponding quotient groups T2.2, T5.4, T9.3, T33.11, T65.9, with a subsequent introduction of a disclination with Frank angle $-\pi/3$.

The corresponding spectra for $h_0/h_1 = 0.38$ are depicted in Fig. 31. The comparison with the flakes without disclinations in Fig. 29 reveals a **filling anomaly** by the appearance of in-gap states. Each spectrum shows a particular selection of these in-gap states in corresponding insets indicated with red dots.

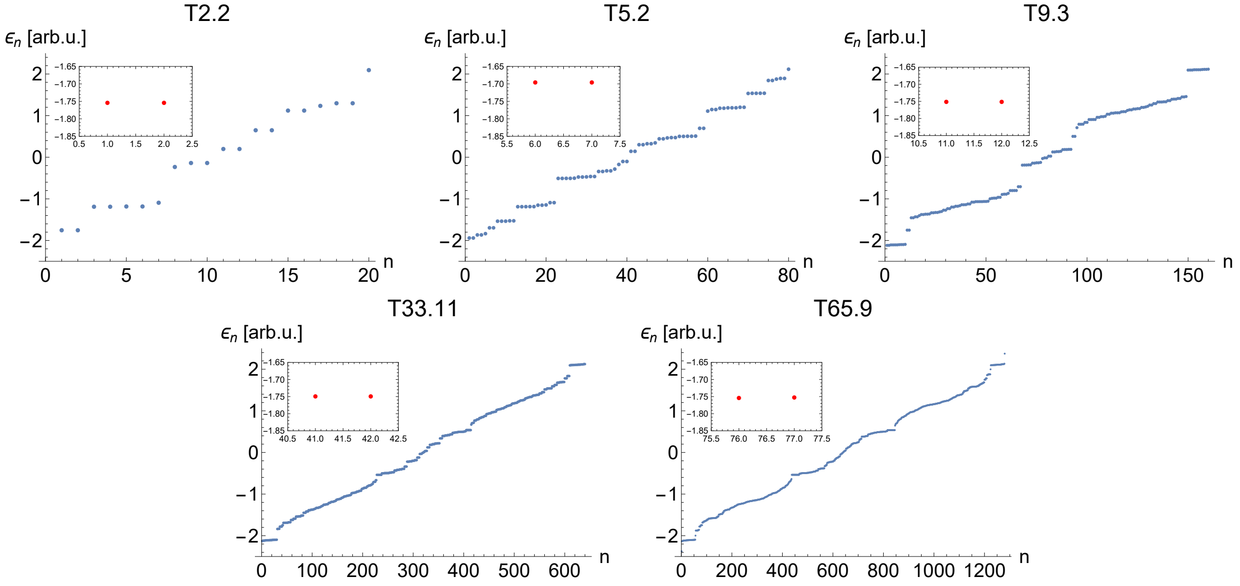

Figure 31: **Energy spectra of finite flakes with disclinations of the $\{6,4\}$-lattice in the BBH model**. Each spectrum corresponds a finite flake with a disclination constructed from sites within a single supercell, labeled according with the corresponding quotient group they have been constructed with. All spectra depict in-gap states, a selection is shown in the corresponding insets.

The spatial distribution of the local density of states (LDOS) can be used as a measure of the spatial localization of states, [63]. Given a set of eigenstates $\psi_j(\mathbf{x})$ with energy E_j, the LDOS is given by $\rho_p(\mathbf{x},\epsilon) = \sum_j |\psi_j(\mathbf{x})|^2\delta(\epsilon - E_j)$. The LDOS of the in-gap states shown in the insets of Fig. 31, are depicted in Fig. 32.

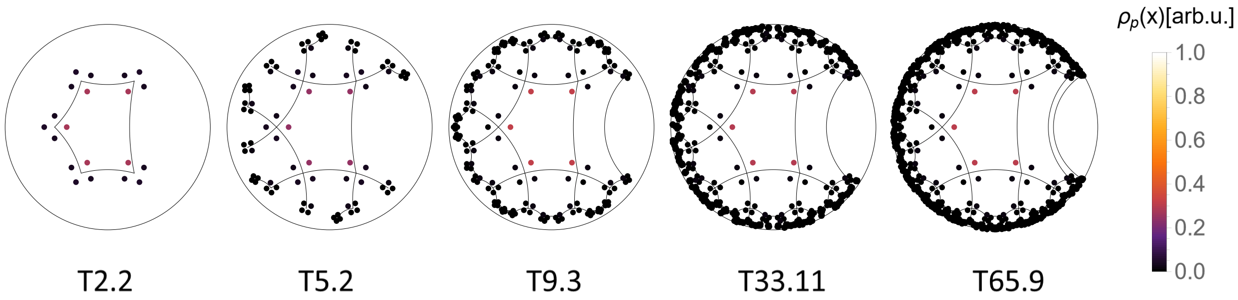

Figure 32: **Local density of states for in-gap states shown in the insets of Fig. 31**.

Analogous to our analysis of the higher-order topological phase in the ruby lattice in Section 5.3.1, we proceed by computing the total charge density at half filling. The Fermi energy is placed at zero energy and the ionic charges are placed at Wyckoff positions $V_{\mathrm{y}}^{\mathrm{cell}}$, which are depicted as black dots in Fig. 30. Each ion contributes 2 electronic charges such that charge neutrality is obeyed. The electronic charge density is computed and redistributed to the Wyckoff positions of ions by identifying the cycle of four orbitals that surround each ion. The ionic contribution of the charge density is subtracted from the redistributed electronic charge density. The corresponding total charge density $\rho_{\mathrm{tot}}(\mathbf{x})$ for the T33.11 flake is shown in Fig. 33.

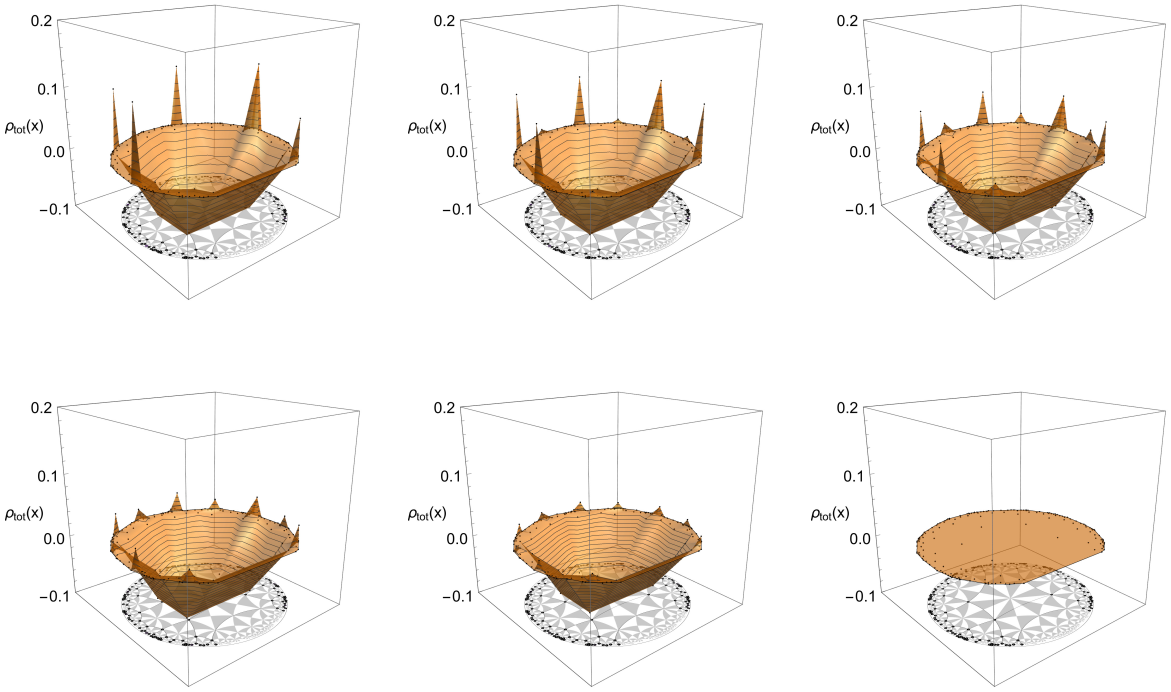

Figure 33: **Total charge density at 1/2 filling of** T33.11 **flake with a disclination for $\{6,4\}$ BBH model**, with $|h_1| = 1$ and flake placed at -0.1 for orientation. The Wyckoff positions $V_{\mathrm{y}}^{\mathrm{cell}}$ are shown as black dots in the flake. The inter-site hopping amplitude is set to: Top row: $h_0 = 0.01, 0.1, 0.2$, respectively; Bottom row: $h_0 = 0.3, 0.4, 1.5$, respectively. The total charge density in all figures is depicted as a 3 dimensional brown surface spanned by interpolating between data points that are indicated as small black dots in the surface.

Consider the figures in the top row and the first two figures in the bottom row of Fig. 33. They depict the total charge density in the topological phase for different values of the inter-site hopping amplitude h_0. The integrated total charge density over the entire flake is always zero, rounded to 12 decimal places. As such the negative total charge at the disclination core compensates the positive total charge at corners, such that charge neutrality is obeyed. The last figure in the right corner of Fig. 33 depicts the trivial phase at $h_0 = 1.5$, where the total charge distribution is uniform.

Further, as the inter-site hopping amplitude h_0 is increased, additional corner modes start to emerge at the flake boundaries. We have not further investigated their origin. However, we have observed that the total charge density in the T9.3 flake with a disclination does not exhibit an appearance of additional corner modes as h_0 is increased. Informally, the boundary of the T33.11 flake is in a sense more irregular then the boundary of the T9.3 flake. This might suggest that the geometry of the flake boundaries may play a role in the appearance of these states, similar to the hybrid higher-order skin-topological effect [9].

The integrated total charge densities over a region in the vicinity of the disclination core Q_d for different inter-site hopping amplitudes are shown in Table 1. The region of integration includes five points at Wyckoff position $V_{\mathrm{y}}^{\mathrm{cell}}$ that are closest to the origin. In the vicinity of the fully dimerized limit for $h_0 = 0.01$ the charge at disclination core approaches a quantized value $Q_d \sim -1/2$. The deviation from $-1/2$ for increasing h_0 is to be expected. As for corner charges, the net electronic charge at the disclination core is expected to be exponentially localized $Q(\mathbf{x}) \propto e^{-\alpha \mathbf{x}}$ [64]. In the trivial phase for $h_0 = 1.5$ the total charge distribution is uniform such that the disclination core binds approximately zero net charge.

h_0	0.01	0.1	0.2	0.3	0.4	1.5
Q_d	-0.49997	-0.49661	-0.48585	-0.46461	-0.42042	-0.00177

Table 1: **Integrated charge density at the disclination core Q_d for T33.11 flake**, rounded to the 5th decimal place, for different values of the inter-site hopping amplitude h_0.

In combination, Fig. 33 and Table 1 show that the introduction of a disclination indeed manifest a fractional charge at the disclination core in the topological phase of the $\{6,4\}$ BBH model. In conclusion, we provided the first explicit evidence of higher-order topological phenomenology associated with the $\{6,4\}$ BBH model introduced in Ref. [3]

6 Non-Hermitian systems

The topological classification of Hermitian Hamiltonians describing isolated systems has been studied extensively, see for example Ref. [24]. Non-Hermiticity is a prevalent property in nature, it appears for example through the introduction of gains and/or losses which can break the Hermiticity of the system and enables effective approximations to study non-equilibrium physics of open quantum systems. The addition of non-Hermitian terms into the Hamiltonian gives rise to features unprecedented in their Hermitian counterparts, such as **point gaps** and **line gaps** in the complex energy spectrum. In this chapter we will consider the introduction of such **Hermiticity breaking** terms on hyperbolic lattices in order to study the topological characterization of a selection of $\{p, q\}$-lattices via winding numbers. To do so, let us first review some key concepts following Ref. [26].

The spectrum of a general non-Hermitian Hamiltonian is complex and thus necessitates a reconsideration of the usual Hermitian notion of topological equivalence. Recall that, if and only if two Hermitian Hamiltonians can be continuously deformed into each other without closing a gap and maintaining the symmetries, they are defined to be topologically equivalent, [40]. This definition is unique for Hermitian systems since the eigenvalues are real, as shown on the left of Fig. 34. However, in general non-Hermitian systems the spectrum resides in the complex plane and eigenvalues can envelope a point gap E_p, or a line in the complex plane can be drawn in an energy range where no states exist, as depicted in the center and on the right of Fig. 34, respectively.

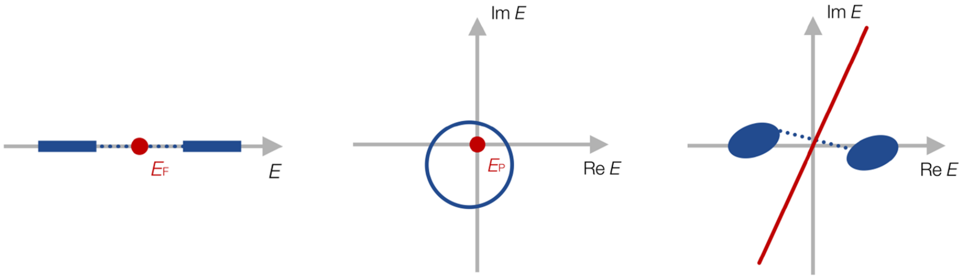

Figure 34: **Energy gaps in Hermitian and non-Hermitian systems**. Left: The systems is Hermitian and all eigenvalues of the Hamiltonian are real, the **Fermi energy** E_F is defined as a point within the gap. Center: The complex spectrum of the non-Hermitian system exhibits a point gap E_p where no states exist. Right: A gap in the complex plane separate regions in the spectrum that do not intersect the complex line gap. Figure adapted from Ref. [26].

In this thesis we will only consider point gaps in non-Hermitian systems on hyperbolic lattices. Formally, a non-Hermitian Abelian Bloch Hamiltonian $H(\mathbf{k})$ on the m'th supercell is defined to have a point gap $E_p \in \mathbb{C}$ if there exists no crystal momentum $\mathbf{k} \in \mathrm{BZ}^{(m,1)}$ in the BZ such that E_p is an eigenvalue of $H(\mathbf{k})$.

Further, a general strategy for topological classifications of non-Hermitian systems is based on the construction of a **double Hamiltonian**, which reduces the problem to a Hermitian one [26]. Thus, consider a non-Hermitian Bloch Hamiltonian $H(\mathbf{k})$ such that $H^\dagger(\mathbf{k}) \neq H(\mathbf{k})$, the Hermitian double is defined as:

$$\tilde{H}(\mathbf{k}) = \begin{bmatrix} 0 & H(\mathbf{k}) \\ H^\dagger(\mathbf{k}) & 0 \end{bmatrix}. \tag{6.1}$$

6.1 Winding numbers

The winding numbers are topological invariants that can be used as indicators for topological insulators. Let us first illustrate the geometrical interpretation of the winding number for a simple 1D Hermitian model following Ref. [65], and subsequently extend the illustration to a 1D non-Hermitian model following Ref. [25].

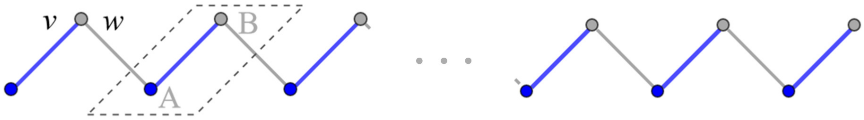

Figure 35: **SSH chain** is a one-dimensional bipartite chain with spin-less fermions coupled to its nearest neighbors by alternating hopping amplitudes v and w, where the unit cell is indicated with dashed lines. The sublattices A, B are indicated as blue and gray dots respectively. Figure reproduced from Ref. [65]

The Su-Schrieffer-Heeger (SSH) model describes a one-dimensional bipartite chain with spin-less fermions with nearest-neighbor coupling by alternating hopping amplitudes v and w, as shown in Fig. 35. The corresponding Hamiltonian is given by:

$$\begin{aligned} \mathcal{H} &= \sum_i (v a_i^\dagger b_i + w a_i^\dagger b_{i-1} + \text{h.c.}) = \sum_k \mathbf{C}_k^\dagger \, (\mathbf{h}(k) \cdot \boldsymbol{\sigma}) \, \mathbf{C}_k \\ \mathbf{h}(k) &= (h_1(k), h_2(k), h_3(k)) = (v + w\cos(k), w\sin(k), 0) \end{aligned} \tag{6.2}$$

where:

$$\mathbf{h}(\mathbf{k}) \cdot \boldsymbol{\sigma} = \begin{bmatrix} 0 & h(k) \\ h^*(k) & 0 \end{bmatrix}, \quad h(k) \equiv h_1(k) - ih_2(k)\,. \tag{6.3}$$

The corresponding eigenvalues:

$$E(k) = \|\mathbf{h}(k)\| = \sqrt{v^2 + w^2 + 2\,v\,w\,\cos(k)}, \tag{6.4}$$

where $\boldsymbol{\sigma} = (\sigma_1, \sigma_2, \sigma_3)$ is a vector of Pauli matrices in the fundamental representation of SU(2) and $\mathbf{C}_k \equiv (a_k, b_k)$. In the fully dimerized limit where $v \neq 0$ and $w = 0$ the system decouples into dimers. The states on each of these dimers are localized between the dimer sites, in the middle of the unit cell. In contrast, in the opposite limit where $v = 0$ and $w \neq 0$ the sites located at the edges of the SSH chain fully decouple, leaving only dimers within the bulk. Consequently, the system develops states at the edges that are localized only on one particular site, i.e. edge states with zero energy.

Naturally, we want to characterize these phases and see whether a topological invariant can be identified. Consider the vector $\mathbf{h}(k)$, it traces out a closed circle in the h_x, h_y plane as we vary $k = 0 \to 2\pi$ in the BZ torus $\mathbb{T}^1$. This circle is centered at $(v, 0)$ and collapses to a point for $w = 0$. As $v < w$ and $w \neq 0$ the loop encircles the origin. This implies that the topology of the loop can be characterized by the number of times the loop winds around the origin [65]: the **winding number**.

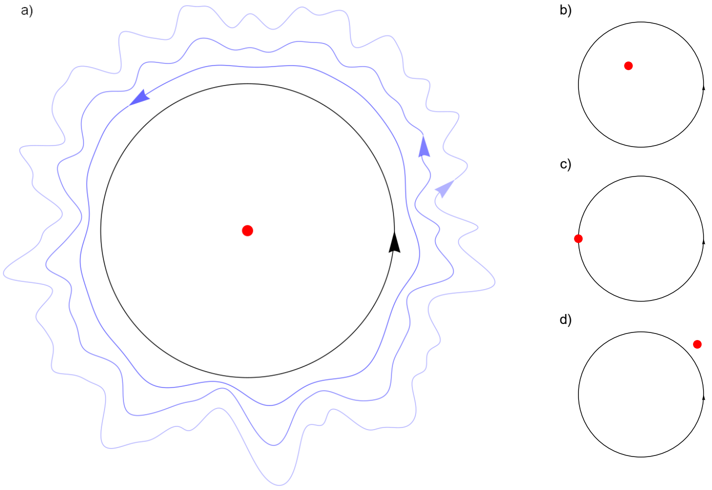

Figure 36: **Winding number and homotopy**. Examples of loops exhibiting quantized values of the 1D winding number, defined at a fixed base point p, indicated in red. a) Deformation of a generic path to a unit circle that winds around the point p once, indicated in red. b) The loop winds around the p once. c) The path crosses the irregular point p, which renders the winding number ill-defined. d) The winding number is zero since the point p is outside the closed path. Cf. Refs. [45, 66]

The construction of the formula for the winding number in 1D follows naturally by the integration of the normalized signed length that $\mathbf{h}(k)$ traverses. Let $\hat{\mathbf{h}}(k) \equiv \mathbf{h}(k)/\left\|\mathbf{h}(k)\right\|$:

$$\omega_{(1)} = \frac{1}{2\pi}\int_{\mathbb{T}^1} dk \left(\hat{\mathbf{h}}(k) \times \frac{d\hat{\mathbf{h}}(k)}{dk}\right)_z = \frac{1}{2\pi i}\int_{\mathbb{T}^1} dk (h(k))^{-1}\frac{dh(k)}{dk}, \tag{6.5}$$

Therefore, the winding number $w_{(1)}$ describes the number of times the BZ wraps onto S^1 defined by the map $\hat{\mathbf{h}}(k) : \mathbb{T}^1 \to S^1$, where S^1 is the unit circle. The subscript (1) indicates the dimensionality of the BZ tours $\mathbb{T}^1$. The relevance of the subscript notation will become clear in what will follow. Further, note that the structure of the winding number takes a similar form as the first Chern number described in Eq. (5.17).

The extension to non-Hermitian models follows analogously. The Hatano-Nelson model [67] describes a 1D chain with **non-reciprocal** nearest-neighbor coupling, as shown in Fig. 37.

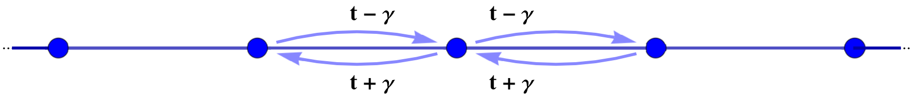

Figure 37: **Hatano-Nelson model in 1D chain**, with asymmetric hopping amplitudes $(t \pm \gamma)$. Cf. Ref. [25]

The corresponding Hamiltonian is given by:

$$\begin{aligned} \mathcal{H}_{HN} &= \sum_i (t+\gamma) c_i^\dagger c_{i-1} + (t-\gamma) c_i^\dagger c_{i+1} = \sum_k h(k)\, c_k^\dagger c_k \,, \\ h(k) &= 2(t\cos(k) + i\gamma\sin(k)). \end{aligned} \tag{6.6}$$

The asymmetric hopping amplitudes render the eigenvalues complex. These eigenvalues form a closed loop in the complex plane around the origin as we vary $k = 0 \to 2\pi$ in the BZ torus, for $t, \gamma \neq 0$. The loop collapses to real line of length $4t$ for $\gamma = 0$ and to a imaginary line of length 4γ for $t = 0$. To describe the topology of the loop traced out by $h(k)$ in the complex plane we can make use of the doubling procedure [26] for non-Hermitian Hamiltonians as described in Eq. (6.1), thus:

$$\tilde{H}(k) = \begin{bmatrix} 0 & h(k) \\ h^*(k) & 0 \end{bmatrix}. \tag{6.7}$$

The doubled Hamiltonian $\tilde{H}(k)$ is structurally equivalent to the Hamiltonian of the SSH chain, therefore, we may ascribe the same topological invariant to the Hatano-Nelson model.

The extension to general non-Hermitian systems compactified on a one dimensional torus with matrix valued Bloch Hamiltonian $H(k)$ is given by [25, 68]:

$$w_{(1)} = \frac{1}{2\pi i} \int_{\mathbb{T}^1} dk\, \mathrm{Tr}[H^{-1}(k) \frac{dH(k)}{dk}]. \tag{6.8}$$

We proceed by adopting the language of differential geometry to describe winding numbers in non-Hermitian systems in hyperbolic $\{p, q\}$-lattices. This will be convenient for our analysis of the transformation behavior of the winding numbers under general hyperbolic symmetries $g \in \Delta(2,q,p)$. The winding number $\mathscr{w}_{(1)}$ in Eq. (6.8) can be expressed as:

$$\mathscr{w}_{(1)} = \frac{1}{2\pi i} \int_{\mathbb{T}^1} \mathrm{Tr}[H^{-1}(k)\mathrm{d}H(k)], \tag{6.9}$$

where $\mathrm{d}H(k)$ is a matrix valued differential form of degree one. The generalization of the winding number in odd dimension for non-Hermitian systems are given by the **winding number density** [26]:

$$\begin{aligned} \mathscr{w}_{(2n+1)}[H(\mathbf{k})] &= \frac{(-1)^{n+1} n!}{(2n+1)!} \left(\frac{i}{2\pi}\right)^{n+1} \mathrm{Tr}[(H^{-1}(\mathbf{k})\, \mathrm{d}H(\mathbf{k}))^{\wedge 2n+1}] \\ &\equiv N_{2n+1}\, \mathrm{d}k^{i_1} \wedge \cdots \wedge \mathrm{d}k^{i_{2n+1}} \mathrm{Tr}[H^{-1}(\mathbf{k})(\partial_{i_1} H(\mathbf{k})) \cdots H^{-1}(\mathbf{k})(\partial_{i_{2n+1}} H(\mathbf{k}))], \end{aligned} \tag{6.10}$$

where $n \in \mathbb{N}_{\geqslant 0}$, $\mathrm{d} \equiv \mathrm{d}/\mathrm{d}\mathbf{k}$ and $\partial_i \equiv \partial/\partial k_i$. The winding numbers that can be calculated are restricted to the dimensionality of the BZ torus. Therefore, for hyperbolic lattices $n \in \{1,2,..,\mathfrak{g}{-}1\}$, where $2\mathfrak{g}$ is the dimension of the BZ torus. We adopt the following short-hand notation introduced in Ref. [7]. Let X be a matrix valued differential form of degree one, then:

$$X^{\wedge j} = \underbrace{X \wedge \cdots \wedge X}_{j \text{ copies of } X}. \tag{6.11}$$

Further, the integration of the winding number density over the BZ torus $\mathbb{T}^{2\mathfrak{g}}$, with $\mathscr{d} \equiv 2n+1$ and $D \equiv 2\mathfrak{g}$, gives us the **winding number tensor**:

$$\begin{aligned} \mathscr{w}^{i_{\mathscr{d}+1}\cdots i_D}_{(\mathscr{d})} &\equiv \frac{N_{\mathscr{d}}}{(2\pi)^{D-\mathscr{d}}} \int_{\mathbb{T}^D} \mathrm{d}k^{i_1} \wedge \cdots \wedge \mathrm{d}k^{i_D} \mathrm{Tr}[H^{-1}(\mathbf{k})(\partial_{i_1} H(\mathbf{k})) \cdots H^{-1}(\mathbf{k})(\partial_{i_{\mathscr{d}}} H(\mathbf{k}))] \\ &= \frac{N_{\mathscr{d}}}{(2\pi)^{D-\mathscr{d}}}\, \epsilon^{i_1 \ldots i_D} \int_{\mathbb{T}^D} \mathrm{d}^D k\, \mathrm{Tr}[H^{-1}(\mathbf{k})(\partial_{i_1} H(\mathbf{k})) \cdots H^{-1}(\mathbf{k})(\partial_{i_{\mathscr{d}}} H(\mathbf{k}))] \\ &\equiv \epsilon^{i_1 \cdots i_D}\, \tilde{\mathscr{w}}_{(\mathscr{d})\, i_1 \ldots i_{\mathscr{d}}}, \end{aligned} \tag{6.12}$$

where $i_j \in \{1,2,..,D\}$. We will refer to $\tilde{\mathscr{w}}_{(\mathscr{d})\, i_1 \ldots i_{\mathscr{d}}}$ as the **winding number components**. The winding numbers can, for example, be used to classify non-Hermitian systems with no internal symmetries exhibiting point gaps [26]. These systems reside in the symmetry class A within the complex Altland-Zirnbauer (AZ) symmetry classes [26]. Further, we will restrict ourself to $\mathscr{d} = 1, 3$ for most of our considerations of the winding numbers, deviating only when we consider hyperbolic lattice symmetries in chapter 7. In the subsequent section we will explicitly investigate the winding numbers in non-Hermitian systems in symmetry class A.

6.2 Hatano-Nelson model on $\{6,4\}$-lattice

We proceed with studying a variation of the Hatano-Nelson model [67] on the hyperbolic $\{6,4\}$-lattice. Let us consider the primitive cell as shown in Fig. 38. The Hatano-Nelson model endows the $\{6,4\}$-lattice with asymmetric hopping amplitudes $(t+\gamma)$ in counter-clockwise direction and $(t-\gamma)$ in the clockwise direction, indicated with orange arrows. This effectively describes an infinite set of decoupled one dimensional chains following the hyperbolic geodesics within the $\{6,4\}$-lattice. Additionally, we introduce a perturbing term proportional to δ, which couples these Hatano-Nelson chains symmetrically, indicated with dashed green lines.

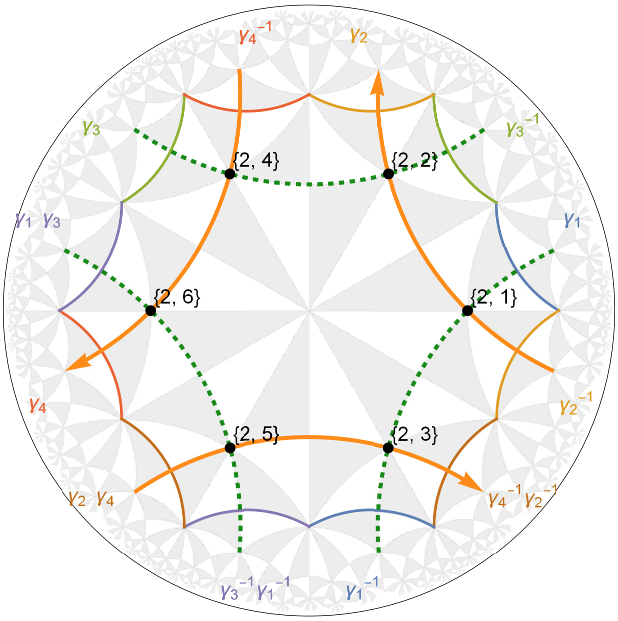

Figure 38: **$\{6,4\}$ Hatano-Nelson model with perturbations**. Asymmetric hopping amplitudes $(t+\gamma)$ in counter-clockwise direction and $(t-\gamma)$ in the clockwise direction are indicated with orange arrows. The Hermitian coupling terms proportional to δ are indicated with dashed green lines.

The corresponding Hamiltonian on the primitive cell is given by:

$$\begin{aligned}\mathcal{H} = \sum_{\gamma\in\Gamma} &(t+\gamma)\left(a^\dagger_{\gamma_2\gamma} b_\gamma + b^\dagger_\gamma a_\gamma + c^\dagger_{\gamma_4\gamma} d_\gamma + d^\dagger_\gamma c_\gamma + e^\dagger_{(\gamma_2\gamma_4)^{-1}\gamma} f_\gamma + f^\dagger_\gamma e_\gamma\right) \\ &+ (t-\gamma)\left(a^\dagger_\gamma b_\gamma + b^\dagger_\gamma a_{\gamma_2\gamma} + c^\dagger_\gamma d_\gamma + d^\dagger_\gamma c_{\gamma_4\gamma} + e^\dagger_\gamma f_\gamma + f^\dagger_\gamma e_{(\gamma_2\gamma_4)^{-1}\gamma}\right) \\ &+ \delta\Big(a^\dagger_\gamma f_\gamma + b^\dagger_{\gamma_3\gamma} c_\gamma + c^\dagger_\gamma b_\gamma + d^\dagger_{(\gamma_1\gamma_3)^{-1}\gamma} e_\gamma + e^\dagger_\gamma d_\gamma + f^\dagger_{\gamma_1\gamma} a_\gamma + \text{h.c.}\Big).\end{aligned} \tag{6.13}$$

The creation and annihilation operators, labeled according to Fig. 38, are given by:

$$\begin{aligned} a_\gamma &\equiv c^{\{2,1\}}_\gamma, \quad & d_\gamma &\equiv c^{\{2,6\}}_\gamma, \\ b_\gamma &\equiv c^{\{2,2\}}_\gamma, \quad & e_\gamma &\equiv c^{\{2,5\}}_\gamma, \\ c_\gamma &\equiv c^{\{2,4\}}_\gamma, \quad & f_\gamma &\equiv c^{\{2,3\}}_\gamma. \end{aligned} \tag{6.14}$$

The Abelian Bloch Hamiltonian in Eq. (3.67) takes the form:

$$H(\mathbf{k}) = \begin{bmatrix} 0 & t{-}\gamma{+}(t{+}\gamma)e^{ik_2} & \delta{+}\delta e^{-ik_1} & 0 & 0 & 0 \\ t{+}\gamma{+}(t{-}\gamma)e^{-ik_2} & 0 & 0 & \delta{+}\delta e^{ik_3} & 0 & 0 \\ \delta{+}\delta e^{ik_1} & 0 & 0 & 0 & t{+}\gamma{+}(t{-}\gamma)e^{i(k_2+k_4)} & 0 \\ 0 & \delta{+}\delta e^{-ik_3} & 0 & 0 & 0 & t{-}\gamma{+}(t{+}\gamma)e^{ik_4} \\ 0 & 0 & t{-}\gamma{+}(t{+}\gamma)e^{-i(k_2+k_4)} & 0 & 0 & \delta{+}\delta e^{i(k_1+k_3)} \\ 0 & 0 & 0 & t{+}\gamma{+}(t{-}\gamma)e^{-ik_4} & \delta{+}\delta e^{-i(k_1+k_3)} & 0 \end{bmatrix} \tag{6.15}$$

In the limit $\delta \to 0$, the one dimensional Hatano-Nelson chains fully decouple and we find the eigenvalues:

$$\begin{aligned} \epsilon_1^{\pm}(\mathbf{k}) &= \pm 2\,(t\mathrm{cos}(\frac{k_2}{2}) + i\gamma\mathrm{sin}(\frac{k_2}{2})), \\ \epsilon_2^{\pm}(\mathbf{k}) &= \pm 2\,(t\mathrm{cos}(\frac{k_4}{2}) + i\gamma\mathrm{sin}(\frac{k_4}{2})), \\ \epsilon_3^{\pm}(\mathbf{k}) &= \pm 2\,(t\mathrm{cos}(\frac{k_2+k_4}{2}) - i\gamma\mathrm{sin}(\frac{k_2+k_4}{2})), \end{aligned} \tag{6.16}$$

which is reminiscent of the eigenvalues for the Hatano-Nelson chain in the one-dimensional Euclidean space Eq. (6.6). The corresponding density of states and the spectrum in the complex plane with $5 \cdot 10^4$ randomly sampled points in the BZ torus $\mathbb{T}^4$ for $t = 1/2$ and $\gamma = 1/5$ are depicted in Fig. 39. The DOS is smoothed by a kernel density estimation with a Gaussian kernel of energy bandwidth 0.01.

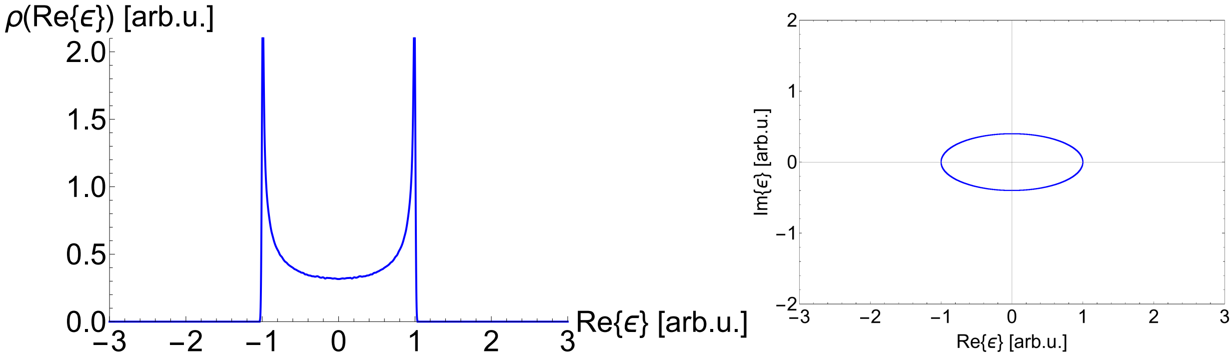

Figure 39: **DOS and complex energy spectrum for the $\{6, 4\}$ Hatano-Nelson model on the primitive cell**, where $t = 1/2$, $\gamma = 1/5$ and $\delta = 0$. Left: The density of states for the real part of the complex energies takes the well know form for a tight-binding model on one dimensional chain. Right: The complex energy spectrum envelops a point gap at zero energy.

In this decoupled limit, the symmetric aggregation of additional primitive cells into m-supercells does not alter the DOS nor the spectrum, as shown in Fig. 40 for 10^4 randomly sampled points in the BZ torus $\mathbb{T}^{2\mathfrak{g}}$. Note, due to the small sample size small fluctuations appear for the T2.2 primitive cell which are not present in Fig. 39 where more samples have been taken.

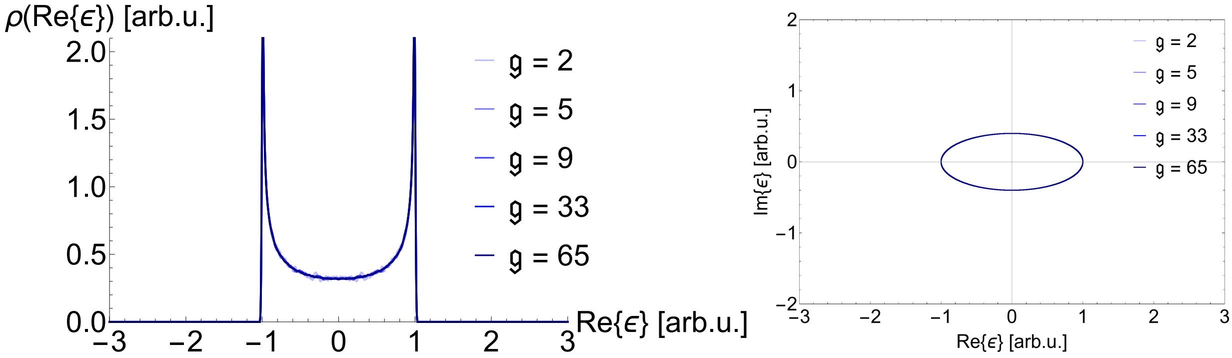

Figure 40: **DOS and complex energy spectrum for the $\{6,4\}$ Hatano-Nelson model on supercells**, where $t = 1/2$, $\gamma = 1/5$ and $\delta = 0$. The sequence of supercells T2.2, T5.4, T9.3, T33.11, T65.9 and the AHBT associated Abelian BZ trous $\mathbb{T}^{2\mathfrak{g}}$. Left: The density of states for the real part of the complex energies takes the well-known form for a tight-binding model on one-dimensional chain.

As such the higher-dimensional irreducible representations that are accessed via the supercell method do not change the spectrum. Thus, the $\{6,4\}$ Hatano-Nelson model in the decoupled limit where $\delta = 0$ on the T2.2 primitive cell using AHBT describes the thermodynamic limit. Perturbing the system by coupling Hatano-Nelson chains through the symmetric hopping amplitudes $\delta = 0.2$ broadens the DOS and the complex energy spectrum, and the model on the T2.2 primitive cell with AHBT no longer describes the thermodynamic limit. The corresponding DOS plots are depicted in Fig. 41.

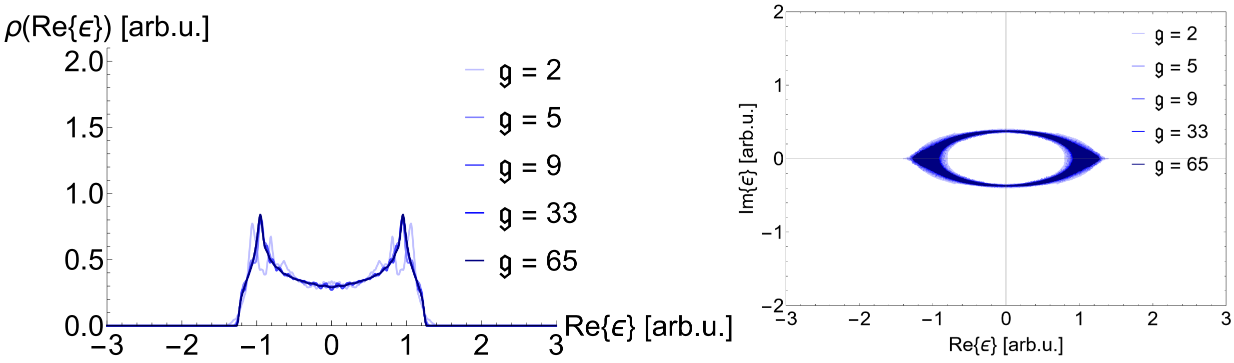

Figure 41: **DOS and complex energy spectrum for the $\{6,4\}$ Hatano-Nelson model on supercells**, where $t = 1/2$, $\gamma = 1/5$ and $\delta = 0.2$. The sequence of supercells T2.2, T5.4, T9.3, T33.11, T65.9 and the AHBT associated Abelian BZ torus $\mathbb{T}^{2\mathfrak{g}}$.

We proceed with computing the winding numbers as defined in Eq. (6.12) for $\mathscr{d} = 1,3$ by setting $t = \gamma = 1/2$ and $\delta = 0$. Specifically, for $\mathscr{d} = 1$ we compute the $\tilde{\omega}_{(1)\,i}$ for all supercells of Eq. (4.7) and for $\mathscr{d} = 3$ we compute $\tilde{\omega}_{(3)\,i,j,k}$ only up to the first supercell T5.4. All winding numbers turn out to be trivial. In fact, we will see in section 8.1 that the hyperbolic lattice symmetries of the

$\{6,4\}$ Hatano-Nelson model are not compatible with any one dimensional winding numbers on any supercell we have considered.

6.3 Hatano-Nelson model on the $\{8,4\}$-lattice

In the last section, we have seen that the winding numbers in the $\{6,4\}$-lattice turned out to be trivial. As such, we consider the $\{8,4\}$ Hatano-Nelson model for two distinct configurations, shown in Fig. 42 on the primitive cell T3.6. The asymmetric hopping amplitudes are indicated with orange arrows, with hopping amplitude $(t+\gamma)$ in the direction of the arrow $(t-\gamma)$ in the opposite direction. The perturbing term δ is indicated with dashed green lines. Since the orange arrows in Fig. 42 travel on the hyperbolic geodesics, we denote the left configuration with anti-parallel orange arrows as the anti-parallel $\{8,4\}$ Hatano-Nelson model and the right configuration as the parallel $\{8,4\}$ Hatano-Nelson model, for convenience.

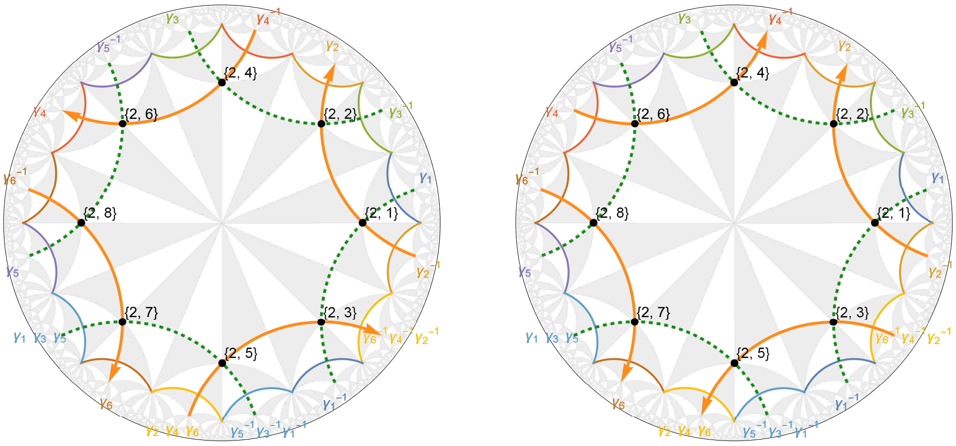

Figure 42: $\{8,4\}$ **Hatano-Nelson model with perturbations**. Asymmetric hopping amplitudes are indicated with orange arrows, with hopping amplitude $(t+\gamma)$ in the direction along the arrow $(t-\gamma)$ in the opposite direction. The Hermitian coupling terms proportional to δ are indicated indicated with dashed green lines.

Note that there exist a lower-order quotient group T2.3 in [39] for the triangle group $\Delta(2,4,8)$; however, the corresponding primitive cell is not compatible with the Hatano-Nelson models we want to consider. As such, the supercell sequence we consider is given by:

$$\{8,4\}\text{-lattice}: \quad \text{T3.6, T5.6, T9.7, T17.8} \tag{6.17}$$

We calculate the winding number components $\tilde{\omega}_{(\mathscr{d})\,i_1,..,i_{\mathscr{d}}}$ in Eq. (6.12) for $\mathscr{d}=1,3$, in the decoupled limit with $t=\gamma=1/2$ and $\delta=0$. Further, for $\mathscr{d}=1$ we compute the $\tilde{\omega}_{(1)\,i}$ for all supercells of Eq. (6.17) and for $\mathscr{d}=3$ we compute $\tilde{\omega}_{(3)\,i,j,k}$ only up to the supercell T5.6.

For the anti-parallel $\{8,4\}$ Hatano-Nelson model we find trivial winding numbers $\tilde{w}_{(1)\,i} = 0$ and $\tilde{w}_{(3)\,i,j,k} = 0$. In contrast, for the parallel $\{8,4\}$ Hatano-Nelson model we again find $\tilde{w}_{(3)\,i,j,k} = 0$, however, the $\tilde{w}_{(1)\,i}$ are not trivial and tabulated in Table 2.

$\Delta^+/\Gamma^{(m)}(2,4,8)$	index: i	$\tilde{w}_{(1)\,i}$
T3.6	1,3-5	0
	2,6	2
T5.6	1-3,5,7,8	0
	4,10	2
	6, 9	-2
T9.7	1-6,8,12-18	0
	7,9-11	4
T17.8	1,3,6,7,9-12,14-18,21,25-34	0
	2,4,5,13,23,24	4
	8,20,21	-4

Table 2: **One dimensional winding number components** $\tilde{w}_{(1)\,i}$, for the parallel $\{8,4\}$ Hatano-Nelson model shown on the right of Fig. 42, with $t = \gamma = 1/2$ and $\delta = 0$. The index i denotes the index in $\tilde{w}_{(1)\,i}$.

7 Hyperbolic lattice symmetries and topological invariants

Hyperbolic lattice symmetries may constrain the degrees of freedom of topological invariants. In this chapter we will build the necessary tools in order to formulate such constraints for winding numbers. For the 1st and 2nd Chern numbers such constraint equations were derived in Ref. [7] and we will use the same methodology in order to find constraint equations for the winding numbers in section 7.2. At the end of this chapter, we briefly state the constraint equations of the first and second Chern numbers, in preparation for the subsequent chapter 8. There, the number of independent winding numbers as well as 1st and 2nd Chern numbers will be calculated explicitly for a selection of already considered models.

7.1 Point-group matrices

In this section we will look at how symmetry elements of the triangle groups act on hyperbolic momenta by reviewing aspects in Ref. [7]. Let $\psi_{\mathbf{k}}(z)$ be the amplitude of an Abelian hyperbolic Bloch state at a position z in the hyperbolic space and momentum $\mathbf{k}$ in the BZ torus. Let S_g be a representation of a general symmetry $g \in \Delta(2,\, q,\, p)$, with triangle group Δ in Eq. (3.15), such that $[S_g,\, H(\mathbf{k})] = 0$ where $H(\mathbf{k})$ is the hyperbolic Abelian Bloch Hamiltonian. To achieve brevity, let us omit the $\{p, q\}$ dependence of the group Δ and likewise for Γ and G given in Eq. (3.18) and Eq. (3.22), respectively. Further, let us also suppress the momentum subscript of the state ψ. Under a general symmetry transformation g the state $\psi(z)$ transforms as:

$$S_g\psi(z) = \psi(g^{-1}(z)) \equiv \psi_g(z). \tag{7.1}$$

Recall from Section 2.3 that according to the Abelian Bloch theorem $\psi(z)$ transform under a translation $\gamma_i \in \Gamma \triangleleft \Delta$ as $S_{\gamma_i}\psi(z) = \chi(\gamma_i)\psi(z)$ where $\chi : \Gamma \to \mathrm{U}(1)$. By extension $\psi_g(z)$ transforms as:

$$\begin{aligned} S_{\gamma_i}\psi_g(z) = (S_g S_{g^{-1}}) S_{\gamma_i} S_g \psi(z) &= S_g S_{g^{-1}\gamma_i g}\psi(z) \\ = S_g \chi(g^{-1}\gamma_i g)\psi(z) &= \chi(g^{-1}\gamma_i g)\psi_g(z), \end{aligned} \tag{7.2}$$

where the third equality follows from the fact that Γ is a normal subgroup of Δ such that $g^{-1}\gamma_i g \in \Gamma$. We can conclude that a general translation of a transformed state $\psi_g(z)$ mixes momenta k_j. Using $\chi(\gamma_j) = e^{ik^j}$, we find:

$$\begin{aligned} &\chi(g^{-1}\gamma_i g) = e^{i\tilde{k}^i} = e^{i(M_g)^i{}_j k^j}, \\ &\text{where} \quad \tilde{k}^i \equiv (M_g)^i{}_j k^j, \end{aligned} \tag{7.3}$$

where $(M_g)^i{}_j \in \mathbb{Z}$ is the number of times γ_j appears in $g^{-1}\gamma_i g$ after abelianization, where negative entries correspond to their inverse. The **point-group matrix** M_g is a representation of

G, since Γ is a normal subgroup of Δ and since for any pair g_1, g_2 that is in the same coset there exists one representative in the transversal $\tilde{g} \in T_\Delta(\Gamma)$, recall Eq. (3.18). For simplicity suppose g_1 is the representative of this coset, then g_2 can be decomposed into $g_2 = \gamma g_1$, therefore: ${g_2}^{-1}\gamma_i g_2 = {g_1}^{-1}\gamma^{-1}\gamma_i\gamma g_1$ and thus $M_{g_1} = M_{g_2}$, therefore $M_g : G \to \mathrm{GL}(2\mathfrak{g}, \mathbb{Z})$. Note that we chose the translation γ to be on the left side of g_1 out of convenience, which is contrary to our convention. We may as well write $g_2 = \gamma g_1$ in terms of another translation operator to the right of g_1 such that $g_2 = g_1\gamma'$.

The extension to anti-unitary symmetry transformations, like time reversal $\mathcal{T}$, follows the same procedure. Under a general symmetry transformation composed with time reversal $g\mathcal{T}$ we find:

$$\begin{aligned} S_{g\mathcal{T}}\psi(z) &= \psi^*(g^{-1}(z)) \equiv \psi_{g\mathcal{T}}(z) \\ S_{\gamma_i}\psi_{g\mathcal{T}}(z) &= S_{g\mathcal{T}}\chi(g^{-1}\gamma_i g)\psi(z) = \chi^*(g^{-1}\gamma_i g)\psi_{g\mathcal{T}}(z). \end{aligned} \tag{7.4}$$

Therefore, under the anti-unitary symmetry transformation $g\mathcal{T}$ the point-group matrix M_g develops a minus sign:

$$M_{g\mathcal{T}} = -M_g\,. \tag{7.5}$$

Thus, the construction of M_g requires the determination of the words $g^{-1}\gamma_i\, g$ in form of the generators γ_j in the translation group Γ and subsequent abelianization. These calculations can efficiently be executed using GAP. We have constructed such an implementation, the pseudo code is provided in the Appendix 10.3. The point-group matrices are essential objects for the symmetry characterization of models on hyperbolic lattices. As such, we will construct them for a set of m'th supercells and study how topological invariants are constrained by symmetry.

7.2 Winding numbers revisited

We are interested in the transformation behavior of the winding numbers under general hyperbolic lattice symmetry transformations $g \in \Delta(2, p, q)$. These symmetries constrain the degrees of freedom of the system and, as such, lead to constraint equations for winding numbers. To this end, we will be following the same methodology as applied by Ref. [7] for non-Hermitian Abelian Bloch Hamiltonians. We will make use of the tools of differential geometry such as the graded cyclicity property G.C. and graded Leibniz rule G.L., [69].

We will start by considering unitary transformations. In order to proceed we need the non-Hermitian Abelian Bloch Hamiltonian $H(\mathbf{k})$ to have the following properties:

- We assume that the Hamiltonian has a gapped spectrum across the entire BZ and that there is no eigenvalue that is zero. This implies that $\det(H(\mathbf{k})) \neq 0$ and therefore H is invertible.
- We further assume that the spectrum of the Hamiltonian has a compact support and therefore $H(\mathbf{k})$ is trace-class. This implies that we can use the graded cyclic property of the trace.

Let g be a general symmetry of the hyperbolic $\{p,q\}$-lattice such that $g \in \Delta(2,q,p)$. Consider any appropriate m'th supercell identified by a normal subgroup $\Gamma^{(m)}_{\{p,q\}}$ obeying Eq. (3.68), together with a non-Hermitian Abelian Bloch Hamiltonian $H(\mathbf{k})$ constructed through the supercell method in 3.6 on that m'th supercell, at momentum $\mathbf{k} \in \mathbb{T}^{2\mathfrak{g}}$. There exists a unitary representation $V_g(\mathbf{k}) \in \ \mathrm{U}(N)$ that transforms $H(\mathbf{k})$ at $\mathbf{k}$ to the Hamiltonian at $M_g\mathbf{k}$, such that $V_g(\mathbf{k})H(\mathbf{k})V_g(\mathbf{k})^\dagger = H(M_g\mathbf{k})$. Further, recall that the dimension $\mathscr{d}$ of the winding number density $\mathscr{w}_{(\mathscr{d})}[H(\mathbf{k})]$ in Eq. (6.10) indicates the dimension of subtori spanned by momenta $\{k_{i_1}, k_{i_2}, .., k_{i_\mathscr{d}}\}$ of the $2\mathfrak{g}$ dimensional BZ torus $\mathbb{T}^{2\mathfrak{g}}$, with $i_j \in \{1, 2, 3, .., 2\mathfrak{g}\}$ and $\mathscr{d} \in \{1, 3, 5, .., 2\mathfrak{g}-1\}$.

Claim 7.1. Let $V \equiv V_g(\mathbf{k})$. Under a general hyperbolic lattice symmetry transformation the winding number density $\mathscr{w}_{(\mathscr{d})}$ transforms as:

$$\begin{aligned}
\mathscr{w}_{(\mathscr{d})}[H(\mathbf{k})] \to \mathscr{w}_{(\mathscr{d})}[H(M_g\mathbf{k})] &= N_\mathscr{d}\ \mathrm{Tr}[(H'^{-1}(\mathbf{k})\,\mathrm{d}H'(\mathbf{k}))^{\wedge\mathscr{d}}] \\
&= N_\mathscr{d}\ \mathrm{Tr}[((VH(\mathbf{k})V^\dagger)^{-1}\,\mathrm{d}(VH(\mathbf{k})V^\dagger))^{\wedge\mathscr{d}}] \\
&= N_\mathscr{d}\ \mathrm{Tr}[(H^{-1}(\mathbf{k})\,\mathrm{d}H(\mathbf{k}))^{\wedge\mathscr{d}}] + \mathrm{d}z \\
&= \mathscr{w}_{(\mathscr{d})}[H(\mathbf{k})] + \mathrm{d}z\,,
\end{aligned} \tag{7.6}$$

where the transformation can at most acquire a total derivative $\mathrm{d}z$ that vanishes when integrating over a closed surface in $\mathrm{BZ}^{(m,1)}$ by Stokes theorem. The symbol ($'$) indicates the transformed object.

Proof of claim 7.1 for $\mathscr{d} = 1, 3$:

Let $H \equiv H(\mathbf{k})$ for convenience. Let us define:

$$\begin{aligned}
&\mathscr{x} = \mathrm{d}V\,HV^\dagger\,, \qquad \mathscr{v} = V\mathrm{d}H\,V^\dagger\,, \\
&\mathscr{y} = VH\mathrm{d}V^\dagger\,, \qquad \mathscr{w} = H'^{-1}\mathscr{v} = VH^{-1}\mathrm{d}H\,V^\dagger\,, \\
&\text{such that} \quad \mathscr{v} + \mathscr{x} + \mathscr{y} = \mathrm{d}(VHV^\dagger).
\end{aligned} \tag{7.7}$$

These are **matrix valued** differential forms of degree one. The following identities will prove useful:

$$\begin{aligned}
\mathscr{x}H'^{-1} = \mathrm{d}V\,V^\dagger \quad &\text{and} \quad H'^{-1}\mathscr{y} = V\mathrm{d}V^\dagger\,, \\
\implies \quad \mathscr{x}H'^{-1} + H'^{-1}\mathscr{y} &= \mathrm{d}(VV^\dagger) = 0\,,
\end{aligned} \tag{7.8}$$

$$\begin{aligned}
&\mathscr{w}H'^{-1} = -V\mathrm{d}H^{-1}V^\dagger \quad , \quad \mathscr{x} \wedge \mathscr{w} = \mathrm{d}V \wedge \mathrm{d}H\,V^\dagger \\
&\text{and} \quad \mathscr{w} \overset{\text{G.L.}}{=} VH^{-1}\mathrm{d}(HV^\dagger) - H'^{-1}\mathscr{y} \overset{(7.8)}{=} VH^{-1}\mathrm{d}(HV^\dagger) + \mathscr{x}H'^{-1}\,.
\end{aligned} \tag{7.9}$$

<u>For $\mathscr{d} = 1$:</u>

$$\begin{aligned}
\mathscr{w}_{(1)}[H(M_g\mathbf{k})] &= N_1\ \mathrm{Tr}[H'^{-1}\,\mathrm{d}H'] = N_1\ \mathrm{Tr}[\mathscr{w} + H'^{-1}(\mathscr{x} + \mathscr{y})] \\
&\overset{\text{G.C.}}{=} \mathscr{w}_{(1)}[H(\mathbf{k})] + N_1\ \mathrm{Tr}[\mathscr{x}H'^{-1} + H'^{-1}\mathscr{y}] \\
&\overset{(7.8)}{=} \mathscr{w}_{(1)}[H(\mathbf{k})]\,.
\end{aligned}$$

In the last line we used Eq. (7.8).

<u>For $\mathscr{d} = 3$:</u>

$$\begin{aligned} \mathscr{w}_{(3)}[H(M_g\mathbf{k})] &= N_3\,\mathrm{Tr}[(H'^{-1}\,\mathrm{d}H')^{\wedge 3}] = N_3\,\mathrm{Tr}[(\mathscr{w} + H'^{-1}(x + y))^{\wedge 3}] \\ &\equiv N_3\,\mathrm{Tr}[\mathscr{w}^{\wedge 3}] + N_3\,\mathscr{Z} = \mathscr{w}_{(3)}[H(\mathbf{k})] + N_3 \mathscr{Z}\,. \end{aligned}$$

Further, for **matrix valued** one-forms a, b, we see that:

$$\mathrm{Tr}[a \wedge b^{\wedge 2} + b \wedge a \wedge b + b^{\wedge 2} \wedge a] \overset{\text{G.C.}}{=} 3\,\mathrm{Tr}[a \wedge b^{\wedge 2}], \tag{7.10}$$

such that $\mathscr{Z}$ can be written as:

$$\begin{aligned} \mathscr{Z} &\equiv \mathscr{Z}_1 + 3\,\mathscr{Z}_2 + 3\,\mathscr{Z}_3 \\ &\overset{(7.10)}{=} \mathrm{Tr}[(H'^{-1}(x + y))^{\wedge 3}] + 3\,\mathrm{Tr}[\mathscr{w} \wedge (H'^{-1}(x + y))^{\wedge 2}] + 3\,\mathrm{Tr}[\mathscr{w}^{\wedge 2} \wedge (H'^{-1}(x + y))]\,. \end{aligned}$$

The first term in $\mathscr{Z}$ reduces to:

$$\begin{aligned} \mathscr{Z}_1 &\overset{(7.10)}{=} \mathrm{Tr}[(H'^{-1}x)^{\wedge 3} + (H'^{-1}y)^{\wedge 3} + 3\,(H'^{-1}x)^{\wedge 2} \wedge H'^{-1}y + 3\,H'^{-1}x \wedge (H'^{-1}y)^{\wedge 2}] \\ &\overset{\text{G.C.}}{=} 3\,\mathrm{Tr}[(xH'^{-1})^{\wedge 2} \wedge (yH'^{-1} - H'^{-1}y) + (H'^{-1}x - xH'^{-1}) \wedge (H'^{-1}y)^{\wedge 2}] \\ &\quad + \mathrm{Tr}[(xH'^{-1} + H'^{-1}y)^{\wedge 3}]\,, \end{aligned}$$

where we have added zeros $(1-1)((xH'^{-1})^{\wedge 2} \wedge H'^{-1}y + xH'^{-1} \wedge (H'^{-1}y)^{\wedge 2})$ in the second line. The last term vanishes by Eq. (7.8). Further:

$$\begin{aligned} \mathscr{Z}_1 &= 3\,\mathrm{Tr}[(xH'^{-1})^{\wedge 2} \wedge (yH'^{-1} - H'^{-1}y) + (H'^{-1}x - xH'^{-1}) \wedge (H'^{-1}y)^{\wedge 2}] \\ &\overset{(7.8)}{=} 3\,\mathrm{Tr}[H'^{-1}x \wedge (xH'^{-1})^{\wedge 2} + (xH'^{-1})^{\wedge 2} \wedge yH'^{-1} + (xH'^{-1})^{\wedge 3} - (xH'^{-1})^{\wedge 3}] \\ &\overset{\text{G.C.}}{=} 3\,\mathrm{Tr}[(xH'^{-1})^{\wedge 2} \wedge (H'^{-1}x + yH'^{-1})]\,. \end{aligned}$$

The second term in $\mathscr{Z}$ reduces to:

$$\begin{aligned} \mathscr{Z}_2 &\overset{(7.9)}{=} \mathrm{Tr}[((VH^{-1}\mathrm{d}(HV^{\dagger}) - H'^{-1}y) \wedge H'^{-1}y \\ &\quad + (VH^{-1}\mathrm{d}(HV^{\dagger}) + xH'^{-1}) \wedge H'^{-1}x) \wedge (H'^{-1}x + H'^{-1}y))] \\ &\overset{(7.8)}{=} -\mathrm{Tr}[\,(xH'^{-1})^{\wedge 2} \wedge (H'^{-1}x + H'^{-1}y)] + \mathrm{Tr}[xH'^{-1} \wedge H'^{-1}x \wedge (H'^{-1}x + H'^{-1}y)] \\ &\quad + \mathrm{Tr}[VH^{-1}\mathrm{d}(HV^{\dagger}) \wedge (H'^{-1}x + H'^{-1}y)^{\wedge 2}]\,. \end{aligned}$$

The third term in $\mathscr{Z}$ reduces to:

$$\begin{aligned} \mathscr{Z}_3 &\overset{(7.9)}{=} \mathrm{Tr}[(VH^{-1}\mathrm{d}(HV^{\dagger}) + xH'^{-1}) \wedge (VH^{-1}\mathrm{d}(HV^{\dagger}) - H'^{-1}y) \wedge (H'^{-1}x + H'^{-1}y)] \\ &= -\mathrm{Tr}[(VH^{-1}\mathrm{d}(HV^{\dagger}) + xH'^{-1}) \wedge (H'^{-1}x + H'^{-1}y)^{\wedge 2}] \\ &\quad + \mathrm{Tr}[(VH^{-1}\mathrm{d}(HV^{\dagger}) + xH'^{-1}) \wedge (VH^{-1}\mathrm{d}(HV^{\dagger}) + H'^{-1}x) \wedge (H'^{-1}x + H'^{-1}y)]\,, \end{aligned}$$

where we have added $(H'^{-1}x - H'^{-1}x)$ in the second bracket in line two. Therefore:

$$\begin{aligned}\mathscr{Z} &= \mathscr{Z}_1 \,+\, 3\,\mathscr{Z}_2 \,+\, 3\,\mathscr{Z}_3 \\ &= 3\,\mathrm{Tr}[((VH^{-1}\mathrm{d}(HV^\dagger) \,+\, xH'^{-1}) \wedge (VH^{-1}\mathrm{d}(HV^\dagger) \,+\, H'^{-1}x) \\ &\quad -\, xH'^{-1} \wedge H'^{-1}y) \wedge (H'^{-1}x \,+\, H'^{-1}y)] \,+\, 3\,\mathrm{Tr}[(xH'^{-1})^{\wedge 2} \wedge (yH'^{-1} - H'^{-1}y)]\,.\end{aligned} \tag{7.11}$$

After some tedious but straightforward manipulations through repeated use of the graded Leibniz rule and the graded cyclicity, see Appendix 10.4, we find:

$$\begin{aligned}\mathscr{Z} &= \,-\,3\,\mathrm{Tr}[\mathrm{d}V \wedge (\mathrm{d}(HV^\dagger)V \wedge \mathrm{d}(H^{-1}V^\dagger) \,-\, \mathrm{d}(H^{-1}V^\dagger)V \wedge \mathrm{d}(HV^\dagger))] \\ &\overset{G.L.}{=} \,-\,3\,\mathrm{d}\mathrm{Tr}[V\mathrm{d}(HV^\dagger)V \wedge \mathrm{d}(H^{-1}V^\dagger)] \\ &\qquad +\, 3\,\mathrm{Tr}[V\mathrm{d}(\mathrm{d}(HV^\dagger)V \wedge \mathrm{d}(H^{-1}V^\dagger)) \,+\, \mathrm{d}V \wedge \mathrm{d}(H^{-1}V^\dagger)V \wedge \mathrm{d}(HV^\dagger)] \\ &\overset{G.L.}{\equiv} 3\,\mathrm{Tr}[V\mathrm{d}(HV^\dagger) \wedge \mathrm{d}V \wedge \mathrm{d}(H^{-1}V^\dagger) \,-\, \mathrm{d}V \wedge \mathrm{d}(H^{-1}V^\dagger)V \wedge \mathrm{d}(HV^\dagger)] \,+\, \mathrm{d}z \\ &\overset{G.C.}{=} 3\,\mathrm{Tr}[\mathrm{d}V \wedge \mathrm{d}(H^{-1}V^\dagger)V \wedge \mathrm{d}(HV^\dagger) \,-\, \mathrm{d}V \wedge \mathrm{d}(H^{-1}V^\dagger)V \wedge \mathrm{d}(HV^\dagger)] \,+\, \mathrm{d}z = \mathrm{d}z\,.\end{aligned}$$

Therefore:

$$\Longrightarrow\ \omega_{(3)}[H(M_g\mathbf{k})] = \omega_{(3)}[H(\mathbf{k})] \,+\, \mathrm{d}z\,.$$

The winding number density does indeed transform as given in Eq. 7.1 for $\mathscr{d} \,=\, 1, 3$. ■

We hypothesize that the claim 7.1 holds for $\mathscr{d} \in \{5, 7, 9, .., D-1\}$ as well and leave the proof for future endeavors.

Claim 7.2. The winding number density is a closed form, i.e.:

$$\mathrm{d}\omega_{(\mathscr{d})}[H(\mathbf{k})] \,=\, 0\,. \tag{7.12}$$

Proof of claim 7.2:

$$\begin{aligned}\mathrm{d}\omega_{(\mathscr{d})}[H(\mathbf{k})] &= N_{\mathscr{d}}\ \mathrm{d}\mathrm{Tr}[(H^{-1}\mathrm{d}H)^{\wedge\mathscr{d}}] = N_{\mathscr{d}}\ \mathrm{Tr}[\mathrm{d}(H^{-1}\mathrm{d}H)^{\wedge\mathscr{d}}] \\ &\overset{G.L.}{=} N_{\mathscr{d}}\ \mathrm{Tr}[\mathrm{d}H^{-1} \wedge \mathrm{d}H \wedge (H^{-1}\mathrm{d}H)^{\wedge\mathscr{d}-1} - (H^{-1}\mathrm{d}H) \wedge \mathrm{d}H^{-1} \wedge \mathrm{d}H \wedge (H^{-1}\,\mathrm{d}H)^{\wedge\mathscr{d}-2} \\ &\quad + (H^{-1}\mathrm{d}H)^{\wedge 2} \wedge \mathrm{d}H^{-1} \wedge \mathrm{d}H \wedge (H^{-1}\mathrm{d}H)^{\wedge\mathscr{d}-3} - \ldots + (H^{-1}\mathrm{d}H)^{\wedge\mathscr{d}-1} \wedge \mathrm{d}H^{-1} \wedge \mathrm{d}H] \\ &\overset{G.C.}{=} \mathscr{d}\,N_{\mathscr{d}}\ \mathrm{Tr}[\mathrm{d}H^{-1} \wedge \mathrm{d}H \wedge (H^{-1}\mathrm{d}H)^{\wedge\mathscr{d}-1}] \\ &= \frac{\mathscr{d}\,N_{\mathscr{d}}}{2}\ \mathrm{Tr}[\mathrm{d}H^{-1} \wedge \mathrm{d}H \wedge (H^{-1}\mathrm{d}H)^{\wedge\mathscr{d}-1} \,+\, \mathrm{d}H^{-1} \wedge \mathrm{d}H \wedge (H^{-1}\mathrm{d}H)^{\wedge\mathscr{d}-1}] \\ &\overset{G.L.}{=} \frac{\mathscr{d}\,N_{\mathscr{d}}}{2}\ \mathrm{Tr}[\mathrm{d}H^{-1} \wedge \mathrm{d}H \wedge (H^{-1}\mathrm{d}H)^{\wedge\mathscr{d}-1} \,+\, (H^{-1}\mathrm{d}H) \wedge \mathrm{d}H^{-1} \wedge \mathrm{d}H \wedge (H^{-1}\mathrm{d}H)^{\wedge\mathscr{d}-2}] \\ &\overset{G.C.}{=} \frac{\mathscr{d}\,N_{\mathscr{d}}}{2}\ \mathrm{Tr}[\mathrm{d}H^{-1} \wedge \mathrm{d}H \wedge (H^{-1}\mathrm{d}H)^{\wedge\mathscr{d}-1} \,-\, \mathrm{d}H^{-1} \wedge \mathrm{d}H \wedge (H^{-1}\mathrm{d}H)^{\wedge\mathscr{d}-1}] = 0\,.\end{aligned}$$

■

Let us proceed by looking at the transformation behavior of the winding number components.

Claim 7.3. The winding number components $\tilde{\mathscr{w}}_{(\mathscr{d})\, i_1 \dots i_{\mathscr{d}}}$ as given in Eq. (6.12) transform under a general hyperbolic lattice symmetry as:

$$\tilde{\mathscr{w}}_{(\mathscr{d})\, i_1 \dots i_{\mathscr{d}}} \;=\; \det(M_g)\,(M_g)^{j_1}{}_{i_1}\;\cdots\;(M_g)^{j_{\mathscr{d}}}{}_{i_{\mathscr{d}}}\,\tilde{\mathscr{w}}_{(\mathscr{d})\, j_1 \dots j_{\mathscr{d}}}\,, \tag{7.13}$$

where $i_j \in \{1, 2, .., D\}$.

Proof of claim 7.3:

Under the symmetry transformation the derivatives ∂_i transform as:

$$\partial_i \;=\; \frac{\partial (M_g \mathbf{k})^j}{\partial k^i}\,\partial'_j \;=\; (M_g)^j{}_i\,\partial'_j \quad \text{where} \quad \partial_i \;=\; \partial/\partial k^i \quad \text{and} \quad \partial'_i \;=\; \partial/\partial (M_g \mathbf{k})^i$$

and the integration measure transforms as:

$$\begin{aligned} \mathrm{d}^D k' &= \mathrm{d}k'^1 \wedge \dots \wedge \mathrm{d}k'^D = \mathrm{d}k^{i_1} \wedge \dots \wedge \mathrm{d}k^{i_D}\,\frac{\partial (M_g\mathbf{k})^1}{\partial k^{i_1}} \cdots \frac{\partial (M_g\mathbf{k})^D}{\partial k^{i_D}} \\ &= \mathrm{d}^D k\,\epsilon^{i_1 \dots i_D} (M_g)^1{}_{i_1} \cdots (M_g)^D{}_{i_D} = \mathrm{d}^D k\,\det(M_g)\,. \end{aligned}$$

We integrate the left-hand side of Eq. 7.1 over the BZ torus $\mathbb{T}^D$:

$$\begin{aligned} \mathscr{w}'^{\;i_{\mathscr{d}+1}\dots i_D}_{\mathscr{d}} &= \frac{1}{(2\pi)^{D-\mathscr{d}}} \int_{\mathbb{T}^D} \mathrm{d}k^{i_1} \wedge \dots \wedge \mathrm{d}k^{i_{\mathscr{d}}} \wedge \mathscr{w}[H(M_g\mathbf{k})] \\ &= \frac{N_{\mathscr{d}}}{(2\pi)^{D-\mathscr{d}}}\,\epsilon^{i_1 \dots i_D} \int_{\mathbb{T}^D} \mathrm{d}^D k\,\mathrm{Tr}[H^{-1}(M_g\mathbf{k})(\partial_{i_1} H(M_g\mathbf{k}))\dots H^{-1}(M_g\mathbf{k})(\partial_{i_{\mathscr{d}}} H(M_g\mathbf{k}))] \\ &= \epsilon^{i_1 \dots i_D}\,\tilde{\mathscr{w}}'_{(\mathscr{d})\, i_1 \dots i_{\mathscr{d}}}\,. \end{aligned}$$

Further:

$$\begin{aligned} \tilde{\mathscr{w}}'_{(\mathscr{d})\, i_1 \dots i_{\mathscr{d}}} &= \frac{N_{\mathscr{d}}}{(2\pi)^{D-\mathscr{d}}} \int_{\mathbb{T}^D} \mathrm{d}^D k\,\mathrm{Tr}[H^{-1}(M_g\mathbf{k})(\partial_{j_1} H(M_g\mathbf{k}))\dots H^{-1}(M_g\mathbf{k})(\partial_{j_{\mathscr{d}}} H(M_g\mathbf{k}))] \\ &= \frac{N_{\mathscr{d}}}{(2\pi)^{D-\mathscr{d}}}\,(M_g)^{j_1}{}_{i_1}\;\cdots\;(M_g)^{j_{\mathscr{d}}}{}_{i_{\mathscr{d}}} \\ &\quad \times \int_{\mathbb{T}^D} \mathrm{d}^D k\,\mathrm{Tr}[H^{-1}(\mathbf{k}')(\partial'_{j_1} H(\mathbf{k}')) \cdots H^{-1}(\mathbf{k}')(\partial'_{j_{\mathscr{d}}} H(\mathbf{k}'))] \\ &= \frac{N_{\mathscr{d}}}{(2\pi)^{D-\mathscr{d}}}(\det(M_g))^{-1}\,(M_g)^{j_1}{}_{i_1}\;\cdots\;(M_g)^{j_{\mathscr{d}}}{}_{i_{\mathscr{d}}} \\ &\quad \times \int_{M_g(\mathbb{T}^D)} \mathrm{d}^D k'\,\mathrm{Tr}[H^{-1}(\mathbf{k}')(\partial'_{j_1} H(\mathbf{k}')) \cdots H^{-1}(\mathbf{k}')(\partial'_{j_{\mathscr{d}}} H(\mathbf{k}'))]\,. \end{aligned}$$

For the final step we follow the same line of reasoning as Ref. [7] in the case of Chern numbers. We presume that the spectrum of the Hamiltonian exhibits a gap throughout the entire BZ torus and that the integral is topological, see Eq. 7.2. As such, a continuous deformation of the BZ torus $M_g(\mathbb{T}^D)$ back to $\mathbb{T}^D$ will leave the integral unchanged, and therefore:

$$\begin{aligned} \tilde{\mathscr{w}}'_{(\mathscr{d})\, i_1 \dots i_{\mathscr{d}}} &= \det(M_g)\,(M_g)^{j_1}{}_{i_1}\;\cdots\;(M_g)^{j_{\mathscr{d}}}{}_{i_{\mathscr{d}}} \\ &\quad \times \frac{N_{\mathscr{d}}}{(2\pi)^{D-\mathscr{d}}} \int_{\mathbb{T}^D} \mathrm{d}^D k\,\mathrm{Tr}[H^{-1}(\mathbf{k})(\partial_{j_1} H(\mathbf{k})) \cdots H^{-1}(\mathbf{k})(\partial_{j_{\mathscr{d}}} H(\mathbf{k}))] \\ &= \det(M_g)\,(M_g)^{j_1}{}_{i_1}\;\cdots\;(M_g)^{j_{\mathscr{d}}}{}_{i_{\mathscr{d}}}\tilde{\mathscr{w}}_{(\mathscr{d})\, j_1 \dots j_{\mathscr{d}}}\,, \end{aligned}$$

where we used the fact that $M_g \in \mathrm{GL}(D, \mathbb{Z})$ and therefore $\det(M_g) = \pm 1$, [7]. We now integrate the right hand side of Eq. 7.1 over the BZ torus $\mathbb{T}^D$:

$$\begin{aligned}
&\frac{1}{(2\pi)^{D-\mathscr{d}}} \int_{\mathbb{T}^D} \mathrm{d}k^{i_1} \wedge \cdots \wedge \mathrm{d}k^{i_{\mathscr{d}}} \wedge \big(\mathscr{w}_{(\mathscr{d})}[H(\mathbf{k})] + \mathrm{d}z\big) \\
&\qquad = \frac{1}{(2\pi)^{D-\mathscr{d}}} \int_{\mathbb{T}^D} \mathrm{d}k^{i_1} \wedge \cdots \wedge \mathrm{d}k^{i_{\mathscr{d}}} \wedge \mathscr{w}_{(\mathscr{d})}[H(\mathbf{k})] = \epsilon^{i_1 \ldots i_D} \tilde{\mathscr{w}}_{(\mathscr{d})\, i_1 \ldots i_{\mathscr{d}}} = \mathscr{w}_{(\mathscr{d})}^{i_{\mathscr{d}+1} \ldots i_D} .
\end{aligned}$$

Therefore:

$$\tilde{\mathscr{w}}_{(\mathscr{d})\, i_1 \ldots i_{\mathscr{d}}} = \det(M_g)\, (M_g)^{j_1}{}_{i_1} \cdots (M_g)^{j_{\mathscr{d}}}{}_{i_{\mathscr{d}}} \tilde{\mathscr{w}}_{(\mathscr{d})\, j_1 \ldots j_{\mathscr{d}}} .$$

■

Next, let us extend the transformation behavior by considering anti-unitary transformations, such as time reversal $\mathcal{T}$.

Claim 7.4. For a general anti-unitary symmetry $g \in \Delta(2, q, p)$ of the hyperbolic $\{p, q\}$-lattice, there exists a anti-unitary representation $V_g(\mathbf{k})\mathcal{K}$ with $V_g(\mathbf{k}) \in \mathrm{U}(N)$ where $\mathcal{K}$ is the complex conjugation. Under this symmetry transformation the winding number components $\tilde{\mathscr{w}}_{(\mathscr{d})\, i_1 \ldots i_{\mathscr{d}}}$ in Eq. (6.12) transforms as:

$$\tilde{\mathscr{w}}_{(\mathscr{d})\, i_1 \ldots i_{\mathscr{d}}} = (-1)^{\frac{\mathscr{d}+1}{2}} \det(M_g)\, (M_g)^{j_1}{}_{i_1} \cdots (M_g)^{j_{\mathscr{d}}}{}_{i_{\mathscr{d}}} \tilde{\mathscr{w}}_{(\mathscr{d})\, j_1 \ldots j_{\mathscr{d}}} . \tag{7.14}$$

Proof of claim 7.4:

The non-Hermitian Hamiltonian transforms as:

$$V \mathcal{K} H(\mathbf{k}) \mathcal{K} V^\dagger = V H^*(\mathbf{k}) V^\dagger = H^*(M_g \mathbf{k}),$$

where $(^*)$ denotes the complex conjugate. By Eq. (7.5) we know that the point-group matrix M_g develops a minus sign under a anti-unitary transformation, however since M_g enters the Hamiltonian via the unitary representation V no additional sign in M_g appears. Given these transformation behaviors, we can follow the proof of claim 7.1 and the proof of claim 7.3 by making the aforementioned adjustments. For the final step we find:

$$\begin{aligned}
\tilde{\mathscr{w}}'_{(\mathscr{d})\, i_1 \ldots i_{\mathscr{d}}} &= \det(M_g)\, (M_g)^{j_1}{}_{i_1} \cdots (M_g)^{j_{\mathscr{d}}}{}_{i_{\mathscr{d}}} \\
&\quad \times \frac{N_{\mathscr{d}}}{(2\pi)^{D-\mathscr{d}}} \int_{\mathbb{T}^D} \mathrm{d}^D k\, \mathrm{Tr}[H^{-1}(\mathbf{k})(\partial_{j_1} H(\mathbf{k})) \cdots H^{-1}(\mathbf{k})(\partial_{j_{\mathscr{d}}} H(\mathbf{k}))]^* \\
&= \det(M_g)\, (M_g)^{j_1}{}_{i_1} \cdots (M_g)^{j_{\mathscr{d}}}{}_{i_{\mathscr{d}}} \\
&\quad \times \frac{N^*_{\mathscr{d}}}{(2\pi)^{D-\mathscr{d}}} \int_{\mathbb{T}^D} \mathrm{d}^D k\, \mathrm{Tr}[H^{-1}(\mathbf{k})(\partial_{j_1} H(\mathbf{k})) \cdots H^{-1}(\mathbf{k})(\partial_{j_{\mathscr{d}}} H(\mathbf{k}))] \\
&= (-1)^{\frac{\mathscr{d}+1}{2}} \det(M_g)\, (M_g)^{j_1}{}_{i_1} \cdots (M_g)^{j_{\mathscr{d}}}{}_{i_{\mathscr{d}}} \tilde{\mathscr{w}}_{(\mathscr{d})\, j_1 \ldots j_{\mathscr{d}}} ,
\end{aligned}$$

where we have used the fact that the winding number is real in the second equality. This implies:

$$\tilde{\mathfrak{w}}_{(\mathscr{d})\,i_1\ldots i_{\mathscr{d}}} = (-1)^{\frac{\mathscr{d}+1}{2}}\det(M_g)\,(M_g)^{j_1}{}_{i_1}\,\cdots\,(M_g)^{j_{\mathscr{d}}}{}_{i_{\mathscr{d}}}\tilde{\mathfrak{w}}_{(\mathscr{d})\,j_1\ldots j_{\mathscr{d}}}.$$

■

We conclude that the symmetry g constrains the winding number components as:

$$\tilde{\mathfrak{w}}_{(\mathscr{d})\,i_1\ldots i_{\mathscr{d}}} = \xi_g^{\mathscr{d}}\det(M_g)\,(M_g)^{j_1}{}_{i_1}\,\cdots\,(M_g)^{j_{\mathscr{d}}}{}_{i_{\mathscr{d}}}\tilde{\mathfrak{w}}_{(\mathscr{d})\,j_1\ldots j_{\mathscr{d}}}, \tag{7.15}$$

where $\xi_g^{\mathscr{d}} = +1$ for unitary transformations and $\xi_g^{\mathscr{d}} = (-1)^{\frac{\mathscr{d}+1}{2}}$ for anti-unitary transformations. The constraint equation (7.15) is sufficient for the determination of the number of independent winding numbers. However, for completeness let us state the transformation behavior of the winding number tensor itself. This is achieved by using the identity given in [7, 70], which we denote as the **Bzdušek identity**:

$$\begin{aligned}\frac{1}{(D-\mathscr{d})!\mathscr{d}!}\epsilon^{i_1\cdots i_{D-\mathscr{d}}k_{D-(\mathscr{d}-1)}\cdots k_D}\epsilon_{j_1\cdots j_{D-\mathscr{d}}l_{D-(\mathscr{d}-1)}\cdots l_D}(M_g)^{j_1}{}_{i_1}\,\cdots\,(M_g)^{j_{D-\mathscr{d}}}{}_{i_{D-\mathscr{d}}}\alpha^{l_{D-(\mathscr{d}-1)}\cdots l_D}&\\ = \det(M_g)({M_g}^{-1})^{k_{D-(\mathscr{d}-1)}}{}_{i_{D-(\mathscr{d}-1)}}\,\cdots\,({M_g}^{-1})^{j_D}{}_{i_D}\alpha^{l_{D-(\mathscr{d}-1)}\cdots l_D}&.\end{aligned} \tag{7.16}$$

Therefore, the winding number tensor $\mathfrak{w}_{(\mathscr{d})}^{i_{\mathscr{d}+1}\cdots i_D}$ transforms under a general hyperbolic lattice symmetry g as:

$$\mathfrak{w}_{(\mathscr{d})}^{k_1\cdots k_{D-\mathscr{d}}} = \frac{\xi_g^{\mathscr{d}}}{(D-\mathscr{d})!\mathscr{d}!}\epsilon^{k_1\cdots k_{D-\mathscr{d}}l_{D-(\mathscr{d}-1)}\cdots l_D}\epsilon_{i_1\cdots i_{D-\mathscr{d}}l_{D-(\mathscr{d}-1)}\cdots l_D}(M_g)_{j_1}{}^{i_1}\cdots(M_g)_{j_{D-\mathscr{d}}}{}^{i_{D-\mathscr{d}}}\mathfrak{w}_{(\mathscr{d})}^{j_1\cdots j_{D-\mathscr{d}}}. \tag{7.17}$$

We conclude this rather technical section by summarizing the properties in $\mathscr{d} = 1, 3$.

For $\mathscr{d} = 1$:

$$\boxed{\begin{aligned}\mathfrak{w}_{(1)}^{i_2\cdots i_D} &= i\frac{\epsilon^{i_1\cdots i_D}}{(2\pi)^D}\int_{\mathbb{T}^D}\mathrm{d}^Dk\,\mathrm{Tr}[H^{-1}(\mathbf{k})(\partial_{i_1}H(\mathbf{k}))]\,,\\ \tilde{\mathfrak{w}}_{(1)\,i} &= \xi_g^1\det(M_g)\,(M_g)^j{}_i\tilde{\mathfrak{w}}_{(1)\,j}\quad\text{where}\quad\mathfrak{w}_{(1)}^{i_2\cdots i_D} = \epsilon^{i_1\cdots i_D}\tilde{\mathfrak{w}}_{(1)\,i_1}.\end{aligned}} \qquad \begin{aligned}(7.18)\\(7.19)\end{aligned}$$

For $\mathscr{d} = 3$:

$$\boxed{\begin{aligned}\mathfrak{w}_{(3)}^{i_4\cdots i_D} &= \frac{\epsilon^{i_1\cdots i_D}}{3!(2\pi)^{D-1}}\int_{\mathbb{T}^D}\mathrm{d}^Dk\,\mathrm{Tr}[H^{-1}(\mathbf{k})(\partial_{i_1}H(\mathbf{k}))H^{-1}(\mathbf{k})(\partial_{i_2}H(\mathbf{k}))H^{-1}(\mathbf{k})(\partial_{i_3}H(\mathbf{k}))]\,,\\ \tilde{\mathfrak{w}}_{(3)\,i_1,i_2,i_3} &= \det(M_g)\,(M_g)^{j_1}{}_{i_1}\,(M_g)^{j_2}{}_{i_2}\,(M_g)^{j_3}{}_{i_3}\tilde{\mathfrak{w}}_{(3)\,j_1,j_2,j_3}\,,\\ &\text{where}\quad\mathfrak{w}_{(3)}^{i_4\cdots i_D} = \epsilon^{i_1\cdots i_D}\tilde{\mathfrak{w}}_{(3)\,i_1,i_2,i_3}\,.\end{aligned}} \qquad \begin{aligned}(7.20)\\ \\(7.21)\end{aligned}$$

Note that in this case $\xi_g^3 = +1$ for unitary and anti-unitary symmetry g alike.

7.3 Chern numbers revisited

In the previous section we have established constraint equations under hyperbolic lattice symmetries for winding numbers by applying the methodology used by A. Chen et al. Ref. [7]. They conducted general hyperbolic lattice symmetry considerations in order to find constrained equations for 1st and 2nd Chern numbers on primitive cells of a selection of $\{p,q\}$-lattices. In this section we will review the general description of 1st and 2nd Chern numbers on hyperbolic lattices and state how they are constraint by hyperbolic lattice symmetries, by reviewing aspects of Ref. [7]. We will extend their study of independent Chern numbers on the primitive cell to m'th-supercells in section 8.2 by reconsidering the $\{6,4\}$ and $\{8,3\}$ Haldane models of section 5.2.

In order to use the first and second Chern numbers for the characterization of topological phases in hyperbolic lattice models, we need to reconsider how they are defined on Brillouin zone tori $\mathbb{T}^{2\mathfrak{g}}$ with genus $\mathfrak{g} > 1$ of the compactified supercells. Consider a hyperbolic $\{p,q\}$-lattice on a $\mathrm{T}\mathfrak{g}.n$ supercell with corresponding BZ torus $\mathbb{T}^{2\mathfrak{g}}$. We can adapt the momentum-space first Chern number by defining the first Chern number on each two dimensional subtorus of the BZ torus $\mathbb{T}^{2\mathfrak{g}}$. Each subtorus is spanned by two pairwise distinct momenta (k^i, k^j) with $i \neq j$ and $k^i, k^j \in \mathbb{T}^{2\mathfrak{g}}$. The collection of these Chern numbers C_{ij} forms an anti-symmetric $2\mathfrak{g} \times 2\mathfrak{g}$ matrix $C_{(1)}$. As such, for non-degenerate energy bands, the b'th band first Chern number C^b_{ij} is defined as:

$$C^b_{(1),ij} = \frac{1}{2\pi i} \int_{\mathbb{T}^2} d^2k \, F^b_{ij}(\mathbf{k}). \tag{7.22}$$

The Berry curvature is given by $F^b_{ij}(\mathbf{k}) = \partial_i A^b_j(\mathbf{k}) - \partial_j A^b_i(\mathbf{k})$ and Berry connections given by $A^b_i(\mathbf{k}) = \langle b(\mathbf{k})|\partial_i|b(\mathbf{k})\rangle$. Each Berry connection is constructed by eigenstates in the b'th band $|b(\mathbf{k})\rangle$ with momenta $k^i \in \mathbb{T}^{2\mathfrak{g}}$. The anti-symmetric property of $C_{(1)}$ is inherited from the Berry curvature. Further, the total first Chern number for a multiplet of n filled bands $\Psi(\mathbf{k}) = \big(|1(\mathbf{k})\rangle, |2(\mathbf{k})\rangle, ..., |n(\mathbf{k})\rangle\big)$ is:

$$C^\Psi_{(1),ij} = \frac{1}{2\pi i} \sum_{b=1}^{n} \int_{\mathbb{T}^2} d^2k \, F^b_{ij}(\mathbf{k}). \tag{7.23}$$

If the system exhibits degenerate energy bands, as we have seen in subsection 5.3.1, the Chern numbers need to be adapted accordingly, analogous to Eq. (5.33). Thus:

$$C^\Psi_{(1),ij} = \frac{1}{2\pi i} \int_{\mathbb{T}^2} d^2k \, \mathrm{Tr}[F^\Psi_{ij}(\mathbf{k})], \tag{7.24}$$

where the Berry connection is replaced by the BWZ connection $(A^\Psi_i(\mathbf{k}))^{ab} = \langle a(\mathbf{k})|\partial_i|b(\mathbf{k})\rangle$ and $F^b_{ij}(\mathbf{k})$ is replaced by the BWZ curvature $F^\Psi_{ij}(\mathbf{k}) = \partial_i A^\Psi_j(\mathbf{k}) - \partial_j A^\Psi_i(\mathbf{k}) + i[A^\Psi_i(\mathbf{k}), A^\Psi_j(\mathbf{k})]$.

The second Chern numbers, closely related to first Chern numbers, are topological invariants in defined on four-dimensional BZ tori [53, 54]. We will refrain from giving a further description of these invariants, instead we will only state how they are constraint by symmetry. Using the notions reviewed in Section 7.1 together with the aspects of differential geometry used in Section 7.2, A. Chen et al. [7] conclude that a general symmetry transformation $g \in \Delta(2, q, p)$ of the hyperbolic $\{p, q\}$-lattice constrain the momentum-space 1st Chern numbers as:

$$C_{(1)\,ij} = \zeta_g (M_g)^k{}_i (M_g)^l{}_j \, C_{(1)\,kl}, \tag{7.25}$$

where $\zeta_g = +1$ if g is a unitary transformation, $\zeta_g = -1$ if g is a anti-unitary transformation, and the 2nd Chern numbers are constraint as:

$$C_{(2)\,i_1 i_2 i_3 i_4} = (M_g)^{j_1}{}_{i_1} (M_g)^{j_2}{}_{i_2} (M_g)^{j_3}{}_{i_3} (M_g)^{j_4}{}_{i_4} \, C_{(2)\,j_1 j_2 j_3 j_4}, \tag{7.26}$$

where M_g are the point-group matrices defined in Section 7.1.

8 Topological band theory of hyperbolic supercells

The various aspects of hyperbolic lattices we have studied so far can now be tied together. In this chapter, the hyperbolic lattice symmetry considerations of chapter 7 will be used on models we have already considered. In Section 8.1 we reconsider the Hatono-Nelson models of sections 6.2 and 6.3 and determine the set of hyperbolic lattice symmetries which leave them invariant. The set of symmetries will be used to explicitly calculate how many winding numbers are left unconstraint. Similarly, in Section 8.2 we reconsider the Haldane models of Section 5.2 and we explicitly calculate how many 1st and 2nd Chern numbers are left unconstraint. At last, in Section 8.3 we return to the very first model we have considered in Section 4.2.1, where we will study the scaling behavior at band edges in the DOS for sequences of supercells.

8.1 Hatano-Nelson model revisited

The hyperbolic lattice symmetry considerations of the previous chapter have revealed constraints imposed on the number of independent winding numbers. In this section we count the number of independent winding numbers for $\mathscr{d} = 1, 3$ by applying the constraints in Eq. (7.18) and (7.20), derived in Section 7.2. To this end, we reconsider the variants of the Hatano-Nelson models from sections 6.2 and 6.3, which are invariant under the action of some hyperbolic lattice symmetries $g \in \Delta$.

Consider the C_3 rotation symmetric $\{6, 4\}$ and the C_4 rotation symmetric $\{8, 4\}$ Hatano-Nelson model with asymmetric hopping amplitudes $(t + \gamma)$ in the counterclockwise and $(t - \gamma)$ in the clockwise direction, shown in Fig. 38 and left Fig. 42, respectively. These systems are invariant under hyperbolic lattice symmetries generated by:

$$I_c = \{\mathrm{a}\mathcal{T}, \mathrm{b}, \mathrm{z}^2\}\,, \tag{8.1}$$

see Fig. 2 for a reference of the symmetry operations. The right action of the reflection a amounts to a sign change of the coupling constants $(t \pm \gamma) \to (t \mp \gamma)$. The original configurations are restored by time reversal. Thus, the composite action of time reversal and reflection $\mathrm{a}\mathcal{T}$ leave the systems invariant. The C_3 and C_4 symmetry imply an invariance under the rotation symmetry z^2.

The parallel $\{8, 4\}$ Hatano-Nelson model with alternating asymmetric hopping amplitudes $(t \pm \gamma)$, shown in the right Fig. 42, is invariant under C_2 rotation symmetry. Due to the alternating asymmetric hopping amplitudes the invariance under C_4 symmetry of the previous $\{8, 4\}$ Hatano-Nelson model is explicitly broken, with a remaining C_2 invariance. The action of z^2 leads to a sign change in the coupling constants $(t \pm \gamma) \to (t \mp \gamma)$, which can be restored by time reversal. As such, the composite action $\mathrm{z}^2\mathcal{T}$ leaves the system invariant. Therefore, the system is left invariant under the hyperbolic lattice symmetries:

$$I_a = \{\mathrm{a}\mathcal{T}, \mathrm{b}, \mathrm{z}^2\mathcal{T}\}\,. \tag{8.2}$$

Further, the application of Eq. (7.18) and (7.20) necessitate the construction of the point-group matrices M_g defined in Section 7.1, with symmetries $g \in I_c, I_a$. Recall, the point-group matrices are representations of the point groups $G^{(m)}$. Each point group is isomorphic to a corresponding quotient group $\Delta/\Gamma^{(m)}$, labeled as T$\mathfrak{g}$.n. We consider quotient groups T$\mathfrak{g}$.n up to genus 11 and construct the corresponding point-group matrices, through the GAP implementation discussed in Appendix 10.3.

Crucially, the $\{6,4\}$ and $\{8,4\}$ Hatano-Nelson models of Sections 6.2 and 6.3 are not necessarily compatible with general supercell sequences, similar to the incompatibility of our $\{8,4\}$ Hatano-Nelson models on the T2.3 primitive cell. We will highlight the sequences that we have checked for compatibility with our models. Our analysis considers general non-Hermitian models exhibiting point gaps that are invariant under the set of hyperbolic lattice symmetries I_c or I_a. We denote the number of independent winding number components which are constraint by the symmetries I_c as $\#\tilde{\mathfrak{w}}^c_{(1)}$, $\#\tilde{\mathfrak{w}}^c_{(3)}$ and those that are constraint by I_a as $\#\tilde{\mathfrak{w}}^a_{(1)}$, $\#\tilde{\mathfrak{w}}^a_{(3)}$. They are tabulated in Table 3.

$\Delta^+/\Gamma^{(m)}(2,4,6)$	$\#\tilde{\mathfrak{w}}^c_{(1)}$	$\#\tilde{\mathfrak{w}}^c_{(3)}$
T2.2	0	0
T3.4	0	2
T4.3	0	0
T5.4	0	3
T6.2	0	13
T9.3	0	7
T9.4	1	19
T10.8	0	12
T10.9	0	26
T11.1	0	36

$\Delta^+/\Gamma^{(m)}(2,4,8)$	$\#\tilde{\mathfrak{w}}^c_{(1)}$	$\#\tilde{\mathfrak{w}}^c_{(3)}$
T2.3	0	0
T3.5	0	2
T3.6	0	1
T5.5	0	1
T5.6	0	3
T9.5	0	13
T9.6	0	11
T9.7	0	12
T9.8	0	16

$\Delta^+/\Gamma^{(m)}(2,4,8)$	$\#\tilde{\mathfrak{w}}^a_{(1)}$	$\#\tilde{\mathfrak{w}}^a_{(3)}$
T2.3	1	0
T3.5	0	4
T3.6	1	2
T5.5	1	6
T5.6	1	6
T9.5	1	26
T9.6	1	26
T9.7	2	28
T9.8	0	32

Table 3: **Number of independent winding number components in $\mathscr{d} = 1, 3$.** $\#\tilde{\mathfrak{w}}^c_{(1)}$, $\#\tilde{\mathfrak{w}}^c_{(3)}$ are constrained by hyperbolic lattice symmetries $g \in \{\mathrm{a}\mathcal{T}, \mathrm{b}, \mathrm{z}^2\}$ and $\#\tilde{\mathfrak{w}}^a_{(1)}$, $\#\tilde{\mathfrak{w}}^a_{(3)}$ are constrained by $g \in \{\mathrm{a}\mathcal{T}, \mathrm{b}, \mathrm{z}^2\mathcal{T}\}$. Rows that are highlighted in gray are compatible with the $\{6,4\}$ and $\{8,4\}$ Hatano-Nelson models of sections 6.2 and 6.3.

The gray rows in Table 3 correspond to a sequence of supercells compatible with the Hatano-Nelson models in Section 6.2 or 6.3. Further, we see that if we follow an appropriate sequence of supercells, under the condition in Eq. (3.48), the number of independent winding number components are monotonically increasing. In fact, we have observed this trend for any sequence of supercells we have considered. Further, in the subsequent section, where we count the number of independent first and second Chern numbers constraint by hyperbolic lattice symmetries, such a trend is also observed.

8.2 Haldane model revisited

We have seen in Section 7.3 that hyperbolic lattice symmetries constrain the number of independent momentum-space Chern numbers. In this section we will explicitly calculate how many 1st and 2nd Chern are left unconstraint when considering sequences of supercells with Abelian hyperbolic band theory. The symmetries that we will consider will be dictated by the underlying model on a given $\{p, q\}$-lattice. Let us return to the $\{p, q\}$ Haldane models considered in Ref. [7], with a particular focus on the $\{6, 4\}$ and $\{8, 3\}$-lattices. The analysis for the $\{7, 3\}, \{8, 4\}, \{10, 5\}\{12, 3\}$ and $\{12, 4\}$-lattices, considered in Ref. [7], are discussed in the Appendices 10.5, 10.6 and 10.7.

Analogous to our hyperbolic lattice symmetry considerations of the winding number components, we proceed with determining the set of symmetries that leave the $\{6, 4\}$ and $\{8, 3\}$ Haldane-models invariant, which comprise two cases. Consider Fig. 19, in the absence of the staggered on-site potential $m = 0$, the systems are left invariant under the action of hyperbolic lattice symmetries:

$$I_{m=0} = \{\mathrm{a}\mathcal{T}, \mathrm{b}\mathcal{T}, \mathrm{c}\mathcal{T}\}\,, \tag{8.3}$$

see Fig. 2 for a reference of the symmetry operations. The lattices are threaded by local magnetic fluxes $\pm\phi$ such that the next-nearest-neighbor hopping amplitudes acquire a phase $t_2 e^{\pm i\phi}$ through the Peierls substitution. Under the action of a reflection symmetry $g \in \{\mathrm{a,b,c}\}$ the sign of the NNN-hopping terms are flipped $t_2 e^{\pm i\phi} \to t_2 e^{\mp i\phi}$. The original configurations can be restored by time reversal. Thus, under the action of reflection symmetries composed with time reversal the systems are left invariant, resulting in a particular type of magnetic [28] hyperbolic space group. In contrast, in the presence of a non-zero staggered on-site potential $m \neq 0$, the C_6 rotation symmetry of the $\{6, 4\}$ Haldane-model and the C_8 rotation symmetry of the $\{8, 3\}$ Haldane-model are explicitly broken, leaving behind only C_3 and C_4 symmetries, respectively. This implies that the systems are no longer invariant under the action of $\mathrm{a}\mathcal{T}$, which interchanges the sublattices A and B. The remaining symmetries C_3 and C_4 imply an invariance under the action of the rotation z^2 instead. Therefore, the systems are left invariant under the action of symmetries:

$$I_{m\neq0} = \{\mathrm{z}^2, \mathrm{b}\mathcal{T}, \mathrm{c}\mathcal{T}\}. \tag{8.4}$$

In order to apply the constraints of Eq. (7.25) and (7.26), we construct the point-group matrices M_g described in Sections 7.1 and 10.3, for the corresponding quotient groups $\mathrm{T}\mathfrak{g}.n$ up to genus $\mathfrak{g} < 50$ and symmetries $g \in I_{m=0}, I_{m\neq0}$. The number of independent 1st and 2nd Chern numbers which are constrained by the symmetries in the set $I_{m=0}$ are denoted as $\#C^{(1)}_{m=0}$, $\#C^{(2)}_{m=0}$ and those that are constrained by $I_{m\neq0}$ are denoted $\#C^{(1)}_{m\neq0}\#C^{(2)}_{m=0}$, respectively.

The number of independent first Chern numbers are shown in the subgroup tree graphs in Fig. 43 and Fig. 44. Note that Fig. 43 is an extension of Fig. 6. As such, recall that each vertex in the graph corresponds to a normal subgroup $\Gamma^{(m)} \triangleleft \Delta$ labeled by its corresponding quotient group $\mathrm{T}\mathfrak{g}.n$, with directed edges indicating a normal subgroup relation. Vertices highlighted in red indicate that a corresponding supercell can be constructed by symmetrically aggregating primitive cells.

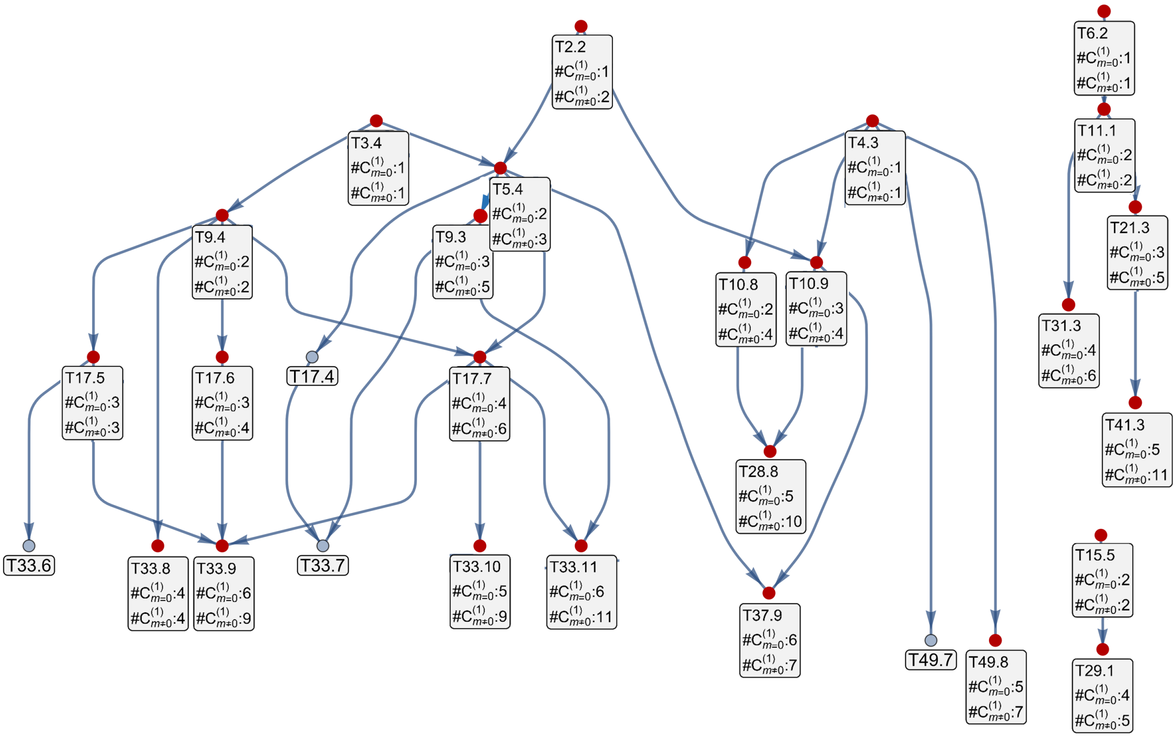

Figure 43: **Number of independent momentum-space 1st Chern numbers** $\#C^{(1)}_{m=0}$, $\#C^{(1)}_{m\neq0}$ **in normal subgroup tree graph for the** $\{6,4\}$ **Haldane model**.

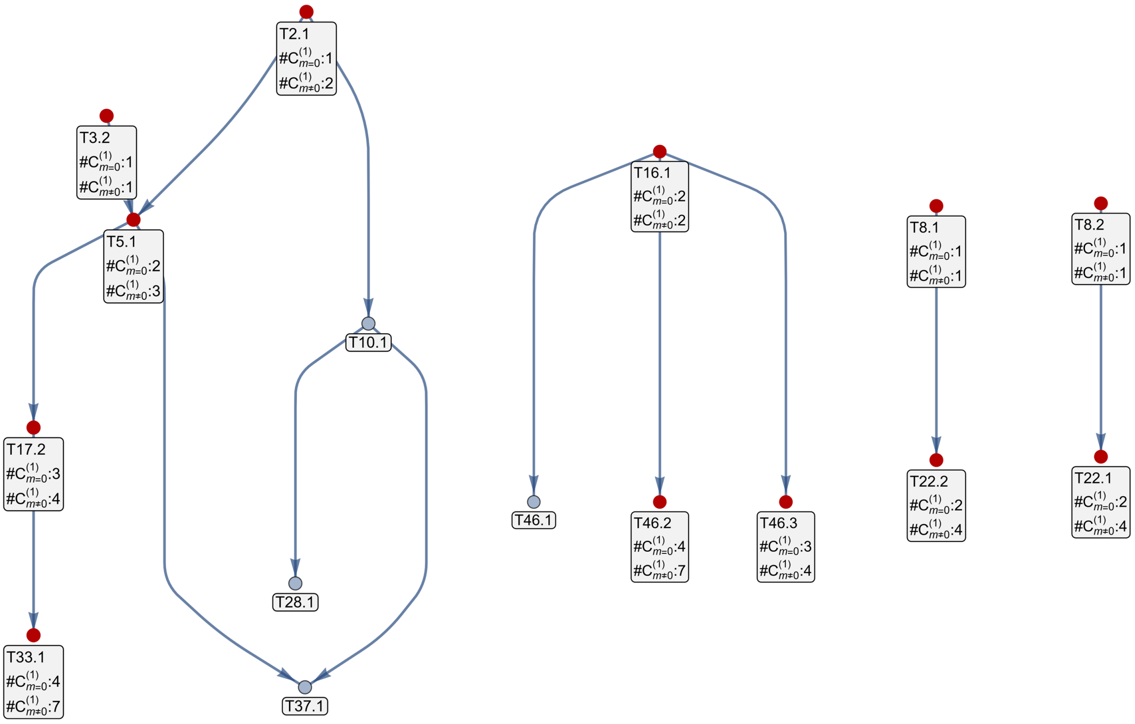

Figure 44: **Number of independent momentum-space 1st Chern numbers** $\#C^{(1)}_{m=0}$, $\#C^{(1)}_{m\neq0}$ **in normal subgroup tree graph for the** $\{8,3\}$ **Haldane model**.

The numbers of independent first Chern numbers for $\{6,4\}$ and $\{8,3\}$ Haldane-model on the primitive cell T2.2 and T2.1, respectively, are in agreement with the results in Ref. [7]. Further, following any of the supercell sequences in Fig. 43 and Fig. 44 shows that $\#C^{(1)}_{m=0}$, $\#C^{(1)}_{m\neq0}$ are monotonically increasing, which is further emphasized in Fig. 45 and Fig. 46.

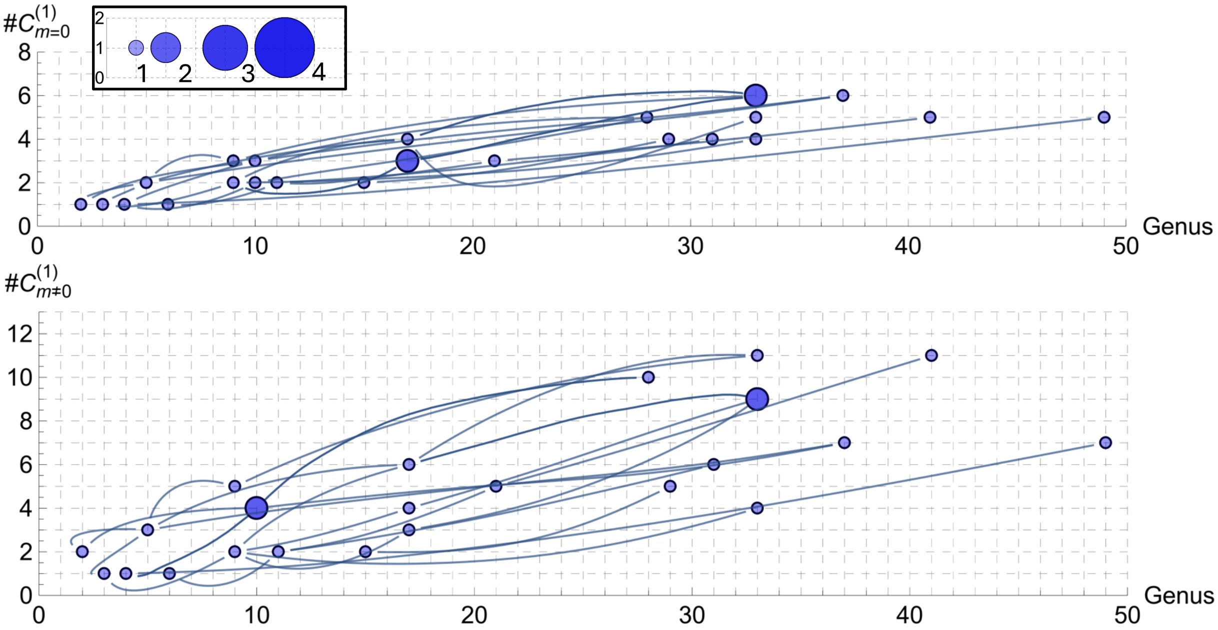

Figure 45: **Evolution of the number of momentum-space 1st Chern numbers for increasingly large supercells on the $\{6,4\}$ Haldane model.** $\#C^{(1)}_{m=0}$, $\#C^{(1)}_{m\neq0}$ plotted against genus $\mathfrak{g}$ of corresponding compactified supercell T$\mathfrak{g}.n$. The radius of each disk is proportional to the number of overlapping points, shown in the inset. Lines connecting pairs of points indicate supercells obeying a group-subgroup relation.

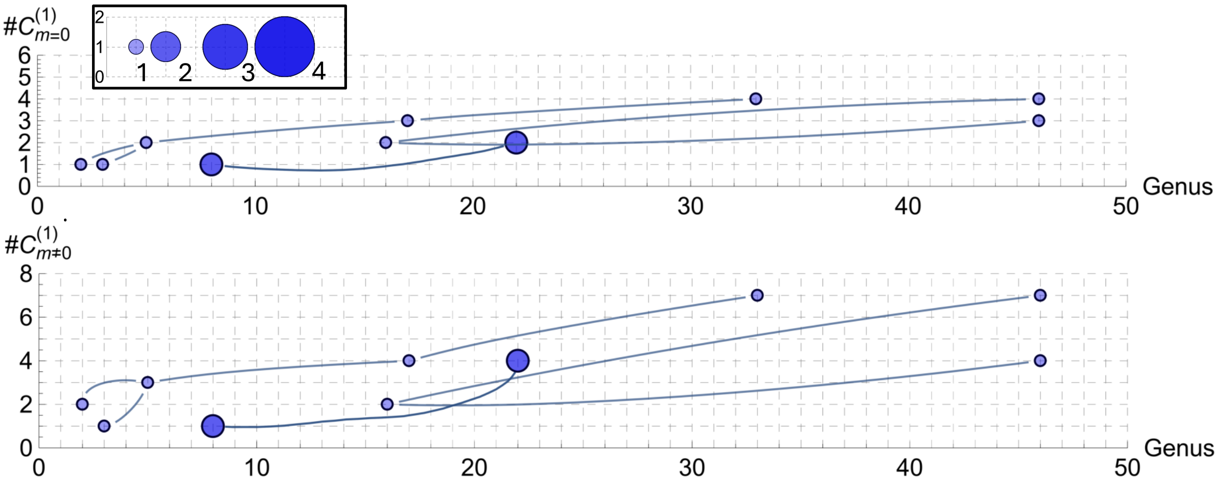

Figure 46: **Evolution of the number of momentum-space 1st Chern numbers for increasingly large supercells on the $\{8,3\}$ Haldane model.** $\#C^{(1)}_{m=0}$, $\#C^{(1)}_{m\neq0}$ plotted against genus $\mathfrak{g}$ of corresponding compactified supercell T$\mathfrak{g}.n$. The radius of each disk is proportional to the number of overlapping points, shown in the inset. Lines connecting pairs of points indicate supercells obeying a group-subgroup relation.

The increasing numbers of independent first Chern numbers in Fig. 45 and Fig. 46 are plotted against the genus $\mathfrak{g}$ of a corresponding compactified supercell $\mathrm{T}\mathfrak{g}.n$, where sequences of supercells are indicated with blue lines. The physical interpretation for the existence of multiple independent momentum-space first Chern numbers and the correspondence between momentum-space and real-space first Chern numbers in two dimensional hyperbolic lattices are currently unknown. In the Haldane models on the primitive cell that were considered in [7], the momentum-space and real-space first Chern numbers were observed to agree if only one independent momentum-space first Chern remains, such as $\{6,4\}$ and $\{8,3\}$ Haldane models on the primitive cell T2.2 and T2.1, respectively. As such, further examinations of the number of independent momentum-space first Chern on higher-dimensional BZ tori are needed.

Further, the number of independent second Chern numbers that are constraint by Eq. (7.26) for sequences of supercells $\mathrm{T}\mathfrak{g}.n$ up to genus $\mathfrak{g} < 10$ are tabulated in Table 4.

$\Delta^+/\Gamma^{(m)}(2,4,6)$	$\#C^{(2)}_{m=0}$	$\#C^{(2)}_{m\neq 0}$
T2.2	1	1
T3.4	1	1
T4.3	2	4
T5.4	3	5
T6.2	3	3
T9.3	15	26
T9.4	9	22

$\Delta^+/\Gamma^{(m)}(2,3,8)$	$\#C^{(2)}_{m=0}$	$\#C^{(2)}_{m\neq 0}$
T2.1	1	1
T3.2	1	1
T5.1	3	4
T8.1	4	7
T8.2	4	8

Table 4: **Number of independent 2nd Chern numbers fo compactified supercells up to genus $\mathfrak{g}$** < 10, in the $\{6,4\}$ and $\{8,3\}$ Haldane models, left and right, respectively.

The numbers of independent second Chern numbers for $\{6,4\}$ and $\{8,3\}$ Haldane-model on the primitive cell T2.2 and T2.1, respectively, are in agreement with the results in Ref. [7]. Similar to our consideration of the first Chern numbers, the number of independent second Chern numbers for any sequence of supercells is monotonically increasing.

8.3 Scaling at the band edge

P. M. Lenggenhager et al. [3] have demonstrated that the density of states for increasingly large supercells is in agreement with the continued fraction method used by R. Mosseri et al. [33]. In particular, they observe a strong suppression of the density of states near the band edges. Under the assumption of a generic quadratic scaling of the energy near a band edge as $E \propto \mathbf{k}^2$, where $\mathbf{k} \in \mathbb{T}^{2\mathfrak{g}}$ the density of states scales as $\rho(E) \propto E^{\mathfrak{g}-1}$, which was observed in the models they considered [3].

We are interested in the scaling behavior in the vicinity of the band edge where states start to overcome this suppression. To this end, we reconsider the nearest-neighbor tight-binding model of Section 4.2.1 for the $\{8,3\}$-lattice. A limiting case for hyperbolic $\{p,3\}$-lattices, called the **Bethe lattice** with $p = \infty$ [71], is well known. Its density of states is given by, [33, 72]:

$$\rho^{\{\infty,3\}}(E) = \frac{3}{2\pi}\frac{\sqrt{8-E^2}}{9-E^2}, \tag{8.5}$$

where $E_\pm = \pm 2\sqrt{2}$, which we will refer to as **band edge energies**. Thus, the density of states in the vicinity of the band edge for the Bethe lattice scales as:

$$\rho^{\{\infty,3\}}(E) \simeq \frac{3\sqrt[4]{2}}{\pi}\sqrt{|E_\pm| \mp E} + \mathcal{O}(E_\pm + E). \tag{8.6}$$

Such a square-root behavior is also well known to occur for non-interacting electron gases in three dimensional Euclidean space [73]. In contrast, two-dimensional Euclidean lattices exhibit a step edge in the DOS, which corresponds to a critical exponent 0. Before we proceed our study of the scaling behavior on the $\{8,3\}$-lattice using the supercell method, recall that we consider sequences of normal subgroups given by:

$$\Delta^+ \triangleright \Gamma^{(1)} \triangleright \Gamma^{(2)} \dots \triangleright \Gamma^{(m)} \triangleright \dots,$$

with $\Gamma^{(m)} \triangleleft \Delta^+$, see Section 3.5. These normal subgroups are constructed by using tabulated quotient groups in [39]. In this section we consider a sequence of normal subgroups of $\Delta^+(2,3,8)$ that branches off into two parts specified by quotient groups T2.1, T5.1, T17.2 branching off to T33.1 and T65.1, with corresponding normal subgroups $\Gamma_{\mathrm{T65.1}} \ntriangleleft \Gamma_{\mathrm{T33.1}}$. It remains to be shown that different sequences of normal subgroups converge to the same limit. However, an apparent convergence of the DOS for the $\{8,3\}$-lattice for two distinct supercell sequences was demonstrated in [3].

The corresponding density of states and subgroup tree graph are depicted in Fig. 47. The density of states, depicted on the left, computed via exact diagonalization with $5 \cdot 10^5$ randomly sampled points in the BZ tori $\mathbb{T}^{2\mathfrak{g}}$ is shown in a histogram with energy binwidth 0.001.

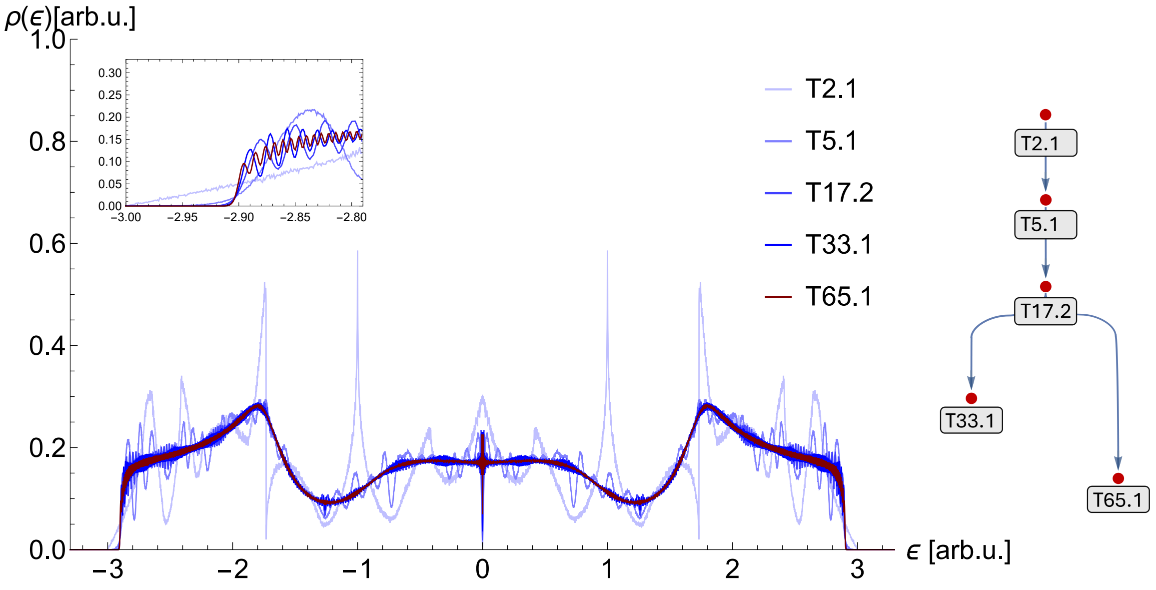

Figure 47: **Density of states for nearest-neighbor tight-binding model on $\{8,3\}$-lattice together with the corresponding subgroup tree graph**. Left: Density of states in a histogram of energy binwidth 0.001, computed via exact diagonalization with $5 \cdot 10^5$ randomly sampled points in the BZ tori $\mathbb{T}^{2\mathfrak{g}}$. The inset, shown in the upper left corner, depicts the DOS in the vicinity of the band edge. Right: Tree graph of the corresponding quotient groups $\mathrm{T2.1}, \mathrm{T5.1}, \mathrm{T17.2}$ branching off to T33.1 and T65.1.

We estimate the band edge energy by determining the intersection of the set of density of states near the band edge $E_- \approx -2.9035$, which is close to the calculated band edge energy in the thermodynamic limit using the continued fraction method $E_- = -2.9048$ [33]. We proceed by performing a non-linear fit of the function:

$$f(E|a,b) = a\,(E - E_-)^b\,\theta(E - E_-) \tag{8.7}$$

where $\theta(E)$ is the Heaviside function and a, b the parameters to be estimated. To do so, we use the Mathematica function **NonlinearModelFit** via **NMinimize** and **differential evolution** method, [74]. The corresponding best fits are depicted in Fig. 48 and 49.

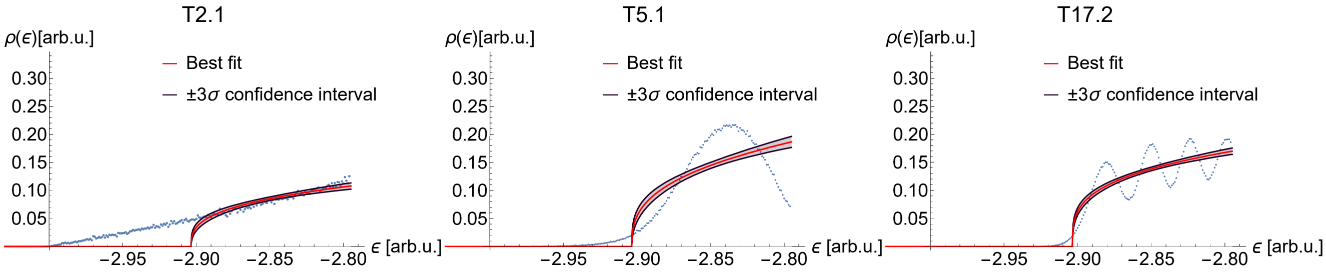

Figure 48: **Non-linear model fits at a band edge of the DOS** in the $\{\mathbf{8},\mathbf{3}\}$ nearest-neighbor tight-binding model for primitive cell T2.1 and supercells $\mathrm{T5.1}, \mathrm{T17.2}$. The red lines correspond to the best fit enveloped by confidence interval of $\pm 3\sigma$, fitted in an energy interval $[-3.499, -2.800]$.

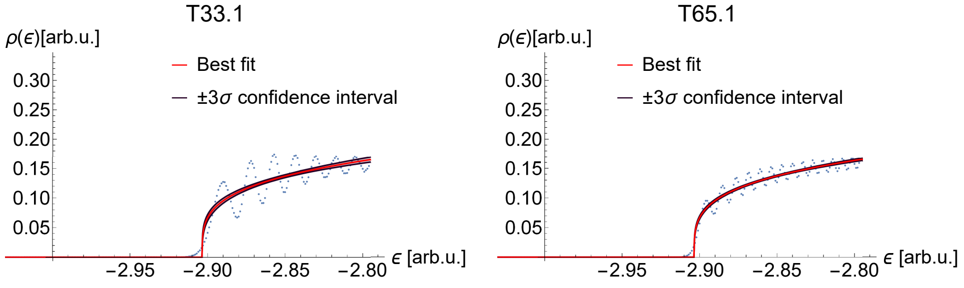

Figure 49: **Non-linear model fits at a band edge of the DOS** in the $\{\mathbf{8},\mathbf{3}\}$ nearest-neighbor tight-binding model for supercells T33.1, T65.1. The red lines correspond to the best fit enveloped by confidence interval of $\pm 3\sigma$, fitted in an energy interval $[-3.499, -2.800]$.

The evolution of the estimated parameters for increasingly large supercells are shown in Fig. 50 and the tabulated values can be found in Table 5. The estimated amplitudes a are shown on the left, seemingly converging to ~ 0.30. The estimated exponents b, shown on the right, seem to converge to ~ 0.27.

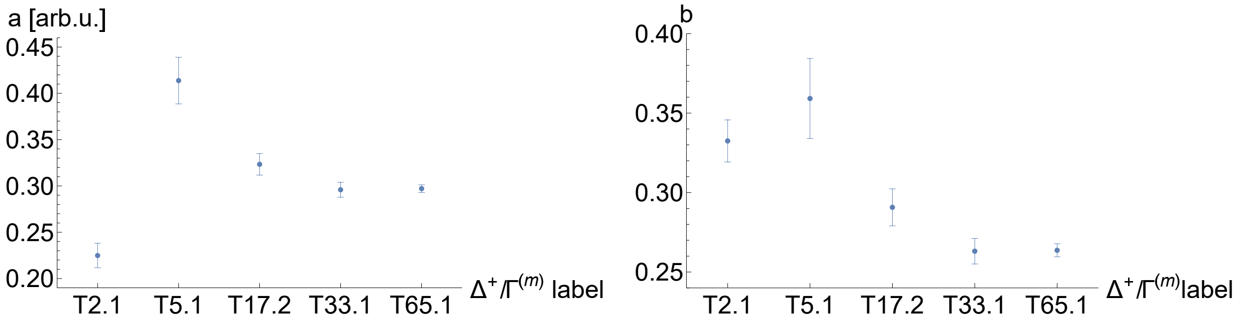

Figure 50: **Estimated parameters of non-linear model fits at the band edge of the DOS** in the $\{\mathbf{8},\mathbf{3}\}$ nearest-neighbor tight-binding model. The estimate parameters together with the standard error SE. The horizontal axis indicates the corresponding supercell.

$\Delta^+/\Gamma^{(m)}$	T2.1		T5.1		T17.2		T33.1		T65.1	
Parameter	Estimate	SE	Estimate	SE	Estimate	SE	Estimate	SE	Estimate	SE
a	0.225	0.013	0.414	0.025	0.323	0.012	0.296	0.008	0.297	0.004
b	0.332	0.020	0.359	0.021	0.291	0.012	0.263	0.009	0.264	0.005

Table 5: **Estimated parameters for the $\{8,3\}$ nearest-neighbor tight-binding model**, where SE is the standard error.

9 Summary and conclusion

In this master thesis we have applied the supercell method [3] to study various aspects of topology and band theory in a selection of hyperbolic $\{p, q\}$-lattices. We have started our endeavor by reviewing the description of lattices in the Euclidean plane in chapter 2. The group theoretical considerations provided an intuitive and natural language for a comprehensive understanding of key concepts, such as space groups and translation groups. This enabled us to understand the bulk description of models in Euclidean lattices through the Bloch theorem via the aggregation of PBC clusters.

Equipped with the basic tools provided in chapter 2, we have built an elementary understanding of hyperbolic lattices in chapter 3. The unprecedented features due to an emergent negative curvature of hyperbolic lattices led us to a review of an adjusted description of band theory, the hyperbolic band theory [18]. Given the recent development of the supercell method [3], we have reviewed how to aggregate primitive cells into supercells in hyperbolic lattices in order to apply Abelian hyperbolic band theory through the supercell method.

In order to comprehend various notions of band theory and topology in models on hyperbolic lattices we have alternated between the study of Euclidean and hyperbolic lattices in the subsequent chapters 4 and 5. Throughout, we have applied the supercell method. In chapter 4, functions of the HyperCells package [2] were used to construct an implementation of hyperbolic Lieb lattices. We have computed the density of states for nearest-neighbor tight-binding models on the $\{6, 4\}$ and $\{8, 3\}$ Lieb lattices in order to calculate the fraction of states within emergent flat-bands. Further, in chapter 5 we've looked at manifestations of conventional topological insulators and higher-order topological insulators. Our analysis demonstrated the appearance of fractional corner charges in a variant of the BBH model on the ruby lattice and fractional charges at a disclination core of finite flakes with disclination defects in the $\{6, 4\}$ BBH model.

The growing interest in non-Hermitian systems has motivated us to study variants of the Hatano-Nelson model on hyperbolic lattices in chapter 6. To this end, we've altered an existing function in the HyperBloch package [1] in order to construct non-Hermitian Abelian Bloch Hamiltonians. Our topological characterization via winding numbers of dimension one and three, revealed a non-trivial phase for a particular $\{8, 4\}$ Hatano-Nelson model with non-vanishing one-dimensional winding numbers. In particular, all three-dimensional winding number were found to be trivial.

In chapter 7 we have reviewed and applied hyperbolic lattice symmetry considerations in order to derive constraint equations for the number of independent winding numbers. Additionally, in preparation for chapter 8, we briefly reviewed the constraint equations for the number of independent 1st and 2nd Chern numbers that were very recently derived in order to study $\{p, q\}$ Haldane models in [7].

Finally, in chapter 8 we tied multiple threads from different chapters together. We have reconsidered the Hatano-Nelson models on a sequence of supercells and determined the set of hyperbolic lattice symmetries which leave them invariant in order to calculate the number of independent winding numbers that are left unconstraint. As such, with our previous calculations of the one-dimensional winding numbers, we were able to illuminate these constraints explicitly. However, such a demonstration was not possible for three-dimensional winding numbers since all were found to be trivial.

Analogous to the hyperbolic lattice symmetry considerations of the Hatano-Nelson models, we calculated the number of independent 1st and 2nd Chern numbers left unconstraint by the symmetries of the $\{p, q\}$ Haldane models surveyed in Ref. [7]. In particular, our calculations for the number of independent momentum-space first Chern numbers included an extensive list of supercell sequences up to compactified unit cells of genus $\mathfrak{g} < 50$. We found that the number of independent 1st and 2nd Chern numbers as well as winding numbers exhibit a monotonically increasing trend for any appropriate sequence of supercells.

In conclusion, the main objectives of this thesis were achieved. Further, we have proposed an addition to the HyperCells package, constituting an implementation of a word simplification function for elements in the groups constructed while applying the functionality of the HyperCells package, based on the Knuth-Bendix completion algorithm in GAP [75]. In tandem with this thesis, we developed an introductory tutorial for the HyperBloch package to facilitate its usage. This will be the first in a series of tutorials for the HyperCells and HyperBloch packages.

10 Appendix:

10.1 Appendix: Open boundary conditions on honeycomb ribbons

The honeycomb lattice can host edge states which are sensitive to a particular termination of the infinite lattice. As such, let us cut the infinite lattice into semi finite ribbons with so-called **Armchair edges** and **Zigzag edges** depicted in Fig. 51 respectively. For each ribbon a unit cell can be defined which ranges across the entire height of the ribbon, indicated with dash-dotted rectangles.

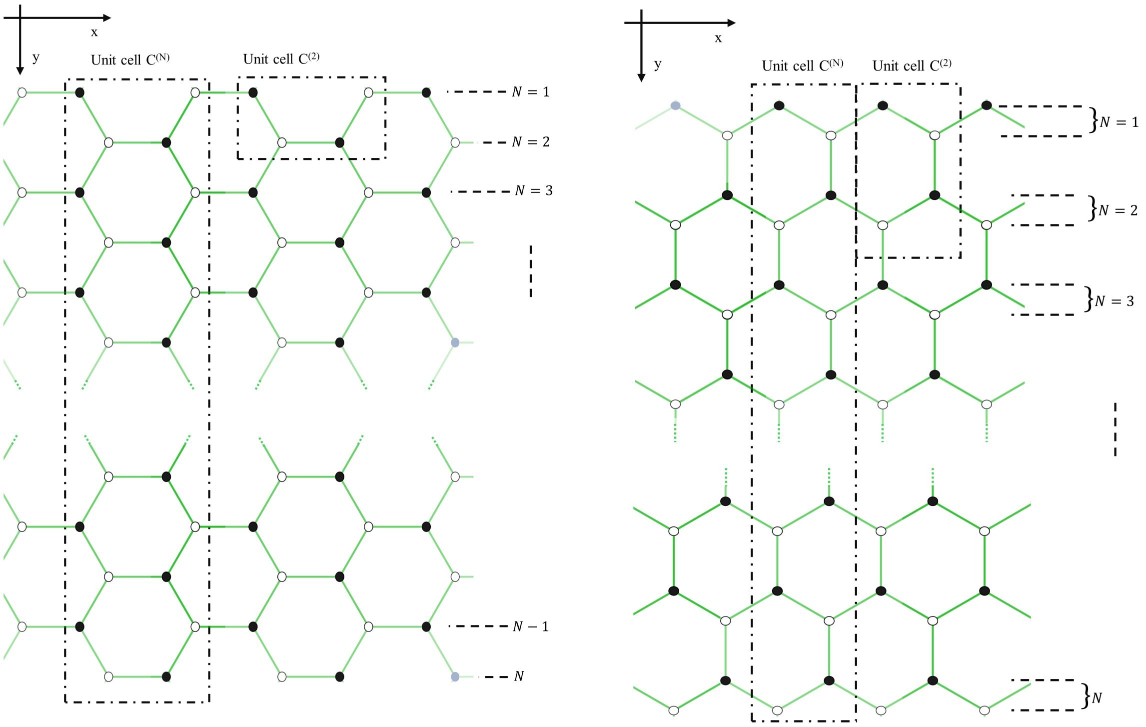

Figure 51: **Honeycomb ribbons**. Left: Honeycomb ribbon with Armchair edges. Right: Honeycomb ribbon with Zigzag edges. Both ribbons are labled by an index N indicating at which **rung** a site is located.

These ribbons can be described by **open boundary conditions** (OBC) on the edges in the y direction and PBCs in the x direction. Let us follow Ref. [76] in order to elaborate the analytic solutions. Let us consider the Armchair edge first. The corresponding Hamiltonian is given by:

$$\mathcal{H}_{N\text{-AC}} = t \sum_{l} \Big(\sum_{j=1}^{N} b^{\dagger}_{j,l+\delta_j} a_{j,l} + \sum_{j=1}^{N-1} (a^{\dagger}_{j+1,l} b_{j,l} + b^{\dagger}_{j+1,l} a_{j,l}) + \text{h.c.} \Big), \tag{10.1}$$

where:

$$\delta_j = \begin{cases} 1 & \text{if } j \text{ is odd} \\ 0 & \text{else} \end{cases} \qquad \delta_j^{-1} = \begin{cases} 0 & \text{if } j \text{ is odd} \\ 1 & \text{else.} \end{cases} \tag{10.2}$$

Taking the thermodynamic limit with imposition of PBCs in the x direction leads to the Hamiltonian given by:

$$\mathcal{H}_{\mathrm{N-AC}} = t\sum_{k_x}\Big(\sum_{j=1}^{N-1}(e^{i\frac{k_x}{2}}a^{\dagger}_{k_x,j+1}b_{k_x,j}+e^{-i\frac{k_x}{2}}a^{\dagger}_{k_x,j}b_{k_x,j+1}+e^{ik_x}a^{\dagger}_{k_x,j}b_{k_x,j})+e^{ik_x}a^{\dagger}_{k_x,N}b_{k_x,N}+\mathrm{h.c.}\Big). \tag{10.3}$$

We will refer to k_x as the longitudinal wavenumber. The eigenvalues can be computed by solving the **Harper equation**. Thus, let us construct the Harper equation by determining the eigenstates of the Hamiltonian. The one-particle field operators are given by:

$$\hat{\Psi}^{\dagger}(k_x) = \sum_{j=1}^{N}(\phi^{\mathrm{A}}_{k_x,j}a^{\dagger}_{k_x,j} + \phi^{\mathrm{B}}_{k_x,j}b^{\dagger}_{k_x,j}), \tag{10.4}$$

where $\phi^{A}_{k_x,j}$, $\phi^{B}_{k_x,j}$ are Bloch states of sublattices A and B respectively, at k_x and rung j. Therefore:

$$\mathcal{H}_{\mathrm{N-AC}}|\Psi(k_x)\rangle = E|\Psi(k_x)\rangle. \tag{10.5}$$

The repeated use of the anti-commutation relation for the fermionic ladder operators $a^{\dagger}_{k_x,j}$ and $b^{\dagger}_{k_x,j}$ and subsequent rearrangement of terms give:

$$\begin{aligned} E\phi^{\mathrm{A}}_{k_x,j} &= -te^{-i\frac{k_x}{2}}(e^{i\frac{3k_x}{2}}\phi^{\mathrm{B}}_{k_x,j} + \phi^{\mathrm{B}}_{k_x,j+1} + \phi^{\mathrm{B}}_{k_x,j-1}),\\ E\phi^{\mathrm{B}}_{k_x,j} &= -te^{i\frac{k_x}{2}}(e^{-i\frac{3k_x}{2}}\phi^{\mathrm{A}}_{k_x,j} + \phi^{\mathrm{A}}_{k_x,j+1} + \phi^{\mathrm{A}}_{k_x,j-1}). \end{aligned} \tag{10.6}$$

We can use the Ansatz:

$$\begin{aligned} \phi^{\mathrm{A}}_{k_x,j} &= A_{k_x}e^{ipj} + B_{k_x}e^{-ipj},\\ \phi^{\mathrm{B}}_{k_x,j} &= C_{k_x}e^{ipj} + D_{k_x}e^{-ipj}. \end{aligned} \tag{10.7}$$

We impose that states beyond the edge, at spurious rows indexed $j = 0$ and $j = N + 1$, vanish, thus $A_{k_x} = -B_{k_x}$, $C_{k_x} = -D_{k_x}$ and:

$$\phi^{\mathrm{A}}_{k_x,N+1} = A_{k_x}(e^{ip(N+1)} - e^{-ip(N+1)}) = 0 \quad\Longrightarrow\quad p = \frac{n}{N+1}\pi, \tag{10.8}$$

where $n = 1, 2, ..., N$, we will refer to p as the transversal wavenumber. We make yet another Ansatz $A_{k_x} = A'e^{-i\frac{k_x}{4}}$ and $C_{k_x} = C'e^{i\frac{k_x}{4}}$. It is sufficient to plug the Ansatz into Eq. (10.6) for $j = 1$, all other solutions for $j > 1$ follow recursively. Thus, we set $j = 1$ and diagonalize the system of equations:

$$E^{\pm}_{k_x,p} = \pm t\sqrt{1 + 4\cos(\frac{3}{2}k_x)\cos(p) + 4\cos^2(p)}. \tag{10.9}$$

Notably, for $k_x = 0$ whenever $p = \frac{2}{3}\pi$, i.e. $N = 3n - 1$, the energy vanishes and the band gap closes. This is apparent in the band structure and density of states as shown in Fig. 52 for $N = 25, 26$.

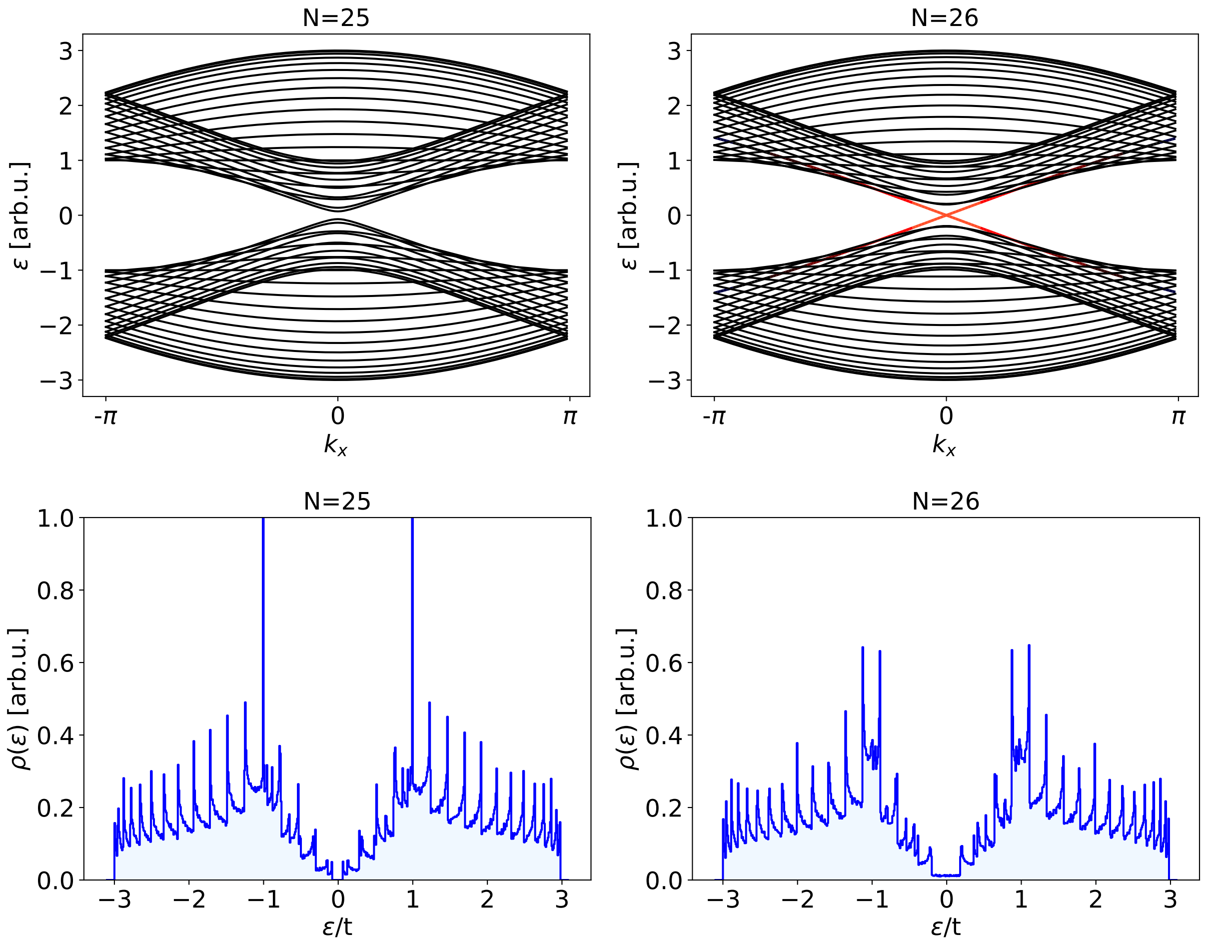

Figure 52: **Example of energy spectra and density of states of Armchair ribbons**. Upper row: The energy spectra of the Armchair ribbon with $N = 25$ and $N = 26$ rungs left and right respectively. The energy gap closes if $p = \frac{2}{3}\pi$, which is the case for $N = 26$ rungs. Note that we have rescaled $k_x \rightarrow \frac{\sqrt{3}}{2}k_x$. Bottom row: The randomly sampled density of states of Armchair ribbon with $N = 25$ and $N = 26$ rungs left and right respectively.

The Bloch eigenstates can be obtained by imposing the normalization condition $\langle \Psi(k_x) \,|\, \Psi(k_x) \rangle = 1$, the solution is given by:

$$\begin{aligned} \phi^{\mathrm{A}}_{k_x,j,\pm} &= \frac{\mp 1}{\sqrt{\mathcal{N}(k_x,p)/t}} \sqrt{e^{i\frac{3k_x}{2}} + 2\cos(p)\, e^{-i\frac{k_x}{4}}} \sin(pj), \\ \phi^{\mathrm{B}}_{k_x,j} &= \frac{1}{\sqrt{\mathcal{N}(k_x,p)/t}} \sqrt{e^{-i\frac{3k_x}{2}} + 2\cos(p)\, e^{i\frac{k_x}{4}}} \sin(pj), \end{aligned} \tag{10.10}$$

where $\mathcal{N}(k_x,p)$ is given by:

$$\mathcal{N}(k_x,p) = (N - \cos((N+1)p)\frac{\sin(Np)}{\sin(p)})|E^{\pm}_{k_x,p}|^2. \tag{10.11}$$

The states indicated in red shown in Fig. 52 are not localized edge states and thus the Armchair ribbon hosts only bulk states. Therefore, let us proceed with the Zigzag edge termination of the honeycomb lattice. The tight-binding Hamiltonian is given by:

$$\mathcal{H}_{N-\mathrm{ZZ}} = t\sum_{l}\Big(\sum_{j=1}^{N} a^{\dagger}_{j+1,l}b_{j,l} + \sum_{j=1}^{N-1}(a^{\dagger}_{j,l}b_{j,l} + a^{\dagger}_{j,l+\delta_j}b_{j,l+\delta_j^{-1}}) + \mathrm{h.c.}\Big). \tag{10.12}$$

Taking the thermodynamic limit with imposition of PBCs in the x direction leads to the Hamiltonian given by:

$$\mathcal{H}_{N-\mathrm{ZZ}} = t\sum_{k_x}\Big(\sum_{j=1}^{N-1}(2\cos(\frac{\sqrt{3}}{2}k_x)a^{\dagger}_{k_x,j}b_{k_x,j} + a^{\dagger}_{k_x,j+1}b_{k_x,j}) + 2\cos(\frac{\sqrt{3}}{2}k_x)a^{\dagger}_{k_x,N}b_{k_x,N} + \mathrm{h.c.}\Big). \tag{10.13}$$

Once again, we define the one-particle field operators as in Eq. (10.4), and construct the Harper equation analogously to the Armchair edge:

$$\begin{aligned} E\phi^{\mathrm{A}}_{k_x,j} &= -t\,(2\cos(\frac{\sqrt{3}}{2}k_x)\phi^{\mathrm{B}}_{k_x,j} + \phi^{\mathrm{B}}_{k_x,j-1}),\\ E\phi^{\mathrm{B}}_{k_x,j} &= -t\,(2\cos(\frac{\sqrt{3}}{2}k_x)\phi^{\mathrm{A}}_{k_x,j} + \phi^{\mathrm{A}}_{k_x,j+1}). \end{aligned} \tag{10.14}$$

We proceed analogously to the Armchair edge. We keep the index j of $\phi^{\mathrm{A}}_{k_x,j}$,$\phi^{\mathrm{B}}_{k_x,j}$ free. The characteristic polynomial of the Harper equation is of the form:

$$u_{k_x,p} + v_{k_x,p}\,e^{2ipj} + w_{k_x,p}\,e^{-2ipj} = 0\,, \tag{10.15}$$

where:

$$\begin{aligned} v_{k_x,p} &= w^{*}_{k_x,p} = E^2_{k_x} - t^2\,(\vartheta^2_{k_x} + 2\vartheta_{k_x}e^{-ip} + 1),\\ u_{k_x,p} &= t^2\,(\vartheta^2_{k_x}\,(1+\zeta_p) + 2\vartheta_{k_x}\,(e^{ip} + \zeta_p e^{-ip}) + e^{2ip} + \zeta_p e^{-2ip}) - E^2_{k_x}\,(1+\zeta_p), \end{aligned} \tag{10.16}$$

where (*) denotes the complex conjugation and $\vartheta_{k_x} = 2\cos(\frac{\sqrt{3}}{2}k_x)$, $\zeta_p = e^{2ip(N+1)}$. The Harper equation is rendered trivial when p is equal to 0 and $\pm\pi$. Correspondingly, the wave functions $\phi^{\mathrm{A}}_{k_x,j}$,$\phi^{\mathrm{B}}_{k_x,j}$ vanish for all k_x and j, which implies that these solutions are unphysical. The three terms must vanish separately due to the dependence on j. The energy eigenvalues can be determined by the combination of the two zero terms $v_{k_x,p} + w_{k_x,p} = 0$:

$$E^{\pm}_{k_x,p} = \pm t\sqrt{1 + 4\cos(\frac{\sqrt{3}}{2}k_x)\cos(p) + 4\cos^2(\frac{\sqrt{3}}{2}k_x)}. \tag{10.17}$$

The values for p are given by the last remaining constraints $u_{k_x,p} = 0$. After some arithmetics we find:

$$\sin(p(N+1))\,\vartheta_{k_x} + \sin(pN) = 0\,. \tag{10.18}$$

The set of solutions to the constraint Eq. (10.18) for $N = 5$ rungs is depicted in Fig. 53 as black lines. The corresponding states are extend over the whole Zigzag ribbon.

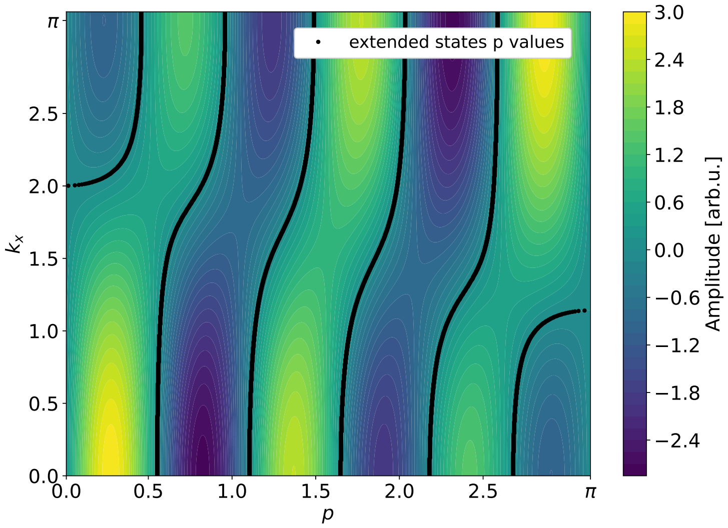

Figure 53: **Set of solutions to the constrained Eq.** (10.18) **for $N = 5$ rungs**, the solutions are indicated as black lines. Note that we have rescaled $k_x \to \frac{\sqrt{3}}{2}k_x$.

Crucially, the set of solutions for p reveals that there exists a remaining degree of freedom at critical longitudinal k_x values, corresponding to solutions for the edge states. Recall that the solution to the Harper equation for $p = 0, \pi$ was trivial. This implies that the Eq. (10.17) for $p = 0, \pi$ has to vanish for all k_x, thus:

$$E^{\pm}_{k_x} = \pm t\sqrt{1 \pm 4\cos(\frac{\sqrt{3}}{2}k_x) + 4\cos^2(\frac{\sqrt{3}}{2}k_x)} = 0\,, \tag{10.19}$$

which is only fulfilled for $k_x = \pm\frac{4\pi}{3\sqrt{3}}$ modulo $\frac{4\pi}{\sqrt{3}}$. We can however, analytically continue the transverse wavenumber p at critical k_x, such that complex p values dampen the wavefunction away from the Zigzag edge. The critical values of k_x by the constraint equation Eq. (10.18) are:

$$k_x^c = \frac{2}{\sqrt{3}}\arccos(\frac{N}{2(N+1)}), \tag{10.20}$$

such that:

$$p \to \begin{cases} 0 \pm i\eta & \text{for} \quad -\pi \le \frac{\sqrt{3}}{2}k_x < -k_x^c \\ \pi \pm i\eta & \text{for} \quad k_x^c < \frac{\sqrt{3}}{2}k_x \le \pi, \end{cases} \tag{10.21}$$

where $\eta \in \mathbb{R}$. Therefore, the edge states have energy eigenvalues:

$$E^{\pm}_{k_x,\eta} = \begin{cases} \pm t\sqrt{1 + 4\cos(\frac{\sqrt{3}}{2}k_x)\cosh(\eta) + 4\cos^2(\frac{\sqrt{3}}{2}k_x)} & \text{for} \quad -\pi \le k_x < -k_x^c \\ \pm t\sqrt{1 - 4\cos(\frac{\sqrt{3}}{2}k_x)\cosh(\eta) + 4\cos^2(\frac{\sqrt{3}}{2}k_x)} & \text{for} \quad k_x^c < k_x \le \pi. \end{cases} \tag{10.22}$$

The values of η are determined by the constraints:

$$\begin{cases} \sinh(p(N+1))\vartheta_{k_x} + \sinh(pN) = 0 & \text{for } -\pi \leq \frac{\sqrt{3}}{2}k_x < -k_x^c \\ \sinh(p(N+1))\vartheta_{k_x} - \sinh(pN) = 0 & \text{for } k_x^c < \frac{\sqrt{3}}{2}k_x \leq \pi. \end{cases} \tag{10.23}$$

The set of solutions to the constraint Eq. (10.23) for $N = 5$ rungs is depicted in Fig. 54 as black lines. The corresponding states are localized at the edges of the Zigzag ribbon.

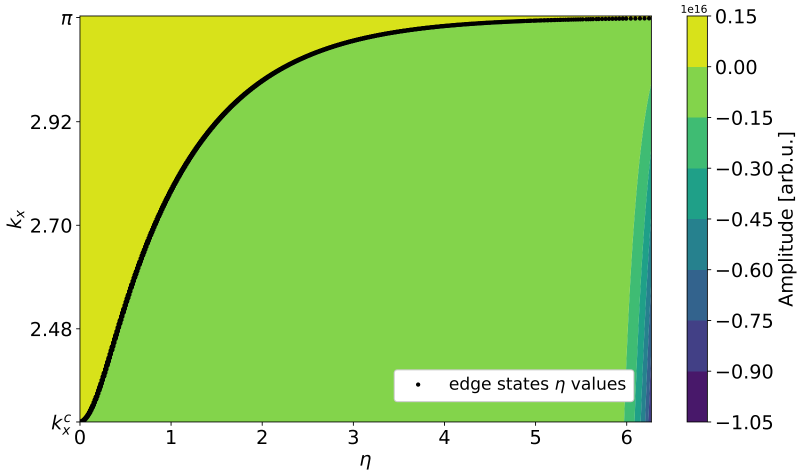

Figure 54: **Set of solutions to the constraint Eq.** (10.23) **for** $N = 5$ **rungs**, the solutions are indicates as black lines. Note that we have rescaled $k_x \rightarrow \frac{\sqrt{3}}{2}k_x$.

Each constraint yields one solution for η. The edge states have zero energy up until the critical k_x^c. These correspond to flat bands in the spectrum of the Zigzag edge and a pronounced peak in the density of states at zero energy, as depicted in Fig. 55. Once the critical value k_x^c is surpassed the localized states begin to hybridize with the bulk and the energy deviates from zero.

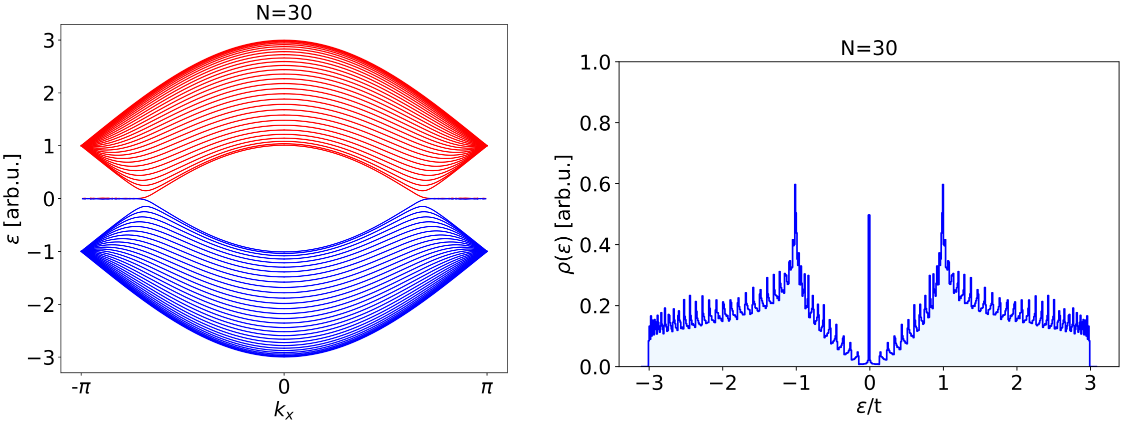

Figure 55: **Example of energy spectrum and density of state for Zigzag ribbon**. Left: The spectrum of a $N = 30$ rungs Zigzag ribbon exhibits flat bands for longitudinal wavenumber $|k_x|$ greater than a critical value $|k_x^c|$, which correspond to eigenvalues of localized edge states. Note that we have rescaled $k_x \rightarrow \frac{\sqrt{3}}{2}k_x$. Right: The edge states lead to a pronounced peak at zero energy in the density of states.

10.2 Appendix: Open boundary conditions and Haldane model

The non-trivial topology, characterized by the first Chern number, gives rise to another feature characteristic for topological insulators. Yet again, let us look at the Armchair, and Zigzag ribbon termination of the honeycomb lattice. We thread the lattice with net zero fluxes and consider **next nearest neighbor** interaction as to describe the Haldane model in this system. The two ribbons for the Haldane model are shown in Fig. 56.

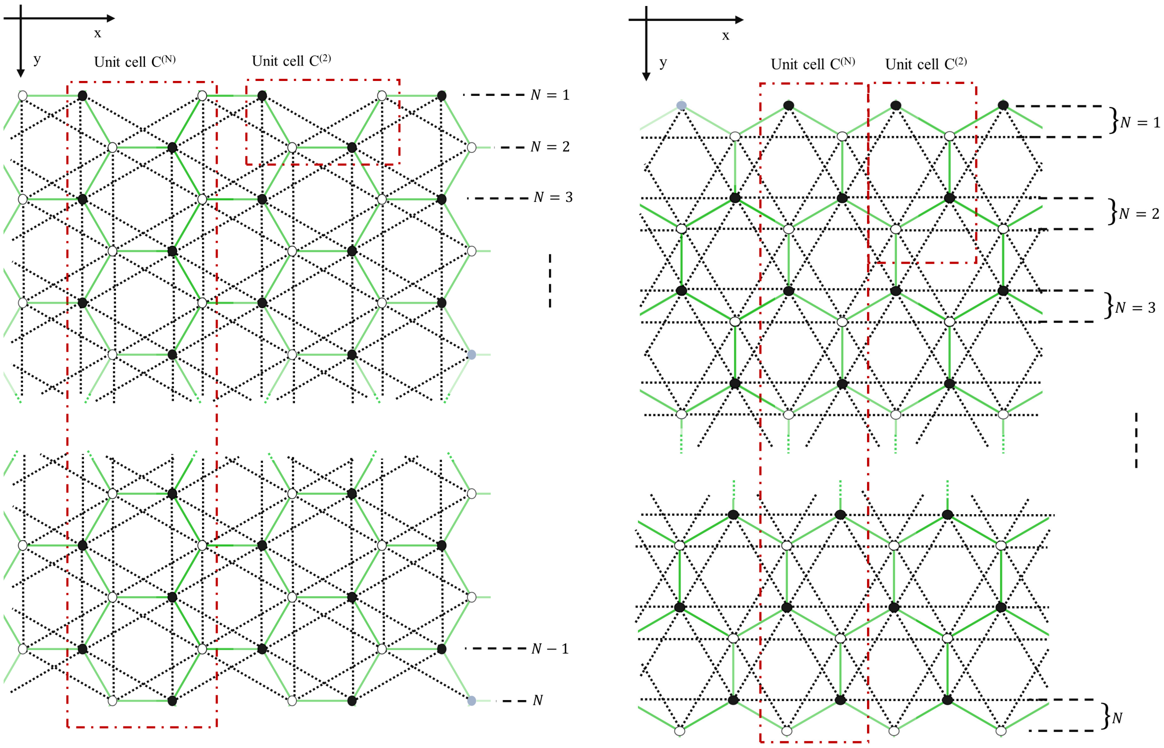

Figure 56: **Open boundary conditions in the Haldane model**. Left: Armchair ribbon. Right: Zigzag ribbon. Both ribbons are labeled by an index N indicating at which **rung** a site is located.

The procedure to construct and evaluate the Hamiltonian is analogous to the tight-binding description of the ribbons in Section 10.1. The Armchair ribbon Hamiltonian is given by:

$$\begin{aligned}\mathcal{H}_{N-\mathrm{AC}} = \sum_{l}\Big(\sum_{j=1}^{N}\big[\frac{M}{2}(a^{\dagger}_{j,l}a_{j,l} - b^{\dagger}_{j,l}b_{j,l}) + t_1 a^{\dagger}_{j,l}b_{j,l+\delta_j} + t_2 e^{i\phi}(a^{\dagger}_{j,l+1}a_{j,l} + b^{\dagger}_{j,l}b_{j,l+1})\big] \\ + \sum_{j=1}^{N-1}\big[t_1(a^{\dagger}_{j+1,l}b_{j,l} + a^{\dagger}_{j,l}b_{j+1,l}) + t_2 e^{i\phi}(a^{\dagger}_{j,l}a_{j+1,l} + a^{\dagger}_{j,l+\delta_j^{-1}}a_{j+1,l+\delta_j}) \\ + t_2 e^{-i\phi}(b^{\dagger}_{j,l}b_{j+1,l} + b^{\dagger}_{j,l+\delta_j^{-1}}b_{j+1,l+\delta_j})\big] + t_2\sum_{j=1}^{N-2}\big[e^{-i\phi}a^{\dagger}_{j,l}a_{j+2,l} + e^{i\phi}b^{\dagger}_{j,l}b_{j+2,l})\big] + \mathrm{h.c.}\Big).\end{aligned} \tag{10.24}$$

The imposition of PBCs in the x direction in the thermodynamic limit gives:

$$
\begin{aligned}
\mathcal{H}_{N\,-\,\mathrm{AC}} = \sum_{k_x} \Big(& \sum_{j=1}^{N} \big[\frac{M}{2}(a^{\dagger}_{k_x,j} a_{k_x,j} - b^{\dagger}_{k_x,j} b_{k_x,j}) + t_1\, e^{ik_x} a^{\dagger}_{k_x,j} b_{k_x,j}\big] + \sum_{j=1}^{N-1} \big[t_1\, (e^{-i\frac{k_x}{2}} a^{\dagger}_{k_x,j+1} b_{k_x,j} \\
& + e^{-i\frac{k_x}{2}} a^{\dagger}_{k_x,j} b_{k_x,j+1}) + 2\,t_2 \cos(\frac{3}{2}k_x)(e^{i\phi} a^{\dagger}_{k_x,j+1} a_{k_x,j} + e^{-i\phi} b^{\dagger}_{k_x,j} b_{k_x,j+1})\big] \\
& + \sum_{j=1}^{N-2} \big[t_2(e^{-i\phi} a^{\dagger}_{k_x,j} a_{k_x,j+2} + e^{i\phi} b^{\dagger}_{k_x,j} b_{k_x,j+2})\big] + \mathrm{h.c.}\Big).
\end{aligned}
\tag{10.25}
$$

We refrain from studing this system analytically and continue numerically by exact diagonalization. Recall, that for the tight-binding model of the honeycomb lattice no edge states were present due to the geometry of the ribbon. The spectrum turned out to have a gap closing under the condition that the transversal wavenumber is exactly $\frac{2}{3}\pi$. The spectrum of the Armchair ribbon in the Haldane model, on the other hand, is always gapless in the topological phase as depicted in Fig. 57. Thus, in the spectrum of the Armchair ribbon two distinct sets of states can be identified, the states that cross the Fermi energy at a given k_x value, indicated in blue and red, and the states that have a gapped spectrum, indicated with black lines.

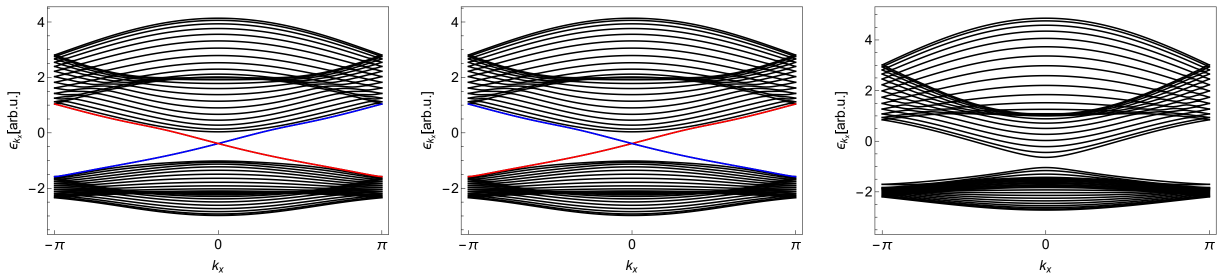

Figure 57: **Spectrum of the Armchair ribbon with $N = 26$ rungs in the Haldane model.** Left and center: The spectrum is gapless for $t_1 = 1$, $\eta = M/t_2 = 3$ and $\phi = \mp\frac{\pi}{3}$ respectively. Right: The spectrum exhibits a gap as we enter the topologically trivial phase for $t_1 = 1$, $\eta = 3$ and $\phi = \frac{\pi}{6}$. Figure reproduced from Ref. [77].

A possible measure to determine if localized edge states are present within a system is the **inverse participation ratio** (IPR) [78]. Let $H(\mathbf{k})$ be a general Bloch Hamiltonian with normalized Bloch eigenstates $\Psi_{\mathbf{k}}(\mathbf{x})$, the IPR is then defined as:

$$
\mathrm{IPR}(\mathbf{k}) = \sum_{\mathbf{x}} |\Psi_{\mathbf{k}}(\mathbf{x})|^4 . \tag{10.26}
$$

The IPR can be thought of as a measure of the inverse spatial extent of a state in the system and, as such, extended states have a vanishing IPR in the thermodynamic limit. Consider for example a one dimensional chain with N sites and a plane wave solution. Then we find that $|\Psi_k(x)| = \frac{1}{\sqrt{N}}$ and thus the IPR is $\mathrm{IPR}(k) = \frac{1}{N}$.

We compute the IPR for the Armchair ribbon with $N = 26$ rungs for 300 equidistantly spaced longitudinal wavenumbers k_x over a range of $(-\pi, \pi]$, shown in Fig. 58. The states that cross the

Fermi energy in the spectrum are indicated in red and blue. In the topological phases for $t_1 = 1$, $\eta = M/t_2 = 3$ and $\phi = \mp\frac{\pi}{3}$, shown in the left and center figure respectively, these states exhibit a higher IPR. This indicates that these states are localized and are distinct from the bulk states indicated in black.

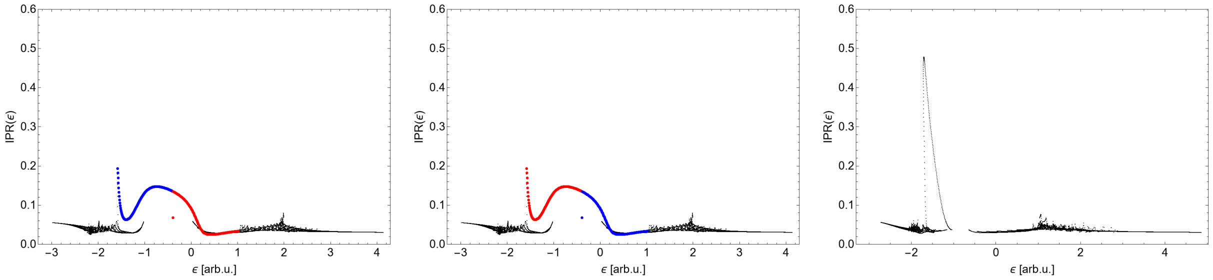

Figure 58: **IPR of the Zigzag ribbon with $N = 26$ rungs in the Haldane model**. topological phase: Left and center: for $t_1 = 1$, $\eta = M/t_2 = 3$ and $\phi = \mp\frac{\pi}{3}$ respectively. Trivial phase: right: for $t_1 = 1$, $\eta = 3$ and $\phi = \frac{\pi}{6}$.

We proceed with the Zigzag ribbon. The Hamiltonian is given by:

$$\begin{aligned}\mathcal{H}_{N-\mathrm{ZZ}} = \sum_{l}\Big(\sum_{j=1}^{N}\big[\frac{M}{2}(a^{\dagger}_{j,l}a_{j,l} - b^{\dagger}_{j,l}b_{j,l}) + t(a^{\dagger}_{j,l}b_{j,l} + a^{\dagger}_{j,l+\delta_j}b_{j,l+\delta_j^{-1}})\\ + t'e^{i\phi}(a^{\dagger}_{j,l+1}a_{j,l} + b^{\dagger}_{j,l}b_{j,l+1})\big] + \sum_{j=1}^{N-1}\big[ta^{\dagger}_{j+1,l}b_{j,l} + t'e^{i\phi(2\delta_j-1)}(a^{\dagger}_{j,l}a_{j+1,l} + b^{\dagger}_{j,l}b_{j+1,l})\\ + t'e^{-i\phi(2\delta_j-1)}(a^{\dagger}_{j,l+\delta_j}a_{j+1,l+\delta_j^{-1}} + b^{\dagger}_{j,l+\delta_j^{-1}}b_{j+1,l+\delta_j})\big] + \mathrm{h.c.}\Big).\end{aligned} \tag{10.27}$$

The imposition of PBCs in the x direction in the thermodynamic limit gives:

$$\begin{aligned}\mathcal{H}_{N-\mathrm{ZZ}} = \sum_{k_x}\Big(\sum_{j=1}^{N}\big[\frac{M}{2}(a^{\dagger}_{k_x,j}a_{k_x,j} - b^{\dagger}_{k_x,j}b_{k_x,j}) + t_1\cos(\frac{\sqrt{3}}{2}k_x)a^{\dagger}_{k_x,j}a_{k_x,j}\\ + t_2(\cos(\sqrt{3}k_x - \phi)b^{\dagger}_{k_x,j}b_{k_x,j} + \cos(\sqrt{3}k_x + \phi)b^{\dagger}_{k_x,j}b_{k_x,j})\big] + \sum_{j=1}^{N-1}\big[t_1\, a^{\dagger}_{k_x,j+1}b_{k_x,j}\\ + 2\,t_2(\cos(\frac{\sqrt{3}}{2}k_x + \phi)a^{\dagger}_{k_x,j}a_{k_x,j+1} + \cos(\frac{\sqrt{3}}{2}k_x - \phi)b^{\dagger}_{k_x,j}b_{k_x,j+1})\big] + \mathrm{h.c.}\Big).\end{aligned} \tag{10.28}$$

Analogous to the Armchair ribbon, the spectrum of the Zigzag ribbon in the Haldane model, is always gapless in the topological phase, as depicted in Fig. 57.

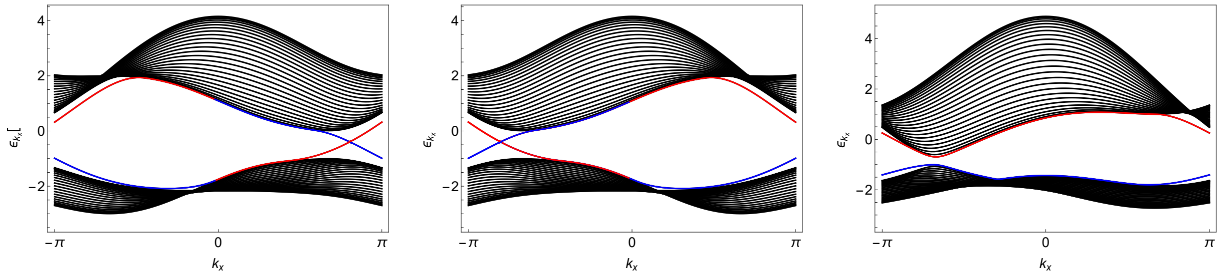

Figure 59: **Spectrum of the Zigzag ribbon with $N = 26$ rungs in the Haldane model.** Left and center: The spectrum is gapless for $t_1 = 1$, $\eta = M/t_2 = 3$ and $\phi = \mp\frac{\pi}{3}$ respectively. Right: The spectrum exhibits a gap as we enter the topologically trivial phase for $t_1 = 1$, $\eta = 3$ and $\phi = \frac{\pi}{6}$. Figure reproduced from Ref. [77].

The IPR for the Zigzag edge is shown in Fig. 60. Once again the IPR is computed for $N = 26$ rungs for 300 equidistantly spaced longitudinal wavenumbers k_x over a range of $(-\pi, \pi]$. In the topological phases for $t_1 = 1$, $\eta = M/t_2 = 3$ and $\phi = \mp\frac{\pi}{3}$, shown in the left and center figure respectively, the states indicated in red and blue exhibit a higher IPR than the states in black. This indicates that these states are localized near one of the edges. Notably, the localized states persist even in the topologically trivial phase shown in the right figure for $t_1 = 1$, $\eta = 3$ and $\phi = \frac{\pi}{6}$. These states are localized due to the geometry of the Zigzag ribbon as we have seen in the tight-binding model description in the previous section.

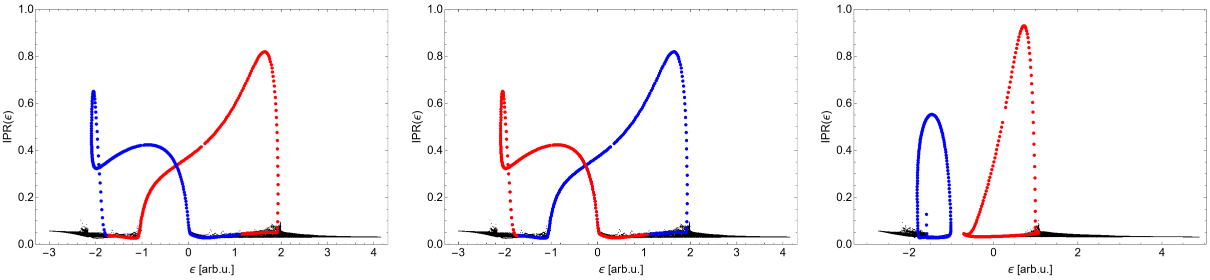

Figure 60: **IPR of the Zigzag ribbon with $N = 26$ rungs in the Haldane model.** topological phase: Left and center: for $t_1 = 1$, $\eta = M/t_2 = 3$ and $\phi = \mp\frac{\pi}{3}$ respectively. Trivial phase: right: for $t_1 = 1$, $\eta = 3$ and $\phi = \frac{\pi}{6}$.

10.3 Appendix: Point group matrix construction in GAP

In order to construct the point-group matrices M_g we use the existing HyperCells package. The algorithm requires the use of group homomorphisms to embed Δ^+ in Δ. The specificities are omitted such that the pseudo code applies in general. The pseudo code for the GAP implementations looks as follows:

Point group matrix construction pseudo code

```
Input: Triangle group signature as a list of 3 integers of the form $(2, q, p)$, index $m$ of quotient
group $\Delta/\Gamma^{(m)}$ as an integer and a function $f_\Delta(m)$ to access a specific $\Gamma^{(m)}$ in a list $I$ of tabulated
quotient groups. A symmetry operator $\tilde{g}$ in terms of generators a, b, c $\in \Delta$ as a string.
Output: Point group matrix $M_g$.
Initialize: List of tabulated quotient groups $I$.

1. Construct the presentation of $\Delta = \Delta(2, q, p)$.
2. Retrieve symmetry operator $g \in \Delta$ by multiplying generators
   a, b, c $\in \Delta$ in the sequence specified by the string $\tilde{g}$.
3. Start: normal subgroup search:
   a) Retrieve any appropriate quotient group through the function $f_\Delta(m)$ such
      that $q_m = \Delta/\Gamma^{(m)}$ with $\Delta = \Gamma^{(0)} \triangleright \Gamma^{(1)} \cdots \triangleright \Gamma^{(m)} \triangleright \cdots$ and $\Delta \triangleright \Gamma^{(m)}$.
   b) Determine the genus $\mathfrak{g}$ of the Riemann surface $\Sigma_\mathfrak{g}$ that $q_m$ acts upon.
   c) Construct $\Gamma^{(m)}$ via the kernel of the group homomorphism $\Phi : \Delta \to q_m$.
4. Start: construction of $M_g$ entries:
   a) Set $i = 1$ and $M_g = []$ as an empty list.
   b) Retrieve generator $\gamma_i^{(m)}$, with $\gamma_i^{(m)} \in \Gamma^{(m)}$.
   c) Construct word $w_i = g\gamma_i^{(m)}g^{-1} \in \Gamma^{(m)}$.
   d) Start: construction of row $i$ of $M_g$:
      i. Set $j = 1$ and $m_g = []$.
      ii. Compute $K_j(w_i)$, where $K_j(w_i)$ corresponds to the number of times the generator
          $\gamma_j^{(m)}$ of $\Gamma^{(m)}$ appears in $w_i$, where $\gamma_j^{(m)-1}$ is counted negatively.
      iii. Append $K_j(w_i)$ to $m_g$ and set $j = j + 1$.
      iv. If $i = j = 2\mathfrak{g}$ append $m_g$ to $M_g$ and stop,
          else if $j = 2\mathfrak{g}$ and $i \neq 2\mathfrak{g}$, append $m_g$ to $M_g$, set $i = i + 1$ and return to step b),
          else return to step ii .
```

10.4 Appendix: Addendum to the proof of claim 7.1:

In this section we show that $\mathscr{Z}$ as given in Eq. (7.11) indeed reduces to the simple form considered in the proof of claim 7.1. As such, let us reconsider Eq. (7.11):

$$\begin{aligned}\mathscr{Z} &= 3\,\mathscr{X}_1 \,+\, 3\,\mathscr{X}_2 \\ &\equiv 3\,\mathrm{Tr}[((VH^{-1}\mathrm{d}(HV^\dagger) \,+\, xH'^{-1}) \wedge (VH^{-1}\mathrm{d}(HV^\dagger) \,+\, H'^{-1}x) \\ &\quad -\, xH'^{-1} \wedge H'^{-1}y) \wedge (H'^{-1}x \,+\, H'^{-1}y)] \,+\, 3\,\mathrm{Tr}[(xH'^{-1})^{\wedge 2} \wedge (yH'^{-1} - H'^{-1}y)]\,.\end{aligned}$$

Let us expand the matrix-valued differential forms:

$$\begin{aligned}\mathscr{X}_2 &= \mathrm{Tr}[(xH'^{-1})^{\wedge 2} \wedge (yH'^{-1} - H'^{-1}y)] \\ &= \,\mathrm{Tr}[\mathrm{d}VV^\dagger \wedge \mathrm{d}VV^\dagger(VH\mathrm{d}V^\dagger VH^{-1}V^\dagger \,-\, V\mathrm{d}V^\dagger)] \\ &\overset{G.L.,G.C.}{=} \,-\,\mathrm{Tr}[H\mathrm{d}V^\dagger \wedge VH^{-1}\mathrm{d}V^\dagger \wedge \mathrm{d}V \,+\, \mathrm{d}V \wedge V^\dagger\mathrm{d}V \wedge \mathrm{d}V^\dagger].\end{aligned}$$

Further:

$$\begin{aligned}\mathscr{X}_1 &= \mathrm{Tr}[((VH^{-1}\mathrm{d}(HV^\dagger) \,+\, xH'^{-1}) \wedge (VH^{-1}\mathrm{d}(HV^\dagger) \,+\, H'^{-1}x) \\ &\quad -\, xH'^{-1} \wedge H'^{-1}y) \wedge (H'^{-1}x \,+\, H'^{-1}y)] \\ &= \mathrm{Tr}[(VH^{-1}\mathrm{d}(HV\dagger) \,+\, \mathrm{d}VV^\dagger) \wedge (VH^{-1}\mathrm{d}(HV^\dagger) \,+\, VH^{-1}V^\dagger\mathrm{d}VHV^\dagger) \\ &\quad \wedge (VH^{-1}\mathrm{d}(HV^\dagger) \,+\, V\mathrm{d}V^\dagger) \,-\, \mathrm{d}VV^\dagger \wedge V\mathrm{d}V^\dagger \wedge (VH^{-1}\mathrm{d}(HV^\dagger) + V\mathrm{d}V^\dagger)]\end{aligned}$$

After some algebra with repeated use of the graded cyclicity and graded Leibniz rule, we find:

$$\begin{aligned}\mathscr{X}_1 =& \mathrm{Tr}[-\mathrm{d}(HV^\dagger) \wedge \mathrm{d}(VH^{-1}) \wedge V^\dagger\mathrm{d}V \,+\, \mathrm{d}(VH^{-1}) \wedge \mathrm{d}(HV^\dagger) \wedge \mathrm{d}VV^\dagger \\ &+\, \mathrm{d}(HV^\dagger) \wedge VH^{-1}V^\dagger\mathrm{d}VV^\dagger \wedge \mathrm{d} \,-\, \mathrm{d}(VH^{-1}) \wedge V^\dagger\mathrm{d}VH \wedge \mathrm{d}V^\dagger \\ &+\, \mathrm{d}(VH^{-1}) \wedge V^\dagger\mathrm{d}VH \wedge \mathrm{d}V^\dagger \,+\, \mathrm{d}V^\dagger \wedge VH^{-1}\mathrm{d}(HV^\dagger) \wedge \mathrm{d}V \\ &+\, \mathrm{d}V \wedge VH^{-1}\mathrm{d}V^\dagger \wedge \mathrm{d}VH \,+\, \mathrm{d}V \wedge H^{-1}V^\dagger\mathrm{d}VH \wedge \mathrm{d}V^\dagger \\ &-\, \mathrm{d}V^\dagger \wedge \mathrm{d}V \wedge H^{-1}V^\dagger\mathrm{d}VH \,-\, \mathrm{d}V \wedge \mathrm{d}V^\dagger \wedge V\mathrm{d}V^\dagger].\end{aligned}$$

We see that many terms cancel each other, such as the 4th and 5th term as well as the 8th and 9th term. Other terms are canceled partially, such as the expanded 3rd and 7th term as well as the expanded 6th and 10th term. Thus, we obtain:

$$\begin{aligned}\mathscr{X}_1 =& \mathrm{Tr}[-\mathrm{d}(HV^\dagger) \wedge \Big(\mathrm{d}(VH^{-1})V^\dagger\Big) \wedge \mathrm{d}V \,+\, \mathrm{d}V\Big(V^\dagger\mathrm{d}(VH^{-1})V^\dagger V\Big)\mathrm{d}(HV^\dagger)] \\ &+\, \mathrm{Tr}[-\mathrm{d}HH^{-1} \wedge \mathrm{d}V^\dagger \wedge \mathrm{d}V \,+\, \mathrm{d}V^\dagger \wedge VH^{-1}\mathrm{d}HV^\dagger \wedge \mathrm{d}V],\end{aligned}$$

where we have inserted the identity $\mathbb{1} = V^\dagger V$ in the big parentheses in the second term. Let us rewrite the differential forms in the big parentheses:

$$\begin{aligned}\mathrm{d}(VH^{-1})V^\dagger \,&=\, \mathrm{d}VH^{-1}V^\dagger \,-\, VH^{-1}\mathrm{d}V^\dagger \,+\, V\mathrm{d}(H^{-1}V^\dagger)\,, \\ V^\dagger\mathrm{d}(VH^{-1})V^\dagger V \,&=\, V^\dagger\mathrm{d}VH^{-1} \,-\, H^{-1}\mathrm{d}V^\dagger V \,+\, \mathrm{d}(H^{-1}V^\dagger)V\,.\end{aligned} \tag{10.29}$$

This enables us to split $\mathcal{X}_1$ into two parts $\mathcal{Y}_1, \mathcal{Y}_2$, where $\mathcal{Y}_1$ is reconsidered in Section 7.1 of the main text. Let us show that the other part vanishes entirely:

$$\begin{aligned}
\mathcal{X}_1 = \mathcal{Y}_1 + \mathcal{Y}_2 \\
&\equiv \mathrm{Tr}[-\mathrm{d}V \wedge (\mathrm{d}(HV^\dagger) \wedge V\mathrm{d}(H^{-1}V^\dagger) - \mathrm{d}(H^{-1}V^\dagger)V \wedge \mathrm{d}(HV^\dagger))] \\
&\quad + (\mathrm{Tr}[-\mathrm{d}V \wedge (\mathrm{d}(HV^\dagger)(\mathrm{d}VH^{-1}V^\dagger - VH^{-1}\mathrm{d}V^\dagger) - (V^\dagger\mathrm{d}VH^{-1} - H^{-1}\mathrm{d}V^\dagger V) \wedge \mathrm{d}(HV^\dagger))] \\
&\quad + \mathrm{Tr}[-\mathrm{d}HH^{-1} \wedge \mathrm{d}V^\dagger \wedge \mathrm{d}V + \mathrm{d}V^\dagger \wedge VH^{-1}\mathrm{d}HV^\dagger \wedge \mathrm{d}V])\,,
\end{aligned}$$

thus:

$$\begin{aligned}
\mathcal{Y}_2 &= \mathrm{Tr}[-\mathrm{d}V \wedge (\mathrm{d}(HV^\dagger) \wedge \mathrm{d}VH^{-1}V^\dagger + H^{-1}\mathrm{d}V^\dagger V \wedge \mathrm{d}(HV^\dagger) \\
&\qquad - \mathrm{d}(HV^\dagger) \wedge VH^{-1}\mathrm{d}V^\dagger - V^\dagger\mathrm{d}VH^{-1} \wedge \mathrm{d}(HV^\dagger))] \\
&\qquad + \mathrm{Tr}[-\mathrm{d}HH^{-1} \wedge \mathrm{d}V^\dagger \wedge \mathrm{d}V + \mathrm{d}V^\dagger \wedge VH^{-1}\mathrm{d}HV^\dagger \wedge \mathrm{d}V] \\
&\overset{G.L.,G.C.}{=} \mathrm{Tr}[\mathrm{d}V \wedge (\mathrm{d}(HV^\dagger) \wedge VH^{-1}\mathrm{d}V^\dagger + V^\dagger\mathrm{d}VH^{-1} \wedge \mathrm{d}(HV^\dagger))] \\
&\qquad + \mathrm{Tr}[-\mathrm{d}HH^{-1} \wedge \mathrm{d}V^\dagger \wedge \mathrm{d}V + \mathrm{d}V^\dagger \wedge VH^{-1}\mathrm{d}HV^\dagger \wedge \mathrm{d}V]\,.
\end{aligned}$$

Further, expanding the remaining terms and applying the graded cyclicity and Leibniz rule repeatedly, reduces $\mathcal{Y}_2$ to:

$$\mathcal{Y}_2 = \mathrm{Tr}[H\mathrm{d}V^\dagger \wedge VH^{-1}\mathrm{d}V^\dagger \wedge \mathrm{d}V + \mathrm{d}V \wedge V^\dagger\mathrm{d}V \wedge \mathrm{d}V^\dagger]$$

and thus we see that $\mathcal{X}_2 + \mathcal{Y}_2 = 0$, therefore:

$$\mathcal{Z} = 3\,\mathcal{Y}_1 = 3\,\mathrm{Tr}[-\mathrm{d}V \wedge (\mathrm{d}(HV^\dagger) \wedge V\mathrm{d}(H^{-1}V^\dagger) - \mathrm{d}(H^{-1}V^\dagger)V \wedge \mathrm{d}(HV^\dagger))].$$

10.5 Appendix: Subgroup treegraphs and evolution of 1st Chern numbers

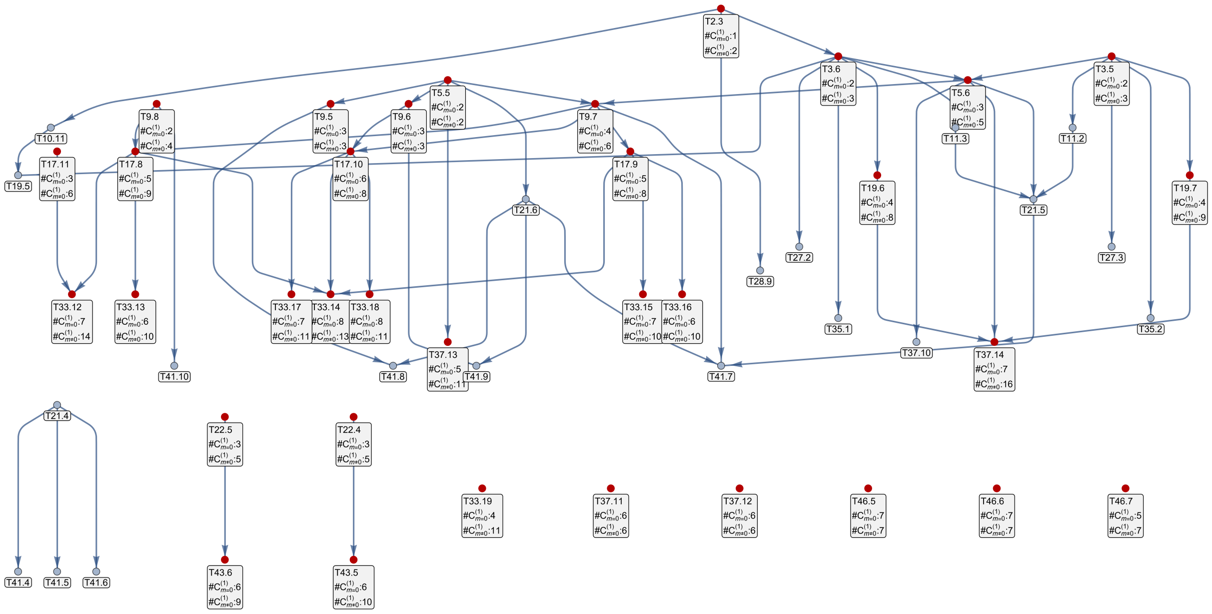

Figure 61: **Number of independent momentum-space 1st Chern numbers $\#C^{(1)}_{m=0}$, $\#C^{(1)}_{m\neq0}$ in normal subgroup tree graph for the $\{8,4\}$ Haldane model**.

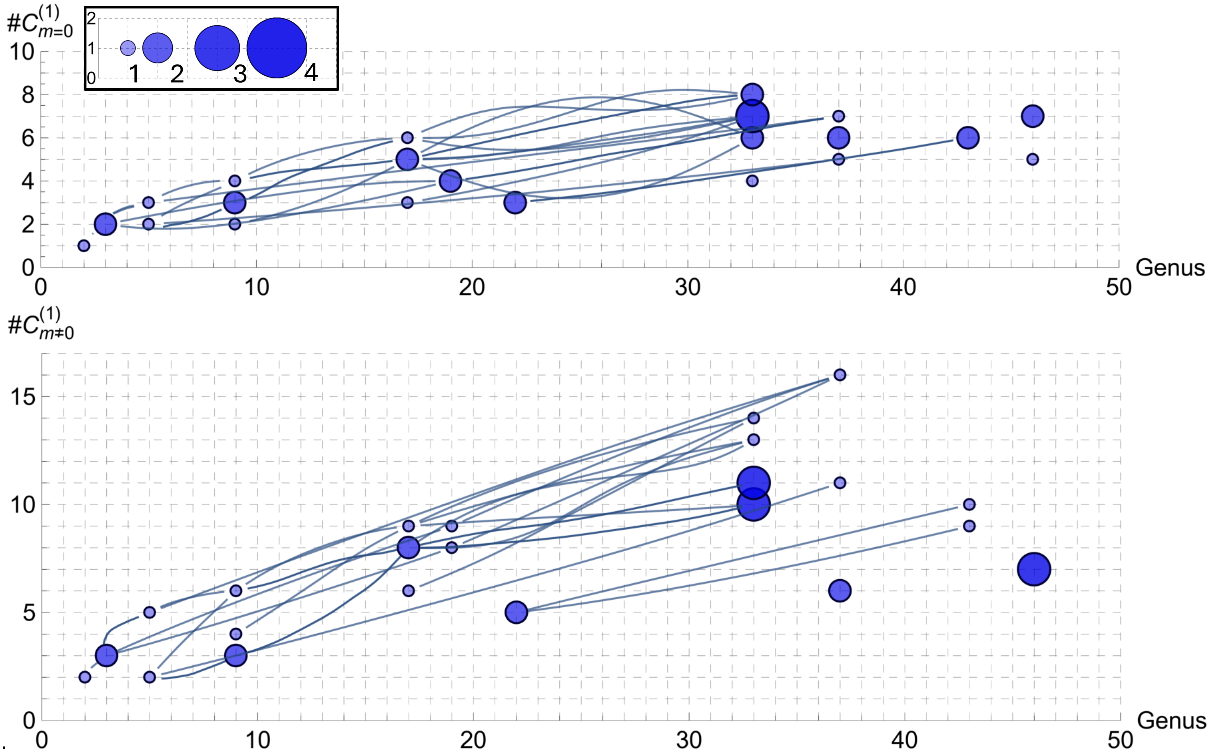

Figure 62: **Evolution of the number of momentum-space 1st Chern numbers for increasingly large supercells on the $\{8,4\}$ Haldane model**. $\#C^{(1)}_{m=0}$, $\#C^{(1)}_{m\neq0}$ plotted against genus $\mathfrak{g}$ of corresponding compactified supercell $\mathrm{T}\mathfrak{g}.n$. The radius of each disk is proportional to the number of overlapping points, shown in the inset.

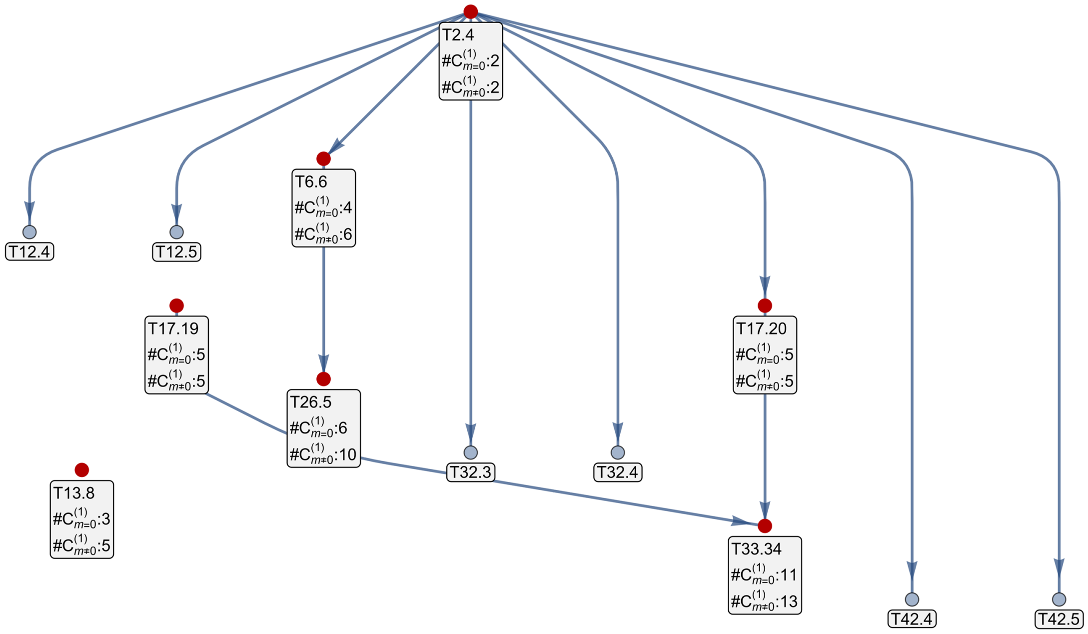

Figure 63: **Number of independent momentum-space 1st Chern numbers $\#C^{(1)}_{m=0}$, $\#C^{(1)}_{m\neq0}$ in normal subgroup tree graph for the $\{10,5\}$ Haldane model.**

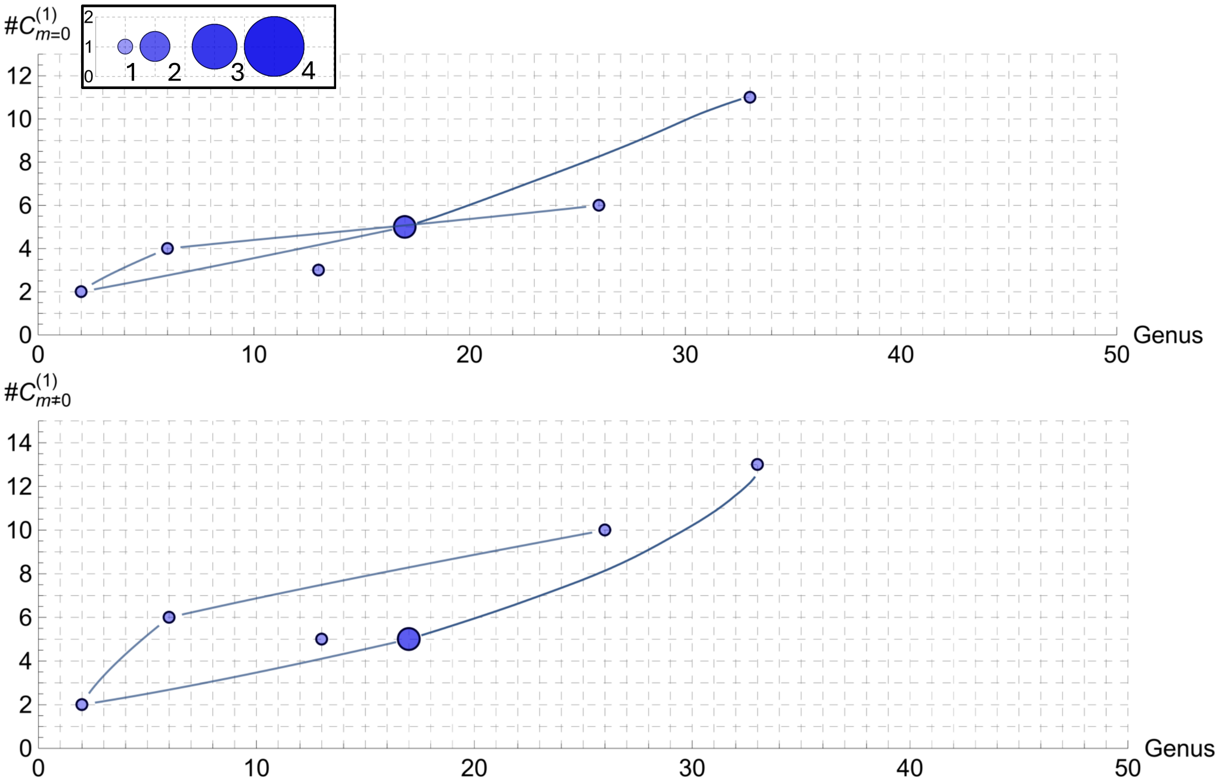

Figure 64: **Evolution of the number of momentum-space 1st Chern numbers for increasingly large supercells on the $\{10,5\}$ Haldane model.** $\#C^{(1)}_{m=0}$, $\#C^{(1)}_{m\neq0}$ plotted against genus $\mathfrak{g}$ of corresponding compactified supercell $\mathrm{T}\mathfrak{g}.n$. The radius of each disk is proportional to the number of overlapping points, shown in the inset.

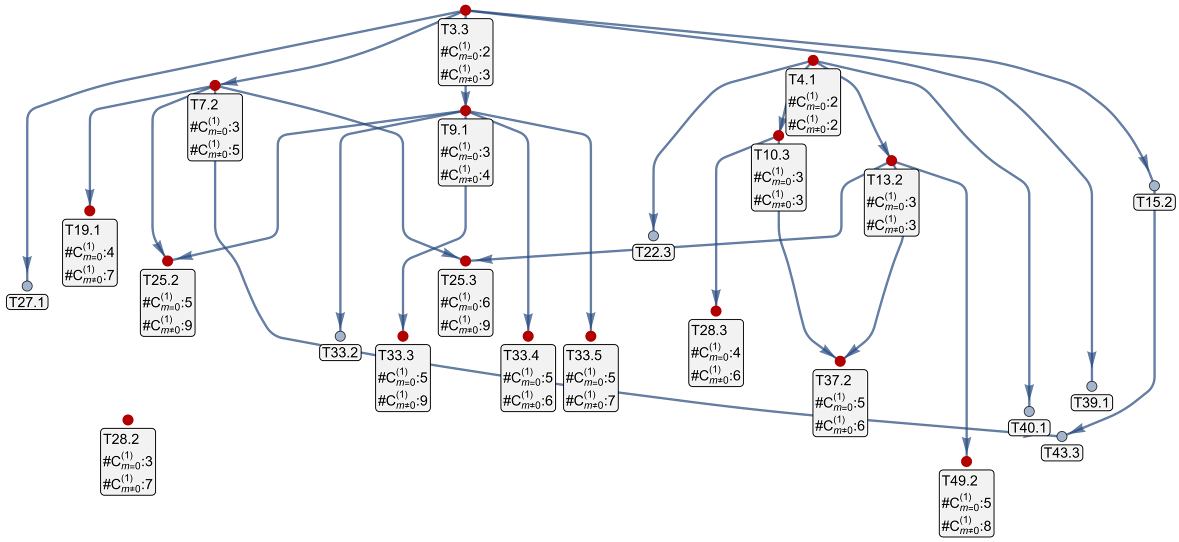

Figure 65: **Number of independent momentum-space 1st Chern numbers $\#C^{(1)}_{m=0}$, $\#C^{(1)}_{m\neq0}$ in normal subgroup tree graph for the $\{12,3\}$ Haldane model.**

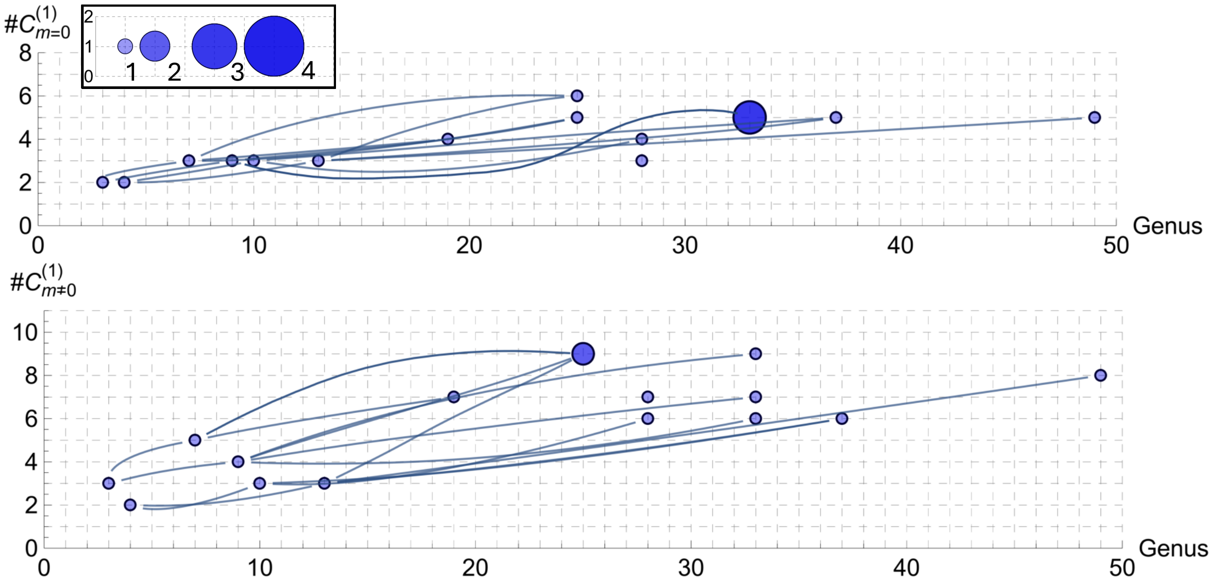

Figure 66: **Evolution of the number of momentum-space 1st Chern numbers for increasingly large supercells on the $\{12,3\}$ Haldane model.** $\#C^{(1)}_{m=0}$, $\#C^{(1)}_{m\neq0}$ plotted against genus $\mathfrak{g}$ of corresponding compactified supercell $\mathrm{T}\mathfrak{g}.n$. The radius of each disk is proportional to the number of overlapping points, shown in the inset.

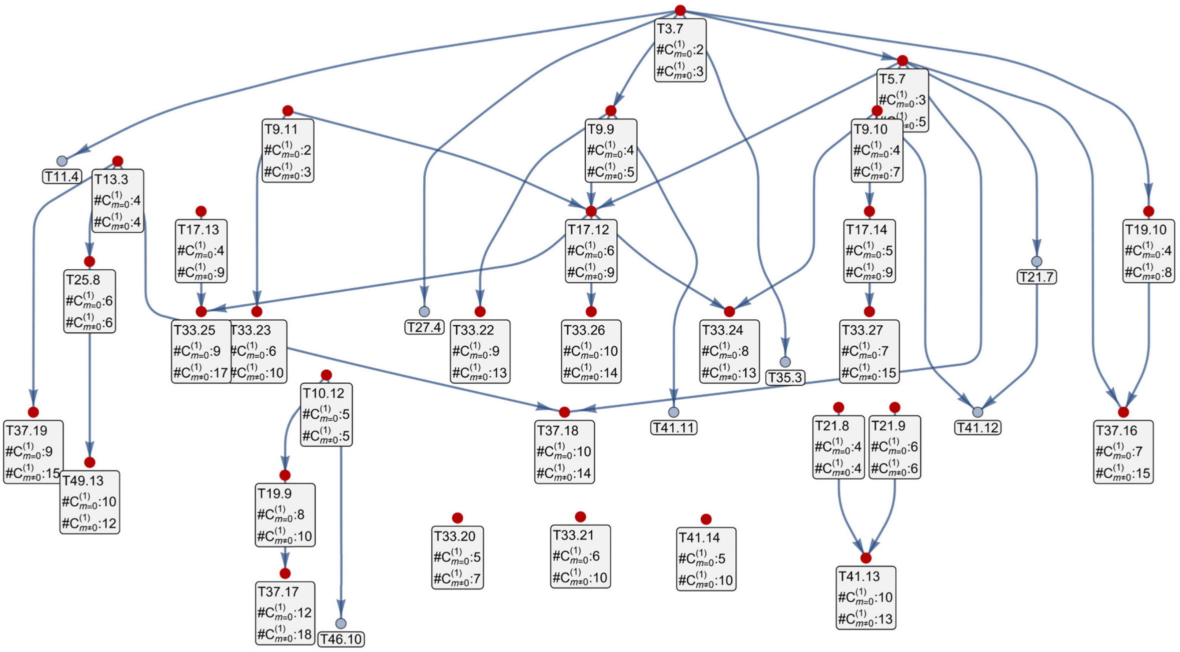

Figure 67: **Number of independent momentum-space 1st Chern numbers $\#C^{(1)}_{m=0}$, $\#C^{(1)}_{m\neq0}$ in normal subgroup tree graph for the $\{12,4\}$ Haldane model.**

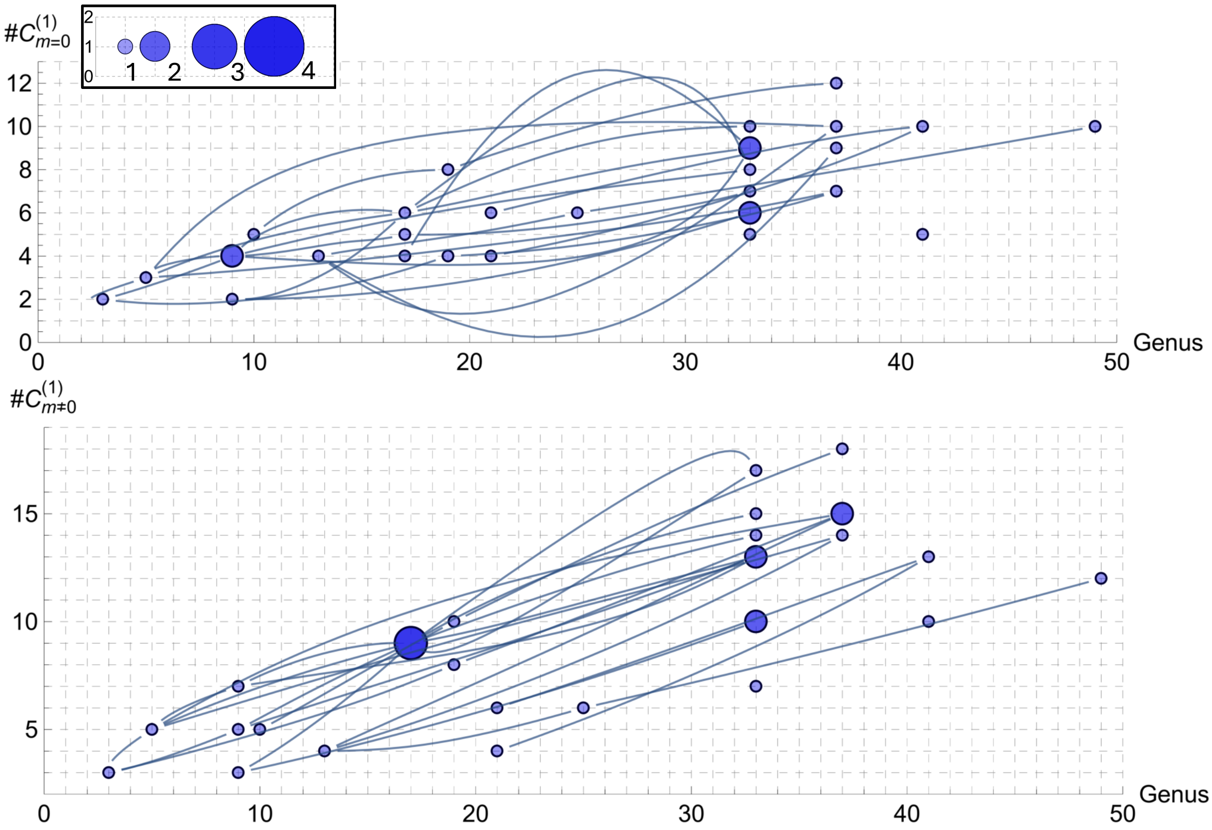

Figure 68: **Evolution of the number of momentum-space 1st Chern numbers for increasingly large supercells on the $\{12,4\}$ Haldane model.** $\#C^{(1)}_{m=0}$, $\#C^{(1)}_{m\neq0}$ plotted against genus $\mathfrak{g}$ of corresponding compactified supercell T$\mathfrak{g}.n$. The radius of each disk is proportional to the number of overlapping points, shown in the inset.

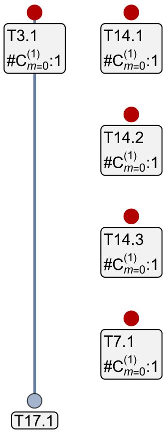

Figure 69: **Number of independent momentum-space 1st Chern numbers** $\#C^{(1)}_{m=0}$**,** $\#C^{(1)}_{m\neq 0}$ **in normal subgroup tree graph for the** $\{7,3\}$ **Haldane model**.

10.6 Appendix: Tabulated numbers of independent 1st Chern numbers

$\Delta^+/\Gamma^{(m)}(2,3,8)$	$\#C^{(1)}_{m=0}$	$\#C^{(1)}_{m\neq0}$
T2.1	1	2
T3.2	1	1
T5.1	2	3
T8.1	1	1
T8.2	1	1
T16.1	2	2
T17.2	3	4
T22.1	2	4
T22.2	2	4
T33.1	4	7
T46.2	4	7
T46.3	3	4

$\Delta^+/\Gamma^{(m)}(2,4,8)$	$\#C^{(1)}_{m=0}$	$\#C^{(1)}_{m\neq0}$
T2.3	1	2
T3.5	2	3
T3.6	2	3
T5.5	2	2
T5.6	3	5
T9.5	3	3
T9.6	3	3
T9.7	4	6
T9.8	2	4
T17.8	5	9
T17.9	5	8
T17.10	6	8
T17.11	3	6
T19.6	4	6
T19.7	4	9
T22.4	3	5
T22.5	3	5
T33.12	7	14
T33.13	6	10
T33.14	8	13
T33.15	7	10
T33.16	6	10
T33.17	7	11
T33.18	8	11
T33.19	4	11
T37.11	6	6
T37.12	6	6
T37.13	5	11
T37.14	7	16
T43.5	6	5
T43.6	6	9
T46.5	7	7
T46.6	7	7
T46.7	5	7

$\Delta^+/\Gamma^{(m)}(2,4,12)$	$\#C^{(1)}_{m=0}$	$\#C^{(1)}_{m\neq0}$
T3.7	2	3
T5.7	3	5
T9.9	4	5
T9.10	4	7
T9.11	2	3
T10.12	5	5
T13.3	4	4
T17.12	6	9
T17.13	4	9
T17.14	5	9
T19.9	8	10
T19.10	4	8
T21.8	4	4
T21.9	6	6
T25.8	6	6
T33.20	5	7
T33.21	6	10
T33.22	9	13
T33.23	6	10
T33.24	8	13
T33.25	9	17
T33.26	10	14
T33.27	7	15
T37.16	7	15
T37.17	12	18
T37.18	10	14
T37.19	9	15
T41.13	10	13
T41.14	5	10
T49.13	10	12

$\Delta^+/\Gamma^{(m)}(2,5,10)$	$\#C^{(1)}_{m=0}$	$\#C^{(1)}_{m\neq0}$
T2.4	2	2
T6.6	4	6
T13.8	3	5
T17.19	5	5
T17.20	5	5
T26.5	6	10
T33.34	11	13

$\Delta^+/\Gamma^{(m)}(2,3,7)$	$\#C^{(1)}_{m=0}$
T3.1	1
T7.1	1
T14.1	1
T14.2	1
T14.3	1

$\Delta^+/\Gamma^{(m)}(2,4,6)$	$\#C^{(1)}_{m=0}$	$\#C^{(1)}_{m\neq0}$
T2.2	1	2
T3.4	1	1
T4.3	1	1
T5.4	2	3
T6.2	1	1
T9.3	3	5
T9.4	2	2
T10.8	2	4
T10.9	3	4
T11.1	2	2
T15.5	2	2
T17.5	3	3
T17.6	3	4
T17.7	4	6
T21.3	3	5
T28.8	5	10
T29.1	4	5
T31.3	4	6
T33.8	4	4
T33.9	6	9
T33.10	5	9
T33.11	6	11
T37.9	6	7
T41.3	5	11
T49.8	5	7

$\Delta^+/\Gamma^{(m)}(2,3,12)$	$\#C^{(1)}_{m=0}$	$\#C^{(1)}_{m\neq0}$
T3.3	2	3
T4.1	2	2
T7.2	3	5
T9.1	3	4
T10.3	3	3
T13.2	3	3
T19.1	4	7
T25.2	5	9
T25.3	6	9
T28.2	3	7
T28.3	4	6
T33.3	5	9
T33.4	5	6
T33.5	5	7
T37.2	5	6
T49.2	5	8

Table 6: **Number of independent momentum-space first Chern numbers**, for compactified supercells T$\mathfrak{g}.n$ up to genus $\mathfrak{g} < 50$, and corresponding BZ torus $\mathbb{T}^{2\mathfrak{g}}$ and BZ$^{(m,1)}$ (3.77), constrained by hyperbolic lattice symmetries $I_{m=0} = \{\mathrm{a}\mathcal{T}, \mathrm{b}\mathcal{T}, \mathrm{c}\mathcal{T}\}, I_{m\neq0} = \{\mathrm{z}^2, \mathrm{b}\mathcal{T}, \mathrm{c}\mathcal{T}\}$

10.7 Appendix: Tabulated numbers of independent 2nd Chern numbers

$\Delta^+/\Gamma^{(m)}(2,3,12)$	$\#C^{(2)}_{m=0}$	$\#C^{(2)}_{m\neq 0}$
T3.3	2	3
T4.1	2	3
T7.2	10	16
T9.1	13	23

$\Delta^+/\Gamma^{(m)}(2,4,12)$	$\#C^{(2)}_{m=0}$	$\#C^{(2)}_{m\neq 0}$
T3.7	2	3
T5.7	9	15
T9.9	23	39
T9.10	28	50
T9.11	26	41

$\Delta^+/\Gamma^{(m)}(2,4,8)$	$\#C^{(2)}_{m=0}$	$\#C^{(2)}_{m\neq 0}$
T2.3	1	1
T3.5	2	3
T3.6	2	3
T5.5	3	6
T6.6	6	10
T9.5	16	30
T9.6	18	35
T9.7	22	42
T9.8	25	42

$\Delta^+/\Gamma^{(m)}(2,5,10)$	$\#C^{(2)}_{m=0}$	$\#C^{(2)}_{m\neq 0}$
T2.4	1	1
T6.6	11	21

$\Delta^+/\Gamma^{(m)}(2,3,7)$	$\#C^{(2)}_{m=0}$
T3.1	1
T7.1	3

Table 7: **Number of independent 2nd Chern numbers**, for compactified supercells T$\mathfrak{g}.n$ up to genus $\mathfrak{g} < 10$, and corresponding BZ torus $\mathbb{T}^{2\mathfrak{g}}$ and BZ$^{(m,1)}$ (3.77), constrained by hyperbolic lattice symmetries $I_{m=0} = \{\mathrm{a}\mathcal{T}, \mathrm{b}\mathcal{T}, \mathrm{c}\mathcal{T}\}\,, I_{m\neq 0} = \{\mathrm{z}^2, \mathrm{b}\mathcal{T}, \mathrm{c}\mathcal{T}\}$

The tabulated numbers of independent 2nd Chern number for the $\{6,4\}$ and $\{8,3\}$-lattices can be found in the main text in Table 4.

11 References

[1] P. M. Lenggenhager, J. Maciejko and T. Bzdušek. HyperBloch: A Mathematica package for hyperbolic tight-binding models and the supercell method. `https://github.com/patrick-lenggenhager/HyperBloch`. (2023). DOI: `10.5281/zenodo.10222865`.

[2] P. M. Lenggenhager, J. Maciejko and T. Bzdušek. HyperCells: A GAP package for constructing primitive cells and supercells of hyperbolic lattices. `https://github.com/patrick-lenggenhager/HyperCells`. (2023). DOI: `10.5281/zenodo.10222598`.

[3] P. M. Lenggenhager, J. Maciejko and T. Bzdušek, "Non-Abelian Hyperbolic Band Theory from Supercells", Phys. Rev. Lett. **131**, 226401 (2023).

[4] N. P. Breuckmann, C. Vuillot, E. Campbell, A. Krishna and B. M. Terhal, "Hyperbolic and semi-hyperbolic surface codes for quantum storage", Quantum Sci. Technol. **2**, 035007 (2017).

[5] P. Basteiro, G. D. Giulio, J. Erdmenger, J. Karl, R. Meyer and Z.-Y. Xian, "Towards explicit discrete holography: Aperiodic spin chains from hyperbolic tilings", SciPost Phys. **13**, 103 (2022).

[6] H. Yan, "Hyperbolic fracton model, subsystem symmetry, and holography", Phys. Rev. B **99**, 155126 (2019).

[7] A. Chen, Y. Guan, P. M. Lenggenhager, J. Maciejko, I. Boettcher and T. Bzdušek, "Symmetry and topology of hyperbolic Haldane models", Phys. Rev. B **108**, 085114 (2023).

[8] Z.-R. Liu, C.-B. Hua, T. Peng, R. Chen and B. Zhou, "Higher-order topological insulators in hyperbolic lattices", Phys. Rev. B **107**, 125302 (2023).

[9] J. Sun, C.-A. Li, S. Feng and H. Guo, "Hybrid higher-order skin-topological effect in hyperbolic lattices", Phys. Rev. B **108**, 075122 (2023).

[10] Y.-L. Tao and Y. Xu, "Higher-order topological hyperbolic lattices", Phys. Rev. B **107**, 184201 (2023).

[11] T. Tummuru, A. Chen, P. M. Lenggenhager, T. Neupert, J. Maciejko and omáš Bzdušek, Hyperbolic Non-Abelian Semimetal, Phys. Rev. Lett. **132**, 206601 (2024).

[12] T. Bzdušek and J. Maciejko, "Flat bands and band-touching from real-space topology in hyperbolic lattices", Phys. Rev. B **106**, 155146 (2022).

[13] D. M. Urwyler, P. M. Lenggenhager, I. Boettcher, R. Thomale, T. Neupert and T. Bzdušek, "Hyperbolic Topological Band Insulators", Phys. Rev. Lett. **129**, 246402 (2022).

[14] A. J. Kollár, M. Fitzpatrick and A. A. Houck, "Hyperbolic lattices in circuit quantum electrodynamics", Nature **571**, 45–50 (2019).

[15] P. M. Lenggenhager, A. Stegmaier, L. K. Upreti, T. Hofmann, T. Helbig, A. Vollhardt, M. Greiter, C. H. Lee, S. Imhof, H. Brand, T. Kießling, I. Boettcher, T. Neupert, R. Thomale and T. Bzdušek, "Simulating hyperbolic space on a circuit board", Nat. Commun. **13**, 4373 (2022).

[16] I. Boettcher, A. V. Gorshkov, A. J. Kollár, J. Maciejko, S. Rayan and R. Thomale, "Crystallography of hyperbolic lattices", Phys. Rev. B **105**, 125118 (2022).

[17] N. Cheng, F. Serafin, J. McInerney, Z. Rocklin, K. Sun and X. Mao, "Band theory and boundary modes of high-dimensional representations of infinite hyperbolic lattices", Phys. Rev. Lett. **129**, 088002 (2022).

[18] J. Maciejko and S. Rayan, "Automorphic Bloch theorems for hyperbolic lattices", Proc. Natl. Acad. Sci. U.S.A. **119**, e2116869119 (2022).

[19] J. Maciejko and S. Rayan, "Hyperbolic band theory", Sci. Adv. **7**, eabe9170 (2021).

[20] F. D. M. Haldane, "Model for a Quantum Hall Effect without Landau Levels: Condensed-Matter Realization of the "Parity Anomaly" ", Phys. Rev. Lett. **61**, 2015–2018 (1988).

[21] G. Shankar and J. Maciejko, "Hyperbolic lattices and two-dimensional Yang-Mills theory", arXiv:2309.03857 (2023).

[22] A. Bhattacharya and B. Pal, "Flat bands and nontrivial topological properties in an extended Lieb lattice", Phys. Rev. B **100**, 235145 (2019).

[23] W. Jiang, M. Kang, H. Huang, H. Xu, T. Low and F. Liu, "Topological band evolution between Lieb and kagome lattices", Phys. Rev. B **99**, 125131 (2019).

[24] C.-K. Chiu, J. C. Y. Teo, A. P. Schnyder and S. Ryu, "Classification of topological quantum matter with symmetries", Rev. Mod. Phys. **88**, 035005 (2016).

[25] Z. Gong, Y. Ashida, K. Kawabata, K. Takasan, S. Higashikawa and M. Ueda, "Topological Phases of Non-Hermitian Systems", Phys. Rev. X **8**, 031079 (2018).

[26] K. Kawabata, K. Shiozaki, M. Ueda and M. Sato, "Symmetry and Topology in Non-Hermitian Physics", Phys. Rev. X **9**, 041015 (2019).

[27] P. M. Lenggenhager, "Emerging avenues in band theory: multigap topology and hyperbolic lattices". (ETH Zürich, 2023).

[28] C. J. Bradley and A. P. Cracknell. "The mathematical theory of symmetry in solids: representation theory for point groups and space groups". (Clarendon Press, Oxford, 1972).

[29] M. S. Dresselhaus, G. Dresselhaus and A. Jorio. "Group theory: Application to the physics of condensed matter". (Springer, Berlin, 2008).

[30] E. Dobardžić, M. Dimitrijević and M. V. Milovanović, "Generalized Bloch theorem and topological characterization", Phys. Rev. B **91**, 125424 (2015).

[31] M. Fruchart, D. Carpentier and K. Gawędzki, "Parallel transport and band theory in crystals", Europhys. Lett. **106**, 60002 (2014).

[32] A. Chen, J. Maciejko and I. Boettcher, "Anderson localization transition in disordered hyperbolic lattices", arXiv:2310.07978 (2024).

[33] R. Mosseri and J. Vidal, "Density of states of tight-binding models in the hyperbolic plane", Phys. Rev. B **108**, 035154 (2023).

[34] M. Ruzzene, E. Prodan and C. Prodan, "Dynamics of elastic hyperbolic lattices", Extreme Mech. Lett. **49**, 101491 (2021).

[35] J. G. Ratcliffe, "Foundations of Hyperbolic Manifolds.", Third Edition. Graduate Texts in Mathematics, Springer Nature Switzerland AG **149** (2019).

[36] J. W. Cannon, W. J. Floyd, R. Kenyon and W. R. Parry. "Hyperbolic geometry," in Flavors of geometry, (Cambridge University Press, Cambridge, England, 1997), Vol. 31.

[37] J. M. Dewhurst, "Hilbert's theorem on immersion of the hyperbolic plane". (University of Chicago REU, 2020).

[38] S. Weinberg. "Gravitation and Cosmology: Principles and Applications of the General Theory of Relativity". (John Wiley and Sons, New York, 1972).

[39] M. Conder. "Quotients of triangle groups acting on surfaces of genus 2 to 101", (2007).

[40] M. Nakahara, "Geometry, Topology and Physics". (CRC Press, Boca Raton, FL, 2003).

[41] A. L. Edmonds, J. H. Ewing and R. S. Kulkarni, "Regular tessellations of surfaces and (p,q,2)-triangle groups", Ann. Math. **116** (1982).

[42] F. R. Lux and E. Prodan, "Converging Periodic Boundary Conditions and Detection of Topological Gaps on Regular Hyperbolic Tessellations", Phys. Rev. Lett. **131**, 176603 (2023).

[43] F. R. Lux and E. Prodan, "Spectral and Combinatorial Aspects of Cayley-Crystals", Ann. Henri Poincaré (2023).

[44] O. Derzhko, J. Richter and M. Maksymenko, "Strongly correlated flat-band systems: The route from Heisenberg spins to Hubbard electrons", Int. J. Mod. Phys. B **29**, 1530007 (2015).

[45] M. Fruchart and D. Carpentier, "An introduction to topological insulators", C. R. Phys. **14**, 779–815 (2013).

[46] M. Z. Hasan and C. L. Kane, "Colloquium: Topological insulators", Rev. Mod. Phys. **82**, 3045–3067 (2010).

[47] S. Q. Shen, "Topological Insulators, Dirac Equation in Condensed Matter", Springer Singapore (2017).

[48] C.-Z. Chang, C.-X. Liu and A. H. MacDonald, "Colloquium: Quantum anomalous Hall effect", Rev. Mod. Phys. **95**, 011002 (2023).

[49] R. Shankar, Quantum Field Theory and Condensed Matter: An Introduction. (Cambridge University Press, 2017).

[50] D. Vanderbilt, "Berry Phases in Electronic Structure Theory: Electric Polarization, Orbital Magnetization and Topological Insulators". (Cambridge University Press, 2018).

[51] M. V. Berry, "Quantal Phase Factors Accompanying Adiabatic Changes", Proc. R. Soc. Lond. A **392**, 45–57 (1984).

[52] M. E. Peskin and D. V. Schroeder. "An Introduction to quantum field theory". (Addison-Wesley, Reading, USA, 1995).

[53] T. Fukui, Y. Hatsugai and H. Suzuki, "Chern Numbers in Discretized Brillouin Zone: Efficient Method of Computing (Spin) Hall Conductances", J. Phys. Soc. Japan **74**, 1674–1677 (2005).

[54] M. Mochol-Grzelak, A. Dauphin, A. Celi and M. Lewenstein, "Efficient algorithm to compute the second Chern number in four dimensional systems", Quantum Sci. Technol. **4**, 014009 (2018).

[55] B. Xie, H.-X. Wang, X. Zhang, P. Zhan, J.-H. Jiang, M. Lu and Y. Chen, "Higher-order band topology", Nat. Rev. Phys. **3**, 520–532 (2021).

[56] Y.-B. Yang, J.-H. Wang, K. Li and Y. Xu, "Higher-order topological phases in crystalline and non-crystalline systems: a review", J. Phys. Condens. Matter **36**, 283002 (2024).

[57] W. A. Benalcazar, B. A. Bernevig and T. L. Hughes, "Electric multipole moments, topological multipole moment pumping, and chiral hinge states in crystalline insulators", Phys. Rev. B **96**, 245115 (2017).

[58] W. A. Benalcazar, T. Li and T. L. Hughes, "Quantization of fractional corner charge in C_n-symmetric higher-order topological crystalline insulators", Phys. Rev. B **99**, 245151 (2019).

[59] Y. Yang, W. Zhou, C. Shu and X. Li, "Topological phase transition on the ruby lattice with Rashba spin–orbit coupling and an exchange field", Physica B Condens. Matter **666**, 415118 (2023).

[60] F. Wilczek and A. Zee, "Appearance of Gauge Structure in Simple Dynamical Systems", Phys. Rev. Lett. **52**, 2111–2114 (1984).

[61] Z. Y. Chen, Z. Zhang, S. A. Yang and Y. X. Zhao, "Classification of time-reversal-invariant crystals with gauge structures", Nat. Commun. **14**, 743 (2023).

[62] T. Li, P. Zhu, W. A. Benalcazar and T. L. Hughes, "Fractional disclination charge in two-dimensional C_n-symmetric topological crystalline insulators", Phys. Rev. B **101**, 115115 (2020).

[63] S. Manna, S. Nandy and B. Roy, "Higher-order topological phases on fractal lattices", Phys. Rev. B **105**, L201301 (2022).

[64] Y. Liu, S. Leung, F.-F. Li, Z.-K. Lin, X. Tao, Y. Poo and J.-H. Jiang, "Bulk–disclination correspondence in topological crystalline insulators", Nature **589**, 381–385 (2021).

[65] J. K. Asbóth, L. Oroszlány and A. Pályi. "A Short Course on Topological Insulators: Band-Structure Topology and Edge States in One and Two Dimensions, Lecture Notes in Physics", (Springer, 2019), Vol. 919.

[66] N. Feng, M. Gillespie and K. Crane, "Winding Numbers on Discrete Surfaces", ACM Trans. Graph. **42**, 1–17 (2023).

[67] N. Hatano and D. R. Nelson, "Vortex pinning and non-Hermitian quantum mechanics", Phys. Rev. B **56**, 8651–8673 (1997).

[68] S. Ryu, A. P. Schnyder, A. Furusaki and A. W. W. Ludwig, "Topological insulators and superconductors: tenfold way and dimensional hierarchy", New J. Phys. **12**, 065010 (2010).

[69] M. Fecko. "Differential Geometry and Lie Groups for Physicists". (Cambridge University Press, 2006).

[70] T. Bzdušek. "Matrix manipulations with Levi-Civita symbol". 2023. URL: `https://math.stackexchange.com/q/4638444` (visited on 03/18/2024).

[71] R. Mosseri and J. Sadoc, "The Bethe lattice: a regular tiling of the hyperbolic plane", J. physique, Lett. **43**, 249–252 (1982).

[72] P. Mnëv, "Discrete Path Integral Approach to the Selberg Trace Formula for Regular Graphs", Commun. Math. Phys. **274**, 233–241 (2007).

[73] R. Gross and A. Marx, "Festkörperphysik". (Oldenbourg Wissenschaftsverlag, 2012).

[74] S. Das, S. S. Mullick and P. Suganthan, "Recent advances in differential evolution – An updated survey", Swarm Evol. Comput. **27**, 1–30 (2016).

[75] D. Holt and T. GAP Team, kbmag, Knuth-Bendix on Monoids and Automatic Groups, Version 1.5.11. Refereed GAP package (2023).

[76] K. Wakabayashi, K. Sasaki, T. Nakanishi and T. Enoki, "Electronic states of graphene nanoribbons and analytical solutions", Sci. Technol. Adv. Mater. **11**, 054504 (2010).

[77] N. Hao, P. Zhang, Z. Wang, W. Zhang and Y. Wang, "Topological edge states and quantum Hall effect in the Haldane model", Phys. Rev. B **78**, 075438 (2008).

[78] B. Kramer and A. MacKinnon, "Localization: theory and experiment", Rep. Prog. Phys. **56**, 1469 (1993).